TOPOLOGY AND GENERATIVE OPTIMIZATION OF SWITCHED RELUCTANCE MACHINES FOR TORQUE RIPPLES AND RADIAL FORCE REDUCTION

TOPOLOGY AND GENERATIVE OPTIMIZATION OF SWITCHED RELUCTANCE MACHINES FOR TORQUE RIPPLES AND RADIAL FORCE REDUCTION

BY

MOHAMED ABDALMAGID, B.Sc., M.Sc.

A THESIS

SUBMITTED TO THE DEPARTMENT OF ELECTRICAL AND COMPUTER ENGINEERING

AND THE SCHOOL OF GRADUATE STUDIES

OF MCMASTER UNIVERSITY

IN PARTIAL FULFILMENT OF THE REQUIREMENTS

FOR THE DEGREE OF

DOCTOR OF PHILOSOPHY

Doctor of Philosophy (2022) McMaster University

(Electrical and Computer Engineering) Hamilton, Ontario, Canada

TITLE:	TOPOLOGY AND GENERATIVE OPTIMIZATION OF SWITCHED RELUCTANCE MACHINES FOR TORQUE RIPPLES AND RADIAL FORCE REDUCTION
AUTHOR:	Mohamed Abdalmagid M.Sc., (Electrical Engineering) Cairo University, Giza, Egypt
SUPERVISORS:	Mohamed Bakr and Ali Emadi
NUMBER OF PAGES:	xxxviii, 266

Abstract

Switched reluctance machines (SRMs) have recently attracted more interest in many applications due to the volatile prices of rare-earth permanent magnets (PMs) used in permanent magnet synchronous machines (PMSMs). They also have rugged construction and can operate at high speeds and high temperatures. However, acoustic noise and high torque ripples, in addition to the relatively low torque density, present significant challenges. Geometry and topology optimization are applied to overcome these challenges and enable SRMs to compete with PMSMs.

Key geometric design parameters are optimized to minimize various objective functions within geometry optimization. On the other hand, the material distribution in a particular design space within the machine domain may be optimized using topology optimization. We discuss how these techniques are applied to optimize the geometries and topologies of SRMs to enhance machine performance. As optimizing the machine geometry and material distribution at the design phase is of substantial significance, this work offers a comprehensive literature review on the current state of the art and the possible trends in the optimization techniques of SRMs. The thesis also reviews different configurations of SRMs and stochastic and deterministic optimization techniques utilized in optimizing different configurations of the machine.

This thesis introduces a new ON/OFF optimization method based on the line

search method to overcome the limitations of the conventional annealing-based ON/OFF optimization. The proposed method shows a faster convergence to optimal solutions than the conventional annealing-based ON/OFF method. The thesis also compares the performance of the generative optimization and the topology optimization of a 6/14 switched reluctance machine with the proposed method and the conventional method. The two methods are applied to two different design domains of the machine for topology and generative optimization and the results are compared to the results of the annealing-based ON/OFF method. The results show the effectiveness of the newly proposed method.

A new technique has been introduced in this thesis for reducing the time of calculating stator radial force density waves of switched reluctance machines (SRMs). The method is based on the finite element (FE) simulation of a fraction of an electrical cycle. The new approach shows that a significant time reduction is achieved as compared to the time required for stator radial force density calculation based on the one mechanical cycle simulation method. As the switched reluctance motors introduce new challenges in aspects such as acoustic noise, vibrations, and torque ripples, the method introduced in this helps reduce the time of the optimization process of switched reluctance machines in the design stage to improve the machine performance. The proposed method is applied to radial flux switched reluctance machines. Three different SRMs configurations were used to show the effectiveness of this technique in different force components with minimal error as compared to the benchmark method based on the FE simulation of one mechanical cycle.

To my wife Hagar Ali and my lovely daughters Sarah and Hania.

Acknowledgements

First and foremost, I want to sincerely thank and appreciate my supervisors, Dr. Mohamed Bakr and Dr. Ali Emadi, for their unending encouragement, excitement, and patience during my research project. They have always been willing to listen and talk. It has been a real honour to be under their supervision. I also want to thank Dr. Ali Emadi for giving the opportunity to be member of his cutting-edge, multidisciplinary and world-leading academic research program on transportation electrification. With his incredible leadership skills and outstanding personality, Dr. Emadi has the power to continue to inspire people like myself for years to come.

To my committee members, Dr. Berker Bilgin and Dr. Mehdi Narimani, I would like to express my sincere gratitude for your guidance, encouragement and support throughout my research.

Furthermore, I would like to thank Dr. Ossama Arafa for supervising me during my Master's study which helped me develop my skills for the Ph.D. journey.

I wish to show my gratitude to Teresa Janes, Theresa Mitchell, Paul Nguyen and Dan Manolescu for managing and coordinating the research needs.

In addition, I wish to express my deepest gratitude to Dr. Ehab sayed for his unconditional and selfness help and support. I also would like to thank Dr. Alan Callegaro and Dr. Giorgio Pietrini for their help and their support. Furthermore, I

would like to thank my team in the research group: Samantha Jones-Jackson, Federico Duperly, Islam Zaher, Srikanth Vasudevan Pillai, Akshay Manikandan, Alexander Forsyth, Kenneth Noronha, Maaz Khalid, Dikhsita Choudhary, Colleen Jenkins, Ethan Pereira and Sarah Gallagher.

I also want to thank my colleagues in the lab: Dr. Phillip J. Kollmeyer, Mohamed Abdelhafiz, Mohamed Omar, Fabricio Machado, and Dr. Deigo Valencia.

This research was undertaken, in part, thanks to funding from the Canada Research Chair in Transportation Electrification and Smart Mobility, and the Natural Sciences and Engineering Research Council of Canada (NSERC). The authors also gratefully acknowledge Powersys Solutions for their support with JMAG software in this research.

My sincere appreciation to my wife Hagar Ali for being my family in Canada and for her love, support, tolerance, and inspiration. She contributed to the enjoyment of the trip. I want to thank you for being by my side during my Ph.D. thesis and for experiencing all the highs and lows with me.

I deeply thank my father, Elsayed Shawer, and my mother, Amal Alkady, who dedicated their lifetime to help me in all my life aspects. All the love and gratitude goes to my brothers, Ahmed Abdalmagid, and Hassan Abdalmagid, and my sister, Nour Abdalmagid.

I would also like to write in memoriam of my brother Karim Abdalmagid.

Finally and above all, I want to express my gratitude to Almighty Allah for providing me with the courage, information, skills, and chance to start this research study, persevere through it, and successfully complete it.

Contents

List of Figures

List of Tables

Abbreviations and Symbols

Abbreviations

SRMs	Switched Reluctance Machines
MEMS	Micro-Electromechanical Systems
IM	Induction Machines
PMSM	Permanent Magnet Synchronous Machines
AFSRMs	Axial-flux Switched Reluctance Machines
LSRMs	Linear Switched Reluctance Machines
PM	Permanent Magnet
TO	Topology Optimization
GO	Generative Optimization
CFD	Central Finite Difference
BFD	Backward Finite Difference

FFD	Forward Finite Difference
CSM	Complex-step Method
AD	Automatic difference method
SQP	Sequential Quadratic Programming
PSO	Particle Swarm Optimization
SA	Simulated Annealing Optimization
GA	Genetic Algorithm
EA	Evolutionary Algorithms
GFA	Genetic Fuzzy Algorithm
ALGA	Augmented Lagrangian Genetic Algorithm
DoE	Design of Experiment
CCD	Central Composite Design
LHD	Latin Hypercube Design
OFAT	One Factor at a Time
FEA	Finite Element Analysis
ANN	Artificial Neural Network
MOPSO	Multi-Objective Particle Swarm Optimization
BSRM	Bearingless Switched Reluctance Machines

PSS	parametric solution selection
ALGA	Augmented Lagrangian Genetic Algorithm
AM	Additive manufacturing
CNN	Convolutional Neural Network
IPM	interior permanent magnet motor
MST	Maxwell stress tensor
AVM	adjoint variable method
VWP	Virtual work principle
GCD	Greatest Common Division

Symbols

$T_{\max}$	The maximum value of the torque profile
$T_{\min}$	The minimum value of the torque profile
T_{av}	The average torque of the machine
$T(t)$	The torque value at time t
t_1	the start time of the torque profile for torque ripple calculation
t_2	the end time of the torque profile for torque ripple calculation
ΔT	The peak-to-peak torque ripple

TR_n	The normalized torque ripple
TR_p	The percentage torque ripple
ΔT_{rms}	The RMS torque ripple
η	SRM efficiency
$P_{\mathbf{mech}}$	Output mechanical power of the machine
$P_{\mathbf{elec}}$	Input electrical power of the machine
$P_{\mathbf{core}}$	Machine core loss
P_{cu}	Machine copper loss
$P_{\mathbf{win}}$	Machine's rotor windage loss
$P_{\mathbf{other}}$	The other loss that such as bearing friction loss
ax	Stator radial force axial order
u	Stator radial force temporal order
v	Stator radial force circumferential order
$f_f(u)$	The forcing frequency of a radial force harmonic with electric temporal u
$f_{\mathbf{mech}}$	The rotor mechanical frequency
N_r	The number of rotor poles
n	The rotor speed in rpm

$\boldsymbol{x}$	The vector of the design variables.
$f(\boldsymbol{x})$	The objective function
$g(\boldsymbol{x})$	Inequality constraints
$h(\boldsymbol{x})$	Equality constraints
$\boldsymbol{y}$	Vector of slack variables
$\boldsymbol{\lambda}$	Lagrange multipliers vector for the inequality constraints
$\boldsymbol{\mu}$	Lagrange multipliers vector for the equality constraints
k	Iteration number
$\nabla f\left(\boldsymbol{x}^k\right)$	The objective function gradient at iteration number k
$\boldsymbol{H}^k$	The objective function Hessian matrix at iteration number k
$\nabla g\left(\boldsymbol{x}^k\right)$	The inequality constraints' gradient at iteration number k
$\nabla h\left(\boldsymbol{x}^k\right)$	The equality constraints' gradient at iteration number k
$\nabla \boldsymbol{L}$	The gradient of the Lagrange function
d	The search direction of the design parameters
$\boldsymbol{A}$	The Jacobian vector of the constraints
$\boldsymbol{V}_i^k$	The velocity of the i^{th} particle of the PSO
$\overline{\boldsymbol{x}}_i$	The best local solution of the i^{th} particle of the PSO
$\tilde{x}$	The best global solution of the i^{th} particle of the PSO

C_1	The cognitive learning factor that connects each particle to its own best value for PSO
C_2	The best global value is connected to each particle through the cognitive learning factor.
w	The acceleration factor for the PSO.
T_k	Temperature fo the k^{th} iteration of the SA.
p	The simulated annealing coefficient.
$E\left(\boldsymbol{x}_{\mathbf{new}}\right)$	The particle energy of the metropolis algorithm.
r_c	The crossover probability for the GA
∇_m	The mutation probability for the GA
$\boldsymbol{x}_{lb}$	Lower limits of the design parameters
$\boldsymbol{x}_{ub}$	Upper limits of the design parameters
L^n	The numner of design evaluations of the DoE
h_s	Stator teeth length
h_r	Rotor teeth length
y_s	Stator yoke thickness
y_r	rotor yoke thickness
β_s	Stator teeth arc angle

β_r	rotor teeth arc angle
θ_s	Stator teeth taper angle
θ_r	rotor teeth taper angle
g	Airgap thickness
R_{sh}	Shaft radius
ρ_i	The density function of the i^{th} element in the Material-density-based methods optimization
Ω_m	is the Ferromagnetic material region of the design
Ω_a	is the air region of the design
$G(\boldsymbol{x})$	Gaussian function at the location $\boldsymbol{x}$
S_c	The cell state in the ON/OFF topology optimization
θ	Rotor position in electrical degrees
i	Machine's phase current
$\psi(\theta, i)$	Phaseflux linkage as a function of the rotor position and the phased current
L	Phase inductance
V	phase voltage
R	Phase resistance

ω_r	Rotor speed in rad/sec
e	The machine back emf voltage
W_m	Mechanical power of the machine
W_s	Stored power in the magnetic field
T	machine torque
$\boldsymbol{B}$	Magnetic flux density vector.
$\boldsymbol{H}$	Magnetic flux strength vector.
$\boldsymbol{J}$	Current density vector.
$\boldsymbol{A}$	Magnetic Vector potential.
μ	The magnetic permeability.
Ω	The FE problem domain
b	The design space boundary
$\vec{n}$	normal vector to the design boundary.
M	The number of the finite element in the FE problem domain.
e	Index for the e^{th} element.
$\boldsymbol{W}_f^e$	The shape function of the e^{th} element
a^e, b^e, **and** c^e	The e^{th} element constants
$\Delta^{(e)}$	The area of the e^{th} element

N_i^e	the shape function of the e^{th} element for the i^{th} node.
ν^e	The reluctivity of the e^{th} element
$\boldsymbol{K}^{(e)}$	The local system matrix for the e^{th} element
$\boldsymbol{F}^{(e)}$	The local system vector for the e^{th} element
$\boldsymbol{K}$	The global system matrix for the problem domain
$\boldsymbol{F}$	The global system vector for the problem domain
$\overrightarrow{\boldsymbol{a_x}}$	The unit vectors in the x direction
$\overrightarrow{\boldsymbol{a_y}}$	The unit vectors in the y direction
$\overrightarrow{\boldsymbol{a_z}}$	The unit vectors in the z direction
B_x^e	The x component of the e^{th} element flux density
B_y^e	The y component of the e^{th} element flux density
P_φ	The magnetic pressure in the air gap in the tangential direction
$\overrightarrow{a_\varphi}$	The unit vector in the tangential direction
$\overrightarrow{a_\rho}$	The unit vector in the radial direction
P_ρ	The magnetic pressure in the air gap in the redial direction
L	The rotor stack length.
r	The rotor radius.
$d\Gamma^e$	The arc length of the toque calculation layer of the e^{th} element.

N_e	The number of elements located on the torque calculation layer of the MST
B_ρ^e	The radial component of the e^{th} element flux density
B_φ^e	The tangential component of the e^{th} element flux density
$\boldsymbol{A}^e$	The magnetic vector potential of the e^{th} element.
Q^e	The Q geometrical vector of the e^{th} element.
R^e	The R geometrical vector of the e^{th} element.
f	Optimization objective function.
$\boldsymbol{D}$	The FEA residual vector.
$\boldsymbol{\alpha}^T$	The adjoin vector.
F_n	The nodal force at the n^{th} node.
F_d	The force density wave.
$f(u, v)$	The complex value of the stator radial force density component with temporal order u and circumferential order v.
R_e	The real part of the complex number.
I_m	The imaginary part of the complex number.
N_p	The number of finite elements with positive sensitivity.
N_n	The number of finite elements with negative sensitivity.

t_i	The rotor torque at the rotor step number i.
N	the number of rotor steps.
ε	Objective function value tolerance.
N_r	Number of rotor teeth.
N_s	Number of stator teeth.
N_{ph}	Number of phases.
$\theta_{\mathbf{shift}}$	Shift angle for force estimation.
F_r	Stator radial force density.
μ_0	free space permeability.
ω_f	Force objective function wight.
$T_{\mathbf{ref}}$	Target average torque for the design.
ω_t	Torque objective function wight.
$F_{\mathbf{norm}}$	The initial value of the radial force density component subject to optimization.
w_p	Target percentage of the radial force density component by the optimization process.
S_t	number of rotor steps.
$T.R$	Torque ripple value

Chapter 1

Introduction

1.1 Background and Motivations

The uncomplicated design, the low cost, and the lack of rare earth materials make the switched reluctance machines (SRMs) suitable for many different industries such as electric vehicles (EV) and hybrid electric vehicles (HEV) [1, 2], micro-electro-mechanical systems [3, 4], and renewable power generation [5]. The lack of rotor windings and magnets from the rotor lets SRMs to operate at high speed and at elevated temperatures. The winding of the stator of SRMs is usually a concentrated winding which reduces the assembly and maintenance cost of the machine. Another advantage of the concentrated winding is that it reduces the magnetic coupling between the SRMs phases as compared to the distributed winding-based machines, which makes the SRMs more fault-tolerant [6]. All the mentioned advantages of the SRMs make these types of machines a reliable choice for different applications [7–9].

However, the double salient structure of the SRMs creates challenges such as high acoustic noise, vibrations, and high machine torque ripples [10]. The radial forces acting on the stator structure are the main cause of the acoustic noise of the machine [11]. However, the torque ripples are mainly due to the rotor tangential force harmonics [12].

Extensive studies were performed to overcome these challenges and improve the SRMs performance [12]. Topology and geometry optimization of the SRMs were used to enhance the machine performance and overcome the machine disadvantages. In geometrical optimization, the main geometrical design variables of the machine are optimized to improve the machine's performance [13]. However, in topology optimization (TO), the material distribution in a selected design domain is optimized

to enhance the machine performance [14]. The main weakness of geometrical optimization is the limited degrees of freedom. Any increase in the number of variables subject to optimization increases the complexity and the time of the optimization process [12]. On the other hand, the TO allows for new designs without being limited by the key design parameters of the machine.

Many published papers use TO to enhance electrical machines performance such as maximizing mean torque, minimizing torque ripples, and minimizing radial force [15–18]. TO was used in [19] to optimize the topology of the stator and rotor teeth of a 6/4 SRM configuration to minimize the torque ripples of the machine. Despite the TO being powerful in improving the SRMs' performance, it suffers from a long computational time.

The motivation of this research is to apply advanced TO and generative optimization to reduce the SRMs torque ripple and radial force with reasonable optimization time.

1.2 Objectives and Contributions

The main objective of this research is to improve the SRM performance through topology and generative optimization and reducing the optimization time. The problem assutated with the conventional methods of TO will be discussed and a new method is introduced to solve these problems. Hence, there are five main contributions introduced:

1. A review of the SRMs configurations, the excising optimization technique, and the key performance parameters of SRMs.

2. Introducing a new linesearch based method for topology and generative optimization of electric machines design.

3. Improving the average torque and reducing torque ripples of a case study 6/14 SRM using the proposed method.

4. Introducing a new technique to reduce the computational time required for stator redial force calculation and decomposition.

5. Improving the average torque, reducing the torque ripple, and reducing the stator redial force of a case study 6/14 SRM using the proposed method.

The discussion in this thesis is limited to electromagnetic design. This thesis will not cover mechanical design, vibrations, cooling design and acoustic noise.

1.3 Thesis Outline

In Chapter 2, the different configurations of SRMs are presented. The advantages, the disadvantages, and the applications of each configuration has been highlighted. A detailed review of the optimization technique used in the literature for SRMs optimization and performance is presented in Chapter 3. The expected future trends in this field are discussed in Chapter 3.

A review of SRMs principle of operation, modeling, and control is shown in Chapter 4. Chapter 4 shows also the finite element (FE) modeling of the redial flux machine and the linking MATLAB optimization script to a FEA commercial software to reduce the optimization time. Chapter 4 shows also the flux density, torque, stator radial

force density, torque sensitivity, and stator radial force density sensitivity calculations based on the information exported from the FEA commercial software.

In Chapter 5, A new linesearch-based ON/OFF method for topology and generative optimization is presented to replace the conventional annealing-based ON/OFF method and solve its long optimization time problem. Chapter 6 shows numerical examples to the linesearch-based method for topology and generative optimization of the stator and rotor design domain of the case study 6/14 SRM to reduce the torque ripple and maximize the average torque of the machine. A comparison between the performance of the conventional annealing-based ON/OFF method and the proposed linesearch-based method is illustrated in Chapter 6.

As one of the objectives of the thesis is to minimize the optimization time, Chapter 7 shows a new technique used to reduce the time required for redial force density calculation. In Chapter 8, the method introduced in Chapter 7 is used for the evaluation of the redial force density components and the sensitivity calculation of the radial force density at each iteration of the Topology and generative optimization of the case study machine. Chapter 8 shows the numerical implantation of the proposed linesearch-based ON/OFF method for redial force density components minimization, average torque maximization and torque ripple minimization of the case study 6/14 SRMs

Chapter 9 concludes the thesis and discusses the future work.

Chapter 2

Switched Reluctance Machines (SRMs)

Switched reluctance machines (SRMs) are now attractive choices for various applications such as electric vehicles and hybrid electric vehicles [20], [1], wind power generation applications [21], and micro-electromechanical systems (MEMS) [22, 23]. The reason is that they have a simple and rugged structure without any magnets or windings on the rotor part [24]. The lack of the PMs and the winding on the rotor allows the machine to run at high temperatures and high speeds [25]. It also reduces the rotor weight, which increases the torque-to-inertia ratio of the machine and improves the dynamic performance as compared to the induction machines (IMs) and PMSMs [26, 27]. Additionally, the lack of rare-earth PMs from the machine design makes SRMs a low-cost substitute to PM-based machines.

SRMs also use concentrated winding for the coils of phases, which decreases the assembly and replacement costs. It also decreases the electromagnetic coupling between the machine phases, which improves the SRMs fault-tolerance capability [6]. These advantages improve the machine's reliability and make SRMs a reliable option for different applications [7–9]. However, the doubly salient nature of SRMs structure introduces challenges such as high torque ripples and high acoustic noise and vibrations [10]. The acoustic noise and vibrations are mainly due to the high radial and axial forces for the radial and the axial SRMs configurations, respectively [10, 28–32]. Moreover, SRMs are characterized by a small air gap thickness between rotor and stator, which requires a precise manufacturing tolerance [33]. The machine drive requires uncommon converters, which is another weak point of the machine drive system [28–30].

Extensive research was performed to overcome these disadvantages and improve the machine's static and dynamic performance [1]. New configurations are developed,

and optimization procedures are applied to enhance the machine's performance. Geometry and topology optimization are used to overcome these disadvantages and allow SRMs to compete with PMSMs [12]. In Geometry Optimization (GO), key design parameters of the motor geometry are optimized to achieve various design objectives. On the other hand, the material distribution in a particular design space within the machine domain is optimized to improve machine performance through Topology Optimization (TO). In this chapter, different SRM configurations are illustrated. The merits, demerits, and application of each of these configurations are described.

2.1 Main Configurations of SRMs

SRMs can be categorized based on the motion type to linear and rotary configurations and based on the flux-flow orientation to radial and axial flux machines. There are various stator/rotor pole combinations of SRMs. The number of rotor and stator teeth, in addition to the number of phases, are determined to ensure a feasible design of SRMs [34]. Most of the possible design stator/rotor poles combinations were illustrated in [35]. The selection of the machine configuration and stator/rotor poles combination defines the performance and depends significantly on the application [35]. A classification of SRMs based on the configuration is shown in figure 2.1.

The number of poles and the flux direction determine the configuration of the SRM. The classical and well-known designs of the SRMs adopt the radial flux machine with a rotor number of poles less than the stator number of poles. These configurations are characterized by high torque ripples and high acoustic noise and vibrations [36]. This issue is solved by increasing the number of rotor poles to be higher than the number of stator poles. The torque density and the noise-causing

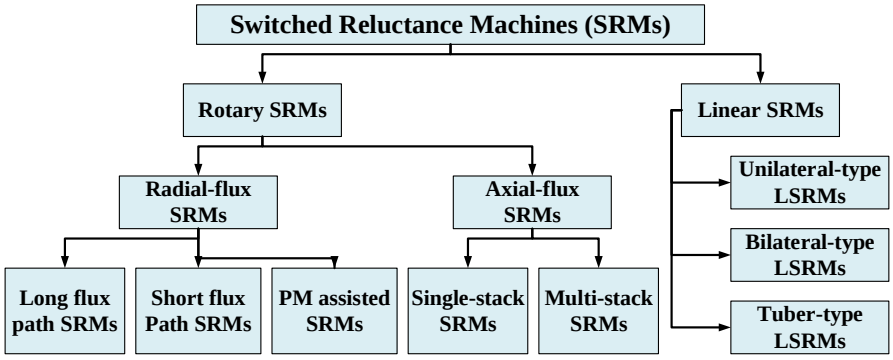

Figure 2.1: The main configurations of SRMs.

radial/axial forces can be improved by selecting the number of the rotor poles to be higher than that of the stator poles [36–38]. However, the high number of rotor poles increases the operating frequency, which increases the machine core loss [39]. It also decreases the conduction period per phase, which results in more switching losses and requires high-cost position sensors [40, 41]. SRMs with a higher number of rotor poles are therefore more suitable for low-power and low-speed applications [35]. On the other hand, machines with a lower ratio of the rotor to stator poles are selected for better utilization of the volt-ampere converter rating [35].

In axial-flux SRMs (AFSRMs), the flux travels axially between the stator and rotor. Due to the relatively shorter flux path, AFSRMs have a higher power density than radialflux SRMs [42]. AFSRMs can be classified into three main categories. These categories include single-stator single-rotor (single-sided) machine, two-airgap (double-sided) machine, and multi-stack machine. The single-sided is the simplest AFSRM structure [43, 44]; however, the disadvantage of this configuration is the imbalance between the axial forces of the stator and rotor [45,46], which produces high acoustic noise and needs to be accommodated in the bearing design [31]. The problem

of the unbalanced axial force is solved by Double-sided AFSRMs configuration [47]. The Double-sided AFSRMs have a higher torque density; however, the structure is more complex than the single-sided AFSRMs configurations [47–49]. The multi-stack designs of the AFSRMs are much more complex structures as they should have at least three rotors or three stators [31]. The advantage of the multi-stack AFSRMs is the higher power and torque densities [31]. There are two types of multistack AFSRMs, either having equal or different numbers of rotors and stators. The equal number of rotors and stators has the disadvantage of unbalanced axial force; however, this configuration has a higher torque density than the multi-stack AFSRMs with different rotors and stators [31].

The linear SRMs configuration has a different function as it provides a linear motion. Linear SRMs (LSRMs) have a similar structure to rotary SRMs, except that the stator and rotor have a linear form. They consist of a stator (stationary part) and a translator (moving part) [50]. LSRMs configurations comprise planar and tubular designs. The planar linear SRMs has two types the unilateral-type and the Bilateral-type. The unilateral type has the advantage of the simple structure as it consists of one translator and one stator. However, the unilateral-type main disadvantage is the high unbalanced axial forces between the stator and the translator, causing immense friction between both parts. The friction potentially reduces the machine lifetime [51]. This disadvantage is solved by the Bilateral-type but with a more complex structure consisting of two stators and a single translator [52]. All the planar Linear SRMs have a common disadvantage of having transversal cuts and uniform magnetic field distribution in the transversal direction. This problem is solved by the tuber-type Linear SRMs that a tuber shape stator with no transversal cuts [53, 54]. However, A

precise shaft installation is needed to prevent unbalanced radial magnetic forces [55]. The construction, advantages, disadvantages, and applications of the different SRM configurations are presented in this chapter.

2.2 Rotary SRMs

As illustrated in figure 2.1, rotary SRMs are divided into two configurations: radial-flux SRMs and axial-flux SRMs. The radial-flux SRMs are divided into three types: long-fluxpath SRMs, short- flux-path SRMs, and PM-assisted SRMs. On the other hand, the axial flux SRMs are divided into single-stack SRMs and multi-stack SRMs. In this subsection, the different configurations of the rotary SRMs are presented.

2.2.1 Radial-flux Rotary SRMs

Radial-flux rotary SRMs configurations comprise conventional long-flux-path, mutually coupled short-flux-path and PM-assisted SRMs. Conventionally, the flux flows through the entire stator back iron. In short-flux-path configurations, the flux flows in short loops containing the rotor and stator yokes and the adjacent poles [56]. The latter configuration has a relatively lower iron loss. However, it has higher mutual inductance between phases, which reduces the machine's fault tolerance capability [57]. Permanent Magnets (PMs) could be added to the stator in PM-assisted machines to increase the machine co-energy, which increases the torque density and efficiency [58, 59]. Radial-flux machines can have either an in-runner structure or out-runner structure. Examples of the in-runner radial flux SRM configuration is

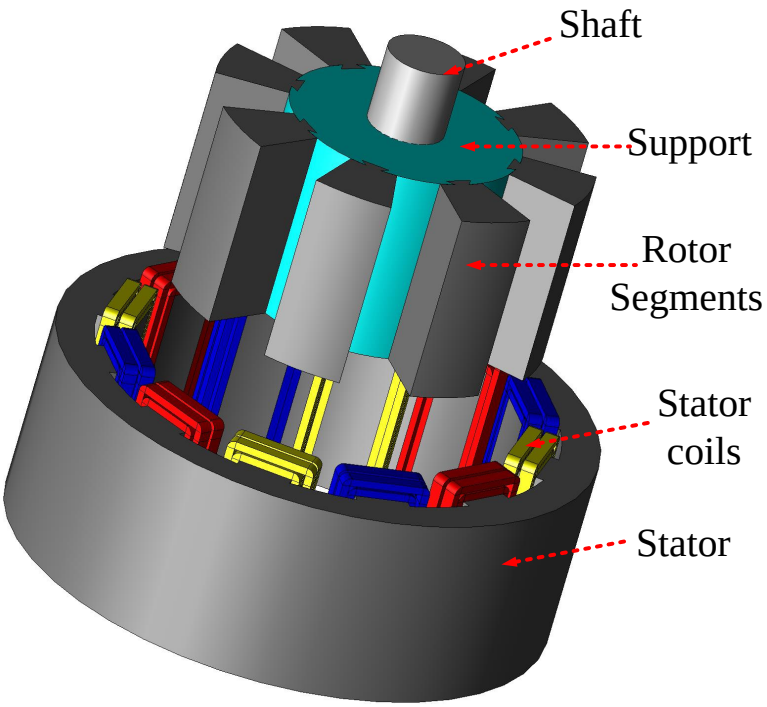

Figure 2.2: An in-runner three-phase 12/8 radial-flux segmented-rotor SRM configuration

shown in figure 2.2 and figure 2.3. Examples of the out-runner radial flux SRM configuration is shown in figure 2.4 and figure 2.5. The out-runner motors are more preferred for in-wheel drive applications as they can reduce the transmission losses significantly [39,41,60–62]. It also has higher torque density due to the extended lever arm, where the torque density may reach 2.4 times that of an in-runner counterpart for the same spatial constraints as indicated in [63].

The rotor can be segmented or non-segmented, as shown in figure 2.2 and figure 2.3 for the in runner configurations and figure 2.4 and figure 2.5 for outrunner configurations. The non-segmented design has a simple structure and provides higher average torque and lower torque ripple [61], [64]. On the other hand, the segmented design

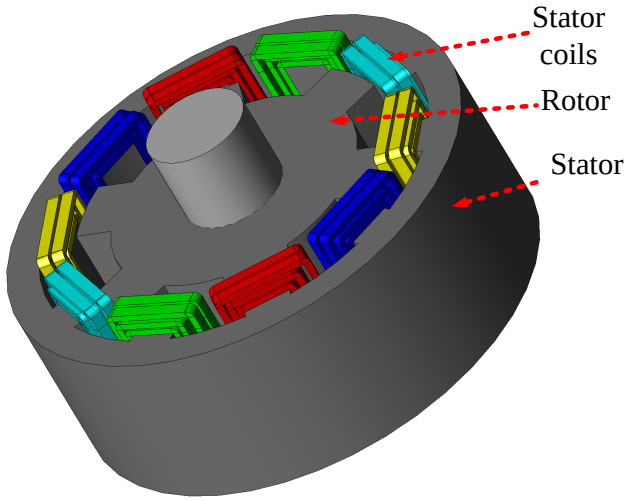

Figure 2.3: an in-runner five-phase 10/6 radial-flux SRM

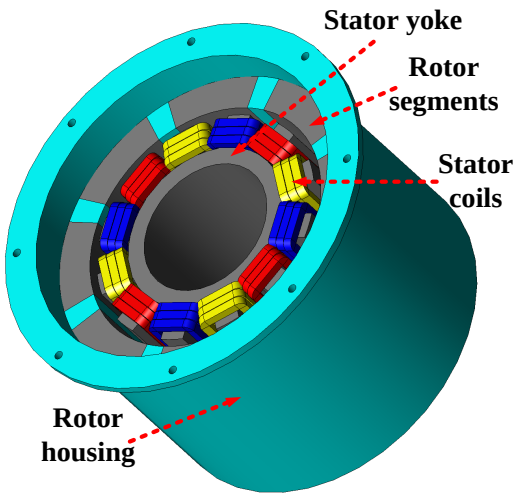

Figure 2.4: a short flux path three-phase 12/8 segmented-rotor out-runner radial-flux SRMs

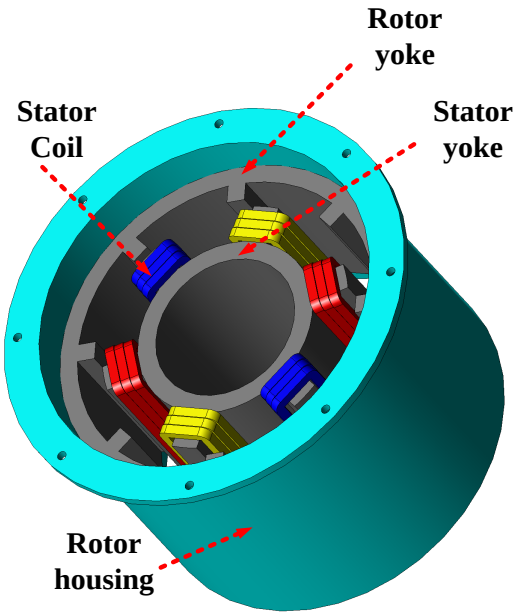

Figure 2.5: a non-segmented-rotor SRM three-phase 6/8 segmented-rotor out-runner radial-flux SRMs

reduces the rotor weight and has higher torque density and lower rotor inertia [39]. The small rotor inertia also improves the machine's dynamic performance [39].

2.2.2 Axial-flux SRMs

In axial-flux SRMs (AFSRMs), the flux travels axially between the stator and rotor. Due to the relatively shorter flux path, AFSRMs have a higher power density than radialflux SRMs [42]. Based on the machine structure and number of stators and rotors used in the machine, AFSRMs can be classified into three main categories, as illustrated in figure 2.6. These categories include single-stator single-rotor (single-sided) machine, two-airgap (double-sided) machine, and multi-stack machine.

The single-sided type has the simplest structure as it consists of a single stator, a single rotor, and one airgap [43, 44]. A crucial problem of this configuration is the

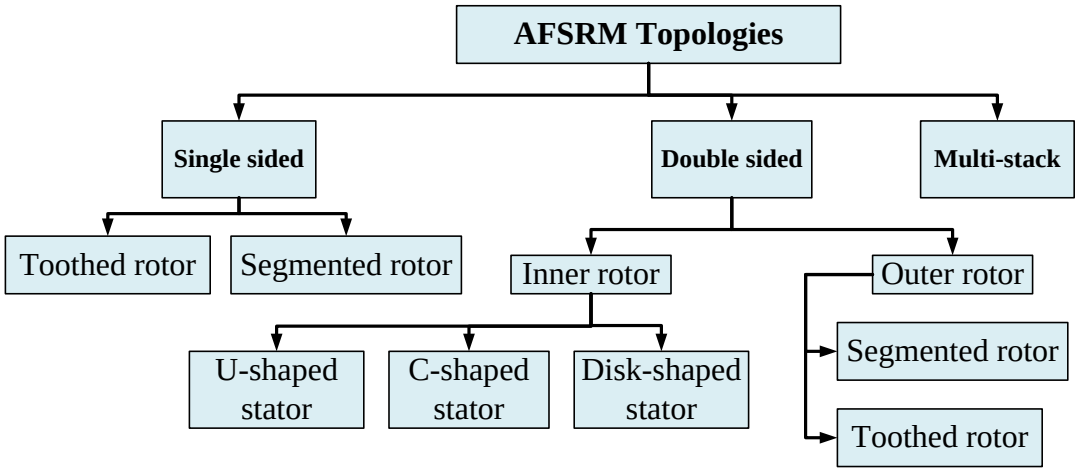

Figure 2.6: The main topologies of axial-flux SRMs (AFSRMs)

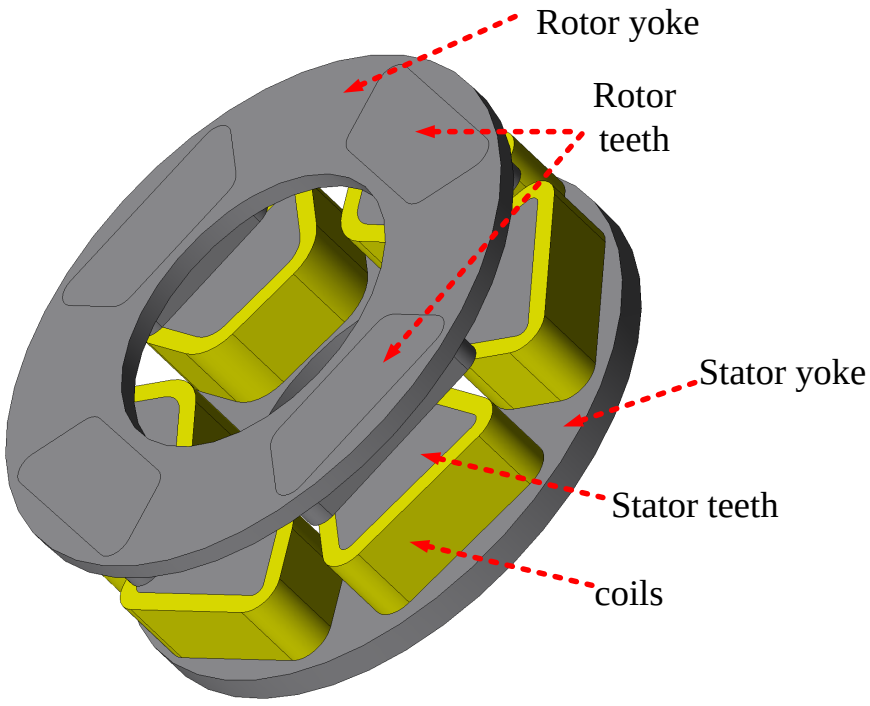

Figure 2.7: A single-sided toothed-rotor AFSRM

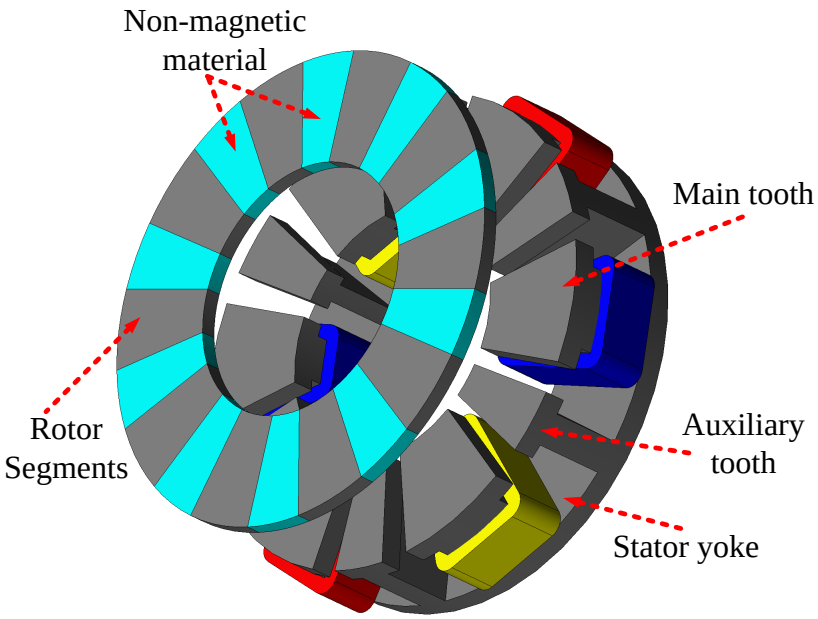

Figure 2.8: A single-sided segmented-rotor AFSRM

imbalance between the axial forces of the stator and rotor [45, 46], which produces high acoustic noise and needs to be accommodated in the bearing design [31]. There are two types of single-sided AFSRMs: the toothed-rotor and segmented-rotor types, as shown in figure 2.7 and figure 2.8, respectively [42].

The toothed-rotor type stator consists of a yoke, teeth, and coils, whereas the rotor comprises a yoke and teeth. Alternatively, the stator of the segmented-rotor type consists of coil-wound teeth, auxiliary teeth, and a yoke [42]. The rotor consists of separate segments held together by a nonmagnetic material such as aluminum or plastic. This SRM configuration has lower copper losses. It also has lower iron loss due to the auxiliary stator poles that provide a shorter flux path. Plastic or aluminum usage in the rotor to hold the rotor segments reduces the motor inertia, which improves the dynamic performance of the machine [65].

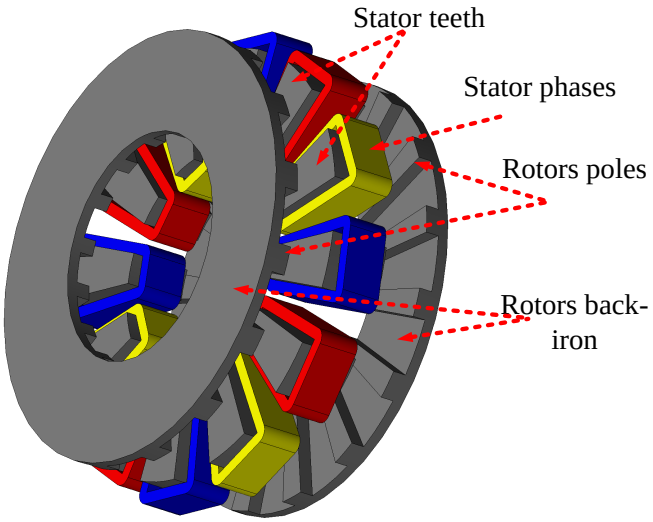

Figure 2.9: A 12/16 dual-rotor single-stator toothed-rotor AFSRM

Double-sided AFSRMs have a balanced axial force, and the available volume of this machine is more effectively used for torque production [45–47]. This configuration may have two outer rotors (dual-rotor configuration) or two outer stators (inner-rotor configuration). The dual-rotor configuration has either toothed [66] or segmented [67] rotors, as shown in figure 2.9 and figure 2.10, respectively. The segmentedrotor topology provides higher torque and efficiency than the toothed-rotor one [68]. The increase of the torque of the segmented-rotor type is due to the short flux path that provides higher flux linkage compared to the toothed-rotor type [68].

The dual-stator inner-rotor AFSRM, shown in figure 2.11, is typically utilized as an in-wheel actuator of electric vehicles [47], [69]. The rotor is segmented and sandwiched by two identical external stators [70]. This topology has a small axial length due to the absence of rotor yoke [69]. A non-magnetic carrier accommodates the rotor segments [71].

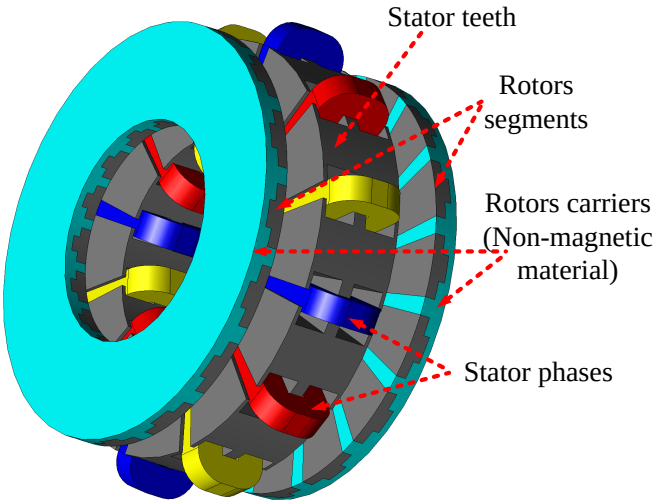

Figure 2.10: A 12/16 dual-rotor single-stator segmented-rotor AFSRM

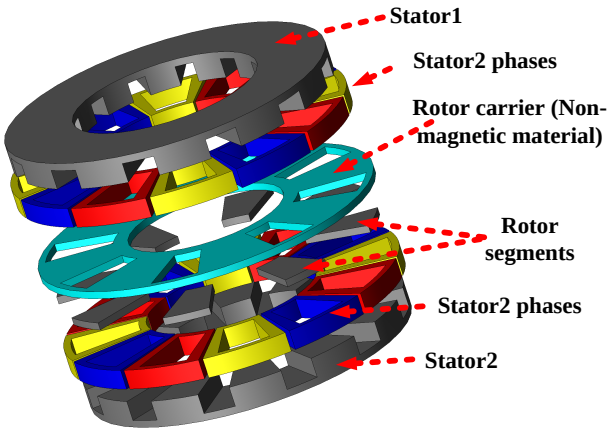

Figure 2.11: A 12/8 three-phase dual-stator inner-rotor axial-flux SRM.

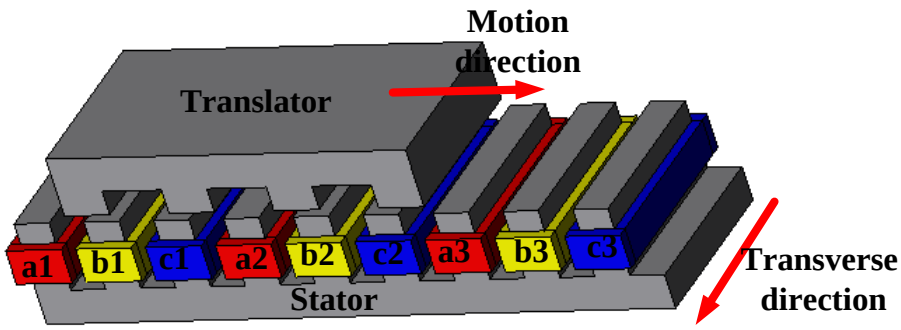

Figure 2.12: A three-phase unilateral-type planar LSRM with a four-pole translator.

2.3 Linear SRMs

Linear SRMs (LSRMs) have a similar structure to rotary SRMs, except that the stator and rotor have a linear form. They consist of a stator (stationary part) and a translator (moving part) [50]. LSRMs configurations comprise planar and tubular configurations. figure 2.12 shows a three-phase unilateral-type planar LSRM with a four-pole translator. The unilateral-type main disadvantage is the high unbalanced axial forces between the stator and the translator, causing immense friction between both parts. The friction potentially reduces the machine lifetime [51]. Bilateral-type (double-sided) LSRMs, with two equal airgaps, could solve this issue [52].

shaft installation prevents unbalanced radial magnetic forces. Unlike unilateral- and bilateral-type LSRMs, the tuber-type LSRM does not have a transversal cut and has a uniform magnetic field distribution in the circumferential direction. The tuber-type LSRM comprises transversal-flux [72,73], and longitudinal-flux [54] types according to the flux direction to the translator. figure 2.13 shows a double excited-winding, where both stator and translator are excited, tubular longitudinal-flux LSRM [73].

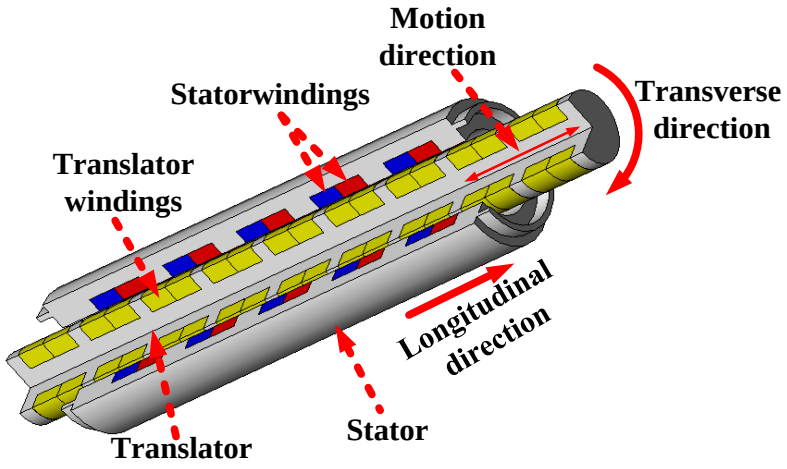

Figure 2.13: A double-excited-winding tubular longitudinal-flux LSRM [73].

2.4 Summary

In this chapter, the different configurations of SRMs are presented. The advantages, the disadvantages, and the applications of each of each configuration has been highlighted. As presented in this chapter, SRMs can be categorized based on the motion type to linear and rotary configurations and based on the flux-flow orientation to radial and axial flux machines. There are various stator/rotor pole combinations of SRMs. The number of rotor and stator teeth, in addition to the number of phases, are determined to ensure a feasible design of SRMs. Rotary SRMs are divided into two configurations: radial-flux SRMs and axial-flux SRMs. The radial-flux SRMs are divided into three types: long-fluxpath SRMs, short- flux-path SRMs, and PM-assisted SRMs. On the other hand, the axial flux SRMs are divided into single-stack SRMs and multi-stack SRMs. Linear SRMs (LSRMs) have a similar structure to rotary SRMs, except that the stator and rotor have a linear form. They consist of a stator (stationary part) and a translator (moving part).

Chapter 3

Optimization Techniques for Switched Reluctance Machines

Switched reluctance machines (SRMs) have recently attracted more interest in many applications due to the volatile prices of rare-earth permanent magnets (PMs) used in permanent magnet synchronous machines (PMSMs). They also have rugged construction and can operate at high speeds and high temperatures. However, acoustic noise and high torque ripples, in addition to the relatively low torque density, present significant challenges. Geometry and topology optimization are applied to overcome these challenges and enable SRMs to compete with PMSMs. Key geometric design parameters are optimized to minimize various objective functions within geometry optimization. On the other hand, the material distribution in a particular design space within the machine domain may be optimized using topology optimization. The stochastic and deterministic optimization techniques applied to optimize the geometries and topologies of SRMs to enhance machine performance are discussed in this chapter. As optimizing the machine geometry and material distribution at the design phase is of substantial significance, the chapter shows a comprehensive literature review on the current state of the art and the possible trends in the optimization techniques of SRMs.

In section 3.1, the objective functions used in the literature for the performance improvement of SRMs is reviewed. The stochastic and deterministic optimization of the techniques used for SRM performance improvements are then reviewed in section 3.2.

3.1 Performance Targets

This section reviews the different measures of the SRMs' performance, which are used as objective functions for performance improvement. These objectives include

the maximization of torque, reduction of torque ripple, maximizing the efficiency, and mitigation of radial force for minimization of acoustic noise and vibration of the machine.

3.1.1 Torque Ripples

The SRM drives have more torque pulsation than other machine types due to the discrete nonlinear torque of each phase and the doubly salient structure of the machine. There are different definitions for torque ripples used in the literature as objective functions as shown in equations (3.1.1) to (3.1.4), where $T_{\max}$ and $T_{\min}$ are the maximum and the minimum values of the torque profile over one electrical cycle, T_{av} is the average torque, $T(t)$ is the instantaneous torque as a function of time.

$$\Delta T = T_{\max} - T_{\min} \tag{3.1.1}$$

$$TR_n = \frac{T_{\max} - T_{\min}}{T_{av}} \tag{3.1.2}$$

$$TR_p = \frac{T_{\max} - T_{\min}}{T_{av}} \times 100\% \tag{3.1.3}$$

$$\Delta T_{rms} = \sqrt{\frac{1}{t_2 - t_1} \int_{t_1}^{t_2} \left(T(t) - T_{av}\right)^2 dt} \tag{3.1.4}$$

The duration $t_2 - t_1$ is the time of one complete electric cycle, ΔT is the peak-to-peak torque ripple, TR_n and TR_p are the normalized and percentage torque ripple respectively, and ΔT_{rms} is the RMS torque ripple. Figure 3.1 shows the average torque

and the peak-to-peak torque ripple in a typical torque waveform of 6/14 radial flux SRM over one electric cycle operating at 1500 rpm.

The peak-to-peak torque ripple, the normalized torque ripple, and the percentage torque ripple, shown in equation (3.1.1), equation (3.1.2), and equation (3.1.3) respectively, are simple, but only the maximum and the minimum values of the torque waveform are used to calculate the torque ripple. However, the RMS torque ripple expression, shown in equation (3.1.4), is a function of all the torque waveform data points. It measures the deviation of the torque data points from the average torque line. The RMS torque ripple formula is often used for optimization to minimize the SRMs torque ripples and improve the machine torque quality [24].

Reducing the torque ripple of SRMs is one of the hot research topics. Geometry and topology optimization are common approaches to minimize the machine torque ripples. In literature, arc angles of rotor and stator poles, the height of rotor and stator poles, stator/rotor back iron thickness, number of phases, and stack length were used to minimize the machine torque ripple. Also, the material distribution inside the rotor and stator cores was optimized to reduce the torque ripple of SRMs [74,75]. Moreover, drive control variables such as converter firing angle for each phase, conduction angle for each phase, reference current, and the current waveform shape were used for torque ripple minimization of SRMs. This research area is out of the thesis scope, but the reader can find more in [24] and [76].

3.1.2 Average Torque and Torque Density

PMSMs have the highest torque density among other machine types due to the permanent magnet excitation. For the SRMs, the average torque and the torque density

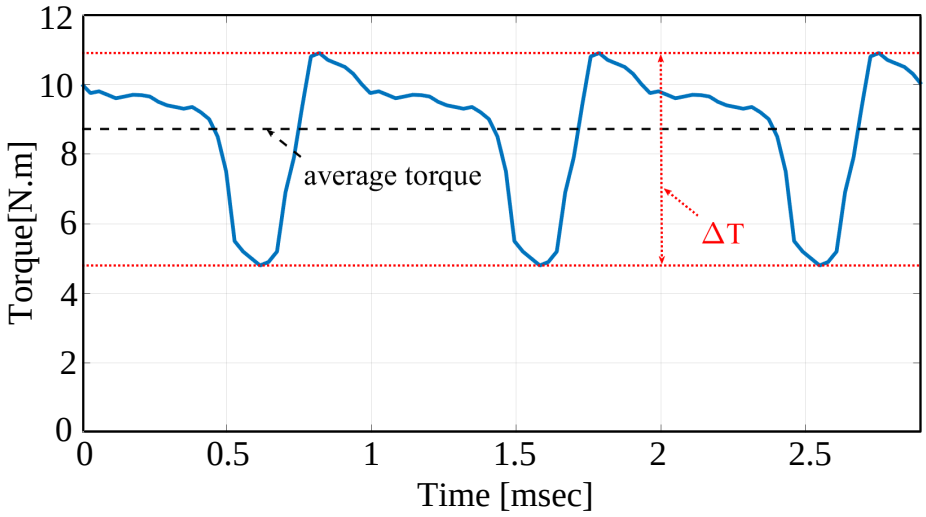

Figure 3.1: Typical torque waveform over one electric cycle of 6/14 SRM at 1500 rpm speed.

can be enhanced through the selection of the rotor and stator core materials and optimizing the machine structure through geometry or topology optimization [77]. The cobalt iron and 6.5% silicon iron are usually used in SRMs to increase the torque density due to the higher saturation limit that boosts the machine's magnetic loading [77, 78]. Figure 3.1 shows the average torque (black dotted line) of a 6/14 SRM torque profile operating at 1500 rpm speed. The average torque can be calculated using the following equation over one complete electric cycle:

$$T_{av} = \frac{1}{t_2 - t_1} \int_{t_1}^{t_2} T(t) dt \tag{3.1.5}$$

The torque density (in N.m/L) of the motor is defined as the motor average torque to the motor volume. Also, the specific torque (in N.m/kg) can be used as an optimization function which is the ratio between the average torque and the motor

weight. Geometry and topology optimizations of SRMs were extensively applied in the literature to enhance the average torque and torque density.

3.1.3 Efficiency Improvement

The SRM efficiency is commonly used as an objective function in literature to improve machine performance. The core losses (P_{core}), the rotor windage loss (P_{win}), and the copper losses (P_{cu}) are the primary loss sources in SRMs. Minimizing these losses can improve the SRMs efficiency, as illustrated in the following equation:

$$\eta = \frac{P_{\text{mech}}}{P_{\text{elec}}} = \frac{P_{\text{mech}}}{P_{\text{mech}} + P_{cu} + P_{\text{core}} + P_{\text{win}} + P_{\text{other}}} \tag{3.1.6}$$

where η is the SRM efficiency, P_{mech} is the output mechanical power, P_{elec} is the input electrical power, and P_{other} is the other losses that are not related to the electromagnetic design as the bearing friction loss. The rotor windage loss is included as an electromagnetically dependent parameter in this equation since it depends on the rotor design due to the salient nature of the rotor structure. The selection of the machine material can improve the machine's efficiency. Copper magnet wires are usually used for the coils due to the high thermal conductivity, high current carrying capacity, and low electric resistivity compared to Aluminum counterparts [24]. The core loss can be reduced by using low-loss magnetic steel, such as 6.5% high silicon steel, low-loss silicon steel, laminated amorphous alloy, high resistivity soft magnetic composites [79–81]. In addition to the materials' selection, the SRMs key design parameters and the material distribution in the design space are optimized to improve the machine efficiency.

3.1.4 Radial Force and Acoustic Noise

The high radial force components of SRMs are considered one of the big challenges. Radial forces are the main sources of SRM vibration and acoustic noise [24, 82]. As mentioned in [82], the acoustic noise radiated from SRMs is relatively harsher compared to induction machines and PMSMs, which limits utilizing the SRMs in noise- and vibration-sensitive applications like white goods [82]. Consequently, analyzing and reducing SRMs acoustic noise receives much attention between researchers [83, 84].

In SRMs and electric machines in general, there are three primary sources of acoustic noise and vibration: mechanical sources, aerodynamic sources, and electromagnetic sources. In this section, the review is focused on the electromagnetic source of acoustic noise. The electromagnetic cause of acoustic noise and vibration of SRMs is related to the machine excitation, which generates radial pressure on the machine structure that can excite its natural frequency at different mode shapes [85]. Figure 3.2 shows a typical radial pressure on the stator structure of three-phase inner rotor 6/4 SRM for one electric cycle. The radial force shown in the figure represents the magnetic attraction between stator teeth and rotor teeth in the radial direction, which deforms the machine stator structure. This deformation appears in different mode shapes [85]. The radial force density acting on the machine's different structures can be decomposed into different axial, circumferential, and temporal harmonic orders (ax, u, v). In some cases, only the first axial mode is considered $(ax = 1)$, and the force density is decomposed to (u, v) harmonic orders. The forcing frequency of each of these harmonics depends on the harmonic temporal order and the mechanical

frequency and can be calculated as follows:

$$f_f(u) = |u| N_r f_{\text{mech}} = |u| N_r \frac{n}{60} [\text{ Hz}] \tag{3.1.7}$$

where f_f is the forcing frequency of a radial force harmonic with electric temporal order u, f_{mech} is the rotor mechanical frequency, N_r is the number of rotor poles, and n is the rotor speed in rpm. Figure 3.3 shows the 2-D FFT of the radial pressure acting on the stator structure that is illustrated in Figure 3.2 as an example of the radial pressure harmonic spectrum. Generally, the stator vibration in radial-flux SRMs is modelled as the vibration of an equivalent cylindrical shell. The vibration modes of SRMs stator are identified in circumferential and axial directions. Figure 3.4 shows examples of different circumferential mode shapes of a cylindrical shell. Each of these modes has a natural frequency depending on the structure dimensions and material properties, such as Young's modulus and Poisson's ratio. The radial force density harmonics excite the stator structure, and the acoustic noise occurs when the forcing frequency of a certain spatial harmonic order becomes close to the natural frequency of the corresponding circumferential mode shape.

Figure 3.5 shows the intersection between the natural frequency of six circumferential mode shapes of a stator structure (Circ $= \{0, 2, 4, 6, 8, 10\}$) with the forcing frequency of five temporal order ($u = \{1, 2, 3, 4, 5\}$) of an inner rotor 6/4 SRMs. In the figure, the rays represent the change of the harmonic pressure frequency with rotor speed. It can be concluded from Figure 3.2 and Figure 3.5 that the motor at the base speed will excite the circumferential mode shapes Circ $= \{2\}$ with the harmonics $(v, u) = \{(2, -1)\}$, Circ $= \{4\}$ with the harmonics $(v, u) = \{(4, -2)\}$, and Circ $= \{4\}$ with the harmonics $(v, u) = \{(6, -3), (6, 3)\}$. The acoustic noise can be mitigated by

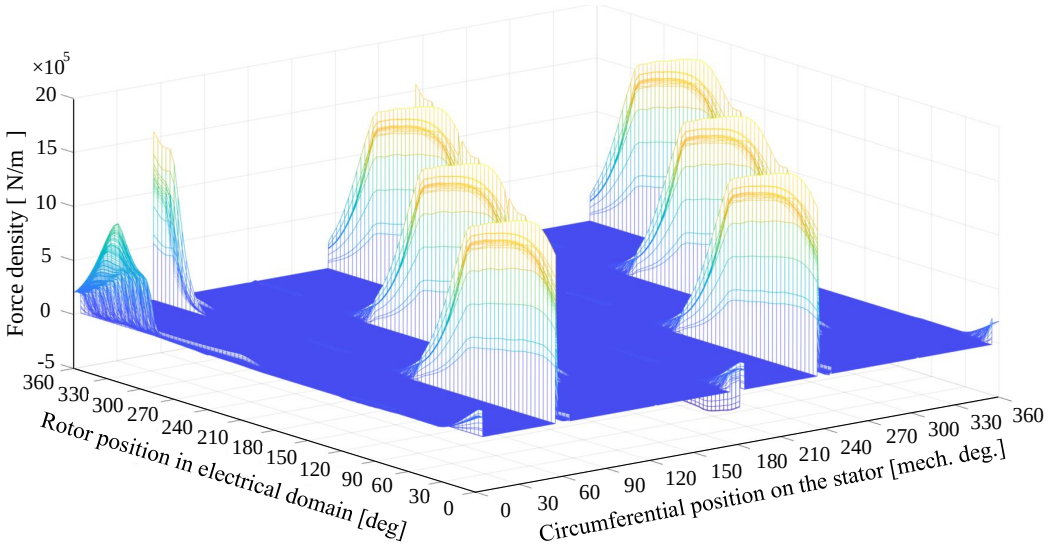

Figure 3.2: A typical radial force density acting on the stator of 6/4 SRM operating at 1103 rpm, and the rotor rotates at the counterclockwise direction.

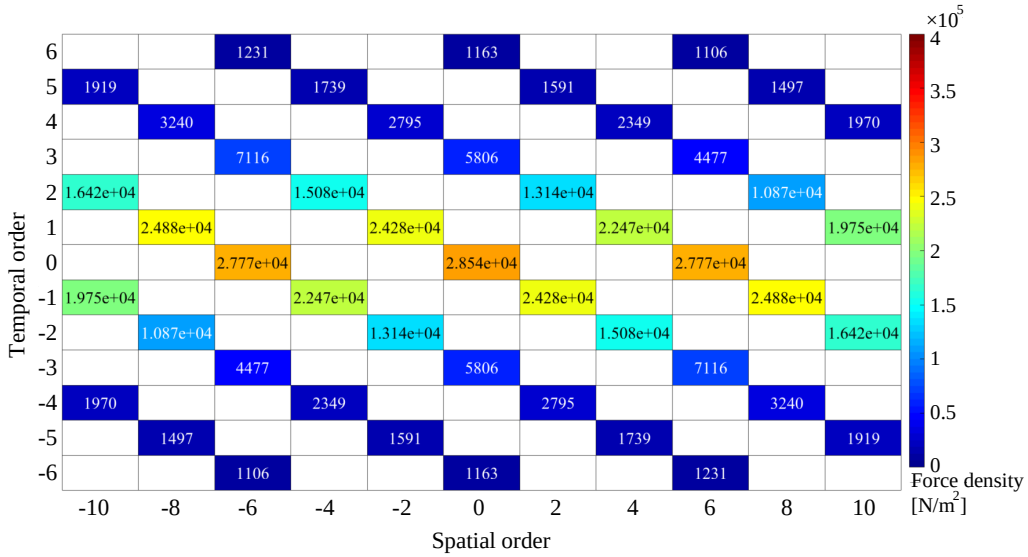

Figure 3.3: 2-D FFT of the radial force density wave shown in Figure 3.2 (the temporal order shown in this figure is the electrical temporal order).

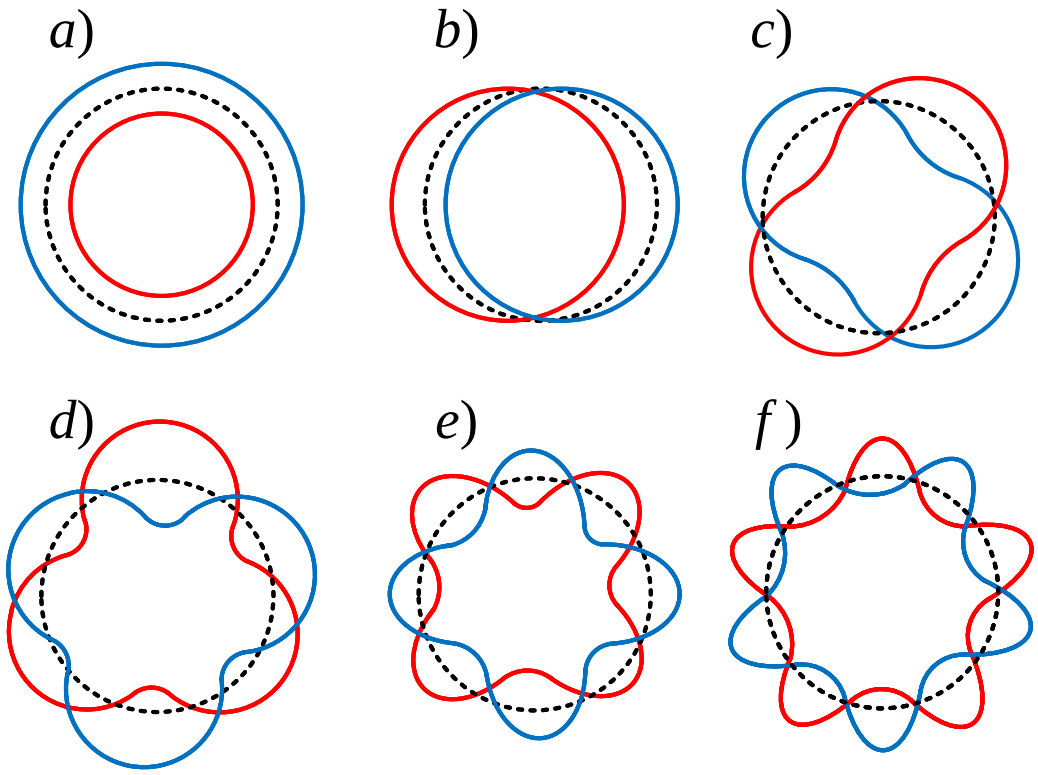

Figure 3.4: Circumferential vibration modes of radial-flux SRMs stator. a) Mode 0, b) Mode 1, c) Mode 2, d) Mode 3, e) Mode 4, f) Mode 5.

either reducing the amplitude of these dominant harmonics or making the machine structure stiffer. A stiffer structure has a higher natural frequency of the different mode shapes, making it difficult to be excited within the motor speed range.

The geometrical design parameters of SRMs can be optimized to minimize the amplitude of the most dominant harmonics that contribute to the acoustic noise [86]. The natural frequency of the different circumferential mode shapes of the machine structure can be controlled by the mechanical design and the used material selection of the stator as illustrated in [83, 87]. The drive control variables such as the phase firing angle, the turnoff-angle, the reference current, and the current profile were used

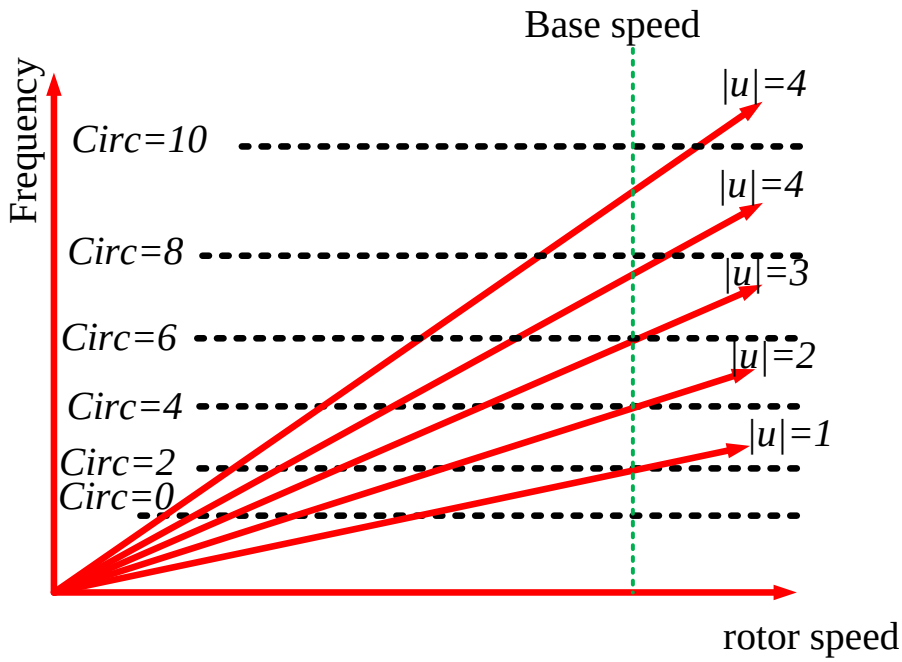

Figure 3.5: An illustration of the forcing frequency versus rotor speed and the excitation of different circumferential vibration modes of a 6/4 SRM.

in the literature to eliminate or reduce the amplitude of selective spatial harmonic orders to minimize the acoustic noise as discussed in [88–91].

3.2 Optimization Methods

Several optimization methods have been applied to the design of SRMs. These optimization methods are generally divided into deterministic and stochastic optimization techniques. Deterministic optimization techniques require gradient information, whereas stochastic optimization techniques search for an optimal solution in a randomized way that does not require the objective function's gradient information. Deterministic optimization techniques reach an optimal solution faster and provide a unique and precise solution [92]. However, the achieved solution is not guaranteed to be the global optimal solution for nonconvex functions [92]. The machine design is usually a nonconvex problem with many local solutions. This makes it challenging for deterministic optimization techniques to reach a global solution. The optimization process can also be divided based on the number of objective functions to single-objective optimization and multi-objective optimization.

This section reviews some of the deterministic and stochastic optimization techniques used in electrical machine design. The deterministic optimization techniques and the different ways to obtain the objective function gradient with respect to the design parameters are discussed first. Then, the stochastic optimization techniques are reviewed. At the end of this section, the multi-objective optimization problem is discussed, and the multi-objective optimization techniques used for SRMs design are reviewed.

3.2.1 DETERMINISTIC OPTIMIZATION METHODS

Deterministic optimization methods use objective function gradients with respect to the design parameters to guide the optimization iterates to the optimal solution [93]. The convergence of a gradient-based optimizer depends on the accuracy of the obtained gradients [94].

In this subsection, the objective function gradient estimation methods are covered first. Then, the deterministic optimization algorithms used for SRMs are reviewed.

3.3.1.1 OBJECTIVE GRADIENT CALCULATION METHODS

The gradient (the objective function sensitivity to the design parameters) can be estimated through numerical methods, adjoint variable methods, or using automatic differentiation, as categorized in figure 3.6. Gradients are routinely computed numerically using forward finite difference (FFD) [95], backward finite difference (BFD) [95], central finite differences (CFD) [96–98], and complex-step methods [98]. The FFD and BFD methods require one additional simulation for each design parameter, whereas the more accurate CFD requires two extra simulations for each design parameter. This means that the FFD and BFD require $n + 1$ simulations, whereas the CFD requires $2n + 1$ simulations per gradient calculation, where n is the number of the design parameters.

The approximations of these three methods when calculating the gradient of the objective function f with respect to x at x_i are illustrated in figure 3.7. A perturbation h is utilized in this figure. All three methods are computationally expensive and may require a convergence study to define the appropriate perturbation size h [98]. On the other hand, the obtained gradients using the complex-step method (CSM) are more

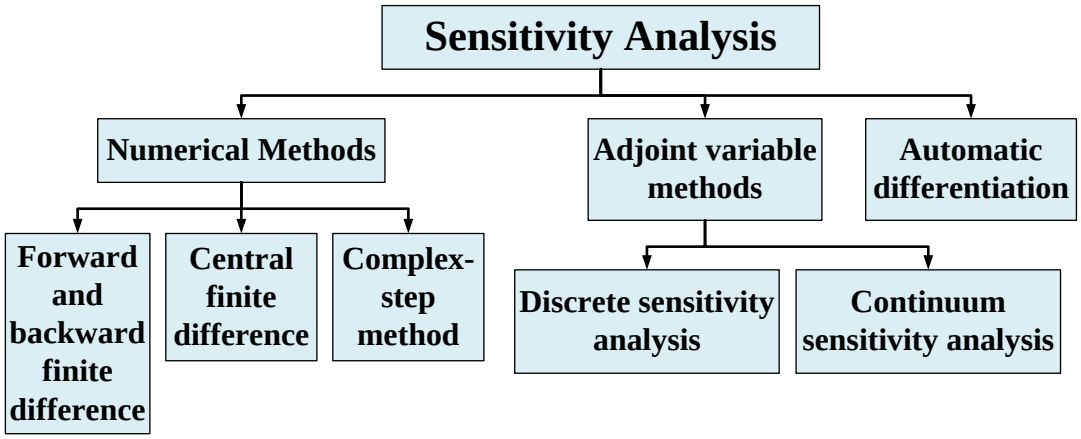

Figure 3.6: Methods of Sensitivity calculation

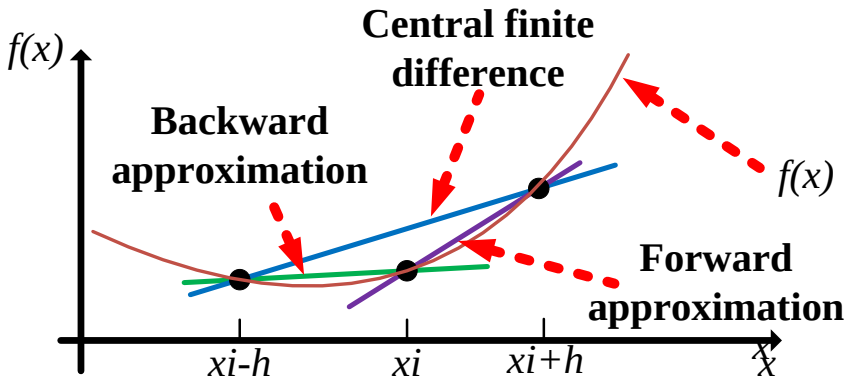

Figure 3.7: A clarification of the finite difference methods

accurate than those obtained with finite difference. methods [94]. The CSM is not subject to round off errors, and it can be generalized to any objective function [99]. However, it deals with a complex number variables, which is not applicable to the SRMs design as all the parameters are real.

The discrete adjoint variable method [100–102] and continuum adjoint variable method [103–106] outperform the finite difference methods in the number of required objective function evaluations at each step [94]. Unlike finite difference methods, they

obtain the objective function gradient with respect to all design parameters using one additional simulation for each iteration [97, 100, 107]. The discrete approach is typical as its equations are applicable to almost all FEA-based problems. However, the sensitivity calculation requires information like the FE system matrix and vector, which are not usually accessible. This limitation has been solved in [86] as the authors were able to use the available data to reconstruct the FE system matrix and vector and use it for discrete adjoint variable sensitivity calculation of SRM radial force with respect to the different design parameters.

On the other hand, the continuum approach does not require extensive access to the FE internal data structures. This method obtains sensitivity by differentiating the governing variational equation before discretization. The sensitivity formulas are formed using the material derivative concept of the continuum mechanics and based on the analytical equations of the state and the adjoint variables as described in [103] and [104].

Lastly, the automatic differentiation (AD) method calculates the derivatives of a computer program output with respect to the inputs. It repeatedly applies the chain rule to the program sequence of elementary arithmetic operations and functions. The AD method has two operating modes, namely forward accumulation and reverse accumulation [108]. The two modes compute the gradient of the function with a seed vector that has the same number of the function's inputs or outputs for forward accumulation and reverse accumulation, respectively [108]. The AD method was used to find the sensitivity of the electromagnetic force to different geometric parameters of a linear actuator in [108].

The optimal solutions determined by deterministic optimization methods are based

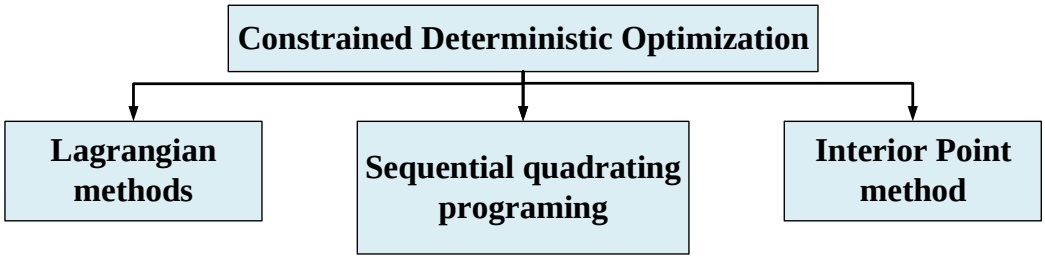

Figure 3.8: Methods of constrained deterministic optimization [12]

on the accuracy of gradient calculations. There is a trade-off between the method accuracy and optimization time, so the most suitable method to be used depends mainly on the application and project timeline.

3.3.1.2 Deterministic optimization Algorithms used for SRMs design

Deterministic optimization methods usually utilize a single objective function. Multiple objectives can be weighted together using aggregation methods such as arithmetic mean operator, harmonic mean operator, and Bonferroni mean [109]. Deterministic optimization methods can also be classified as unconstrained and constrained methods. The constrained methods are considered here since there are usually spatial constraints on the different design parameters of SRMs and electric machines design in general [110]. There are many constrained optimization methods that were applied to electric machines design. These include sequential quadratic programming, Lagrangian method, and interior point method, as shown in figure 3.8 [92].

A general optimization problem (given in equation (3.2.1), equation (3.2.2), and

equation (3.2.3)) is used to describe and illustrate the different deterministic optimization methods throughout this section.

$$\text{minimize: } f(\boldsymbol{x}) \tag{3.2.1}$$

$$\text{Subject to: } g_i(\boldsymbol{x}) \leq 0, \quad i = 1, 2, \dots m \tag{3.2.2}$$

$$\text{Subject to: } h_j(\boldsymbol{x}) = 0, \quad j = 1, 2, \dots l \tag{3.2.3}$$

where $f(\boldsymbol{x})$ is the objective function, $\boldsymbol{x}$ is the vector of the design variables, The design space is also subject to m inequality constraints and l equality constraints as described in equation (3.2.2) and equation (3.2.3), respectively. The upper and the lower values of the design variables are considered here a part of the inequality constraints in equation (3.2.2). We consider in what follows some of the key optimization methods used in the optimization problem solution given by equations (3.2.1) to (3.2.3).

LAGRANGIAN METHOD: The Lagrangian method [93] creates and solves a sub-problem obtained by linearizing the constraints and applying Lagrange function approximation at each step. In the algorithm, the objective function and all the equality and inequality constraints are combined in a single function as shown in equation (3.2.4). m slack variables, $\boldsymbol{\delta} = [\delta_1, \delta_2, \dots, \delta_m]$, are added to the inequality constraints to create the Lagrange function:

$$(\boldsymbol{x}, \boldsymbol{\delta}, \boldsymbol{\lambda}, \boldsymbol{\mu}) = f(\boldsymbol{x}) + \sum_{i=1}^{m} \lambda_i \left(g_i(\boldsymbol{x}) + \delta_i^2 \right) + \sum_{j=1}^{l} \mu_j \left(h_j(\boldsymbol{x}) \right), \tag{3.2.4}$$

where $\boldsymbol{\lambda} = [\lambda_1, \lambda_2, \ldots, \lambda_m]$ are the Lagrange multipliers for the inequality constraints and $\boldsymbol{\mu} = [\mu_1, \mu_2, \ldots, \mu_l]$ are the Lagrange multipliers for the equality constraints. The problem described in equation (3.2.4) has $(n + 2m + l)$ unknown variables, where n is the number of the design variables. A system of equations can be formed to solve all of these unknowns by forming the gradient of the Lagrange function with respect to all unknowns, as illustrated in [93]. The sequential quadratic programming, NLPQLP, and the interior point methods are based on the Lagrangian function to solve the optimization problem [86].

SEQUENTIAL QUADRATIC PROGRAMMING (SQP): This is an iterative method that uses the objective function's gradient for nonlinearly constrained problems [111]. This method is considered one of the most effective methods for solving constrained nonlinear optimization problems. The method solves subproblems in which the cost function is approximated as a quadratic function with linearized constraints [92]. The SQP is a time-efficient method if the number of design parameters is not too large, the objective function and its gradients can be obtained with high accuracy, the problem is smooth, and the design parameters are well scaled [112].

The basic idea of this method is to form a quadratic programming subproblem at each step based on a quadratic approximation of the Lagrange function, equation (3.2.4). Then the quadratic programming can be formed as follows [93]:

$$\min_{\boldsymbol{d}} \nabla f\left(\boldsymbol{x}^k\right)^T \boldsymbol{d} + \frac{1}{2}\boldsymbol{d}^T \boldsymbol{H}^k \boldsymbol{d} \tag{3.2.5}$$

$$\text{Subject to: } \nabla g_i\left(\boldsymbol{x}^k\right)^{\mathrm{T}} \boldsymbol{d} + g_i\left(\boldsymbol{x}^k\right) \leq 0,\ i = 1, 2, \ldots m \tag{3.2.6}$$

$$\text{Subject to: } \nabla h_i\left(\boldsymbol{x}^k\right)^{\mathrm{T}} \boldsymbol{d} + h_i\left(\boldsymbol{x}^k\right) = 0,\ i = m+1, \ldots m+l \tag{3.2.7}$$

where $\boldsymbol{d}$ is the search direction of the design parameters, $\nabla f\left(\boldsymbol{x}^k\right)$ and $\boldsymbol{H}^k$ are the objective function gradient and the Hessian matrix of the Lagrangian function at iteration number k, respectively, and $\nabla g_i\left(\boldsymbol{x}^k\right)$ and $\nabla h_i\left(\boldsymbol{x}^k\right)$ are the gradient of the inequality and equality constraints at iteration number k, respectively.

At each iteration, the Hessian matrix of the Lagrange function is approximated. The Hessian matrix can be approximated by the Broydon Fletcher Goldfarbo Shanno (BFGS) approximation as follows [113]:

$$\boldsymbol{H}^{k+1} = \boldsymbol{H}^k + \frac{\left[\boldsymbol{V}^k\right]^T \boldsymbol{V}^k}{\left[\boldsymbol{V}^k\right]^T \boldsymbol{U}^k} - \frac{\boldsymbol{H}^k \boldsymbol{U}^k \left[\boldsymbol{U}^k\right]^T \left[\boldsymbol{H}^k\right]^T}{\left[\boldsymbol{U}^k\right]^T \boldsymbol{H}^k \boldsymbol{U}^k} \tag{3.2.8}$$

$$\boldsymbol{V}^k = \nabla \boldsymbol{L}^{k+1} - \nabla \boldsymbol{L}^k \tag{3.2.9}$$

$$\boldsymbol{U}^k = \boldsymbol{x}^{k+1} - \boldsymbol{x}^k \tag{3.2.10}$$

where $\nabla\ \boldsymbol{L}$ is the gradient of the Lagrange function.

After solving the quadratic programming subproblem for the search direction $\boldsymbol{d}$, a linear search algorithm can be used to minimize the objective function along the search direction and update the variable vector as follows:

$$\boldsymbol{x}^{k+1} = \boldsymbol{x}^k + \alpha \boldsymbol{d} \tag{3.2.11}$$

where α is the optimal change of the design variable.

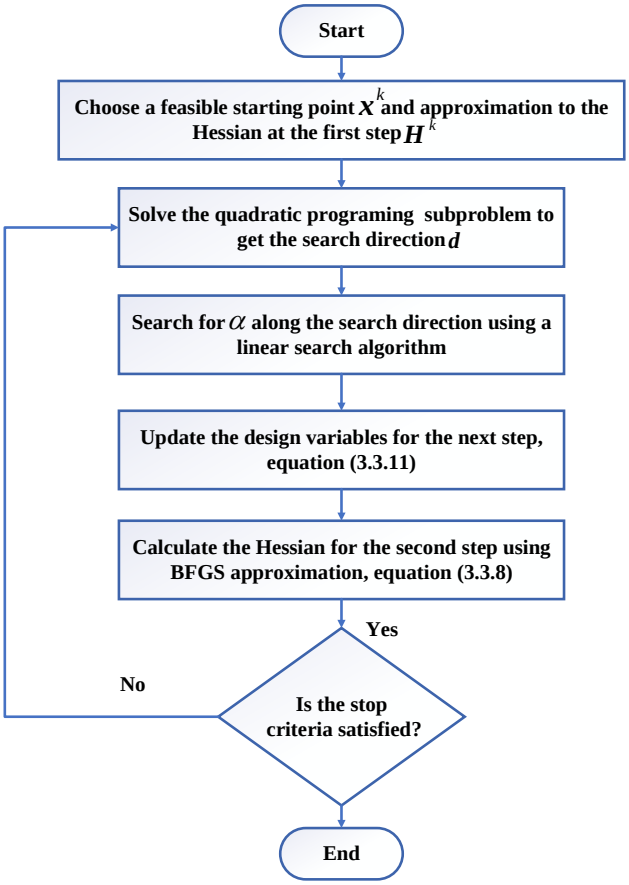

Figure 3.9: A flow chart of the sequential quadratic programming algorithm.

After determining the new design variable, the process is repeated till it reaches the termination conditions. Figure 3.9 shows a flowchart of the sequential quadratic programming method.

The SQP is considered one of the powerful deterministic optimization techniques. The only problem related to this technique is the high computational cost for each optimization step [114].

INTERIOR-POINT METHOD: The interior-point method (IPM) is a constrained optimization method used for SRMs and electrical machines design optimization. The IPM is a linear optimization technique based on the logarithmic barrier method to solve the linear and nonlinear optimization problem as discussed in [115]. By using a barrier function in IPM, consider a nonlinear optimization problem such as in equations (3.2.1) and (3.2.2), the constrained optimization problem is transformed into an unconstrained optimization problem as follows [116]:

$$R(\boldsymbol{x}, \mu) = f(\boldsymbol{x}) - \mu \sum_{i=1}^{m} \log\left(g_i(\boldsymbol{x})\right) \tag{3.2.12}$$

where μ is a positive scalar variable and called the barrier coefficient. As μ converges to zero, the minimum of equation (3.2.12) converges to the solution of equation (3.2.1). The gradient of the barrier function given in equation (3.2.12) is given as follows:

$$\nabla R = \nabla f(\boldsymbol{x}) - \mu \sum_{i=1}^{m} \frac{1}{g_i(\boldsymbol{x})} \nabla g_i(\boldsymbol{x}) \tag{3.2.13}$$

In addition to the function variable $\boldsymbol{x}$, the Lagrange multiplier $\boldsymbol{\lambda}$ is introduced as follows:

$$g_i(\boldsymbol{x})\lambda_i = \mu, \quad \forall_i = 1, \ldots, m \tag{3.2.14}$$

From equations (3.2.13) and (3.2.14), the gradient of the barrier function becomes:

$$\nabla f(\boldsymbol{x}) - \boldsymbol{A}^T \boldsymbol{\lambda} = 0 \tag{3.2.15}$$

where $\boldsymbol{A}$ is the Jacobian vector of the constraints. The Newton's method is then

applied to equation (3.2.14) and equation (3.2.15) as follows:

$$\begin{pmatrix} \boldsymbol{H} & -\boldsymbol{A}^T \\ \boldsymbol{\Lambda A} & \boldsymbol{G} \end{pmatrix} \begin{pmatrix} \boldsymbol{S}_x \\ \boldsymbol{S}_\lambda \end{pmatrix} = \begin{pmatrix} -\nabla f(\boldsymbol{x}) + \boldsymbol{A}^T \boldsymbol{\lambda} \\ \mu - \boldsymbol{G\lambda} \end{pmatrix} \tag{3.2.16}$$

where $\boldsymbol{H}$ is the Hessian matrix of the barrier function, equation (3.2.12), $\boldsymbol{G}$ is a diagonal matrix with $G_{ii} = g_i(\boldsymbol{x})$. The system of equations in equation (3.2.16) is solved for the design variable search direction, and the Lagrange coefficients search direction, then the design variables and the Lagrange coefficients are updated for the next step as follows:

$$\begin{aligned} \boldsymbol{x}^{k+1} &= \boldsymbol{x}^k + \alpha \boldsymbol{S}_x \\ \boldsymbol{\lambda}^{k+1} &= \boldsymbol{\lambda}^k + \alpha \boldsymbol{S}_\lambda \end{aligned} \tag{3.2.17}$$

The best value of α can be found by the linear search along the search direction of the design variables and the Lagrange coefficients. The Hessian matrix in equation (3.2.16) can be estimated for the next step by the BFGS approximation, as illustrated in equation (3.2.8). The algorithm iterates till the termination condition of the algorithm occurs [117].

In summary, this subsection reviewed the deterministic optimization technique used in the literature for electric machine design. The reader can find a detailed review of the various constrained deterministic optimization methods in terms of simplicity, reliability, and efficiency in [92].

3.2.2 STOCHASTIC OPTIMIZATION METHODS

Stochastic optimization techniques search for an optimal solution with randomness. They can deal with either single objective or multi-objective optimization problems.

Different stochastic algorithms considered in this section include:

1. Swarm Optimization (SO) [118–121]: The algorithm mimics natural beings' social behavior, such as birds and wolves, in searching for food.

2. Simulated Annealing (SA) [122, 123]: The algorithm simulates the heat treatment annealing process to reach the best value of the design objectives.

3. Genetic Algorithms (GA) [124]: The algorithm imitates the evolution process of species.

4. Evolutionary Algorithms (EAs) [125]: These algorithms mimic the evolution process of species based on the concept of natural selection. GA can be considered as a subdivision of the EAs. The main difference is that the parent selection in EAs is based on an equal probability of each individual, whereas the parent selection in GA is based on the likelihood of success and the parents' fitness values.

3.3.2.1 SWARM OPTIMIZATION TECHNIQUES

Many optimization techniques are inspired by the social behavior of beings in searching for food such as particle swarm optimization [118, 119], ant colony [126], and artificial bee colony [127–129]. The swarm optimization algorithms are simple, robust, and do not require the implementation of complex mathematical formulations [130].

Particle swarm optimization (PSO) was introduced by Kennedy and Eberhart more than 25 years ago [118]. It is a heuristic optimization technique that mimics the social behaviour of a group of beings that search for food and follow the group's leader. A flowchart that describes the particle swarm optimization algorithm is shown

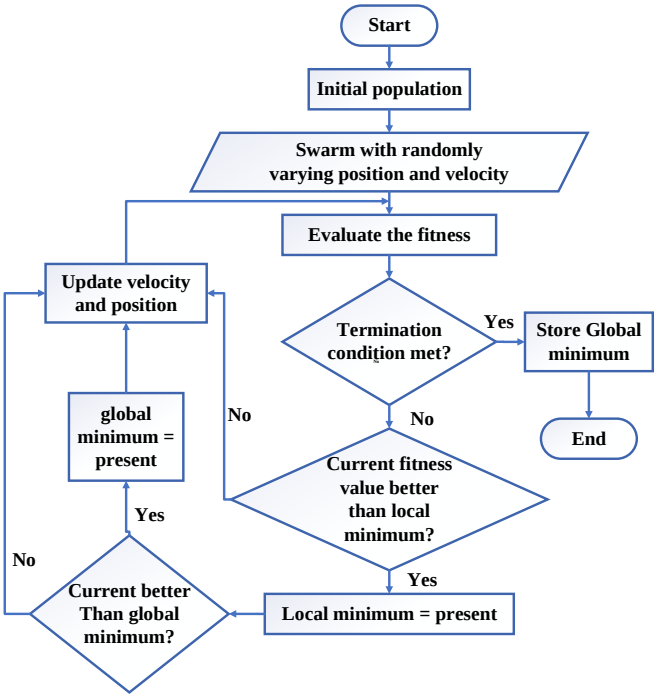

Figure 3.10: A flowchart of the particle swarm optimization algorithm.

in figure 3.10. In PSO, each particle (individual) location is a point in the design space. Each individual particle of the swarm is shifted at each iteration with a velocity that is a function of the best achieved self and global locations at the current iteration. This is represented mathematically as given in equations (3.2.18) and (3.2.19).

$$\boldsymbol{x}_i^k = \boldsymbol{x}_i^{k-1} + \boldsymbol{V}_i^k \tag{3.2.18}$$

$$\boldsymbol{V}_i^k = w\boldsymbol{V}_i^{k-1} + C_1 d_1 \left(\overline{\boldsymbol{x}}_i - \boldsymbol{x}_i^{k-1}\right) + C_2 d_2 \left(\tilde{\boldsymbol{x}} - \boldsymbol{x}_i^{k-1}\right) \tag{3.2.19}$$

where $\boldsymbol{x}_i^k$ and $\boldsymbol{V}_i^k$ are the position and the velocity of the i^{th} particle at the k^{th} iteration, respectively. $\overline{\boldsymbol{x}}_i$ is the best local solution of the i^{th} particle and $\tilde{\boldsymbol{x}}$ is the

best global solution of all particles. C_1 represents the cognitive learning factor that connects each particle to its own best value. The best global value is connected to each particle through the cognitive learning factor C_2.w is an acceleration factor that should be high at the first few iterations to explore a larger area in the parameters space. It then gets smaller to make the algorithm converge faster. d_1 and d_2 take random values between 0 and 1 .

As shown in figure 3.10, the algorithm starts by evaluating a random population's fitness with random positions and velocities. Then, the local minimum of that population is stored and compared to that of the next population. The algorithm updates the velocity and the positions of all population particles based on equations (3.2.18) and (3.2.19). The algorithm keeps running till the termination conditions are satisfied.

3.3.2.2 SIMULATED ANNEALING OPTIMIZATION

Simulated annealing algorithm is one of the stochastic optimization methods used extensively in the literature in electrical machines design optimization [75, 123, 131]. The algorithm is based on the heat treatment process of steel. It starts from a condition where the steel particles have high energy and in high instability and motion conditions. The particles cool down and reach a thermal equilibrium where they are arranged in a structure with lower internal energy through the optimization process. Through this process, the temperatures of the particles gradually decrease, and the objective function tends to reach the optimal solution. Figure 3.11 illustrates a typical procedure of the simulated annealing optimization technique. The algorithm starts from an initial feasible point $\boldsymbol{x}^k$ in the design space where the objective function

$f\left(\boldsymbol{x}^k\right)$ is evaluated. The equivalent temperature T_k at the k^{th} iteration is estimated based on equation (3.2.20).

$$T_k = T_{k-1}\left(1 - \frac{k-1}{k_{\max}-1}\right)^p \tag{3.2.20}$$

where T_{k-1} and $k_{\max}$ are the temperature of the previous step and the maximum number of allowable iterations, respectively, with the annealing coefficient $p > 1$. This is not the only cooling formula used in simulated annealing optimization algorithm and the reader can find other cooling formulas in [92].

The Metropolis rule is a step to accept the solution with a probability, y, based on the new particle energy, $E\left(\boldsymbol{x}_{\text{new}}\right)$, and the old particle energy $E\left(\boldsymbol{x}_{\text{old}}\right)$ as follows [132]:

$$y = \begin{cases} 1 & \text{if } E\left(\boldsymbol{x}_{\text{new}}\right) < E\left(\boldsymbol{x}_{\text{old}}\right) \\ \exp\left(-\frac{E(\boldsymbol{x}_{\text{new}})-E(\boldsymbol{x}_{\text{old}})}{T}\right) & \text{if } E\left(\boldsymbol{x}_{\text{new}}\right) \geq E\left(\boldsymbol{x}_{\text{old}}\right) \end{cases} \tag{3.2.21}$$

Based on the algorithm flowchart in figure 3.11, the Metropolis algorithm is a very important step in the SA algorithm to find the optimal solution of the problem.

In [131], a general multi-objective SA algorithm was utilized in a machine-related optimization process. The algorithm was compared to the classical PSO, attractionrepulsion-based PSO, Gaussian mutation-based PSO, and quadratic interpolation-based PSO. The SA algorithm outperformed all these algorithms in terms of accuracy, robustness, stability, and convergence rate.

The SA algorithm could improve the performance of classical PSO. Classical PSO does not have an effective global search, so it may not converge to the global solution

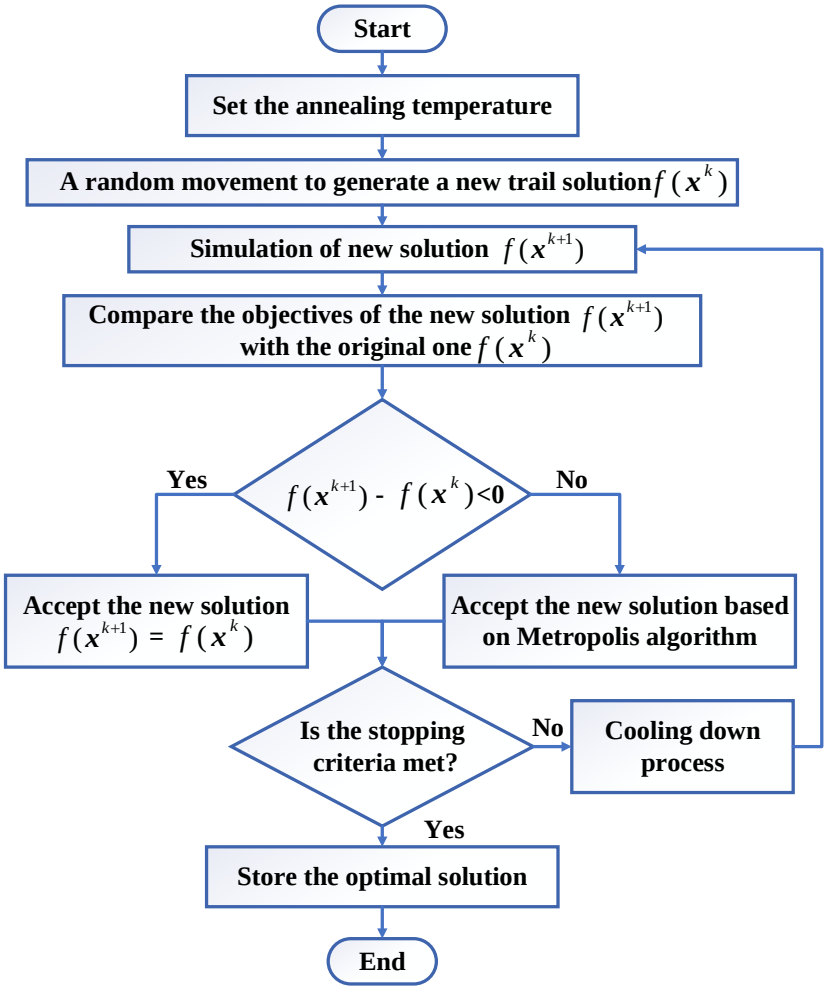

Figure 3.11: A flowchart of the simulated annealing optimization algorithm.

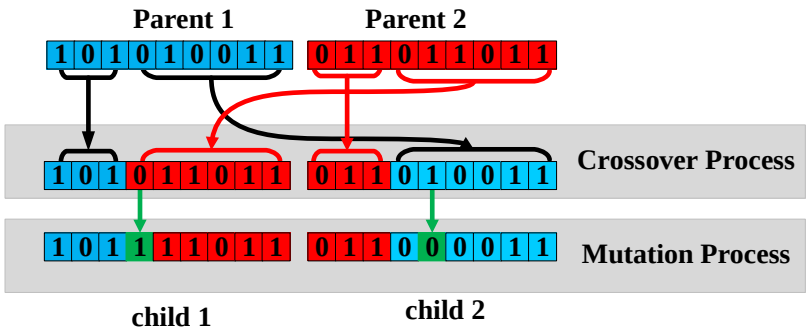

Figure 3.12: The crossover and mutation processes of the GA optimization technique.

and converge instead to a local one [133]. SA can enhance PSO robustness and effectiveness through the discrete PSO-SA algorithm at the expense of longer convergence time since more computations are required [133].

3.3.2.3 GENETIC ALGORITHM OPTIMIZATION

The genetic algorithm (GA) was first introduced in the 1960s [92]. It mimics the evolution process of the species and the concept of natural selection. This is mainly performed through the processes of parents' selection, crossover, and mutation, as illustrated in figure 3.12. The parents (parameters values) are selected first based on their fitness value (objective function value). The selection is generally based on a probability function that uses high-fitness individuals to produce offspring from their chromosomes. This means that the community fittest elements have the highest chance to produce the next generation. The algorithm encodes the values of the parents into binary strings. All the variables' binary strings are connected to a chromosome. As shown in figure 3.12, the parents' strings, blue and red, breed through the crossover process where the parents share their chromosomes to generate children. A random bit in each child string is then selected and inverted through the mutation

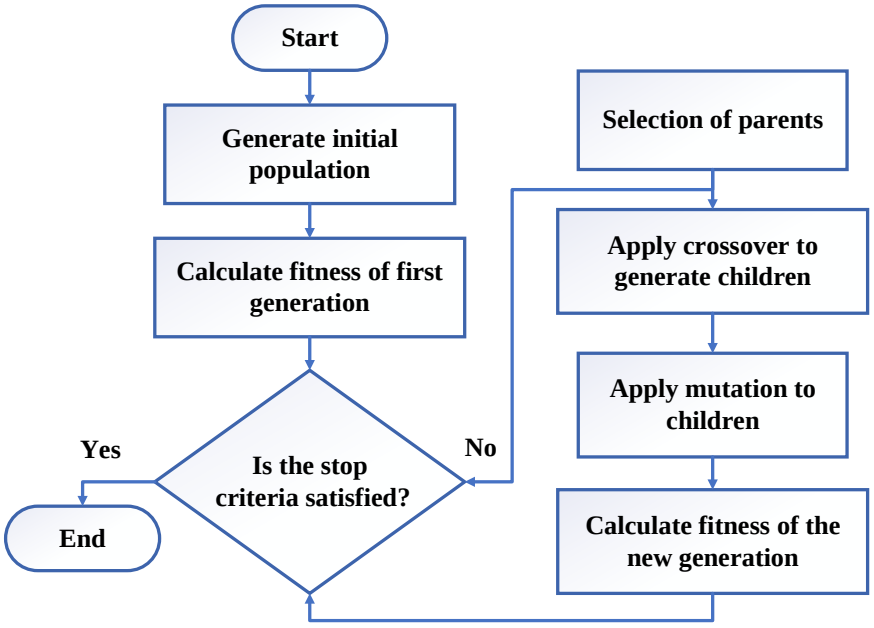

Figure 3.13: A flowchart of GA optimization.

process.

Figure 3.13 shows a flow chart of the GA procedure [134]. The algorithm begins with an initial population with m individuals. The fitness of each of these design points (individuals) is calculated. In the k^{th} generation, two individuals are chosen as parents. The crossover process is then applied with a high probability of up to 0.9 to all the individuals with high fitness. Two children are created when the crossover happens. The crossover probability, r_c, controls the exploitation of the high fitness individuals to generate offsprings. In contrast, if there is no crossover, the two children will be copies of their parents. The mutation is then applied with a minimal probability of up to 0.01 to each of the two children. The mutation probability, r_m, controls the exploration process and prevents the early convergence to a local optimum solution. The new population replaces the old one, and the fitness of the

m^{th} population individual is evaluated. The crossover and the mutation processes are repeated until the termination condition is reached [134].

The formulation of the population for a new generation in the GA is directly influenced by r_c and r_m. In [135], the author showed that the fixed values of these two parameters are less effective than the adapted values, and a better improvement in the problem of global optimal point convergence can be achieved if these two parameters become adaptive and dynamic. A fuzzy inference system was proposed in [136] to adapt the values of r_c and r_m which improve the GA performance. This algorithm is called genetic fuzzy algorithm (GFA) and is used in SRMs design in the literature [13]. In order to deal with the nonlinear constraint, an augmented Lagrangian genetic algorithm (ALGA) is proposed in [137]. The optimization problem solved by ALGA is defined as follows:

$$\text{minimize: } f(\boldsymbol{x}) \tag{3.2.22}$$

$$\text{Subject to: } g_i(\boldsymbol{x}) \leq 0, \quad \text{i} = 1, 2, \ldots m \tag{3.2.23}$$

$$\text{and } h_j(\boldsymbol{x}) = 0, \quad j = 1, 2, \ldots l \tag{3.2.24}$$

$$\text{and } \boldsymbol{A}\boldsymbol{x} \leq \boldsymbol{B} \tag{3.2.25}$$

$$\text{and } \boldsymbol{x}_{lb} \leq \boldsymbol{x} \leq \boldsymbol{x}_{ub} \tag{3.2.26}$$

where $\boldsymbol{x}_{lb}$ and $\boldsymbol{x}_{ub}$ are the lower and upper limits of the design, respectively. The constraints in this method are divided into two types: the nonlinear constraints, equation (3.2.23) and equation (3.2.24), and linear constraints, equation (3.2.25) and equation (3.2.26). A subproblem is formulated by combining the nonlinear equality and inequality constraints with the objective functions using the Lagrangian and the penalty functions as follows:

$$R(\boldsymbol{x}, \boldsymbol{\lambda}, \boldsymbol{s}, \rho) = f(\boldsymbol{x}) - \sum_{i=1}^{m} \lambda_i s_i \log\left(s_i - g_i\right) + \sum_{j=1}^{l} \lambda_{(j+m)} h_j + \frac{\rho}{2} \sum_{j=1}^{n} h_j^2 \qquad (3.2.27)$$

where λ is the Lagrangian multiplier estimate, s is a nonnegative shift, and ρ is a penalty parameter. The algorithm starts with an initial value of ρ. The GA algorithm minimizes a series of subproblems. At each one of the subproblems $\boldsymbol{\lambda}, \boldsymbol{s}$ and ρ are constants. When the subproblem is minimized with the required accuracy, the values of λ, s and ρ are updated to form the next subproblem. This process is repeated till reaching the stop criteria [137]. In this way, the GA algorithm can solve optimization problems with nonlinear equality and inequality constraints [137].

3.2.3 OTHER OPTIMIZATION TECHNIQUES USED IN THE DESIGN OF SRMs

This subsection reviews the optimization techniques that are not categorized as stochastic or deterministic techniques and used for SRMs design. This includes the design of experiments, response surface method, and Taguchi's method. This part also discusses the concept of multi-objective optimization.

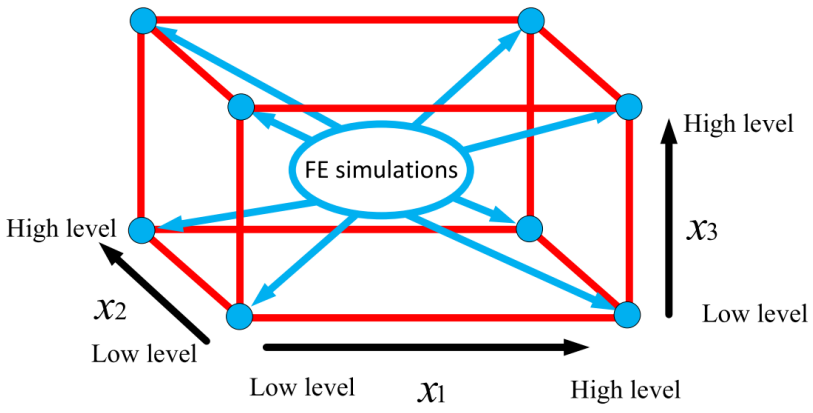

Figure 3.14: An example of the number of FE simulations DoE required when using the OFAT method for three variables with two levels.

3.3.3.1 DESIGN OF EXPERIMENTS METHOD

One of the time-efficient multi-objective optimization methods used for electrical machine design is the design of experiments method (DoE). DoE is a statistical optimization tool that effectively quantifies the effects of changing the geometrical design variables on the SRMs responses [120]. For a small number of design variables, the one factor at a time (OFAT) method is used. However, this method becomes impractical after a certain number of design variables as the number of FE evaluations increases exponentially with the number of design variables. As shown in figure 3.14, with only three variables and two levels for each design variable, eight FE evaluations are required with the OFAT method. In general, the number of process evaluations for this method is L^n, where L is the number of levels and n is the number of the design parameters.

The central composite design (CCD) and the Latin hypercube design (LHD) methods are used to overcome the OFAT limitation on the number of parameters. In the

CCD, the sample points are distributed at the center and the corners of the design space [138]. However, with a wide design space range, it is difficult for the CCD to gather the global response information of the electric machine [120]. The LHD covers the design space by random samples with the advantage of flexibility and better space-filling [139].

3.3.3.2 RESPONSE SURFACE METHOD

Another method used for multi-objective optimization is the response surface (RS) method. In the response surface method, the responses of the different objectives are evaluated at different points in space, then the response at any other point in the design space is evaluated by interpolation. The RS becomes the surrogate model of the SRM for multi-objective optimization using multi-objective optimization methods, such as PSO or GA [140].

3.3.3.3 TAGUCHI'S METHOD

According to this method, the optimization process consists of four steps: planning, conducting, analyzing, and validating [141]. The method starts with the planning phase, where the design parameters are selected and the required simulations are determined. The method is based on an idea called orthogonal array to determine the number of simulations required for the optimization. Table 3.1 presents a typical orthogonal array used in an optimization process consisting of four parameters and three levels for each parameter. This array is called $L_9\,(3^4)$, which means that nine simulations need to be conducted to optimize four parameters with three levels.

Table 3.1: $L_9\,(3^4)$ Taguchi's method orthogonal array for four design variables: with three design levels for each variable.

Simulation number	Design variables			
	A	B	C	D
I	1	1	1	1
II	2	2	2	1
III	3	3	3	1
IV	3	2	1	2
V	1	3	2	2
VI	2	1	3	2
VII	2	3	1	3
$VIII$	3	1	2	3
IX	1	2	3	3

The second phase of Taguchi's method is to conduct all the simulations planned in phase 1 . The results are then analyzed to know the effect of each parameter on the objective function through a statistical study, and the best performance is selected [142]. Taguchi's method was utilized in the design of SRMs, and more details can be found in [142–144].

3.3.3.4 MULTI-OBJECTIVE OPTIMIZATION DESIGN OF SRMs

As discussed in section 3.1, different performance indices can be used as objective functions when optimizing SRMs. In multi-objective optimization, more than one performance index of SRMs are considered, and solution candidates are processed differently, as discussed in this section.

Most of the research efforts to improve the SRMs performance utilized only one objective function. However, improving only one performance metric at a time may have adverse effects on the other indices. On the other hand, multiobjective optimization provides a set of optimal solutions, which considers the behaviour of more

than one performance index [145]. Therefore, multi-objective optimization can provide better SRM designs from different perspectives compared to the single-objective optimization to fit the needs of the different applications [120, 146].

The multi-objective optimization problems of SRMs can be described as follows:

$$\text{minimize: } \boldsymbol{f}(\boldsymbol{x}) \tag{3.2.28}$$

$$\text{Subject to: } g_k(\boldsymbol{x}) \leq 0, \quad k = 1, 2, \ldots m \tag{3.2.29}$$

$$\text{Subject to: } h_j(x) = 0, \quad j = 1, 2, \ldots l. \tag{3.2.30}$$

$$\boldsymbol{x}_{low} \leq \boldsymbol{x} \leq \boldsymbol{x}_{up} \tag{3.2.31}$$

where $\boldsymbol{f}(\boldsymbol{x}) = [f_1, f_2, \ldots\ldots\ldots f_h] : \boldsymbol{x} \rightarrow \mathbb{R}^h$ is the objective functions vector, h is the number of objective functions, $\boldsymbol{x}$ is the design variable vector defined in the design space $\mathbb{R}^n, n$ is the number of the design parameters, whereas $\boldsymbol{x}_{up}, \boldsymbol{x}_{\text{low}}$ are the upper and lower boundary vectors of the design variables, respectively. The design space is subject to m inequality constraints and l equality constraints, as shown in equation (3.2.29) and equation (3.2.30), respectively.

In multi-objective optimization, the notation of "optimum" is called a "Pareto optimal solution". A multiobjective optimization solution is called a Pareto optimal solution or non-dominant solution if there is no way to improve one objective without adversely affecting one or more of the other objectives. The group of Pareto optimal solutions of the optimization problem is called the Pareto front set of solutions. A graphical representation of a multiobjective optimization solution of a two-objective function problem is shown in figure 3.15. The solutions A and B are nondominant, whereas solution C is dominant. C is not an element of the set of the optimal solutions as other solutions can improve both objective functions simultaneously compared to

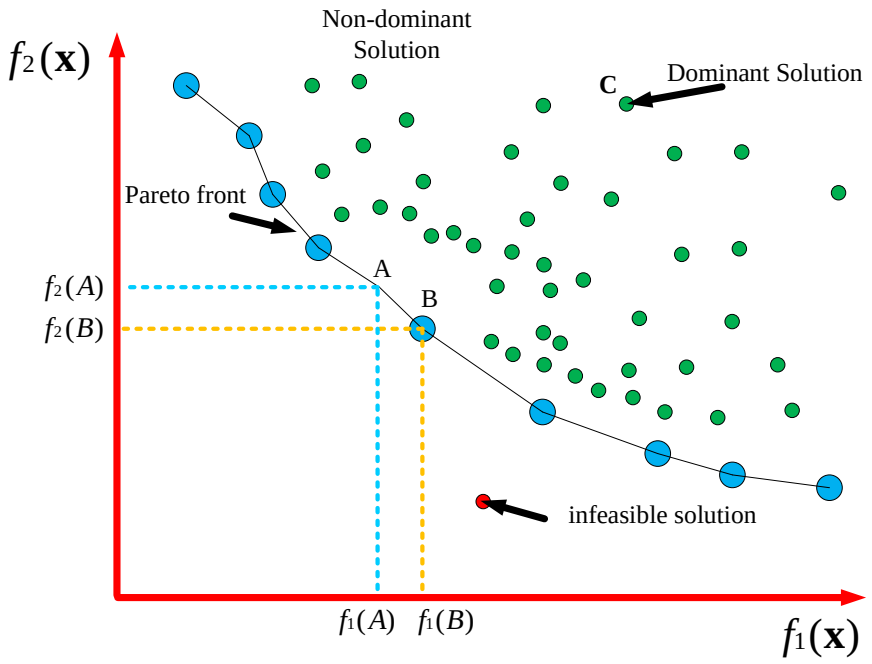

Figure 3.15: A graphical representation of the solutions of a two-objective optimization problem and the Pareto front set of solutions.

the objective functions' values of solution C.

After defining the set of Pareto front solutions, a decision making method should be used to select one of the Pareto front set elements as an optimal solution based on the design requirements. The decision-making process is based on the trade off between the different objectives to satisfy the design requirements [147].

Stochastic optimization techniques such GA [13, 123, 148–150], PSO [151, 152], and SA [75, 123], were used for multi-objective optimization of SRMs in the literature. A more detailed literature review of the single-objective and the multi-objective optimization of SRMs is discussed in the next chapter.

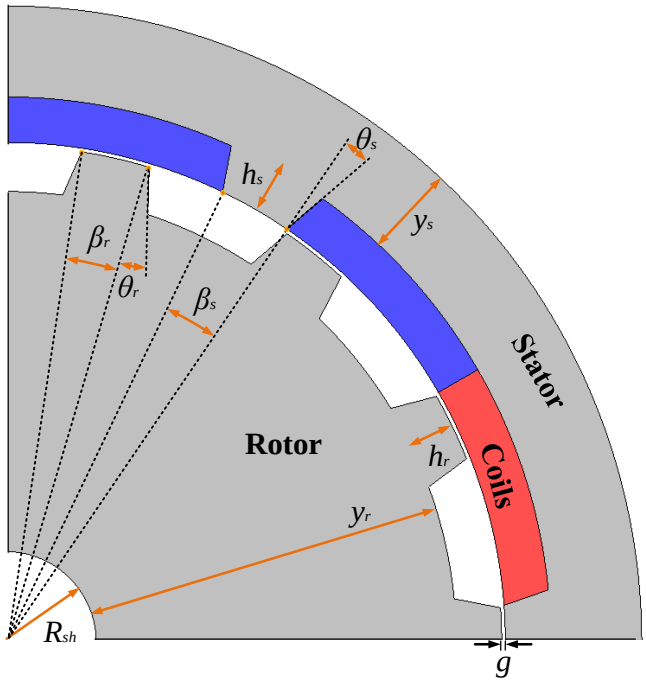

Figure 3.16: Main optimizable design parameters of SRMs.

3.3 Geometry Optimization of SRMs

After reviewing the different deterministic and stochastic optimization methods used in literature for electric machines design, this section illustrates how these techniques were applied to enhance the performance of SRMs. The geometry of electric machines is usually optimized to enhance performance. Section 3.3 shows the geometrical optimizable design parameters of SRMs. The parameters h_s and h_r are the length of the stator and rotor teeth, respectively. The parameter y_s is the stator yoke thickness, whereas y_r is the rotor yoke thickness. The parameters β_s and β_r are the arc angles of the stator and rotor teeth, respectively. The parameter θ_s represents the taper angle of stator teeth, whereas θ_r is the rotor teeth taper angle. The parameter g is the airgap length and R_{sh} is the shaft radius. The stator outer diameter and stack length

are not commonly optimized since they are constrained by the application [153].

In [123], GA and SA were used to optimize the stator and rotor teeth arc angles, rotor diameter, and stack length of a 1 kW four-phase 8/6 radial-flux SRM to maximize the motor power density. The SA algorithm was able to achieve more than twice the power density increase achieved by GA [123]. However, SA required ten times longer time compared to GA.

The same geometric parameters were optimized in [75] to improve the power density of a two-phase 4/2 unidirectional radial-flux SRM by GA and SA. The SA algorithm was found to be more effective as it increased the machine power density by $\sim$ 27% as compared to an 11.7% increase using GA. The results show the fast convergence of the SA algorithm as compared to GA. Despite its superior performance, there is no much-reported research on using SA in the geometry optimization of SRMs.

In [152], a classic multi-objective PSO algorithm was applied to minimize the torque ripple and maximize the average torque of a four-phase 8/6 1.1-kW radial-flux SRM by optimizing the machine geometry. The considered geometric parameters are stator outer diameter, outer rotor diameter, stack length, air gap length, and stator and rotor teeth arc angles. The achieved results were compared to those of GA. The PSO increased the average torque by 5% and reduced the torque ripple by 7% as compared to the average torque and the torque ripple achieved by using GA.

A hybrid PSO-GA algorithm was applied to maximize the average torque and minimize the magnetic loss of a fourphase 8/6 radial-flux SRM [148]. The arc angles of the stator and rotor teeth and the thickness of the stator and rotor yokes were used in the optimization process. It was found that a proper selection of the weighting

factors (C1 and C2 in equation (3.2.19)) and the acceleration factor w, increases the convergence rate of the PSO algorithm [148].

To decrease the computation time of FEA-based SRM optimization, the authors in [152] used an artificial neural network ANN-based model to predict and optimize the performance of a four-phase 8/6 3.7-kW radial-flux SRM. The rotor and stator teeth arc angles were optimized to increase the average torque and reduce the torque dip. The PSO and GA algorithms were used for the optimization problem. The GA algorithm increased the average torque by 27.9% and reduced the torque dip by 34.4% as compared to the initial design. On the other hand, the proposed PSO algorithm increased the average torque by 29.1% and reduced the torque dip by 34.7% as compared to the initial design. The PSO algorithm also showed a faster convergence than the GA algorithm in this study.

In [154], the objective was to maximize both the average torque and the inductance ratio (to minimize the torque ripple) of a four-phase 8/6 3.7-kW SRM using PSO and GA. The inductance ratio is the ratio between the unaligned and aligned inductances. The PSO and GA increased the inductance ratio by 88.9% and 85.9% and the average torque by 29.1% and 27.9% as compared to the initial design, respectively. The PSO outperformed the GA in terms of design space exploration, speed of convergence, and robustness.

In [153], a multi-objective PSO (MOPSO) algorithm was used to simultaneously maximize the average torque, torque to copper loss ratio, and torque to motor active volume ratio (torque density). The considered optimization parameters are the stator and rotor pole arc angles. Weighting factors were used to provide a single objective

out of the required three objectives. A prototype of the optimized motor was implemented, and a good match was found between the experimental and simulation results.

In [153], a multi-objective PSO (MOPSO) algorithm was used to simultaneously maximize the average torque, torque to copper loss ratio, and torque to motor active volume ratio (torque density). The considered optimization parameters are the stator and rotor pole arc angles. Weighting factors were used to provide a single objective out of the required three objectives. A prototype of the optimized motor was implemented, and a good match was found between the experimental and simulation results.

A novel multi-objective genetic particle swarm optimization algorithm (MOGPSO) was proposed in [151] to increase the torque density and efficiency of a three-phase $12/81.5-$kW bearingless SRM (BSRM). The rotor yoke thickness, rotor pole height, and stator pole height and width were considered for the optimization process. The torque density increased by 287.6%, and the efficiency of the machine increased by 1.54% compared to the initial design. The process was based on an analytical model of the BSRM. The results were validated by FEA, where the analytical model showed a maximum error of 12.12% as compared to the FEA model. The results showed that the proposed MOGPSO could search for more accurate non-dominated solutions in the Pareto front than the MOPSO [151].

The ant colony, artificial bee colony, and firefly algorithms are not commonly utilized to optimize the geometries of SRMs. Instead, they are used to optimize the control parameters of the machine drive circuit to increase the average torque and reduce the torque ripple [155–159]. A metaheuristic ant colony algorithm was

used in [160] to maximize the average torque and efficiency of a three-phase 18/12 outrunner radial-flux SRM based on the motor analytical model. The optimization process considered five geometric parameters: the arc angles of stator and rotor teeth, the thickness of stator and rotor yokes, and rotor bore diameter. The average torque increased to 426.4Nm, and the motor efficiency increased to 95.66% at the operating speed. A maximum error of 6.5% was found between the analytical and FEA model results.

GA is prevalent in the geometry optimization of SRMs. It is very suitable for such an application due to the existence of many local minima that arise from the machine's nonlinearity [161, 162]. GA was used in [163] to maximize the torque of a three-phase 6/4 radial-flux SRM. The considered geometric parameters were the thickness of the stator and rotor yokes, shaft radius, height and arc angles of the stator and rotor teeth, air gap length, and stack length. The GA algorithm increased the average torque by 3.75% higher than the heuristically optimized machine. In [162], GA was utilized to maximize the torque density of a $10-$kW 48/50 low-speed slotted SRM (SSRM) for direct-drive wind energy generation. The optimization process was based on a 2D-FEA motor model to increase the accuracy at the expense of a longer optimization time. The thickness of the stator and rotor yokes, in addition to the stator and rotor teeth parameters, were optimized.

The GA algorithm and the SQP algorithm were used to optimize three-phase 6/4 60 kW SRM to maximize the torque per ampere ratio of the machine in [164]. The GA optimization results showed that it is independent of the initial design. However, the SQP final design was changed by changing the initial design.

In [165], the Augmented Lagrangian Genetic Algorithm (ALGA) was compared

to the parametric solution selection (PSS) method in optimizing a four-phase 8/14 radial-flux SRM based on a 2D FEM model of the machine. The objective is to maximize the average torque, torque factor (product of peak and average static torques of half electric cycle), loss factor (ratio of average torque to motor copper losses), torque density, and torque quality factor (ratio of average to peak static torques) and to minimize the torque ripple. The objective function was formed by the weighted sum of the different mentioned objectives. In the ALGA optimization, the considered parameters are the arc angles and taper angles of stator and rotor teeth, the thickness of stator and rotor yokes, and stator pole teeth height. Only stator and rotor teeth arc angles were considered in the case of the PSS optimization. The peak steady-state torque increased by 4.65%, the average steady-state torque increased by 4.8%, the torque factor increased by 7.02%, the torque quality factor increased by 2.73%, the torque density increased by 1%, the loss factor increased by 38.59%, and the torque ripple decreased by 2.34% in the case of using ALGA compared to PSS. However, the comparison does not seem reasonable as the considered parameters are different in both cases.

Multi-objective GA optimization was used in [149] to optimize the geometry of a four-phase 24/18 18.6-kW SRM for an aerospace application. The stator and rotor teeth arc angles, outer rotor diameter, and stack length were optimized to increase the flux linkage to maximize the torque and the power per unit volume. The GA optimization results were compared to those resulting from a heuristic approach. The power density and maximum torque of the GA-optimized design are 13.97% and 12.1% higher than the heuristically optimized one.

The authors in [13] used the genetic fuzzy algorithm optimization method to

maximize the efficiency and minimize the torque ripple of a four-phase 8/6 4-kW radialflux SRM. As previously explained, the conventional GA algorithm selects the parents based on a probability function that gives the fittest individuals more chance to produce offspring from their chromosomes. The objective functions are combined with fuzzy weights in [13] to ensure that the fittest individuals for all objective functions have the highest probability of being selected. Nine different geometric parameters and the number of turns per phase were considered in the optimization process. The method improved motor performance as the efficiency increased by 4%, and the torque ripple decreased by 18% compared to the initial design.

In [166], a kriging-method-based surrogate model of a two-phase unidirectional 4/2SRM was used to reduce the optimization time of the Pareto archived evolution strategy algorithm by reducing the number of the FEA simulations. The objective was to minimize the torque ripple and maximize the starting torque per phase. Each rotor tooth was divided into two parts of different heights in this design, as shown in Section 3.3. The considered optimization parameters are β_0, I_{g1} and I_{g2}. This procedure increased the starting torque by 25% and reduced the torque ripple by 57.6% compared to the initial design.

The complexity of multi-variable geometry optimization of a 12/8 low-speed SRM, used in micro electric vehicles, was minimized in [167] using a subset quasi-orthogonal algorithm. The algorithm optimizes the outer rotor diameter, arc angles of stator and rotor teeth, and stator and rotor yoke thicknesses to minimize the torque ripple and maximize the average torque. The proposed optimization technique comprises four steps. The constraints were first determined. Then, the sensitivities of the torque and torque ripple to the considered parameters were obtained. Thirdly, the multi-variable

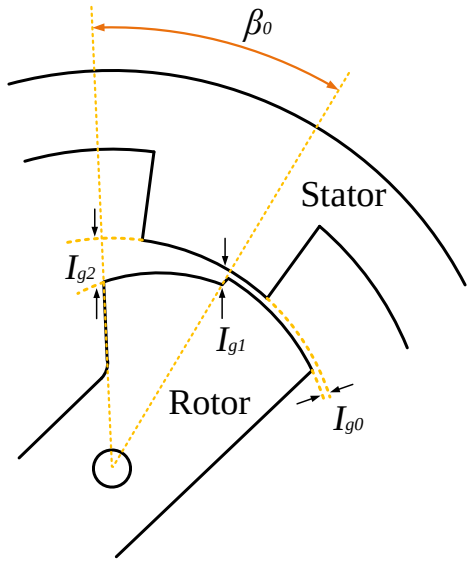

Figure 3.17: The optimizable geometric parameters in [166]

optimization problem was divided into three subsystems according to the sensitivity with respect to the parameters. Finally, subsystem optimization was sequentially performed. A significant drawback of this procedure is that the sensitivities were calculated once based on the initial design. The change in the sensitivities, as the design changes, was not and the average torque increased by more than 8% compared to the initial design.

The concept of reducing the number of design variables based on their sensitivities was also presented in [120]. Based on the sensitivity analysis of the torque density, efficiency, and torque ripples to the different design parameters, the number of design parameters decreased from 13 to 6 . The 6 design parameters are selected based on their objective function sensitivity.

The authors of [168] utilized a Pareto-based multiobjective differential evaluation

method to maximize the static torque, efficiency, and torque per volume of a three-phase 18/12 outer-rotor radial-flux SRM for in-wheel EV application. The considered parameters are stator outer diameter, stator and rotor teeth arc angles, and stator and rotor yokes' thicknesses. In the Pareto-based optimization, the algorithm provides a set of nondominant solutions and level the selection process to the decision-maker [168]. An analytical model of the SRM was used in the optimization process to reduce the computational time. The optimized design was validated numerically, using 3D FEA simulations, and experimentally.

The average torque and the inductance ratio coefficient of an 8/6 SRM were maximized in [152] using a PSO method with an adaptive accelerating factor. The stator and rotor outer diameters, stack length, airgap thickness, and the arc angles of stator and rotor teeth were considered. The PSO optimization method was able to increase the average torque by 32.5% and decrease the torque ripple by 34.97% compared to the initial design.

The GA algorithm was used to maximize efficiency and minimize the torque ripple of a four-phase 8/6 4-kW SRM [13]. The stator and rotor outer diameters, number of phase turns, air gap length, the thickness of stator and rotor yokes, and the height and arc angles of the stator and rotor teeth were considered in the optimization process. A magnetic equivalent circuit model of the machine was used to reduce the optimization time. The objective functions were joint with fuzzy membership functions such that the fittest chromosomes for all objective functions have a higher probability of continuing to the next generation [13]. However, the other chromosomes could be considered in the next generation according to their fuzzy weights [13]. The fuzzy expert performance predictor is designed based on a sensitivity analysis of the

motor parameters [13].

In [95], an interior-point optimization algorithm used the adjoint-based sensitivities to optimize the geometry of a 6/14 radial-flux SRM to maximize the machine static torque characteristics. The considered parameters were rotor teeth height, stator yoke thickness, rotor yoke thickness, stator pole arc angle, rotor pole arc angle, stator teeth taper angle, and rotor teeth taper angle. The average value of the static torque half-cycle increased by 33.52% compared to the initial design.

The average torque and torque per inertia of a fourphase 8/6 SRM for high-acceleration applications were maximized in [169] using one factor at a time (OFAT) design of experiments optimization. OFAT is a method of designing experiments that simulates one parameter change at each step instead of multiple factors. It does not require previous knowledge about the optimization problem. However, the number of simulations needed increases exponentially with the number of design parameters [121].

In [170], Taguchi method was used to decrease the required number of simulations and the simulation time. Eight geometric parameters were considered in the optimization process [169]. After 2189 simulations, the peak static torque increased by 5%, and the average static torque increased by $\sim 2\%$ compared to the initial design.

The influence of different stator and translator geometric parameters of planar and tuber LSRMs on the electromagnetic force and electromagnetic force ripples were studied in [171, 172]. In [171], the number of phases, pole stroke (distance covered by the translator's teeth from two consecutive aligned positions when two successive phases are excited), and the current density were optimized to maximize the force per copper mass and the force density of a longitudinal flux double-sided LSRM. The

force density increased by 132%, and the force per copper mass increased by 78% compared to the initial design.

The study in [172] shows that increasing the translator pole width of single-sided LSRM, Figure 2.12, increases the trust force but decreases the specific force of the machine at the same time. The study also shows that increasing the translator pole pitch increases the trust force but also increases the cogging force at the same time. The stator pole width has to be carefully selected to maximize the average trust force and minimize the force ripples of that machine [172]. The effect of the stator pole shoe shape of the single-sided LSRM is also discussed in [172]. One way to maximize the thrust force and minimize the force ripple is to optimize the skew and taper angles of stator poles [172]. One of the critical parameters of the LSRM is the airgap length, the length of the gap between the translator and the stator. The length reduction increases the trust force but increases the force ripple at the same time, so this parameter should be carefully optimized based on the application needs [172].

In [173], an EA-based optimization algorithm was used to optimize the stator and translator pole width and height and stator yoke thickness of a double-sided longitudinalflux LSRM. The optimization objective was to achieve a low mass to force ratio and improve the force quality for verticalmotion applications. The mass-to-force ratio was decreased by 8.15%, and the force ripple decreased by 76.5% compared to the initial design.

The authors of [174] used the different geometrical parameters sensitivities to minimize the force dip ratio and to maximize the active payload ratio of a segmented-stator single-sided planar LSRM. A high payload ratio means a high on-load capacity, which indicates a high conveyance efficiency. The distance between two stator segments,

translator pole width, translator pole tip width and height, and the stator segment slop angle are the parameters used for optimization. The payload ratio increased by 43.8%, and the force dip ratio decreased by 21.3% compared to the machine's initial design.

The authors of [174] used the different geometrical parameters sensitivities to minimize the force dip ratio and to maximize the active payload ratio of a segmented-stator single-sided planar LSRM. A high payload ratio means a high on-load capacity, which indicates a high conveyance efficiency. The distance between two stator segments, translator pole width, translator pole tip width and height, and the stator segment slop angle are the parameters used for optimization. The payload ratio increased by 43.8%, and the force dip ratio decreased by 21.3% compared to the machine's initial design.

In [153], the one factor at a time DoE was used to optimize the stator and the rotor pole arc angles of an inner-stator outer rotor 8/6 SRM with four-level for each variable to maximize the mean torque, mean torque per copper loss ratio, and torque density. The weighted average method was used to select the solution that satisfies the design requirements.

In [140], the central composite design (CCD) method was used to build the response surface models of the torque ripple and efficiency of a four-phase 8/6 inner-rotor SRM. The design variables were stator and rotor pole arc angles and phase turn-off angles. A multi-objective GA method was used to minimize the torque ripple and maximize the motor efficiency. Finally, the Pareto front was drawn to select the optimal solution. The torque ripple decreased by 33.25%, and the motor efficiency increased by 3.43% compared to the initial design.

Geometry optimization was used in the literature for SRMs core losses reduction. In [175], the tooth width to pole arc angle ratio, the rotor diameter to the machine outer diameter ratio, and the pole arc angle to the airgap length ratio were used to minimize the torque per ohmic loss and maximize the efficiency of a three-phase 6/4 SRM. The stack length, the airgap thickness, and the number of turns were optimized in [176] to maximize the machine efficiency of an SRM. The efficiency of the considered machine increased to 86%.

These studies and more are summarized in Table 3.2 to give the reader an overview of the methods and the objective functions that were used in the literature for SRMs geometry optimization.

3.4 Topology Optimization of SRMs

In geometry optimization, geometric parameters, such as those shown in Section 3.3, are optimized to enhance the machine performance. The number of design parameters is fixed in geometry optimization, and the geometry follows a predetermined template. Another type of optimization, topology optimization (TO), allows the topology of the structure to evolve to a new topology in an iterative way. For example, flux barriers inside the rotor or the stator design spaces could be added and optimized for performance improvement [184–186]. These barriers increase the number of optimizable parameters if geometry optimization is used, which increases computation time and complexity [187]. Also, geometric parameterization and optimization of flux barriers are not flexible to reach the best shape [187]. Topology optimization provides more smooth barrier designs as it allows a flexible material distribution in the considered domain to achieve the objective functions [188]. An example of the flux barrier design

Table 3.2: Summary of the reviewed studies and some other studies about geometry optimization of SRMs.

Reference	Machine Configuration	Optimization		Objective Function					Experimental Validation of the Design
		Optimization Type	Optimization Method	Average Torque	Torque Ripple	Torque Density	Radial Force	Efficiency .	
[123]	4-phase 8/6	Geometry	SA/GA	-	*	*	-	-	No
[153]	4-phase 8/6	Geometry	DOE	*	-	*	-	*	YES
[175]	3-phase 6/4	Geometry	N/M	*	–	–	–	*	No
[13]	4-phase 8/6	Geometry	GA	–	*	–	–	*	No
[176]	N/M	Geometry	Response surface	–	–	–	–	*	No
[74]	3 -phase 6/14	Geometry/ topology	Interior point& On/off TO	*	*	–	–	–	No
[150]	3 -phase 12/8	Geometry	GA	*	*	–	*	–	No
[163], [177] [148], [152]	4-phase 8/6	Geometry	PSO& GA	*	*	–	–	–	No
[87]	4-phase 8/6	Geometry	Trial and error& using FEA	–	–	–	*	–	YES
[151]	3-phase 12/8	Geometry	Genetic PSO	–	–	*	–	*	NO
[160]	3-phase 18/12	Geometry	Ant Colony	*	–	–	–	*	NO
[162]	3-phase 12 / 64	Geometry	GA	–	–	*	–	–	NO
[163]	3-phase 6 / 4	Geometry	GA	*	–	–	–	–	NO
[165]	4-phase 8/14	Geometry	ALGA	*	*	*	–	*	NO
[149]	4-phase 24/18	Geometry	GA	*	–	*	–	–	NO
[13]	4-phase 8/6	Geometry	GFA	–	–	*	–	*	NO
[166]	2-phase 4 / 2	Geometry	N/M	*	*	–	–	–	NO
[152]	4-phase 8 / 6	Geometry	PSO	*	*	–	–	–	NO
[178]	3 -phase 12 / 8 AFSRM	Geometry	Trial and error& using FEA	*	–	–	–	–	YES
[179]	LSM	Geometry	EA	*	*	*	–	–	YES
[174]	LSM	Geometry	Proposed technique	*	*	–	–	–	YES
[180]	4-phase 8 / 6	Geometry	Penalty/Lagrangian methods	–	*	–	–	–	NO
[181]	3 -phase 12 / 8	Geometry	Trial and error& using FEA	*	*	–	–	*	YES
[182]	LSRM	Geometry	N/M	*	*	*	–	–	No
[164], [183]	3-Phase 6 / 4	Geometry	SQP/GA methods	*	–	*	–	–	No
[140]	4-phase 8/6	Geometry + control	CCD+RS+GA	–	*	–	–	*	No
[120]	3-phase 6 / 10	Geometry	PSO & DoE	*	*	–	–	*	No
[143]	4-phase 16 / 14	Geometry	Taguchi method	*	*	–	–	*	YES
[171]	LSRM	Geometry	N/M	*	–	*	–	–	YES

"*" Considered as an objective function.
"-" Not considered as an objective function.
"N/M" Not mentioned in the article.

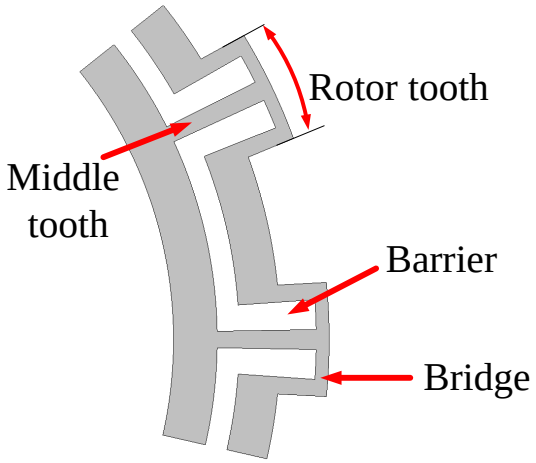

Figure 3.18: A rotor flux barrier design for 6/14 radial flux SRM.

in SRM is shown in Figure 3.18.

Several published articles use topology optimization to improve SRMs performance. Topology optimization was first applied to SRMs in [189] to maximize the machine magnetic energy profile. It was then used in [15] to reduce the vibration caused by the magnetic forces. In [19], it was applied to the rotor and stator poles of a 6/4SRM to reduce the torque ripples.

This optimization type could lead to novel SRM geometries [19, 190]. Manufacturability constraints could be added to the optimization problem to ensure the feasibility of the design. Additive manufacturing (AM) could also help to manufacture resulting complex shapes [191].

Figure 3.19 shows various topology optimization methods were used for the performance improvement of electric machines in the literature. TO methods are classified into two main categories: gradient-based and non-gradient-based methods.

The level set method is a gradient-based TO method. It gives a more feasible

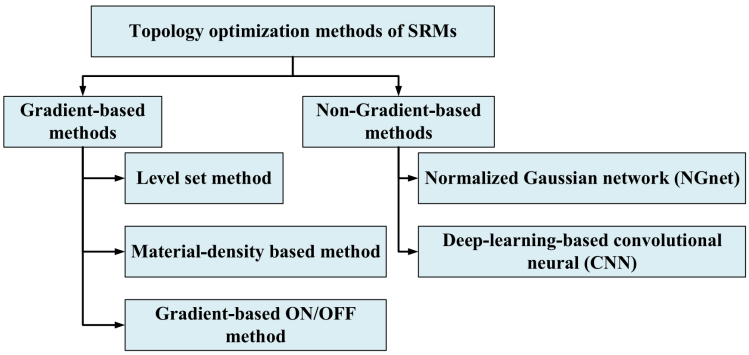

Figure 3.19: Main topology optimization methods of SRMs.

solution but with a slower convergence as compared to the material-density-based method [192]. The design space and boundaries are represented with a level set continuous function [193]. For a given design space S with a boundary B, as shown in Figure 3.20, the level set function is given as follows:

$$\begin{cases} \varphi(x,y) > 0, & \text{Magnetic material} \\ \varphi(x,y) = 0, & \text{Boundary edge} \\ \varphi(x,y) < 0, & \text{Air.} \end{cases} \tag{3.4.1}$$

The objective of the level set topology optimization is to find the value of $\varphi(x,y)$ at each location (x,y) and to effectively distribute the material on the design space to satisfy the design objectives. The method usually falls into local optima as it relies on the sensitivity of the different design space elements [194].

The level set method was used in [192] to increase the torque to mass ratio of an 8/6 SRM. The TO applied to the rotor region in this study was able to increase the torque density of the motor by 7.75%. This was, however, coupled with a reduction of the mean torque by 1.2% as compared to the reference design.

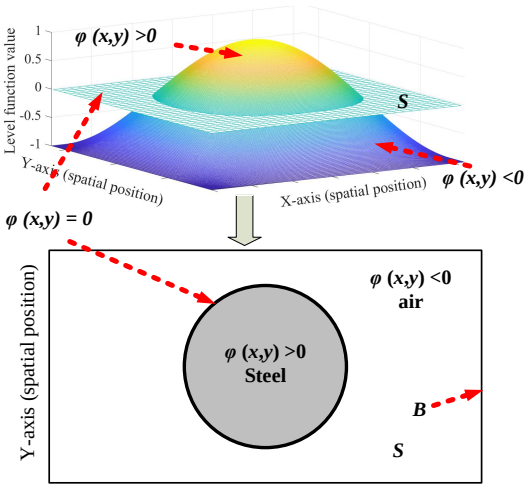

Figure 3.20: A level set function and the corresponding material distribution in the design space.

Another topology optimization technique called Material-density-based methods or method of moving asymptotes was used for SRMs design [195]. Material density-based methods have faster convergence than the level set method [192, 196]. The objective function is minimized by defining the material type (air or ferromagnetic material) based on the value of the density function ρ_i of the i^{th} element as follows:

$$\rho_i \begin{cases} 1, & i \in \Omega_m \\ 0, & i \in \Omega_a \end{cases} \tag{3.4.2}$$

where Ω_m and Ω_a are the ferromagnetic and air regions, respectively. Although the material status should be either 0 or 1 , the method allows the density function to be continuous between 0 and 1 by replacing the density function in (40) with a smooth Heaviside function $\rho(\psi)$, defined by an auxiliary optimization variable, ψ [196]. This procedure helps to make the density function continuous and prevent

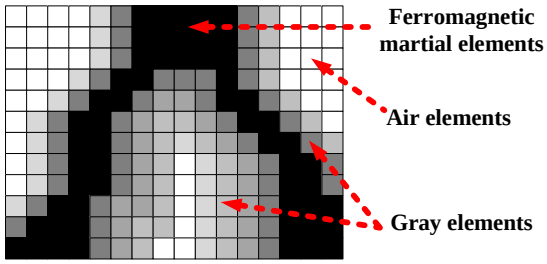

Figure 3.21: The design space after material-density-based TO optimization.

discontinuity [191]. However, as shown in Figure 3.21, it leads to gray elements whose material does not exist in reality. In the auxiliary optimization variable method [196], the density is described by a smoothed Heaviside function with a switch level:

$$\rho(\psi) = \frac{3}{16}\left(\frac{\psi}{h}\right)^5 - \frac{5}{8}\left(\frac{\psi}{h}\right)^3 + \frac{15}{16}\left(\frac{\psi}{h}\right) + \frac{1}{2}, (-h \leq \psi \leq h), \tag{3.4.3}$$

where h is the half of the switch width between $\rho(h) = 1$ and $\rho(-h) = 0$

The magnetic reluctivity of the i^{th} element is then defined as follows [192, 197] :

$$v_i\left(\psi_i, \left|B^2\right|\right) = (1 - \rho\left(\psi_i\right))^p * v_{\text{air}} + (\rho\left(\psi_i\right))^p * v_F\left(\left|B^2\right|\right) \tag{3.4.4}$$

where v_i, v_{air} , and v_F are the reluctivity of the i^{th} element, the reluctivity of air, and the reluctivity of ferromagnetic material, respectively. v_F is a function of the square of the flux density B at that element. The variable p is the penalization coefficient. The proper selection of p prevents the presence of gray elements with $0 < \rho_i < 1$.p was suggested to be equal to 3 in [197] to ensure good convergence to the white and black elements with a small number of gray elements.

In [192], material-density-based TO resulted in thin parts that need to be structurally evaluated. A material-densitybased TO exploiting sequential linear programming was used in [19] to minimize the torque ripple of a three-phase 6/4 radial-flux SRM. The considered design space included the rotor and part of the stator teeth. The torque ripple decreased to 27% compared to a torque ripple of 245% for the initial design.

The authors of [191] used the method of moving asymptotes to optimize the rotor teeth topology of a four-phase 8/6 radial-flux SRM to maximize the average torque and reach the target torque for two different applications. After optimizing the two motors, the torque of the final designs reached target torque of 0.12 and 0.16 N.m.

The authors of [198] used a gradient-based ON/OFF TO method in designing electromagnetic devices for the first time. The method is based on the objective function sensitivity with respect to the reluctivity of each element in the design space [198, 199].

Figure 3.22 shows a flowchart of the method. The algorithm starts by evaluating the objective function value of the initial SRM topology. Then, the objective function sensitivities are computed with respect to the reluctivity of the elements of the design space [74]. Ferromagnetic material and air are assigned to elements with positive and negative sensitivities, respectively. This applies to the highest-sensitivity elements until the allowable number of designable elements N is attained. Designable elements are those elements inside the design space allowed to change their material. If the objective function value decreases, the topology changes and the new topology sensitivities are calculated. However, if the objective function value increases, N decreases in the annealing process. The overall process continues until N reaches

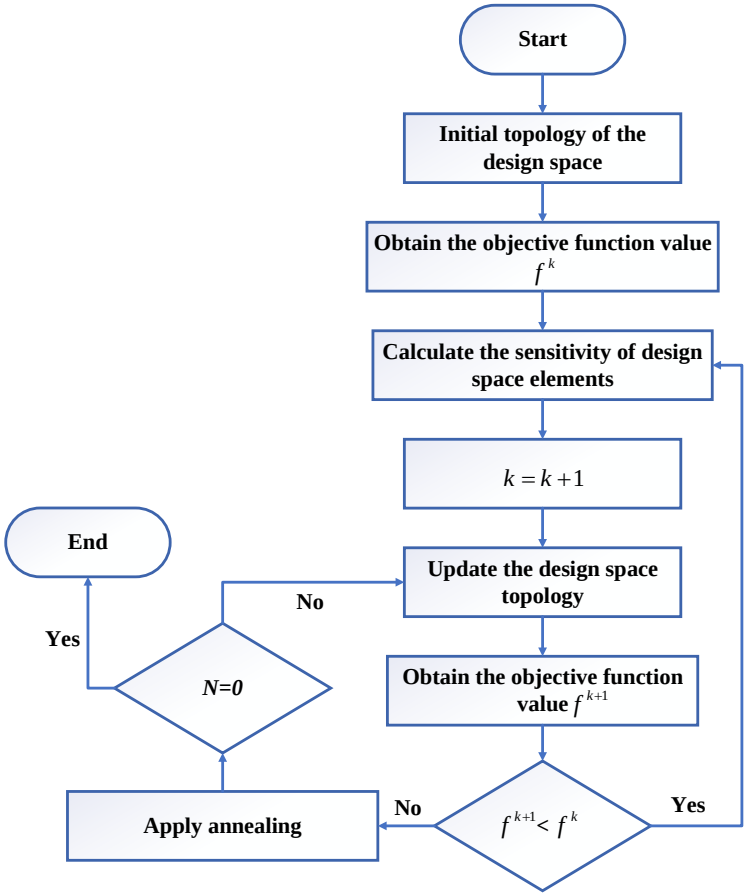

Figure 3.22: The design space after material-density-based TO optimization.

zero.

The gradient-based ON/OFF topology optimization deals with a large number of design variables and has faster convergence characteristics than the material-density-based method [198]. This topology optimization has less computational time than GA-based ON/OFF topology optimization, but it may terminate at a local optimum solution, unlike GA.

A gradient-based ON/OFF topology optimization was used to minimize the torque

ripple of a 6/14 SRM for Heating, Ventilation, and Air Conditioning (HVAC) application in [74]. A part of the stator tooth was considered as the design space. The torque ripple gradients to all the design space elements were computed using the discrete adjoint variable method [199]. The motor torque ripple was reduced by $\sim 14\%$, but the average torque also slightly decreased since the introduced flux barriers reduced the machine flux linkage.

The main disadvantage of gradient-based topology optimization is the difficulty of evaluating non-differentiable objective functions such as iron losses [187]. A nongradient-based ON/OFF topology optimization, also known as stochastic topology optimization, can be applied in this case [194,200]. This approach does not require any gradient information [201], but it may result in unacceptable and complex shapes with isolated magnetic regions, as shown in Figure 3.21 [202, 203]. In [155], the authors proposed the immune algorithm that overcame this issue and produced a TO-based manufacturable design. Figure 3.22 shows a flowchart of the ON/OFF TO with the immune algorithm. The algorithm is based on the mammalian immune system [194]. It starts with evaluating an N number of initial solutions called antibodies. If any solution satisfies the termination condition, it will be selected as the final solution. If this is not the case, P% of the low-ranked antibodies will be eliminated. Several clones are created for each survived antibody based on its rank; more clones are developed as the rank increases. The affinity maturation process is then applied to the different clones. Different clones are modified by changing the material in the surrounding elements of some random nodes to air or steel, as shown in Figure 3.23. $P\%$ of antibodies is randomly generated, and the process repeats. This algorithm was used to optimize the topology of the rotor of an SRM to maximize the average torque in [204].

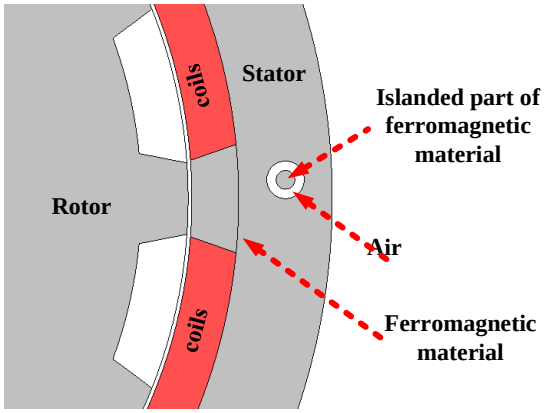

Figure 3.23: The design space after material-density-based TO optimization.

Another non-gradient-based TO method is the Normalized Gaussian Network (NGnet) [14]. This method avoids isolated elements and leads to smooth manufacturable structures [187]. The design space is divided into Ncells number of cells (elements). Each cell's state is defined by the NGENT function's output that is determined based on the weighted sum of the normalized Gaussian function. The output of the NGnet is obtained from:

$$y(\boldsymbol{x}) = \sum_{i=1}^{N} w_i b_i(\boldsymbol{x}) \tag{3.4.5}$$

$$b_i(\boldsymbol{x}) = \frac{G_i(\boldsymbol{x})}{\sum_{j=1}^{N} G_j(\boldsymbol{x})} \tag{3.4.6}$$

where $G_i(\boldsymbol{x})$ is a Gaussian function at the location $\boldsymbol{x}$. The variables i and j represent cell indices, and w_i is the weighting coefficient of the normalized function

$b_i(\boldsymbol{x})$. The state S_c of cells is determined from:

$$S_c = \begin{cases} \text{on} & y(\boldsymbol{x}_c) \geq 0 \\ \text{off} & y(\boldsymbol{x}_c) < 0 \end{cases} \tag{3.4.7}$$

where $\boldsymbol{x}_c$ is the center of cell c. When the state of the cell is on, its material is set to iron, whereas the material is set to air when the state is off.

Figure 3.24 shows the process of determining the state of each cell's based on the weighted sum of the associated normalized Gaussian function. The NGnet topology optimization requires substantial computational cost as FEA-based computation is needed at each generation [14].

To the authors' best knowledge NGnet was not used for SRM topology optimization. However, this method showed a significant performance improvement for other types of electrical machines such as Synchronous reluctance motor [187] and interior permanent magnet motor [14]. This is considered a potential opportunity to enhance the performance of SRMs by using the NGnet topology optimization method in the future. The drawback of this method is the high computational cost, as indicated in [14].

Recently, topology optimization gained more attention thanks to the additive manufacturing technologies that allow manufacturing more complex shapes than traditional manufacturing, [191,191,192]. Topology optimization results in a honeycomb structure of the rotor and stator. This structure is complicated to be realized by traditional manufacturing methods [191]. The complete process, including design optimization, 3D printing of the SMC parts, and assembly, was investigated in [191,205]. In [205], additive manufacturing was used to manufacture a complex rib structure

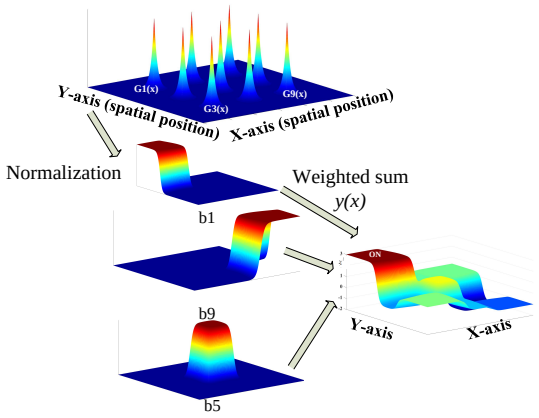

Figure 3.24: The output of the NGnet weighted sum function in the case of nine Gaussian functions for nine cells.

rotor for a three-phase 6/4 SRM with a novel rotor structure to minimize the torque ripple and the windage loss. The torque ripple of that motor decreased by 35.8% compared to the original design without the complex structure rib. Besides, the windage loss decreased by introducing a thin rib on the outer part of the rotor.

On the other hand, the change in the material properties due to the additive manufacturing process should be considered. Additive manufacturing and 3D printing of the optimized parts change the material magnetic, electric, and mechanical characteristics [206]. Eddy-current loss in the 3D printed solid cores is higher than that of the laminated cores [191]. In [191], the author depends on selecting an SMC material that has the highest possible resistivity to limit the eddy current loss of the optimized part.

Topology optimization is sensitive to mesh density and material $B-H$ characteristics [192]. Representing the material with a linear reluctivity model and decreasing the mesh density decreases the optimization time; however, the optimized machine performance accuracy decreases, and the optimized shape becomes coarse [192]. In [207],

it was concluded that different material reluctivity models, linear and nonlinear, lead to different results. This can be addressed by using a section of the machine with symmetrical boundaries.

A summary of the studies that used topology optimization for improving the performance of SRMs in the literature is organized in Table 3.3.

3.5 Topology Optimization Based on Deep Learning

Machine learning is used for electrical machines optimization through automating surrogate model building within the optimization loop [210]. Using surrogate models reduces the ON\OFF or GA-based topology optimization time. Different surrogate models can be used based on different methods such as the response surface method [211,212], kriging method [213], space mapping method [214], artificial neural network method [215], and convolutional neural network [14]. In that way, the optimization method time can be reduced significantly.

Many machine learning methods were used in literature for electric machine design. These methods include deep learning, random forest technique, extreme learning, support vector machines, and artificial neural network. The deep-learning-based convolutional neural network (CNN) was used in literature for the topology optimization of electric machines. However, to the authors' best knowledge, no machine learning method was used for SRM topology optimization. This section reviews the effectiveness of machine learning on optimizing other types of electric machines to

show that it could be a potential opportunity for enhancing the topology optimization of SRMs.

In [14], deep learning was used to reduce the NGnet topology optimization computational burden and time of interior permanent magnet motor (IPM motor) design optimization. The algorithm is divided into learning and optimization phases. In the learning phase, the training data was developed by performing a preliminary topology optimization using a small number of individuals (design elements). The motor 2D images were used to train a convolutional neural network (CNN).

In the optimization phase, the convolutional neural network was used to replace the FEA. The CNN was trained to classify different motor models based on the model performance index, such as motor efficiency, average torque and torque ripple. If the performance index is low, such as low average torque or high torque ripple, the CNN is used for motor performance evaluation; However, if the motor performance is predicted to be high, FEA of the motor topology is performed for motor performance evaluation. With this technique, the number of FEA execution for NGnet reduced by around 30% [14].

There are two feasible deep learning techniques for topology optimization computational acceleration: online and offline techniques [191, 207]. The former technique performs the training process during the optimization phase, whereas the latter performs the learning phase first. The method used in [14] is illustrated in Figure 3.25. The red path in the figure represents the preliminary process for the initial CNN training. The green path represents the evaluation of the design performance within the optimization loop based on CNN. The yellow path represents categorizing the

performance evaluated by CNN to check the probability of FEA evaluation requirement. The blue path represents the FEA of the design and the possibility of using this evaluation on the online training of CNN.

The main problem of CNN is that it requires a large number of data points for the training process prior to the optimization process [216]. The authors in [216] proposed a method for CNN training based on transfer learning which required a small number of data for the training process. In this method, a single VGG-16 CNN, which is CNN trained with 1.2 million learning data and composed of 1000 different classes [217], was used as a surrogate model for two different IPM motors. The preliminary training data was obtained from a GA topology optimization with a small population size of two different IPM motors with variations in the rotor structure. The motor performance is shown to be correctly inferred by the transfer learning with small data used for learning. In the optimization stage, the CNN was used to evaluate all the individuals of the GA optimization except the Pareto front individuals evaluated by FEA. The method was used to optimize two different IPM motors with different rotor structures. The computational cost of the GA-based topology optimization was reduced to 15% using CNN with transfer learning concept compared to the conventional GA method where FEA is used for fitness evaluation for all individuals.

In [218], the number of the required finite element electromagnetic evaluations of the target machine was reduced by 50% compared to the number required by GA-based topology optimization. An initial topology was optimized first by GA with a small population size to train the CNN. The CNN is then used as a surrogate model in the main topology optimization with large population size. This technique reduced

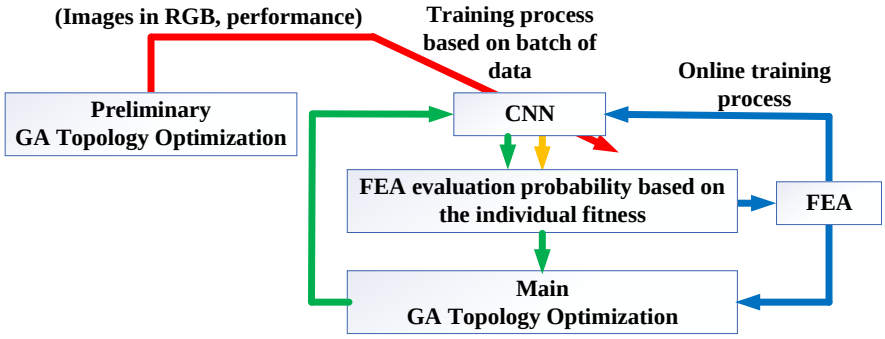

Figure 3.25: A flowchart of topology optimization based on offline trained CNN for electric machine design.

the number of finite element simulations by 50% compared to GA-based topology optimization.

3.6 Trends and Opportunities

There is currently increasing interest in the geometry and the topology optimization of SRMs to address the machine limitations such as high torque ripple, low average torque, and high acoustic noise. That will help widen the application areas of SRMs. Design optimization of SRMs configurations like the axial flux SRMs and LSRMs were not covered well in the literature, and the number of publications that covered this area is around 10% of the total publications of SRMs optimization (covered in this research). The authors expect an increase in these percentages in the future due to the advantages of these configurations.

In general, according to our research, the number of publications for topology optimization of SRMs is around 20% of the total publications of the SRMs design optimization. The authors of this review study believe that this percentage will

increase in the future due to the effectiveness of the topology optimization and the significant advance in additive manufacturing.

On the other hand, CNN deep learning shows a significant reduction in the topology optimization time of electrical machines; however, it was not used for SRMs design yet. It is currently trending as a non-gradient-based topology optimization method and could be a research opportunity to use such a technique in SRM performance improvement.

There are abundant opportunities for topology optimization techniques like NGnet and non-gradient-based ON/OFF methods for SRMs topology optimization. These methods show a significant performance improvement for other types of electric machines, and according to our best knowledge, these methods have not been used yet for SRMs design optimization. These techniques are considered an excellent opportunity to improve the performance of the SRMs.

3.7 Summary

The chapter provides a comprehensive review of different optimization techniques used to enhance SRMs performance metrics. The discussion starts with a brief discussion about various configurations of SRMs. Radial and axial, rotating and linear, and other categories are reviewed.

Then, the chapter investigates deterministic and stochastic optimization procedures. The main techniques under each category used for SRMs optimization are explained. Although deterministic optimization techniques are faster than stochastic techniques, the latter guarantee achieving a globally optimum solution. Unlike

stochastic optimization, deterministic optimization requires the gradients of the objective functions with respect to the design parameters. Finite difference and adjoint variable methods could be used to calculate these gradients. Although the finite difference methods are accurate with acceptable error, they are computationally expensive compared to the less accurate adjoint variable methods.

After reviewing the performance metrics of SRMs that were used as objective functions in literature, the chapter then reviews the geometry optimization of SRMs to improve these objective functions.

Finally, the topology optimization of SRMs is reviewed, and most of the topology optimization methods used for SRMs performance optimization are reported. Topology optimization could result in complex shapes. Different techniques that solve this issue were reported. Besides, additive manufacturing makes achieving TO-based intricate designs easier.

Topology optimization techniques are very timeconsuming processes. There is abundant opportunity to decrease its time by using CNN deep learning, which is not covered in the literature. The CNN deep learning showed a significant reduction in the topology optimization of electrical machines such as PMSM, and it is recommended to investigate its performance with SRMs.

Table 3.3: Summary of the studies used topology optimization for improving the performance of SRMs in the literature.

Reference	**Machine configuration**	**Optimization**		**Objective function**					**Exp. validation of design**
		method	design space	Average torque	Torque ripple	Torque density	Radial force	Other	
[74]	3-phase 6 /14	Interior point method & ON/OFF TO	Stator teeth	*	*	-	-	-	No
[15]	3-phase 6 /4	Level set method	Stator	-	-	-	*	Minimize frequency response of the stator structure	No
[19], [195] [208]	3-Phase 6/4	Material-density-based TO	Stator teeth and rotor	-	*	-	-	-	Yes [208]
[204]	3-phase with 24 slot new rotor topology	ON/OFF TO with immune algorithm	Rotor	*	*	-	-	-	No
[209]	4-phase 8/6	level set method	Rotor teeth	*	*	-	-	-	No
[192]	4-phase 8/6	Materia l-density-based methods (GCMMA)	Rotor teeth	*	-	-	-	Minimize mass	No
[75]	3-phase 6/4	ON/OFF TO based on GA and SA	-Rotor -Stator -Copper	*	-	-	-	-	No
[191]	4-phase 8/6	Material-density-based methods	Rotor teeth	*	*	-	-	-	No

"*" Considered as an objective function.
"-" Not considered as an objective function.

Chapter 4

Torque and Force Calculations of SRMs

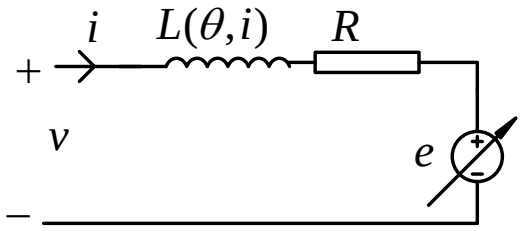

Figure 4.1: The phase equivalent resistance of SRMs ignoring the mutual inductance between phases.

4.1 A review in SRM Principle of Operation

The SRMs generate the torque by varying the magnetic reluctance of the magnetic circuit. The switched reluctance machine presents highly nonlinear characteristics due to double saliency. The double saliency nature of the SRMs means the machine has saliency in the rotor, and it has saliency in the stator as well. The phase flux linkage $\psi(\theta, i)$ and hence the phase inductance $L(\theta, i)$ of the machine are functions of the phase current, i, and the rotor position, θ. The equivalent phase circuit of SRM is shown in Figure 4.1 neglecting the mutual inductance between phases.

The phase voltage can be calculated based on the phase equivalent circuit shown in Figure 4.1 as follows:

$$V = iR + \frac{d\psi(\theta, i)}{dt} \tag{4.1.1}$$

Considering that $L(\theta, i) = \psi(\theta, i)/i$, the phase voltage can be calculated as follows:

$$V = iR + L(\theta, i)\frac{di}{dt} + \frac{dL(\theta, i)}{d\theta}\frac{d\theta}{dt}i = iR + L(\theta, i)\frac{di}{dt} + \frac{dL(\theta, i)}{d\theta}\omega_r i \tag{4.1.2}$$

where ω_r is the rotor speed in rad/sec, i is the phase current, and R is the phase resistance. the last term of the equation can be considered as the back emf voltage which is equivalent to the brushed DC motor emf. the back emf voltage can be calculated as follows:

$$e = \frac{dL(\theta, i)}{d\theta}\omega_r i \tag{4.1.3}$$

So, the phase voltage equation of SRM can be given as follows:

$$V = iR + L(\theta, i)\frac{di}{dt} + e \tag{4.1.4}$$

It is worth to mention that, the back emf of SRM, e, can not be measured experimentally. However, it is a term proposed in the literature to make the phase voltage equation similare to that of the brushed DC machine.

The input power to the switched reluctance motor can be found by multiplying the phase voltage ,the Equation (4.1.1), by the phase current as follows:

$$P = Vi = i^2R + i\frac{d\psi(\theta, i)}{dt} \tag{4.1.5}$$

The first term of the power equation, i^2R represents the DC copper losses. The second part of the power equation, $id\psi(\theta, i)/dt$, represents the mechanical output power plus the stored energy in the machine magnetic circuit. As the power is the change in energy in a certain amount of time, the second term of the power equation can be given as follows:

$$P = \frac{dW}{dt} = i\frac{d\psi(\theta, i)}{dt} = \frac{dW_m}{dt} + \frac{dW_f}{dt} \tag{4.1.6}$$

where dW_m/dt is the mechanical power of the motor and dW_f/dt is the power stored in the magnetic field. The output mechanical power of the SRM can be expressed as a function in the output torque T and the motor speed ω_r.

$$\frac{dW_m}{dt} = T\omega_r = T\frac{d\theta}{dt} \tag{4.1.7}$$

From Equations (4.1.6) and (4.1.7), The torque can also be expressed as follows:

$$T = i\frac{d\psi}{d\theta} - \frac{dW_f}{d\theta} \tag{4.1.8}$$

The magnetic energy storage can then be expressed by:

$$W_f = \int_0^{\psi} id\psi \tag{4.1.9}$$

The co-energy storage can be expressed as follows:

$$W_c = \int_0^{i} \psi di \tag{4.1.10}$$

By adding the magnetic stored energy in Equation (4.1.9) to the magnetic co-energy in Equation (4.1.10),this gives Equation (4.1.11) as described by 4.2:

$$W_f + W_c = i\psi \tag{4.1.11}$$

Equation (4.1.11) can be differentiated as follows:

$$dW_f + dW_c = id\psi + \psi di \tag{4.1.12}$$

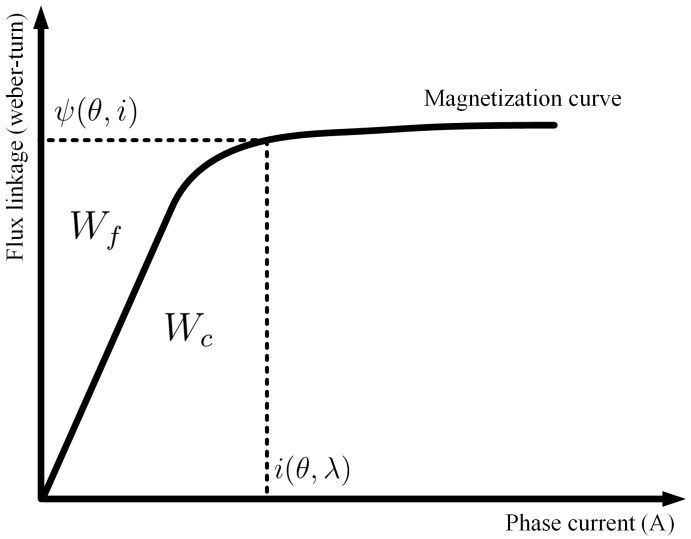

Figure 4.2: The phase flux linkage versus phase current and resultant co-energy and magnetic field energy.

Equation (4.1.12) can be inserted in Equation (4.1.8) as follows:

$$T = \frac{dW_c - \psi di}{d\theta} \tag{4.1.13}$$

The co-energy is the area under the magnetization curve in Figure 4.2. As the co-egergy is function of the current, i, and the rotor position, θ, Equation (4.1.13) can be rewritten as follows by applying the partial differentiation:

$$dW_c = \frac{\partial W_c}{\partial i} di \bigg|_{\theta = \text{ const}} + \frac{\partial W_c}{\partial \theta} d\theta \bigg|_{i = \text{ const}} = \psi di + T d\theta \tag{4.1.14}$$

If constant current is used, Equation (4.1.14) can be written as follows:

$$T = \frac{dW_c}{d\theta} \tag{4.1.15}$$

At constant current, the phase inductance is function of the rotor position and

can be expressed as follows:

$$L(\theta) = \frac{\psi(\theta, i)}{i} \tag{4.1.16}$$

So, the co-energy in Equation (4.1.10) can be expressed as follows:

$$W_c = \int_0^i L(\theta) i di = \frac{i^2}{2} L(\theta) \tag{4.1.17}$$

Then, the phase torque can be expressed as follows:

$$T = \frac{i^2}{2} \frac{dL(\theta)}{d\theta} \tag{4.1.18}$$

Equations (4.1.3), (4.1.4) and (4.1.18) are used to model the SRM machine.

4.2 Radial Flux SRM Modeling and Control

Due to the double salient structure of the SRM and the non-linearity of materials of the machine's rotor and stator, the flux linking the coils, the coils inductance, and the torque are functions of the rotor position and the current value. To get close to an accurate model of SRM, FEA software, such as JMAG or Ansys maxwell , are used to obtain the static characteristics of the SRM. These static characteristics are then used to model the motor operation at the dynamic conditions as discussed in Section 4.1. As indicated in [4], when the coils of the conventional design of SRM is energized most of the generated flux links the coils of the same phase. So, the mutual coupling between the different phases is neglected in this work. As a result, once the static characteristics of one phase is determined, they can be applied to the different phases. In this research, JMAG is used to determine the static characteristics of

the machine. The torque and the flux linkage based one phase excitation for one electric cycle and at different level of currents are the required characteristics to build a MATLAB\Simulink model of the machine.

The way to obtain the static characteristic of the machine is by applying different levels of constant current for one electric cycle. From this simulation, the flux linkage and the torque can be recorded at different rotor positions at one current level. The simulation is repeated for different currents and 2D lookup table is generated to describe the machine flux at different rotor positions and different phase currents.

4.3 FE Modeling of Radial Flux SRMs

Some basic principles of finite element analysis (FEA) are presented in this section. The FEA approaches utilized to derive finite element equations are the variational and Galerkin methods [219]. In this section, the system of equations used for the 2D electromagnetic field problems are presented. These equations are then used for the sensitivity analysis as presented in Sections 4.6 and 4.8

4.3.1 Magnetostatic field analysis

In the magnetostatic field analysis, the magnetic material is considered with linear properties, i.e., constant permeability. The Field can be Modeled using the following maxwell's equations:

$$\nabla \cdot \boldsymbol{B} = 0, \tag{4.3.1}$$

$$\nabla \times \boldsymbol{H} = \boldsymbol{J}, \tag{4.3.2}$$

$$\boldsymbol{B} = \mu \boldsymbol{H}, \tag{4.3.3}$$

$$\boldsymbol{B} = \nabla \times \boldsymbol{A}, \tag{4.3.4}$$

where $\boldsymbol{B}$ is the magnetic filed density vector, $\boldsymbol{H}$ is the magnetic field strength vector, $\boldsymbol{J}$ is the current density vector, $\boldsymbol{A}$ is the magnetic vector potential, and μ is the magnetic permeability.

By combining Equations (4.3.1) to (4.3.4), the field problem can be represented using the following equation [95]:

$$\nabla \times \boldsymbol{H} = \nabla \times \frac{\boldsymbol{B}}{\mu} = \nabla \times \left(\frac{1}{\mu} \nabla \times \boldsymbol{A} \right) = \boldsymbol{J}. \tag{4.3.5}$$

As in the 2D problem the current density has only z component, normal to the x − y plane, $\boldsymbol{H}$ and $\boldsymbol{B}$ have x and y components only based on equations (5.3.2) and (5.3.3) and $\boldsymbol{A}$ has only z component based on equation (5.3.4). So, these vectors can be expressed as $\boldsymbol{J} = [0, 0, J_z]$, $\boldsymbol{H} = [H_x, H_y, 0]$, $\boldsymbol{B} = [B_x, B_y, 0]$, and $\boldsymbol{A} = [0, 0, A_z]$.

So, equation Equation (4.3.5) becomes Poisson's equation and given as follows:

$$\frac{1}{\mu} \frac{\partial^2 A_z}{\partial x^2} + \frac{1}{\mu} \frac{\partial^2 A_z}{\partial y^2} = -J_z, \tag{4.3.6}$$

Substituting an approximation, $\hat{A}_z$, for A_z, The residual can be calculated for an approximate calculation of A_z as follows [220]:

$$R = \frac{1}{\mu} \frac{\partial^2 \hat{A}_z}{\partial x^2} + \frac{1}{\mu} \frac{\partial^2 \hat{A}_z}{\partial y^2} + J_z. \tag{4.3.7}$$

The integration of the residual value multiplied by the weighting function w_f over

the problem domain Ω equals zero [220]:

$$\int_{\Omega} W_f R \, dxdy = 0 \tag{4.3.8}$$

$$-\iint_{\Omega} W_f \left(\frac{1}{\mu} \frac{\partial^2 \hat{A}_z}{\partial x^2} + \frac{1}{\mu} \frac{\partial^2 \hat{A}_z}{\partial y^2} \right) dxdy = \iint_{\Omega} W_f J_z dxdy \tag{4.3.9}$$

By integrating the left hand side of Equation (4.3.9) by part [220]:

$$\begin{array}{c} \iint_{\Omega} W_f \left(\frac{1}{\mu} \frac{\partial^2 \hat{A}_z}{\partial x^2} + \frac{1}{\mu} \frac{\partial^2 \hat{A}_z}{\partial y^2} \right) dxdy = \\ \iint_{\Omega} \frac{1}{\mu} \left(\frac{\partial W_f}{\partial x} \frac{\partial \hat{A}_z}{\partial x} + \frac{\partial W_f}{\partial y} \frac{\partial \hat{A}_z}{\partial y} \right) dxdy - \oint_b \frac{1}{\mu} W \frac{\partial \hat{A}_z}{\partial \vec{n}} db \end{array} \tag{4.3.10}$$

where b is the space boundary and $\vec{n}$ is the normal vector to boundary pointing outwards of the design space. By substituting Equation (4.3.10) into Equation (4.3.9):

$$\iint_{\Omega} \frac{1}{\mu} \left(\frac{\partial W_f}{\partial x} \frac{\partial \hat{A}_z}{\partial x} + \frac{\partial W_f}{\partial y} \frac{\partial \hat{A}_z}{\partial y} \right) dxdy - \oint_b \frac{1}{\mu} W \frac{\partial \hat{A}_z}{\partial \vec{n}} db = \iint_{\Omega} W_f J_z dxdy \tag{4.3.11}$$

In the FEA, the design domain is discretized into small elements, and Equation (4.3.11) is applied to each element of the design space. In this study, the design space is discretized into triangle shapes, finite elements. The integration over the entire domain in Equation (4.3.11) can be replaced by the summation of the integration over the finite elements to solve the magnetostatic filed problem as follows:

$$\sum_{M} \frac{1}{\mu^e} \iint_{\Omega_e} \left\{ \frac{\partial W_f^e}{\partial x} \frac{\partial \hat{A}_z^e}{\partial x} + \frac{\partial W_f^e}{\partial y} \frac{\partial \hat{A}_z^e}{\partial y} \right\} dxdy - \sum_{M} \frac{1}{\mu^e} \frac{\partial \hat{A}_z^e}{\partial \vec{n}} \int_b W_f^e db = \sum_{M} J_z^e \iint_{\Omega_e} W_f^e dxdy \tag{4.3.12}$$

where M is the number of the finite elements in the problem domain, and e is an

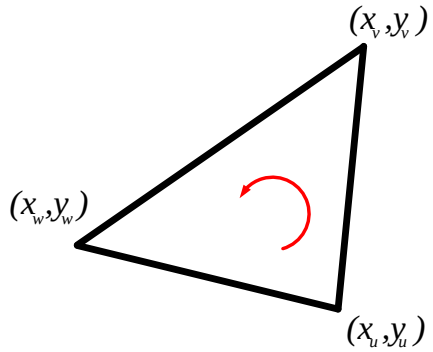

Figure 4.3: One triangular finite element.

index for the e^{th} element.

The line integral in Equation (4.3.12) is only performed over the elements which have at least one edge in common with the boundary of the problem domain. Typically, this integration is set to zero, insinuating that $\frac{\partial A}{\partial \vec{n}} = 0$ which is the so-called natural boundary condition [220]. As there are no symmetry condition will be used in the simulation the term $\frac{\partial A}{\partial \vec{n}}$ will be always equals 0. This leads to:

$$\sum_{M} \frac{1}{\mu^e} \iint_{\Omega_e} \left\{ \frac{\partial W_f^e}{\partial x} \frac{\partial \hat{A}_z^e}{\partial x} + \frac{\partial W_f^e}{\partial y} \frac{\partial \hat{A}_z^e}{\partial y} \right\} dxdy = \sum_{M} J_z^e \iint_{\Omega_e} W_f^e dxdy \qquad (4.3.13)$$

As indicated in [220], the weighting function for each element W_f^e is the shape function of the finite element; in this case, we considered triangle shape. A typical finite triangle element is shown in Figure 4.3. The triangle element has three nodes (u, v, w), and the numbering of the element vertices is counterclockwise. The z-component of the magnetic vector potential at each of this nodes, $\hat{A}_z^e\Big|_u$, $\hat{A}_z^e\Big|_t$, and $\hat{A}_z^e\Big|_v$, is unknown.

In this study, the magnetic vector potentiality is assumed to vary linearly inside the triangular element, called a linear triangle first-order element. So, the z-component

of the magnetic vector potential at any point inside the triangular element shown in Figure 4.3 is a function of the nodes' values of the magnetic vector potential and can be calculated as follows:

$$\hat{A}_z^e(x,y) = a^e x + b^e y + c^e \tag{4.3.14}$$

where a^e, b^e, and c^e are constants to be found for each element. So, the magnetic vector potential at the different nodes of the finite element (u, v, w) based on Equation (4.3.14) can be found as follows:

$$\hat{A}_z^e\Big|_u = a^e x_1 + b^e y_1 + c^e \tag{4.3.15}$$

$$\hat{A}_z^e\Big|_v = a^e x_2 + b^e y_2 + c^e \tag{4.3.16}$$

$$\hat{A}_z^e\Big|_w = a^e x_3 + b^e y_3 + c^e \tag{4.3.17}$$

If the magnetic vector potential at each node and the location of nodes of the finite element are known, the triangle constants, a^e, b^e, and c^e, can be determined based on the system of equation as follows:

$$a^e = \frac{\begin{vmatrix} 1 & \hat{A}_z^e\Big|_1 & y_1 \\ 1 & \hat{A}_z^e\Big|_2 & y_2 \\ 1 & \hat{A}_z^e\Big|_3 & y_3 \end{vmatrix}}{\begin{vmatrix} 1 & x_1 & y_1 \\ 1 & x_2 & y_2 \\ 1 & x_3 & y_3 \end{vmatrix}} \tag{4.3.18}$$

or,

$$a^e = \frac{\begin{vmatrix} 1 & \hat{A}_z^e\Big|_1 & y_1 \\ 1 & \hat{A}_z^e\Big|_2 & y_2 \\ 1 & \hat{A}_z^e\Big|_3 & y_3 \end{vmatrix}}{\begin{vmatrix} 1 & x_1 & y_1 \\ 1 & x_2 & y_2 \\ 1 & x_3 & y_3 \end{vmatrix}} = \frac{1}{2\Delta^{(e)}}\left[\hat{A}_z^e\Big|_1 (y_2 - y_3) + \hat{A}_z^e\Big|_2 (y_3 - y_1) + \hat{A}_z^e\Big|_w (y_1 - y_2)\right], \tag{4.3.19}$$

where $\Delta^{(e)}$ is the element area and can be calculated as follows:

$$\Delta^{(e)} = \frac{1}{2}\begin{vmatrix} 1 & x_1 & y_1 \\ 1 & x_2 & y_2 \\ 1 & x_3 & y_3 \end{vmatrix} \tag{4.3.20}$$

so,

$$b^e = \frac{\begin{vmatrix} 1 & x_1 & \hat{A}_z^e\Big|_1 \\ 1 & x_2 & \hat{A}_z^e\Big|_2 \\ 1 & x_3 & \hat{A}_z^e\Big|_3 \end{vmatrix}}{\begin{vmatrix} 1 & x_1 & y_1 \\ 1 & x_2 & y_2 \\ 1 & x_3 & y_3 \end{vmatrix}} = \frac{1}{2\Delta^{(e)}}\left[\hat{A}_z^e\Big|_1 (x_3 - x_2) + \hat{A}_z^e\Big|_2 (x_1 - x_3) + \hat{A}_z^e\Big|_3 (x_2 - x_1)\right], \tag{4.3.21}$$

and

$$c^e = \frac{1}{2\Delta^{(e)}} \left[\hat{A}_z^e \Big|_1 (x_2 y_3 - x_3 y_2) + \hat{A}_z^e \Big|_2 (x_3 y_1 - x_1 y_3) + \hat{A}_z^e \Big|_3 (x_1 y_2 - x_2 y_1) \right], \quad (4.3.22)$$

The coefficient of Equation (4.3.14) for each element can be re-written as follows:

$$a^e = \frac{1}{2\Delta^{(e)}} \left[\hat{A}_z^e \Big|_1 q_1^e + \hat{A}_z^e \Big|_2 q_2^e + \hat{A}_z^e \Big|_3 q_3^e \right] \quad (4.3.23)$$

$$b^e = \frac{1}{2\Delta^{(e)}} \left[\hat{A}_z^e \Big|_1 r_1^e + \hat{A}_z^e \Big|_2 r_2^e + \hat{A}_z^e \Big|_3 r_3^e \right] \quad (4.3.24)$$

$$c^e = \frac{1}{2\Delta^{(e)}} \left[\hat{A}_z^e \Big|_1 t_1^e + \hat{A}_z^e \Big|_2 t_2^e + \hat{A}_z^e \Big|_3 t_3^e \right] \quad (4.3.25)$$

were

$$\begin{aligned} q_1^e &= y_2 - y_3, \\ q_2^e &= y_3 - y_1, \\ q_3^e &= y_1 - y_2, \end{aligned} \quad (4.3.26)$$

$$\begin{aligned} r_1^e &= x_3 - x_2, \\ r_2^e &= x_1 - x_3, \\ r_3^e &= x_2 - x_1, \end{aligned} \quad (4.3.27)$$

$$\begin{aligned} t_1^e &= x_2 y_3 - x_3 y_2, \\ t_2^e &= x_3 y_1 - x_1 y_3, \\ t_3^e &= x_1 y_2 - x_2 y_1, \end{aligned} \quad (4.3.28)$$

by substituting Equations (4.3.23) to (4.3.25) into Equation (4.3.17) and rearrange

the equation, the magnetic vector potential can be expressed as follows:

$$\hat{A}_z^e(x,y) = \frac{(q_1^e x + r_1^e y + t_1^e)\ \hat{A}_z^e\Big|_1 + (q_2^e x + r_2^e y + t_2^e)\ \hat{A}_z^e\Big|_2 + (q_3^e x + r_3^e y + t_3^e)\ \hat{A}_z^e\Big|_3}{2\Delta^{(e)}} \tag{4.3.29}$$

the magnetic vector potential equation can be rewritten as follows:

$$\hat{A}_z^e(x,y) = \sum_{i=1}^{3} \frac{q_i^e x + r_i^e y + t_i^e}{2\Delta^{(e)}}\ \hat{A}_z^e\Big|_i = N_1^e\ \hat{A}_z^e\Big|_1 + N_2^e\ \hat{A}_z^e\Big|_2 + N_3^e\ \hat{A}_z^e\Big|_3 = \sum_{i=1}^{3} N_i^e\ \hat{A}_z^e\Big|_i \tag{4.3.30}$$

where

$$\begin{aligned} N_1^e &= \frac{(q_1^e x + r_1^e y + t_1^e)}{2\Delta^{(e)}}, \\ N_2^e &= \frac{(q_2^e x + r_2^e y + t_2^e)}{2\Delta^{(e)}}, \\ N_3^e &= \frac{(q_3^e x + r_3^e y + t_3^e)}{2\Delta^{(e)}}. \end{aligned} \tag{4.3.31}$$

The coefficients of Equation (4.3.30), which are shown in Equation (4.3.31), are called the shape functions. The shape function has a value between 0 and 1 inside the element. The shape function has value of 1 at its node, for example $N_1^e = 1$ at the node 1 . The value of the shape function is zero at any other node, for example $N_1^e = 0$ at the nodes 2&3.

Based on Equation (4.3.30), the gradient of the magnetic vector potential of the

e^{th} element is given as follows:

$$\begin{aligned}\frac{\partial \hat{A}_z^e}{\partial x} &= \frac{1}{2\Delta^{(e)}} \begin{bmatrix} q_1^e & q_2^e & q_3^e \end{bmatrix} \begin{bmatrix} \hat{A}_z^e\big|_1 \\ \hat{A}_z^e\big|_2 \\ \hat{A}_z^e\big|_3 \end{bmatrix}, \\ \frac{\partial \hat{A}_z^e}{\partial y} &= \frac{1}{2\Delta^{(e)}} \begin{bmatrix} r_1^e & r_2^e & r_3^e \end{bmatrix} \begin{bmatrix} \hat{A}_z^e\big|_1 \\ \hat{A}_z^e\big|_2 \\ \hat{A}_z^e\big|_3 \end{bmatrix}.\end{aligned} \tag{4.3.32}$$

The element's shape function is chosen to be the weighting function of the Galerkin [220], as follows:

$$\boldsymbol{W}_f^e = \begin{pmatrix} N_1^e \\ N_2^e \\ N_3^e \end{pmatrix} \tag{4.3.33}$$

so, the gradient of the weighting function is given as follows:

$$\frac{\partial \boldsymbol{W}_f^e}{\partial x} = \frac{1}{2\Delta^{(e)}} \begin{pmatrix} q_1^e \\ q_2^e \\ q_3^e \end{pmatrix} \quad , \frac{\partial \boldsymbol{W}_f^e}{\partial y} = \frac{1}{2\Delta^{(e)}} \begin{pmatrix} r_1^e \\ r_2^e \\ r_3^e \end{pmatrix} \tag{4.3.34}$$

It can be concluded from Equations (4.3.32) and (4.3.34) that $\frac{\partial \hat{A}_z^e}{\partial x}$, $\frac{\partial \hat{A}_z^e}{\partial y}$, $\frac{\partial \boldsymbol{W}_f^e}{\partial x}$, and $\frac{\partial \boldsymbol{W}_f^e}{\partial y}$ are constants for each element. So, the left hand side of Equation (4.3.13) can be written as follows:

$$\sum_M \frac{1}{\mu^e} \left\{ \frac{\partial \boldsymbol{W}_f^e}{\partial x} \frac{\partial \hat{A}_z^e}{\partial x} + \frac{\partial \boldsymbol{W}_f^e}{\partial y} \frac{\partial \hat{A}_z^e}{\partial y} \right\} \iint_{\Omega_e} dxdy \tag{4.3.35}$$

The integration in Equation (4.3.35) is the area of the e^{th} element:

$$\iint_{\Omega_e} dxdy = \Delta^{(e)} \tag{4.3.36}$$

The left hand side of Equation (4.3.13) for each element can be written as follows:

$$\begin{aligned} &\tfrac{1}{\mu^e}\left\{\tfrac{\partial \boldsymbol{W}_f^e}{\partial x}\tfrac{\partial \hat{A}_z^e}{\partial x}+\tfrac{\partial \boldsymbol{W}_f^e}{\partial y}\tfrac{\partial \hat{A}_z^e}{\partial y}\right\}\iint_{\Omega_e} dxdy = \\ &\tfrac{1}{4\mu^e\Delta^{(e)}}\begin{pmatrix} (q_1^e)^2+(r_1^e)^2 & q_1^eq_2^e+r_1^er_2^e & q_1^eq_3^e+r_1^er_3^e \\ q_1^eq_2^e+r_1^er_2^e & (q_2^e)^2+(r_2^e)^2 & q_2^eq_3^e+r_2^er_3^e \\ q_1^eq_3^e+r_1^er_3^e & q_2^eq_3^e+r_2^er_3^e & (q_3^e)^2+(r_3^e)^2 \end{pmatrix}\begin{pmatrix} \hat{A}_z^e\big|_1 \\ \hat{A}_z^e\big|_2 \\ \hat{A}_z^e\big|_3 \end{pmatrix} \end{aligned} \tag{4.3.37}$$

The equation can be writen in terms of the element reluctivity as follows:

$$\begin{aligned} &\tfrac{1}{\mu^e}\left\{\tfrac{\partial \boldsymbol{W}_f^e}{\partial x}\tfrac{\partial \hat{A}_z^e}{\partial x}+\tfrac{\partial \boldsymbol{W}_f^e}{\partial y}\tfrac{\partial \hat{A}_z^e}{\partial y}\right\}\iint_{\Omega_e} dxdy = \\ &\tfrac{\nu^e}{4\Delta^{(e)}}\begin{pmatrix} (q_1^e)^2+(r_1^e)^2 & q_1^eq_2^e+r_1^er_2^e & q_1^eq_3^e+r_1^er_3^e \\ q_1^eq_2^e+r_1^er_2^e & (q_2^e)^2+(r_2^e)^2 & q_2^eq_3^e+r_2^er_3^e \\ q_1^eq_3^e+r_1^er_3^e & q_2^eq_3^e+r_2^er_3^e & (q_3^e)^2+(r_3^e)^2 \end{pmatrix}\begin{pmatrix} \hat{A}_z^e\big|_1 \\ \hat{A}_z^e\big|_2 \\ \hat{A}_z^e\big|_3 \end{pmatrix} \end{aligned} \tag{4.3.38}$$

The coefficient matrix in Equation (4.3.37) is the local system matrix $\boldsymbol{K}^{(e)} \in \mathfrak{R}^{3\times 3}$ which can be obtained as follows:

$$K_{ij}^{(e)} = \frac{\nu^{(e)}}{4\Delta^{(e)}}\left(q_iq_j + r_ir_j\right), \quad i,j = 1,2,3 \tag{4.3.39}$$

Similarly, the right hand side of Equation (4.3.13) for each element can be written

as follows:

$$J_z^e \iint_{\Omega_e} \boldsymbol{W}_f^e dxdy = J_z^e \iint_{\Omega_e} \begin{pmatrix} N_1^e \\ N_2^e \\ N_3^e \end{pmatrix} dxdy = J_z^e \iint_{\Omega_e} \frac{1}{2\Delta^{(e)}} \begin{pmatrix} q_1^e x + r_1^e y + t_1^e \\ q_2^e x + r_2^e y + t_2^e \\ q_3^e x + r_3^e y + t_3^e \end{pmatrix} dxdy \tag{4.3.40}$$

The right hand side of Equation (4.3.13) for each element after performing the surface integration in Equation (4.3.40) can be written as follows:

$$J_z^e \iint_{\Omega_e} \frac{1}{\Delta^{(e)}} \begin{pmatrix} q_1^e x + r_1^e y + t_1^e \\ q_2^e x + r_2^e y + t_2^e \\ q_3^e x + r_3^e y + t_3^e \end{pmatrix} dxdy = J_z^e \begin{pmatrix} \frac{q_1^e x_c + r_1^e y_c + t_1^e}{2} \\ \frac{q_2^e x_c + r_2^e y_c + t_2^e}{2} \\ \frac{q_3^e x_c + r_3^e y_c + t_3^e}{2} \end{pmatrix} \tag{4.3.41}$$

where x_c and y_c are coordinates the finite element centroid and can be calculated as follows:

$$\begin{aligned} x_c &= \frac{1}{3}\left(x_1 + x_2 + x_3\right), \\ y_c &= \frac{1}{3}\left(y_1 + y_2 + y_3\right). \end{aligned} \tag{4.3.42}$$

By substituting the centroid values in Equation (4.3.42) into Equation (4.3.41), the right hand side of Equation (4.3.13) for each element can be written as follows:

$$J_z^e \iint_{\Omega_e} \boldsymbol{W}_f^e dxdy = \frac{J_z^e}{3\Delta^{(e)}} \begin{pmatrix} 1 \\ 1 \\ 1 \end{pmatrix} \tag{4.3.43}$$

The coefficient vector in Equation (4.3.43) is the local system vector $\boldsymbol{F}^{(e)} \in \mathfrak{R}^{3\times 1}$

which can be obtained as follows:

$$f_i^{(e)} = \frac{J_z^e}{3\Delta^{(e)}}, \quad i = 1, 2, 3 \tag{4.3.44}$$

The right hand side matrix in Equation (4.3.37) and the right had side vector in Equation (4.3.43) are called the system matrix and the system vector, respectively. The local system matrix and the local system vector are obtained for all the finite elements in the filed domain. The local system matrices and the local system vectors are assembled to get the global system matrix $\boldsymbol{K} \in \mathfrak{R}^{N_n \times N_n}$ and the global system vector $\boldsymbol{F} \in \mathfrak{R}^{N_n \times 1}$, where N_n is the total number of nodes in the filed domain. In the assembly process all the local matrices are added together to form the global matrix. The global system matrix is sparse, symmetric and singular matrix [220].

After the assembly process, the boundary conditions are imposed to the global matrix. As illustrated in [220], there are two types of the boundary conditions for the magnetostatic problems. In order to get a unique solution to the magnetostatic problem either the value of the magnetic vector potential or the value of its normal derivative must be given at each node on the problem boundaries. Dirichlet boundary condition is applied by assigning a the same value to the magnetic vector potential on to the boundary nodes. Typically, dirichlet boundary condition is applied by assigning zero to the magnetic vector potential on to the boundary nodes; however any other value can be used but it should be the same value for all the nodes. The Neumann condition, the normal derivative of the magnetic vector potential to the boundary surface, has been assigned during derivation of the system equation [220].

The magnetic vector potential solution of the field problem, $\boldsymbol{A}_z \in \mathfrak{R}^{N_n \times 1}$ can be obtained after the assembly process and applying the boundary conditions by solving

the following system equation:

$$\boldsymbol{K}\boldsymbol{A}_z = \boldsymbol{F}. \tag{4.3.45}$$

4.3.2 Linking the optimization algorithm to a commercial FEA software

The in-house implementation of the non-linear magnetostatic field analysis is computational demanding, which leads to a very long optimization time as presented in [95]. In order to avoid this, a commercial software, JMAG, is used in this work for the FE simulation of the SRM. The required information for the sensitivity analysis is then extracted from the final solution of the commercial software after the FE solution conversions.

Figure 4.4 shows the flow of the optimization process. The process starts with obtaining the static curves of the initial design. In that stage, a MATLAB mfile writes an VBS file which calls the JMAG to run the initial design several time at a predefined set of DC current as indicated in Section 4.2. The static characteristics used for a MATLAB\Simulink model which is used to obtain the optimal turn on and turn off angles of the machine drive converter switches. An electromagnetic FE transient simulation is then run for one complete electrical cycle based on the dynamic current obtained from the previous step. After the conversions of the FE simulation, the necessary information for the torque calculation, the radial force calculation, the torque sensitivity calculation, and the radial force sensitivity calculation is extracted. The torque, the radial force, and their sensitivities are then calculated. Based on the objective function of the optimization algorithm and the calculated sensitivity

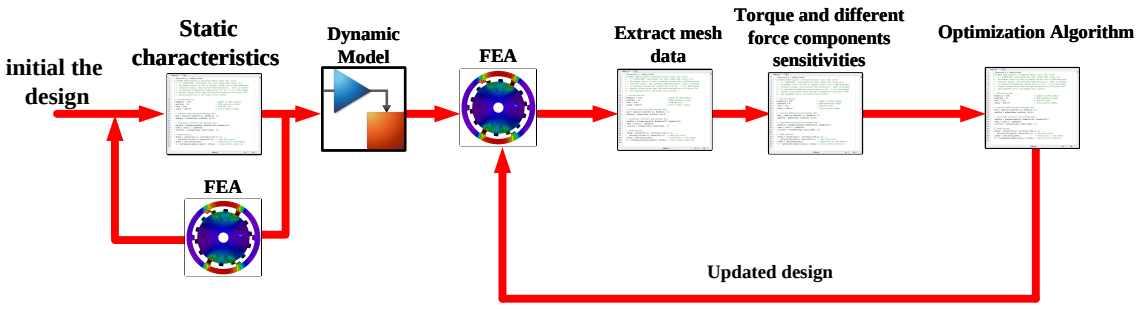

Figure 4.4: System level flow chart of the optimization process.

information, the design is changed. the optimization algorithm stays inside this loop till the termination condition is achieved.

At each iteration and after the FEA conversions, all the finite elements reluctivity, all the nodes locations are exported for each rotor position. A mangnetiostatic field problem is then formulated based on these information to calculate, the magnetic vector potential at each node, the magnetic flux density. These post-processing calculations are then used to calculate the machine torque, the stator radial force, the sensitivity of torque and radial force with respect to the design variables as discussed in Sections 4.4, 4.5, 4.7 and 4.8

4.4 Flux Density

The case study SRM in this research is discritized into triangle elements as shown in Figure 4.5. The finite element field problem is solved in JMAG software for one electrical cycle, 100 rotor steps. The field problem's nodes coordinates, the elements' nodes, the reluctivity of all the finite elements are exported from JMAG after the problem conversions for all the rotor positions. These information are used to construct the local system matrix and the local system vector for each element based on

Equations (4.3.38) and (4.3.44). The local matrices and the local system vectors are then used to assemble the global system matrix and the global system vector then solve the system equation shown in Equation (4.3.45).

The reason behind extracting the final solution from JMAG and resolve it in MATLAB is that the magnetic vector potential is not available for each node in JMAG. The magnetic vector potential is required for each node for the sensitivity calculation as indicated in Sections 4.6 and 4.8. After solving the system equation, the magnetic flux can be obtained for each element in the design space based on Equation (4.3.4) as follows:

$$\boldsymbol{B^e} = \nabla \times \boldsymbol{A^e} = \begin{bmatrix} \boldsymbol{a_x} & \boldsymbol{a_y} & \boldsymbol{a_z} \\ \frac{\partial}{\partial x} & \frac{\partial}{\partial y} & \frac{\partial}{\partial z} \\ A_x^e & A_y^e & A_z^e \end{bmatrix} \tag{4.4.1}$$

were $\boldsymbol{a_x}$, $\boldsymbol{a_y}$, and $\boldsymbol{a_z}$ are the unit vectors in the x, y, and z direction, respectively. As, in the 2D FEA, the magnetic vector potential has only z component, the element's magnetic flux density can be calculated as follows:

$$\boldsymbol{B^e} = \begin{bmatrix} \boldsymbol{a_x} & \boldsymbol{a_y} & \boldsymbol{a_z} \\ \frac{\partial}{\partial x} & \frac{\partial}{\partial y} & \frac{\partial}{\partial z} \\ 0 & 0 & A_z^e \end{bmatrix} = \frac{\partial A_z^e}{\partial y}\boldsymbol{a_x} - \frac{\partial A_z^e}{\partial x}\boldsymbol{a_y} \tag{4.4.2}$$

By substituting Equation (4.3.32) to Equation (4.4.2), the x and y components of

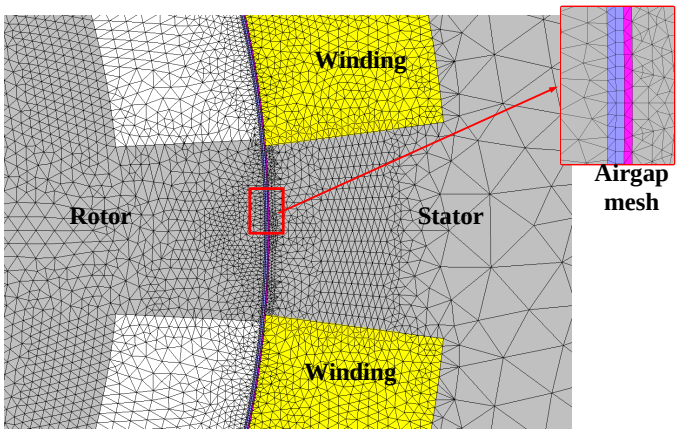

Figure 4.5: An example of discritized the case study SRM in this research.

magnetic flux density for any element can be calculated as follows:

$$B_x{}^e = \frac{1}{2\Delta^{(e)}} \begin{bmatrix} r_1^e & r_2^e & r_3^e \end{bmatrix} \begin{bmatrix} \hat{A}_z^e\big|_1 \\ \hat{A}_z^e\big|_2 \\ \hat{A}_z^e\big|_3 \end{bmatrix} \tag{4.4.3}$$

$$B_y{}^e = \frac{-1}{2\Delta^{(e)}} \begin{bmatrix} q_1^e & q_2^e & q_3^e \end{bmatrix} \begin{bmatrix} \hat{A}_z^e\big|_1 \\ \hat{A}_z^e\big|_2 \\ \hat{A}_z^e\big|_3 \end{bmatrix} \tag{4.4.4}$$

4.5 Torque Calculation of SRMs

The Maxwell stress tensor (MST) is one of the common methods for torque and force calculation of electric machines [221, 222]. MST is used in this study for the torque calculation. The MST torque calculation starts with calculating the tangential airgap magnetic pressure. The magnetic pressure in the air gap in the tangential direction

is given by:

$$P_{\varphi} = \frac{1}{\mu_0} \left(\boldsymbol{B} \cdot \boldsymbol{a}_{\boldsymbol{\varphi}} \right) \boldsymbol{B} - \frac{1}{2\mu_0} |\boldsymbol{B}|^2 \boldsymbol{a}_{\boldsymbol{\varphi}}, \tag{4.5.1}$$

where μ_0 is the permeability of the free space, $\boldsymbol{B}$ is the air gap magnetic flux density vector, and $\boldsymbol{a}_{\boldsymbol{\varphi}}$ is the unit vector in the tangential direction. The magnetic pressure in the radial direction is calculated as follows:

$$P_{\rho} = \frac{1}{\mu_0} \left(\boldsymbol{B} \cdot \boldsymbol{a}_{\boldsymbol{\rho}} \right) \boldsymbol{B} - \frac{1}{2\mu_0} |\boldsymbol{B}|^2 \boldsymbol{a}_{\boldsymbol{\rho}}, \tag{4.5.2}$$

where $\boldsymbol{a}_{\boldsymbol{\rho}}$ is the unite vector in the radial direction.

As the torque is the cross product of the lever arm direction and the force direction, the only component of the magnetic pressure that contributes to the torque production is the tangential component, and the torque is given as follows [221]:

$$T = L \oint \left\{ r \cdot \boldsymbol{a}_{\boldsymbol{\rho}} \times \left(\frac{1}{\mu_0} \left(\boldsymbol{B} \cdot \boldsymbol{a}_{\boldsymbol{\varphi}} \right) \boldsymbol{B} - \frac{1}{2\mu_0} |\boldsymbol{B}|^2 \boldsymbol{a}_{\boldsymbol{\varphi}} \right) \right\} r d\theta \tag{4.5.3}$$

where L is the rotor stack length r is the rotor radius.

The Maxwell stress tensor is very sensitive to the enclosed surface used for torque calculation. As indicated in [222], to get accurate torque results, the air gap should be divided into three circular layers equal in thickness, and the torque is calculated on a closed surface of the air gap layer closer to the rotor. It was found that the most accurate torque can be found if that torque calculation surface is exactly in the middle of the layer near the rotor, as shown in Figure 4.6.

In the finite element system, the closed linear integral can be performed by summing the contribution of the different segments on the closed line, so Equation (4.5.3)

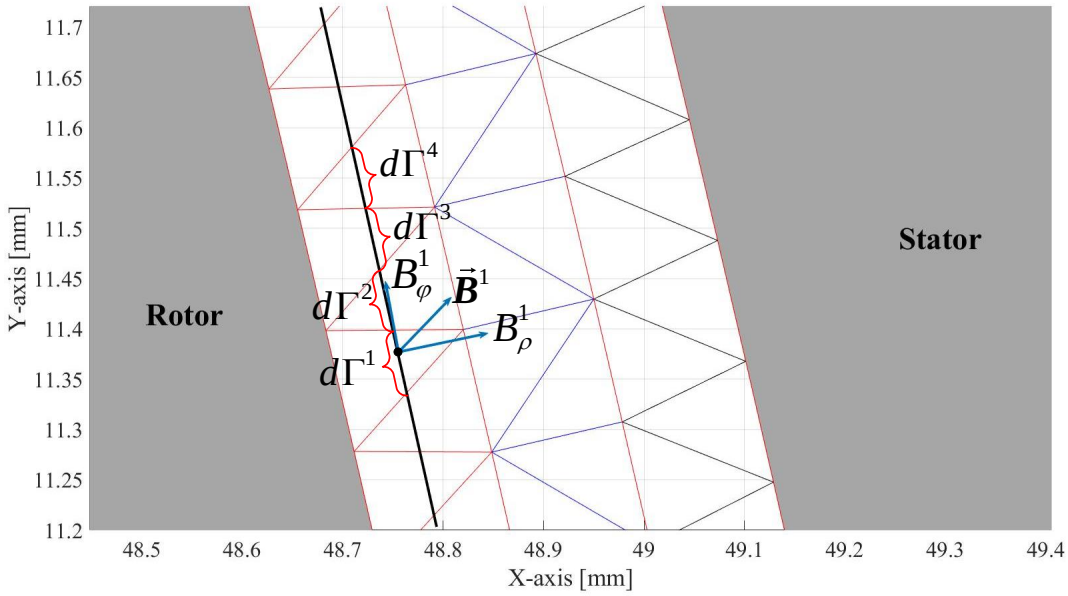

Figure 4.6: The calculation of the flux density components at airgap for torque computation.

can be discretized as follows:

$$T = L \sum_{e=1}^{N_e} \left\{ r \cdot \boldsymbol{a_\rho} \times \left(\frac{1}{\mu_0} \left(\boldsymbol{B}^e \cdot \boldsymbol{a_\varphi} \right) \boldsymbol{B}^e - \frac{1}{2\mu_0} \left| \boldsymbol{B}^e \right|^2 \boldsymbol{a_\varphi} \right) \right\} d\Gamma^e \tag{4.5.4}$$

where $\boldsymbol{B}^e$ is the flux density vector of the e^{th} element, r is the level arm length (rotor radius), and $d\Gamma^e$ is the arc length of the torque calculation layer located on the e^{th} element as shown in Figure 4.6. By performing the cross product and simplifying Equation (4.5.4), the rotor torque can be calculated as follows:

$$T = L \sum_{e=1}^{N_e} \frac{1}{\mu_0} B_\rho^e B_\varphi^e r d\Gamma^e \tag{4.5.5}$$

where B_ρ^e and B_φ^e are the radial and tangential flux density components of the e^{th} element. The radial and the tangential flux density of the i^{th} element can be calculated by transforming Equations (4.4.3) and (4.4.4) from the cartesian coordinate to the cylindrical coordinate as follows:

$$B_\rho^e = \frac{1}{2\Delta^{(e)}} (-\boldsymbol{Q^e} \cos(\varphi^e) + \boldsymbol{R^e} \sin(\varphi^e))^T \boldsymbol{A}^e \tag{4.5.6}$$

$$B_\varphi^e = \frac{1}{2\Delta^{(e)}} (-\boldsymbol{Q^e} \cos(\varphi^e) - \boldsymbol{R^e} \sin(\varphi^e))^T \boldsymbol{A}^e \tag{4.5.7}$$

where φ^e is the angle between x-axis and the line between the origin and the e^{th}

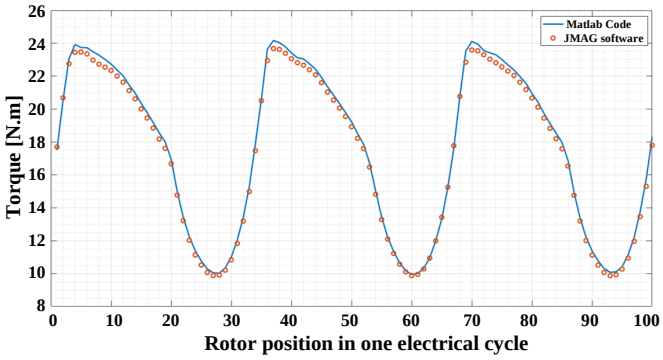

Figure 4.7: The torque Calculation base on the MATLAB code and the JMAG software at the base speed (1500 r.p.m) for one complete electric cycle at 100 different rotor positions.

element centroid. The $\boldsymbol{Q^e}$ and $\boldsymbol{R^e}$ vectors are given as follows:

$$\boldsymbol{Q^e} = \begin{pmatrix} q_1^e \\ q_2^e \\ q_3^e \end{pmatrix}, \quad \boldsymbol{R^e} = \begin{pmatrix} r_1^e \\ r_2^e \\ r_3^e \end{pmatrix} \tag{4.5.8}$$

The sensitivity of the torque with respect to a design parameter can be calculated as follows:

$$\frac{\partial T}{\partial p_i} = L \sum_{e=1}^{N_e} \frac{1}{\mu_0} \left(B_\rho^e \frac{\partial B_\varphi^e}{\partial p_i} + B_\varphi^e \frac{\partial B_\rho^e}{\partial p_i} \right) d\Gamma^e \tag{4.5.9}$$

The torque is calculated based on the MATLAB code and compared with the JMAG torque results, based on equation Equation (4.5.5). As shown in Figure 4.7, there are a good agreement between calculated torque from the MATLAB code and the one calculated by the JMAG software. The Percentage error between the torque calculated and the JMAG software-based motor torque is illustrated in Table 4.1.

Table 4.1: The percentage error between the JMAG torque calculation and MATLAB Code torque calculation.

	MATLAB code	JMAG Software	Percentage error
Mean torque	17.6044 N.m	17.3306 N.m	1.58%
Torque ripple	80.79%	79.69%	1.1%

4.6 Torque Sensitivity Calculation for Topology and Geometry Optimization

In the gradient-based topology and generative optimization methods, the sensitivity of the objective function, f, with respect to the reluctivity of the e^{th} element, $\frac{df}{d\nu^e}$, determines the material in that element. The adjoint variable method is chosen to determine the objective function sensitivity for each finite element in the design domain [86].

The sensitivity of the radial and tangential flux density are first required to be calculated to compute the sensitivity of the torque as indicated in Equation (4.5.9). In this section the method is illustrated for a function f_t which represents both B^e_ρ and B^e_φ. The sensitivity of the function f_t with respect to the reluctivity of the e^{th} element, ν^e, is calculated as follows [86]:

$$\frac{df_t}{dv^e} = \frac{\partial f_t}{\partial \nu^e} + \left(\frac{\partial f_t}{\partial \boldsymbol{A}}\right)^T \frac{\partial \boldsymbol{A}}{\partial \nu^e} \tag{4.6.1}$$

where $\boldsymbol{A}$ is the magnetic vector potential at each node of the finite element system. The first part of the right-hand side of Equation (4.6.1) denotes the explicit dependency of the flux component function on the reluctivity of the design domain elements. The second term of Equation (4.6.1) denotes the implicit dependency of the function

on the design domain elements reluctivity. This can be obtained by solving the finite element system in Equation (4.3.45). The residual vector of Equation (4.3.45) is given by:

$$\boldsymbol{D} = \boldsymbol{K}\boldsymbol{A} - \boldsymbol{F} \tag{4.6.2}$$

The residual vector derivative with respect to the reluctivity of the e^{th} element is determined as follows:

$$\frac{d\boldsymbol{D}}{d\nu^e} = \frac{\partial \boldsymbol{D}}{\partial \nu^e} + \frac{\partial \boldsymbol{D}}{\partial \boldsymbol{A}}\frac{\partial \boldsymbol{A}}{\partial \nu^e} \tag{4.6.3}$$

Similar to Equation (4.6.1), Equation (4.6.3) shows the explicit and the implicit dependency of the residual vector sensitivity on the reluctivity of the e^{th} element of the design domain. By substituting the value of $\boldsymbol{D}$ in Equation (4.6.2) into Equation (4.6.3), the derivative of the residual vector can be determined as follows:

$$\frac{d\boldsymbol{D}}{d\nu^e} = \frac{\partial \boldsymbol{K}}{\partial \nu^e}\boldsymbol{A} - \frac{\partial \boldsymbol{F}}{\partial \nu^e} + \left(\boldsymbol{K} + \frac{\partial \boldsymbol{K}}{\partial \nu}\frac{\partial \nu}{\partial \boldsymbol{B}^2}\frac{\partial \boldsymbol{B}^2}{\partial \boldsymbol{A}}\boldsymbol{A} - \frac{\partial \boldsymbol{F}}{\partial \boldsymbol{B}^2}\frac{\partial \boldsymbol{B}^2}{\partial \boldsymbol{A}}\right)\frac{\partial \boldsymbol{A}}{\partial \nu^e} \tag{4.6.4}$$

The excitation vector $\boldsymbol{F}$, in the SRMs finite element simulation, is the current density vector of all elements in the finite element domain. So, if the eddy current effect is neglected in the simulation, the derivative of $\boldsymbol{F}$ with respect to ν and $\boldsymbol{B}^2$ is zero. Now, the derivative of the residual vector with respect to the element's reluctivity can be determined as follows:

$$\frac{d\boldsymbol{D}}{d\nu^e} = \frac{\partial \boldsymbol{K}}{\partial \nu^e}\boldsymbol{A} + \left(\boldsymbol{K} + \frac{\partial \boldsymbol{K}}{\partial \nu}\frac{\partial \nu}{\partial \boldsymbol{B}^2}\frac{\partial \boldsymbol{B}^2}{\partial \boldsymbol{A}}\boldsymbol{A}\right)\frac{\partial \boldsymbol{A}}{\partial \nu^e} = 0 \tag{4.6.5}$$

If the design domain of the optimization problem does not include the torque calculation elements (the airgap layer near the rotor teeth), the explicit dependency

of the function f_t, which represents B_ρ^i and B_φ^i, on the reluctivity of the design domain elements is zero [86]. So, equation Equation (4.6.1) can be calculated as follows:

$$\frac{df_t}{d\nu^e} = \left(\frac{\partial f_t}{\partial A}\right)^T \frac{\partial A}{\partial \nu^e} \tag{4.6.6}$$

By substituting Equation (4.6.5) into Equation (4.6.6), the sensitivity of the function with respect to the reluctivity of element number is determined as:

$$\frac{df_t}{dv\nu^e} = -\left(\frac{\partial f_t}{\partial \boldsymbol{A}}\right)^T \left(\boldsymbol{K} + \frac{\partial \boldsymbol{K}}{\partial \nu}\frac{\partial \nu}{\partial \boldsymbol{B}^2}\frac{\partial \boldsymbol{B}^2}{\partial \boldsymbol{A}}\boldsymbol{A}\right)^{-1} \frac{\partial \boldsymbol{K}}{\partial \nu^e}\boldsymbol{A} \tag{4.6.7}$$

The adjoint system can be formed and solved for the adjoint vector as follows [86]:

$$\left(\boldsymbol{K} + \frac{\partial \boldsymbol{K}}{\partial \nu}\frac{\partial \nu}{\partial \boldsymbol{B}^2}\frac{\partial \boldsymbol{B}^2}{\partial \boldsymbol{A}}\boldsymbol{A}\right)^T \boldsymbol{\alpha} = \left(\frac{\partial f_t}{\partial \boldsymbol{A}}\right) \tag{4.6.8}$$

The adjoint vector $\boldsymbol{\alpha}$ is calculated only once for each iteration and can be used to get the sensitivity of B_ρ^i and B_φ^i with respect to the reluctivity of each of the design domain elements as follows:

$$\frac{df_t}{d\nu^e} = -\boldsymbol{\alpha}^T \frac{\partial \boldsymbol{K}}{\partial \nu^e}\boldsymbol{A} \tag{4.6.9}$$

The adjoint variable method is then used to calculate the sensitivity of the radial and tangential flux components of all the elements of the torque calculation layer with respect to the reluctivity of each element in the design space based on Equation (4.6.8). For both B_ρ^i and B_φ^i, the adjoint vector equation terms are the same except the left-hand side which is needed to be calculated for each component separately.

After calculating the sensitivities of the flux density components using the adjoint vector for each component in Equation (4.6.9), the values of the sensitivities are used to calculate the torque sensitivity as indicated in Equation (4.6.1). The sensitivity of the objective function is then used to determine the status of that element in the design domain as illustrated in the previous section.

4.7 Stator Radial Force Calculation for SRMs

In this section, the nodal force calculation is illustrated. The virtual work principle method (VWP) is used to calculate the radial force on the inner stator boundary nodes where the force component is required to measure and optimize the acoustic noise of the SRM. Figure 6 shows the stator elements and the stator boundary nodes. Figure 4.8 illustrates an example of the elements surrounding a stator node in the inner boundary used for the radial force calculation of that node.

The nodal force is obtained by differentiating the magnetic energy with respect to a virtual nodal movement in the force direction at a constant magnetic vector potential [23]. The nodal force at node n, shown in Figure 4.9, is computed by summing the derivatives of the magnetic energy of all surrounding elements to a virtual node displacement, assuming a constant magnetic vector potential.

The element magnetic energy is given by [23]:

$$M^e = \frac{L}{2} \left(\boldsymbol{A}^e\right)^{\mathrm{T}} \boldsymbol{K}^e \boldsymbol{A}^e \tag{4.7.1}$$

The radial force of the n^{th} node (shown in Figure 4.10) is calculated from [23], [24]

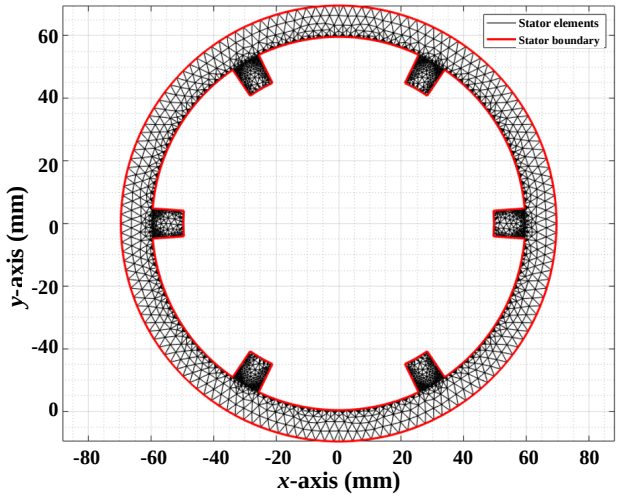

Figure 4.8: The stator elements and the stator boundary; the nodal forces which are required for the acoustic noise are the forces at the inner boundary of the stator (the inner red boundary).

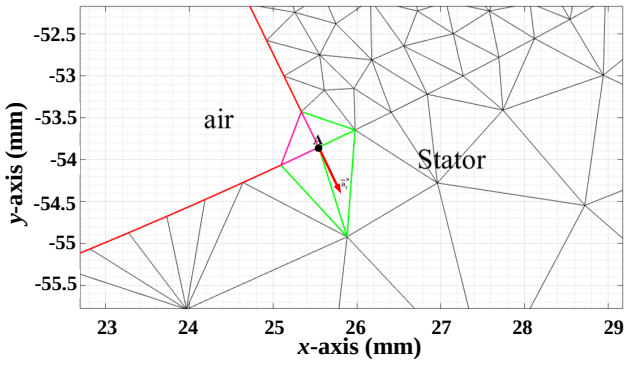

Figure 4.9: Example of the elements required to calculate the radial force for node A at the stator boundary. There are two types of elements: air elements (the purple element) and iron elements (green elements).

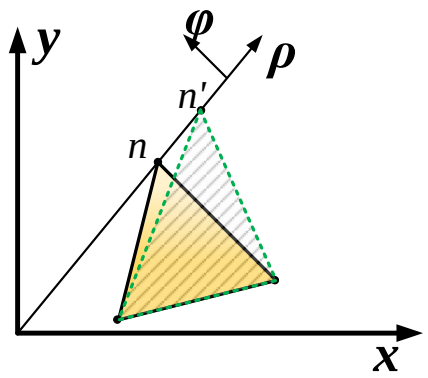

Figure 4.10: A virtual radial displacement of the nth node of an element of the surrounding elements for radial force calculations.

as follows:

$$F_n \cdot \boldsymbol{a_\rho} = \sum_{\mathrm{e}=1}^{\mathrm{m}} F_n^e = -\sum_{\mathrm{e}=1}^{\mathrm{m}} \frac{\partial M^e}{\partial \rho} \tag{4.7.2}$$

where $F_n \cdot \boldsymbol{a_\rho}$ is the n^{th} node radial force, ${F_n}^e$ is the e^{th} element contribution to the n^{th} node radial force, and m is the number of elements surrounding the n^{th} node.

From Equation (4.7.1) and Equation (4.7.2), it can be concluded that:

$$F_n \cdot \overrightarrow{\boldsymbol{a}_{\boldsymbol{\rho}}} = -\sum_{\mathrm{e}=1}^{\mathrm{m}} \frac{\partial}{\partial \rho}\left(\frac{L}{2}\left(\boldsymbol{A}^e\right)^T \boldsymbol{K}^e \boldsymbol{A}^e\right) = -\sum_{e=1}^{m} \frac{L}{2}\left(\boldsymbol{A}^e\right)^T \frac{\partial \boldsymbol{K}^e}{\partial \rho} \boldsymbol{A}^e \tag{4.7.3}$$

Using Equation (4.3.39), the term $\frac{\partial \boldsymbol{K}^e}{\partial \rho}$ is calculated as follows:

$$\frac{\partial K_{ij}^{(e)}}{\partial \rho} = \nu^{(e)} \frac{\Delta^{(e)}\left(\frac{\partial q_i}{\partial \rho} q_j + q_i \frac{\partial q_j}{\partial \rho} + \frac{\partial r_i}{\partial \rho} r_j + r_i \frac{\partial r_j}{\partial \rho}\right) - \left(q_i q_j + r_i r_j\right) \frac{\partial \Delta^{(e)}}{\partial \rho}}{4\Delta^{(e)2}}, i, j = 1, 2, 3 \tag{4.7.4}$$

Equation Equation (4.7.3) is used in this chapter to calculate the radial nodal forces at the stator teeth at 100 rotor positions covering a complete electrical cycle

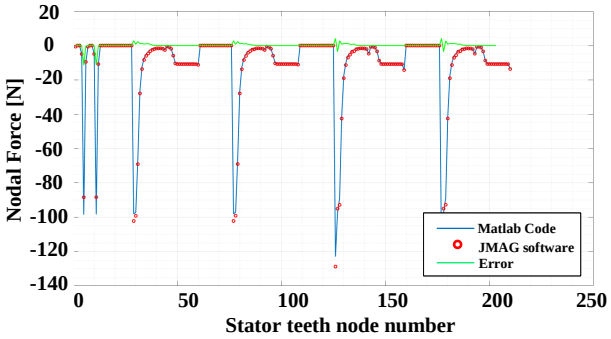

Figure 4.11: The nodal forces at the stator teeth edge nodes facing the air gap at the aligned rotor position.

of 6/14 SRM. The force values are compared to those obtained using the JMAG software [25]. Figures 4.11 and 4.12 show the forces at the aligned and unaligned rotor positions. As shown in the figures, the estimated forces using Equation (4.7.3) are in good agreement with the ones obtained using JMAG.

The force density surface wave, shown in Figure 4.13, is computed using a developed FEA-based MATLAB code. A 2D Fast Fourier Transform (FFT) is used to calculate the different surface wave components as shown in Figure 4.14.

4.8 Force Density Sensitivity Calculation Using Adjoint Variable method

In this section, the Force Sensitivity using the variable method for Geometry and topology optimization is presented. First, the sensitivity of the radial force with respect to the geometrical parameters, such as rotor and the stator teeth heights, are

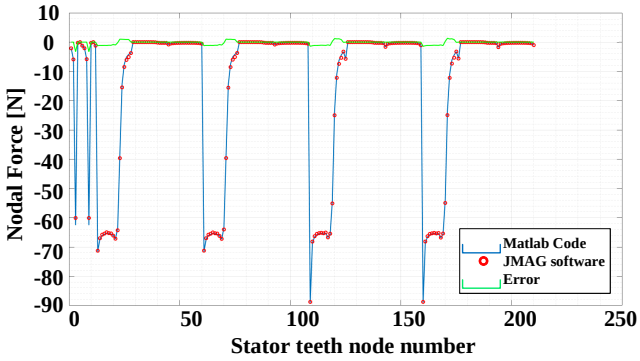

Figure 4.12: The nodal forces at the stator teeth edge nodes facing the air gap at the unaligned rotor position.

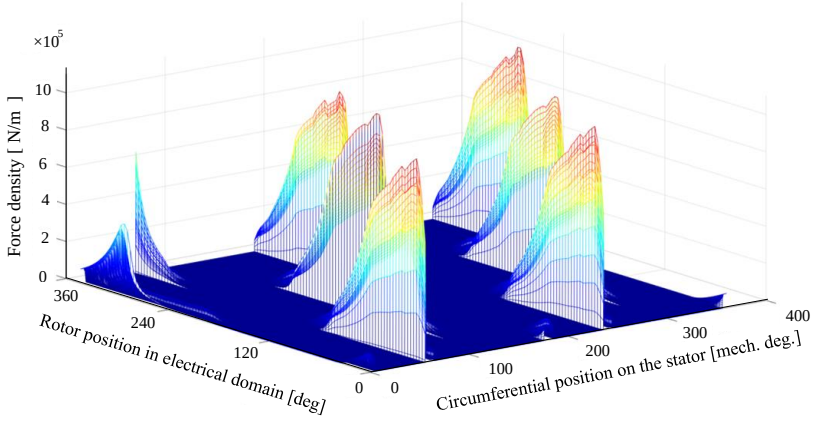

Figure 4.13: The force density surface wave of a 6/14 SRM at 1500 rpm.

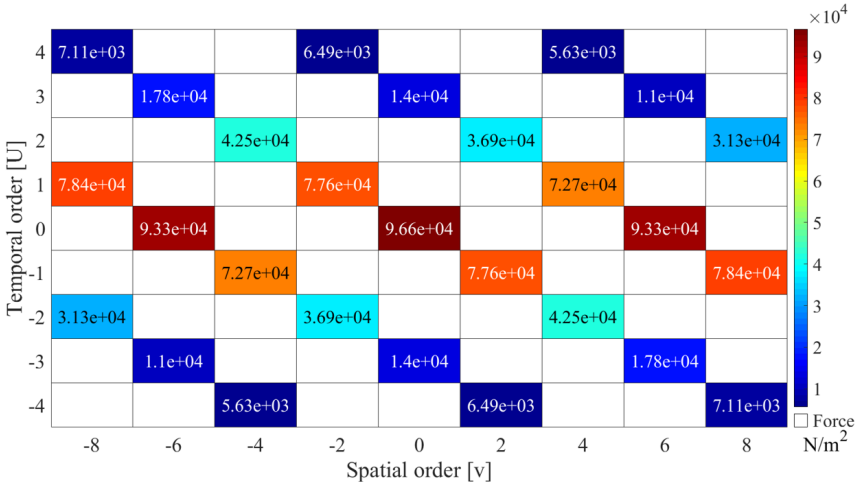

Figure 4.14: The amplitudes of the force density wave components of a 6/14 SRM at 1500 rpm.

presented to compare the adjoint variable method results with the CFD results. Then, the radial force density components sensitivity with respect to the finite elements' reluctivity, which is required for topology optimization as described in Chapter 8.

4.8.1 Force Senstivity Using Central Finite Difference

The Central finite difference (CFD) sensitivity of the force density surface wave with respect to the i^{th} design variable, p_i, is computed using (4).

$$\frac{\partial \boldsymbol{F_d}}{\partial p_i} = \frac{\left(\boldsymbol{F_d}|_{p_i+\Delta p_i} - \boldsymbol{F_d}|_{p_i-\Delta p_i} \right)}{2\Delta p_i} \tag{4.8.1}$$

where $\boldsymbol{F_d}$ is the force density surface wave and Δp_i is the perturbation of the parameter p_i. The CFD sensitivity surface wave is decomposed using 2D-FFT to get the sensitivities of the harmonic components. As previously mentioned, this method requires $2N + 1$ simulations to find the sensitivities of the radial force surface wave

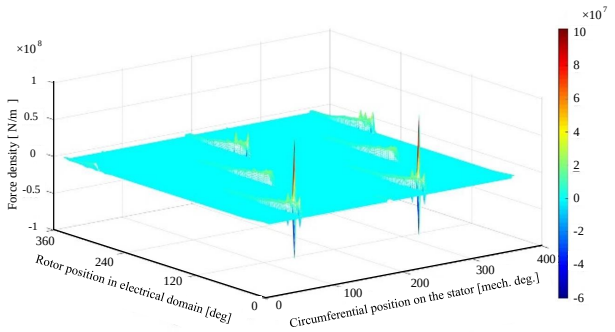

Figure 4.15: The CFD Sensitivity of the radial force density surface wave to the rotor teeth height.

components with respect to N design variables. For each design variable p_i, two iterative FEA simulations with positive and negative perturbations, $\pm\Delta p_i$, are required.

For example, positive and negative perturbations of 0.01 mm are applied to the rotor teeth height to calculate the CFD sensitivities shown in Figure 4.15. A 2D-FFT is then used to calculate the real and imaginary CFD sensitivities of the different harmonic components. The sensitivity of the magnitude of the force density component $f_{(u,v)}$ is then calculated using the following equation:

$$f_{(u,v)} = f(u,v)_{Re} + jf(u,v)_{Im}, \tag{4.8.2}$$

where f is the surface wave force density component of temporal order u and circumferential order v. The subscripts Re and Im indicate the real and imaginary parts, respectively.

4.8.2 Force Sensitivity Using Adjoint Variable Method (AVM)

As shown in Equations (4.3.39) and (4.3.45), the system matrix, $\boldsymbol{K}$, is function of the nodes locations and the magnetic vector potential. Equation (4.3.45) can thus be written as follows:

$$\boldsymbol{K}\left(\boldsymbol{A},\boldsymbol{P}\right)\boldsymbol{A}=\boldsymbol{F}, \tag{4.8.3}$$

where $\boldsymbol{P}$ is the design variables vector.

As discussed in Section 4.7, the radial nodal force is calculated at each node by summing up the change of the magnetic energy of the surrounding element, assuming a virtual displacement of this node in the radial direction.

As presented in Equation (4.7.3), the nodal forces are a function of the magnetic vector potential and the stiffness matrix. Hence, the sensitivity of the nodal force at each of the stator teeth node facing the air gap with respect to the geometrical parameters can be calculated as follows:

$$\frac{\partial F_n}{\partial p_i}=\left(\frac{\partial F_n}{\partial p_i}\right)_{\text{explicit}}+\left(\frac{\partial F_n}{\partial \boldsymbol{A}}\right)^{\mathrm{T}}\cdot\frac{\partial \boldsymbol{A}}{\partial p_i},\qquad \forall i \tag{4.8.4}$$

The term $\frac{\partial A}{\partial p_i}$ can be found from the differentiating the residual vector equation with respect to the geometrical parameter p_i as follows:

$$\frac{\partial \boldsymbol{D}}{\partial p_i}=\frac{\partial \boldsymbol{D}}{\partial p_i}+\frac{\partial \boldsymbol{D}}{\partial \boldsymbol{A}}\frac{\partial \boldsymbol{A}}{\partial p_i}=0 \tag{4.8.5}$$

By substituting the value of $\boldsymbol{D}$ in equation Equation (4.6.2) into equation Equation (4.8.5), the derivative of the residual vector can be determined as follows:

$$\frac{d\boldsymbol{D}}{\partial p_i} = \frac{\partial \boldsymbol{K}}{\partial p_i}\boldsymbol{A} + \left(\boldsymbol{K} + \frac{\partial \boldsymbol{K}}{\partial \boldsymbol{A}}\boldsymbol{A}\right)\frac{\partial \boldsymbol{A}}{\partial p_i} = 0 \tag{4.8.6}$$

So,

$$\frac{\partial \boldsymbol{A}}{\partial p_i} = -\left[\boldsymbol{K} + \frac{\partial \boldsymbol{K}}{\partial \boldsymbol{A}}\boldsymbol{A}\right]^{-1}\frac{\partial \boldsymbol{K}}{\partial p_i}\boldsymbol{A} \tag{4.8.7}$$

Hence, the nodal radial force sensitivity to any design variables,p_i, is obtained as:

$$\frac{\partial F_n}{\partial p_i} = \left(\frac{\partial F_n}{\partial p_i}\right)_{\text{explicit}} - \left(\frac{\partial F_n}{\partial \boldsymbol{A}}\right)^{\mathrm{T}} \cdot \left[\boldsymbol{K} + \frac{\partial \boldsymbol{K}}{\partial \boldsymbol{A}}\boldsymbol{A}\right]^{-1}\frac{\partial \boldsymbol{K}}{\partial p_i}\boldsymbol{A}, \qquad \forall i \tag{4.8.8}$$

Equation (4.8.8) can be rewritten in terms of the adjoint system as follow:

$$\frac{\partial F_n}{\partial p_i} = \left(\frac{\partial F_n}{\partial p_i}\right)_{\text{explicit}} - \boldsymbol{\alpha}\frac{\partial \boldsymbol{K}}{\partial p_i}\boldsymbol{A}, \qquad \forall i \tag{4.8.9}$$

where $\boldsymbol{\alpha}$ is the adjoint vector and can be calculated as follows:

$$\cdot\left[\boldsymbol{K} + \frac{\partial \boldsymbol{K}}{\partial \boldsymbol{A}}\boldsymbol{A}\right]^{\mathrm{T}}\boldsymbol{\alpha}^{\mathrm{T}} = \left(\frac{\partial F_n}{\partial \boldsymbol{A}}\right) \tag{4.8.10}$$

To confirm the calculation of the force density wave sensitivity using the AVM, the force density wave sensitivity with respect to the rotor teeth height and the stator teeth high of a 6/14 SRM is calculated using the CFD and the AVM.

The CFD sensitivities of the radial force density surface wave with respect to the rotor teeth high were calculated as illustrated in Section 4.8.1. The AVM sensitivities of the radial force density wave are also calculated, as illustrated in Section 4.8.2. Then, A 2D-FFT is used to calculate the real and imaginary components of both

sensitivities (CFD and the AVM) of different surface waves harmonics components. The sensitivity of the magnitude of the force density component f is then calculated as follows:

$$\frac{\partial \left| f_{(u,v)} \right|}{\partial p_i} = \frac{\partial}{\partial p_i} \sqrt{f(u,v)_{Re}{}^2 + f(u,v)_{Im}{}^2}, \tag{4.8.11}$$

where $f(u,v)_{Re}$ and $f(u,v)_{Im}$ are the real and imaginary parts of the force density component of temporal order u and circumferential order v.

Equation (4.8.11) is rewritten as follows:

$$\frac{\partial \left| f_{(u,v)} \right|}{\partial p_i} = \frac{1}{\sqrt{f(u,v)_{Re}^2 + f(u,v)_{Im}^2}} \left(2^* f(u,v)_{Re} * \frac{\partial f(u,v)_{Re}}{\partial p_i} + 2^* f(u,v)_{Im} * \frac{\partial f(u,v)_{Im}}{\partial p_i} \right) \tag{4.8.12}$$

The CFD sensitivity of the amplitude of radial force density components with respect to the stator teeth height is calculated based on Equations (4.8.1) and (4.8.12) (See Figure 4.16). The corresponding AVM sensitivities are calculated based on Equations (4.8.9), (4.8.10) and (4.8.12), as shown in Figure 4.17. It can be noticed from both figures that CFD and AVM sensitivities are in good agreement.

The percentage error between the two sets of sensitivities is shown in Figure 4.18, with a maximum error of $\sim 4.9\%$.

The CFD and the AVM sensitivities of the radial force density components to the rotor teeth height were also computed, as shown in Figure 4.19 and Figure 4.20,

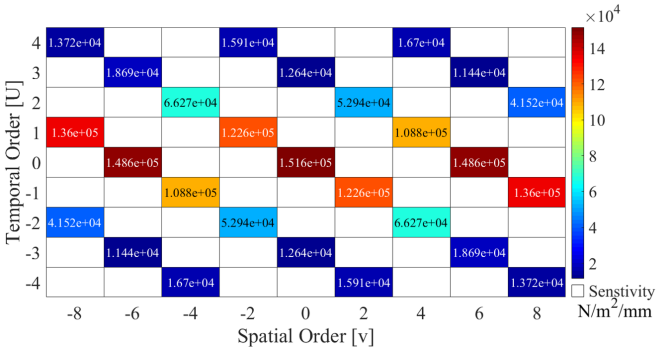

Figure 4.16: The CFD sensitivities of the amplitude of radial force density components to the stator teeth height.

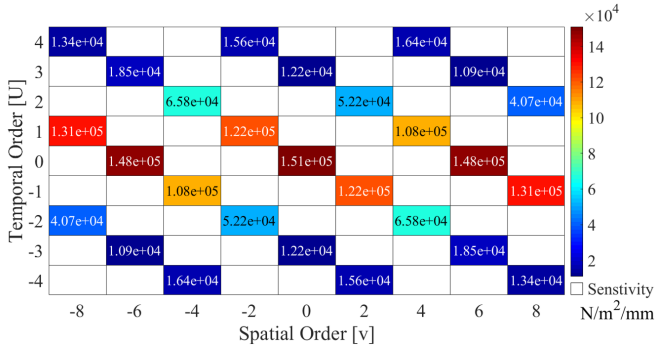

Figure 4.17: The AVM sensitivities of the amplitude of radial force density components to the stator teeth height.

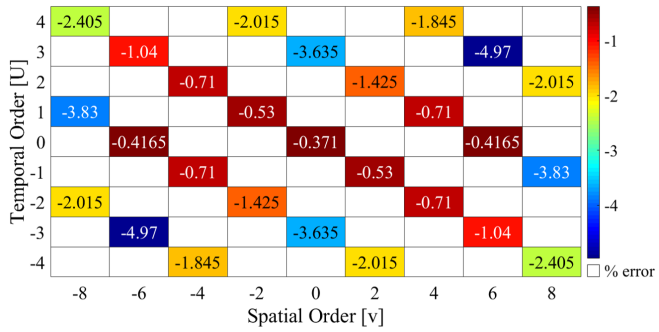

Figure 4.18: The percentage error between the CFD and AVM radial force density sensitivities to the stator teeth height.

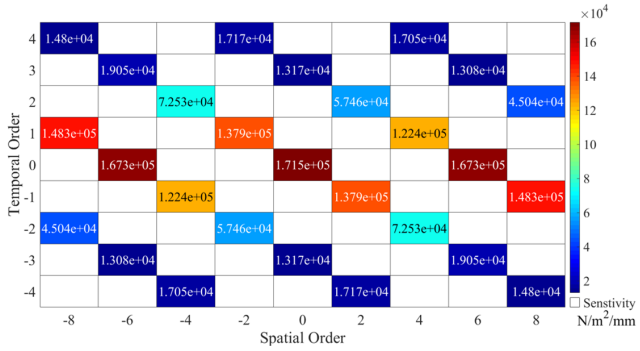

Figure 4.19: The CFD sensitivities of the amplitude of radial force density components to the rotor teeth height.

respectively. A maximum error of 3.5% is found between the two results (See Figure 4.21).

It was also noticed that the AVM sensitivities of radial force with respect to the different geometrical parameters results are susceptible to the number of air gap elements. The accuracy of AVM sensitivities could be improved by increasing the number of airgap elements and, hence, stator teeth nodes facing the air gap. However, this increases the simulation times in JMAG and MATLAB. The number of stator teeth edge nodes used in this research was 210.

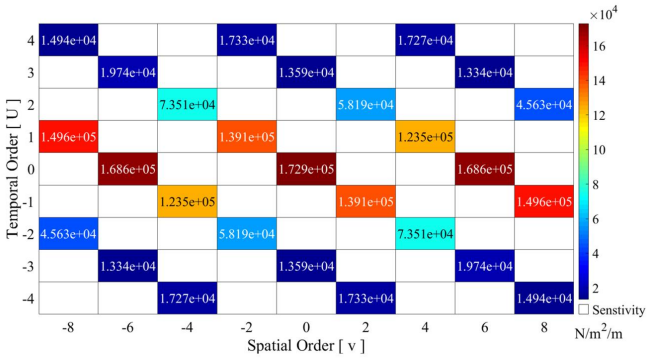

Figure 4.20: The AVM sensitivities of the amplitude of radial force density components to the rotor teeth height.

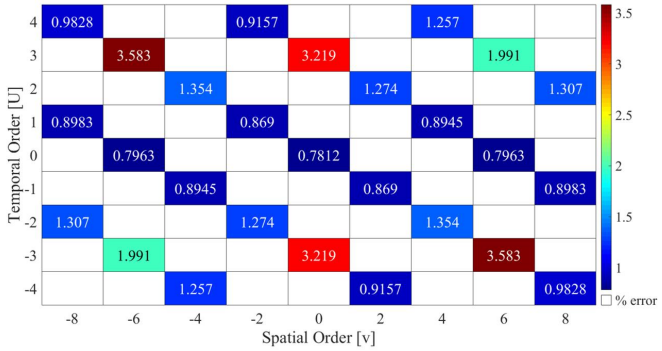

Figure 4.21: The percentage error between the CFD and AVM radial force density sensitivities to the rotor teeth height.

4.9 Summary

As discussed in this chapter, The AVM can be used to estimate the sensitivities of the radial forces with respect to any design variables. Linking the developed MATLAB toolbox of sensitivity analysis calculation for torque and radial force is linked to JMAG as discussed in this chapter. A 6/14 SRM with an operating speed of 1500 rpm was considered to evaluate the AVM technique of calculating the radial force density sensitivity with respect to two geometrical parameters to show the effectiveness of using that method. The obtained AVM sensitivities were compared to those calculated by the more accurate but time-intensive CFD. A good agreement between the two sets of results is achieved, and the maximum error between the two methods for any radial force density component sensitivity was about 4.9%. The number of airgap elements and stator teeth nodes facing the air gap should be carefully selected to guarantee a more accurate AVM sensitivity calculation.

The calculated radial force sensitivities will be used to optimize the machine geometry for acoustic noise minimization in future work.

Chapter 5

New linesearch-Based Topology Optimization Method

The double salient structure of the SRMs creates challenges such as high acoustic noise, vibrations, and high machine torque ripples [10]. The radial forces acting on the stator structure are the main cause of the acoustic noise of the machine [11]. However, the torque ripples are mainly due to the rotor tangential force harmonics [12]. Extensive studies were performed to overcome these challenges and improve the SRMs performance [12]. Topology and geometry optimization of the SRMs were used to enhance the machine performance and overcome the machine disadvantages. In geometrical optimization, the main geometrical design variables of the machine are optimized to improve the machine's performance [13]. However, in topology optimization (TO), the material distribution in a selected design domain is optimized to enhance the machine performance [14]. The main weakness of geometrical optimization is the limited degree of freedom. Any increase in the number of variables subject to optimization increases the complexity and the time of the optimization process [12]. On the other hand, the TO allows for new designs without being limited by the key design parameters of the machine.

Many published papers use TO to enhance electrical machines performance such as maximizing mean torque, minimizing torque ripples, and minimizing radial force [15–18]. TO was used in [19] to optimize the topology of the stator and rotor teeth of a 6/4 SRM configuration to minimize the torque ripples of the machine. In [15], topology optimization was used to optimize the stator structure of an SRM to reduce the vibration caused by the radial magnetic forces on the stator structure. The TO techniques can be divided into gradient-based and non-gradient-based methods, as described in [12] (See Figure 5.1). The gradient-based methods, such as the level set method [193], the material-density-based method [196], and the annealing-based

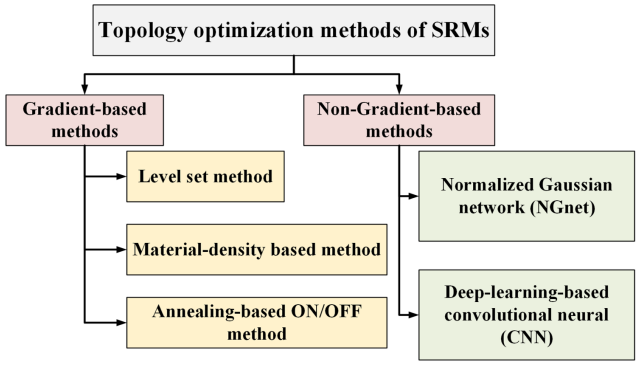

Figure 5.1: The main gradient-based and non-gradient-based TO methods.

ON/OFF optimization method [19], require the sensitivity information of the objective function with respect to the design elements at each iteration. However, the non-gradient-based methods, such as the normalized gaussian network [223] and the deep-learning-based convolutional neural network [14], do not require sensitivity information of the objective function. Also, the gradient-based topology methods have less computational time as compared to the non-gradient-based optimization methods. The gradient-based methods may converge, however, at local optimum solutions, unlike Non-gradient-based methods [12].

The initial topology of the TO is the design domain filled with magnetic material and the optimization method tries to remove parts of the magnetic material to reach the optimal solution. The generative optimization (GO), however, starts with empty design space and the optimization method fills a subset of that space with a magnetic material to decrease the objective function [224]. The GO shows an improvement in the final objective function as compared to the TO with the same optimization method and the same design domain [225]. To our best knowledge, GO has not been utilized before in the optimization of the electric machine. Figure 5.2 shows the

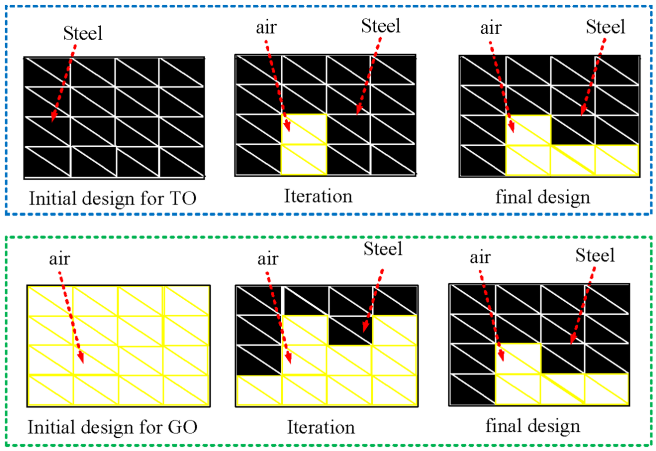

Figure 5.2: The difference between topology optimization and generative optimization.

difference between the GO and the TO.

Topology optimization is used in the literature to enhance the dynamic performance of the switched reluctance machines. This chapter introduces a new ON/OFF optimization method based on the line search method to overcome the limitations of the conventional annealing-based ON/OFF optimization.

As illustrated in [12, 198], The annealing-based ON/OFF TO can handle a large number of design elements in the design domain. Also, it has a much less convergence time than the other two gradient-based ON/OFF TO methods mentioned in Figure 5.1, [12]. The annealing-based ON/OFF TO method was applied in the literature for electromagnetic designs. In [198], the method was used for the first time for electromagnetic design. The method was also applied in [199] to optimize the shape of a magnetic shield of a magnetic recording system. In [19], the shape of the front part of the stator teeth of an SRM for an air conditioning application was optimized by the annealing-based ON/OFF TO method to reduce the torque ripples

of the machine.

In this chapter, a new technique based on the line search is used to replace the annealing process of the annealing-based ON/OFF TO algorithm. The newly proposed technique shows an enhancement in the final value of the objective function and faster convergence as compared to the annealing-based ON/OFF TO algorithm. The new proposed method shows a good improvement in final solution of both the topology and generative optimizations compared to the annealing-based ON/OFF method. Using the same computer and the same optimization example, the new technique shows a hug reduction on the optimization time. The reason behind the fast convergence of the new proposed approach is that the method seeks for the optimal number of element subject to change at each iteration. However, the annealing-based algorithm starts each iteration with changing a high number of elements and then reduce the number of elements subject to change with a fixed step till hitting a reduction in the objective function.

5.1 Conventional Annealing-Based Topology Optimization Method

The annealing-based ON/OFF topology optimization is illustrated in this section. The flowchart shown in Figure 5.3 illustrates the method. In the annealing-based ON/OFF topology optimization, the sensitivity of the objective function with respect to the reluctivity of each element in the design space is calculated to determine the direction of the elements' material change in each iteration. The annealing-based ON/OFF TO method saves time as compared to the random changes utilized in

stochastic-based topology optimization methods [12].

At each iteration, the material of each element is changed in the direction of the negative gradient of the objective function with respect to that element's reluctivity. For example, if the objective function gradient is positive with respect to the reluctivity of an element, the reluctivity of that element should be decreased to decrease the objective function. In that case, if the element material is iron, the element should be changed to air. However, if the element material is already air, the element material is kept air as the reluctivity of the element can not be decreased further.

The optimization algorithm starts with evaluating the initial design. The objective function sensitivities with respect to the elements' reluctivities are then obtained. According to the annealing process, the sensitivities of the objective function are then used to change the element material based on its sign and value. The annealing process in this algorithm is used to select the optimum number of elements to modify the design space topology at each iteration. As the sensitivity of the objective function is calculated for each element in the design space assuming no change on the other elements, this could lead to an increase in the objective function if a high number of elements is considered for topology change. The annealing process used in this work is highlighted in Figure 5.3. The process starts by sorting of the objective function's sensitivities with respect to the reluctivities of all the elements. Then, N_p number of elements that have the highest positive sensitivities are selected, and the materials of these elements are changed to air.

Similarly, N_n number of elements that have the lowest negative sensitivities are selected to be iron. The newly formed topology is then evaluated. If the objective function is reduced, the annealing algorithm ends. If the objective function does not

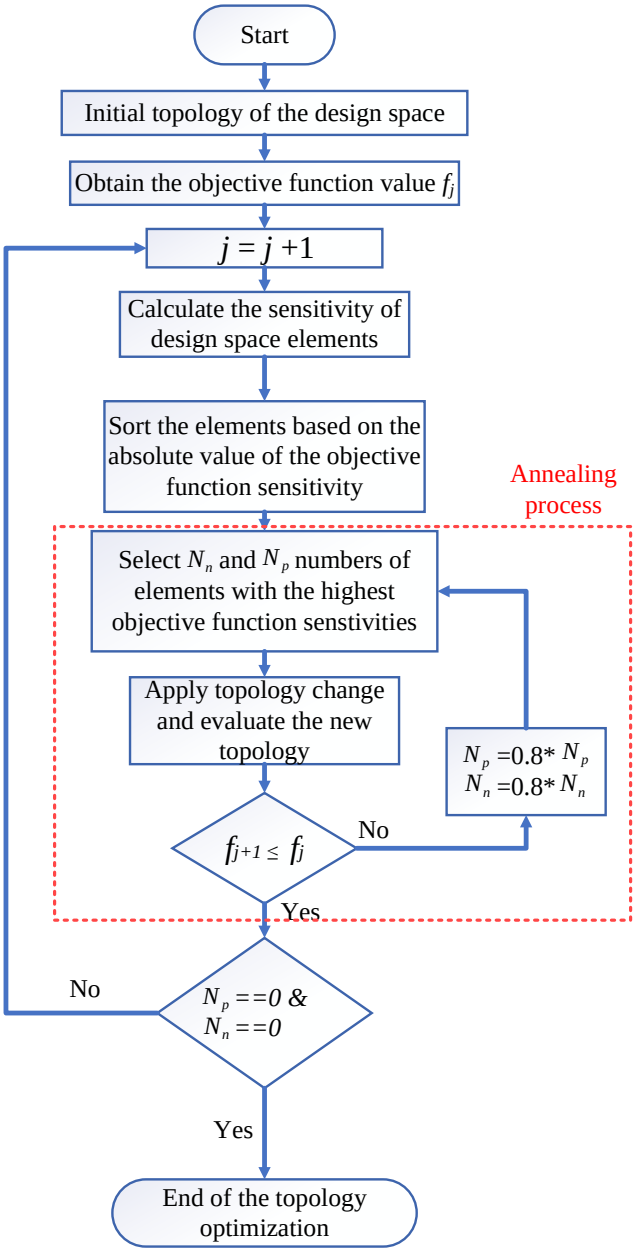

Figure 5.3: A flow chart of the annealing-based ON/OFF TO algorithm.

improve, N_p and N_n are successively decreased by 20% till the objective function is improved. If the N_p and N_n reach zero and there is no reduction in the value of the objective function, the topology optimization is terminated.

the annealing-based method suffers from two weaknesses. The first weakness is that at each iteration, the optimal number of elements subject to change is not considered. That is because the number of perturbed elements is decreased till a reduction of the objective function, even a small reduction, is achieved as illustrated in the flowchart in Figure 5.3. This slows the convergence to the optimal solution. The second weakness, the final design and the final local objective function depend on the initial design topology.

5.2 Linesearch-Based Topology Optimization Method

As indicated in [16,74,199,226], the annealing-based ON/OFF TO is based on considering a fixed number of elements for material change at each iteration. If the material changes of these elements do not reduce the objective function, the number of considered elements for change decreases until any decrease in the objective function is achieved even a small reduction. If the number of the changed elements reaches zero without any reduction of the objective function, the optimization algorithm terminates, and this condition is considered as the end of the optimization algorithm. Figure 5.4 illustrates an example of considering 40% of the elements with the highest absolute objective function sensitivity for change.

To illustrate the first weak point of the annealing-based ON/OFF TO, the sensitivity of the objective function shown in Equation (5.2.1) is calculated for the elements of the stator teeth of a 6/14 SRM presented in Figure 5.5.a. The design domain of

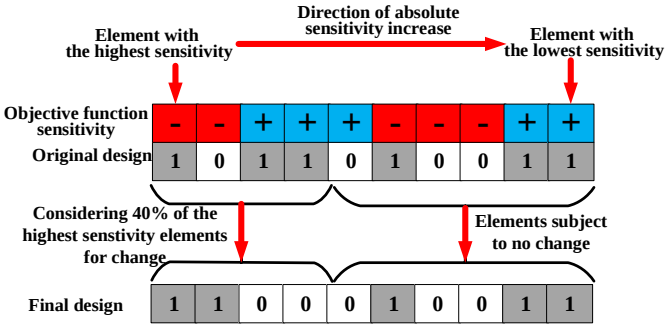

Figure 5.4: An example for considering part of the design domain for change based on the value of the absolute sensitivity.

the machine is indicated in Figure 5.5.b. The objective of the design is to reduce the torque ripple while keeping the mean torque value of the machine around 6 N.m.

$$f = \frac{\sum_{i=1}^{N} (t_i - 6)^2}{N} \tag{5.2.1}$$

where t_i is the motor torque at the rotor step number i.N is the number of rotor steps for one electrical cycle. In this optimization example, $N = 100$.

The sensitivity of the objective function with respect to each element's reluctivity in the design space is calculated. The elements are then sorted based on their corresponding objective function sensitivities. The percentage of elements subject to material change is then swept from 0% to 100% with a 5% step. The objective function is evaluated after each step change as illustrated in Figure 5.6.

It is clear from Figure 5.6 that if the annealing-based ON/OFF TO is used with 40% or 50% of the design space element being subject to change, the objective function will be reduced as compared to the initial design (0%). This is not, however, the optimal reduction. The optimal percentage of elements that should be subject to change is between 90% and 95%. Even if the percentage of elements subject to

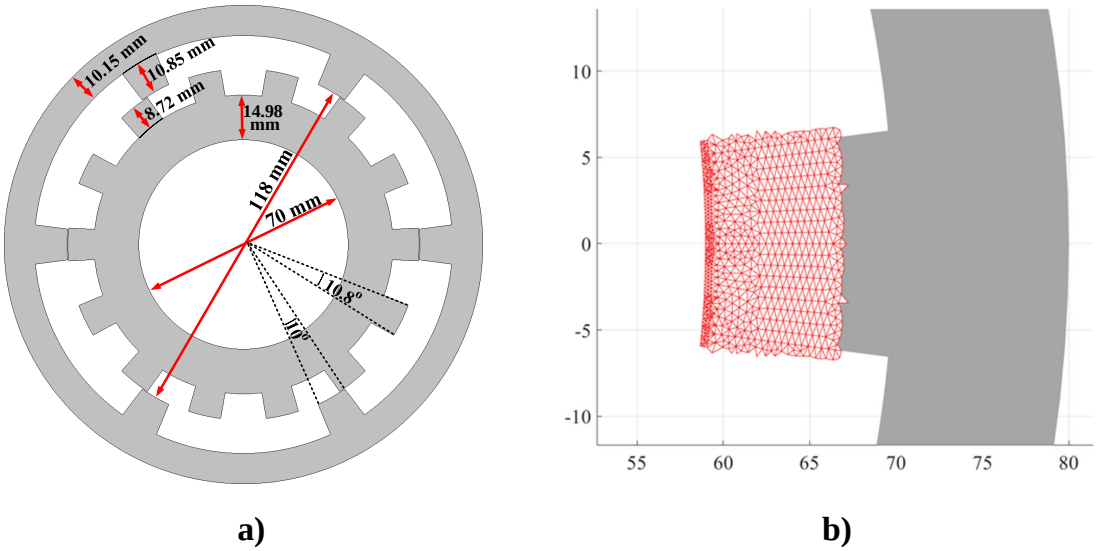

Figure 5.5: The 6/14 SRM used for topology optimization a) the full machine before optimization b) the design domain elements on one of the stator teeth selected for topology optimization.

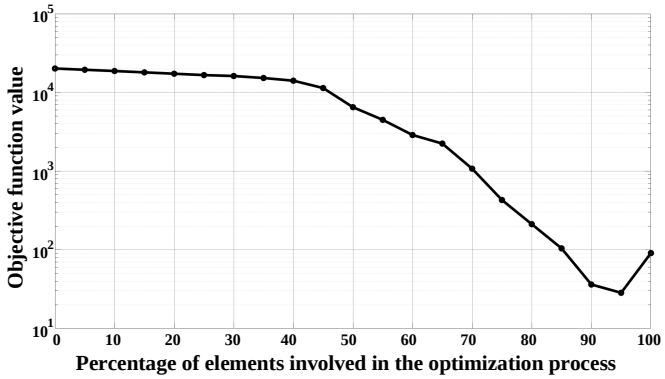

Figure 5.6: the objective function value at different percentages of elements considered for change at the first iteration of the optimization algorithm.

change is chosen to be 95%, this percentage will not be the optimal number for the next iteration.

To solve these issues, a new sensitivity-based ON/OFF optimization with a line search technique is proposed to search for the optimal number of elements that should be subject to change at each iteration. The line search technique replaces the annealing process of the conventional ON/OFF optimization.

The sign of the sensitivity of each element in this proposed algorithm is used to determine the element's type in the next iteration (either air or magnetic material). However, the absolute value of the objective function sensitivity is used to sort the elements according to their importance in achieving the objective function.

The line search method starts with sorting the elements of the design domain according to the absolute value of their objective function sensitivity. The objective function is then evaluated at $0\%, 50\%$, and 100% of topology elements subject to change, the change is done based on the sign of the sensitivities as illustrated before. As shown in Figure 5.7.a, the objective function at three points, $0\%, 50\%$, and 100%, are called f_1, f_c and f_2, respectively. Then, if $f_2 < f_1$ the distance between 50% and the 100% is halved and the function is evaluated at 75% and called f_c and the old value of f_c is assigned to f_1 as indicate in Figure 5.7.b. But, if $f_2 > f_1$ the distance between 0% and the 50% is halved and the function is evaluated at 25% and called f_c and the old value of f_c is assigned to f_2. The line search is kept inside this loop until $|f_2 - f_1| < \varepsilon$, where ε is a very small tolerance. This procedure is similar to some of the approaches utilized in line search algorithms [93].

After reaching this condition, the iteration is ended and the objective function sensitivities with respect to all the design elements are calculated for the new iteration

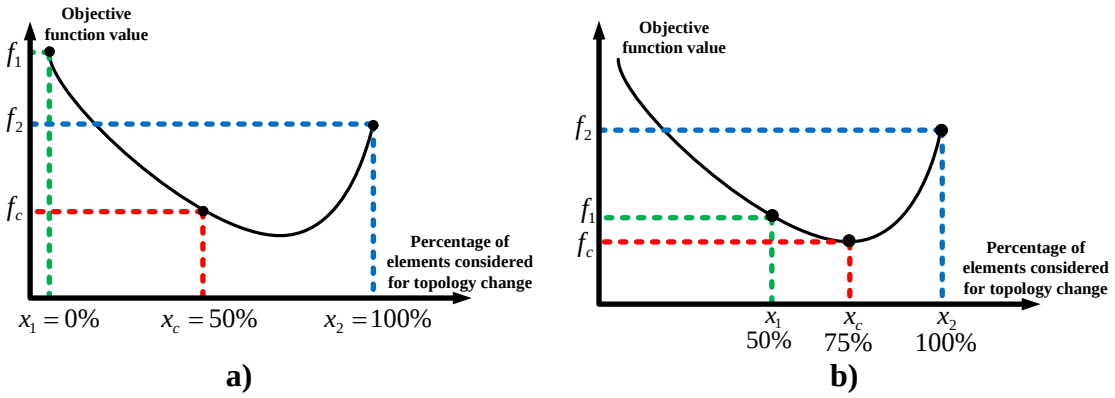

Figure 5.7: The internal halving line search technique used to search for the optimal percentage of elements at each ON/OFF topology optimization iteration a) step 1 b) step 2.

and the line search is performed again. The algorithm stops when the line search finds that the optimal number of elements subject to change equals 0. As discussed in the rest of the paper, The algorithm shows great performance and is able to solve the two weak points of the annealing-based topology optimization that are illustrated before.

5.3 Smoothing Algorithm of The Final Topology Optimized Design

The final design after the optimization process is refined with a smoothing algorithm. The objective of the smoothing algorithm is to avoid having an iron element that is surrounded by air. Such an islanded element is challenging to be realized in machine manufacturing. There are two options to remove the islanded elements; the first option is to simply convert the element's material to air. The second option is to create

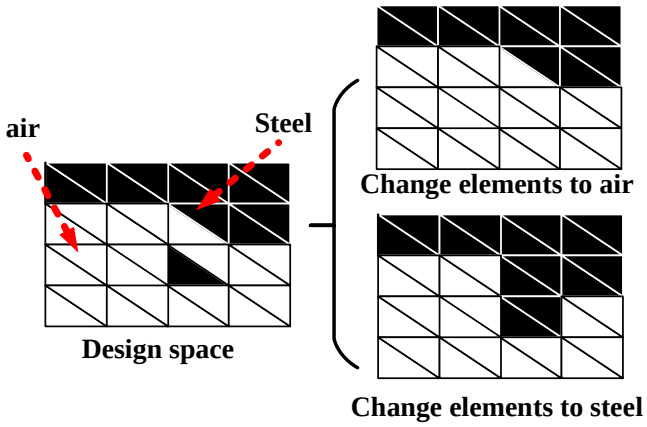

Figure 5.8: The different options of the smoothing algorithm; some elements are either converted to steel or to air to avoid having steel elements surrounded by air.

a support to that element by linking it to the nearest iron elements as shown in Figure 5.8. Either way affects the objective function value as the smoothing changes the optimal material distribution selected by the ON/OFF optimization algorithm. The smoothing algorithm applies both options for each islanded element and selects the smoothing option with the smallest effect on the objective function. This operation can protect the design from having magnetic material floating in air without support.

5.4 Summary

A new linesearch-based ON/OFF optimization method for topology and generative optimization of electric machines is proposed and illustrated in this chapter. The new method is developed to overcome the limitations of the conventional annealing-based ON/OFF method. A comparison between the performance of the newly proposed method and the conventional method is presented in Chapter 6.

Chapter 6

Topology and Generative Optimization of the 6/14 SRM for Torque Ripple Reduction

Topology optimization is used in the literature to enhance the dynamic performance of the switched reluctance machines. In this chapter a performance comparison of the generative optimization and the topology optimization of a 6/14 switched reluctance machine with the linesearch-based method proposed, introduced in Chapter 5, and the conventional annealing-based method. The two methods are applied to two different design domains of the machine for topology and generative optimization and the results are compared to the results of the annealing-based ON/OFF method. The results show the effectiveness of the newly proposed method. The proposed method shows a faster convergence to optimal solutions than the conventional annealing-based ON/OFF method.

6.1 Case study Machine Parameters

In this Section, the optimization results obtained using the conventional annealing-based ON/OFF optimization method and the proposed linesearch-based optimization method are compared to show the proposed method's effectiveness. The topology and generative optimizations are used to optimize the stator teeth of a 6/14 SRM to reach a mean torque of 6 N.m and minimize the torque ripples. The initial design of the machine is shown in Table 6.1. The machine is designed for HVAC and the objective of the study is to reduce the torque ripple of the machine for that application [227].

The reason for selecting the Somaloy 700HR 3P, [229], material for the machine design is to have different ways to manufacture the complex designs resulting from the machine's topology and generative optimization. The soft magnetic composite materials, such as the Somaloy material, can be 3D printed as shown [230, 231]. The 3D print considered in this paper as the main manufacturing technique to realize the

Table 6.1: The rated parameters of the initial design of the machine.

Case study machine	6/14 SRM
DC link voltage (V)	170
Machine max speed (r.p.m)	1103
Peak power RMS phase current (A)	3.89
Reference current (A)	6.5
Core loss of the initial design (W)	105.4
Rated speed (RPM)	1103
Peak torque required for the application (N.m)	5.83
Torque ripple r.m.s (N.m)	1.2820(21.99%)
Stator OD (mm)	160
Rotor ID (mm)	70
Stator back iron thickness (mm)	10.15
Rotor back iron thickness (mm)	14.98
Stator teeth height	10.85
Rotor teeth height	8.72
Stator/rotor axial length	78
Rotor pole arc angle	10.8deg
Stator pole arc angle	10deg
Mechanical airgap thickness	0.3
Number of turns	120
Number of strands per turn	2
Wire size	AWG 20
Wire insulation	0.05 mm of PEEK insulation (240 C)
Stator and rotor core material	Somaloy 700HR 3P [228]

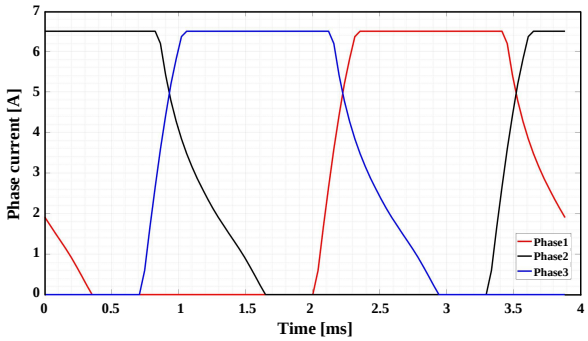

Figure 6.1: The machine phase-current waveform after optimizing the firing angle of the 6/14 SRM drive converter.

complex design results after the topology.

To maximize the mean torque and minimize torque ripples of the initial design, the firing angles of the converters are optimized, and the resulting current waveform is shown in Figure 6.1. Hysteresis control with soft switching is used to control the machine current to the reference value [24]. It can be noted from Figure 6.1 that the machine's current waveform is filtered out from the current ripple. The reason behind that is that the current ripple is reflected in the torque waveform as a torque ripple, and the purpose of the study is to reduce the electromagnetic torque ripples due to the double saliency of the machine. The torque ripples due to the current hysteresis effect can be improved by the converter control parameters and the control strategy, which is not the scope of this paper. The reader can refer to [232–234].

Both the conventional ON/OFF optimization method [198, 199] and the proposed method are applied to satisfy the design requirements. The initial design of TO is the design domain filled with magnetic material. The GO, however, starts with empty design domain. The optimization method fills a subset of that space to minimize the objective function [224]. The GO shows an improvement in the final objective

function as compared to the TO with the same optimization algorithm and the same design domain [225]. According to the authors' best knowledge, GO has not been utilized before in the optimization of the electric machine.

Figure 6.2 shows the main parts of the optimization process. As presented in Figure 6.2, the optimization process consists of three main steps. In the first step, a MATLAB script calls JMAG to apply the initial design of the machine and run the model. The MATLAB script then exports the mesh information and the electromagnetic solution in all the simulation steps. The information exported from the FEA simulation is the magnetic vector potential at all the nodes and the reluctivity of all the elements, which are required for the sensitivity calculation as described in section IV. Based on the exported mesh information, the nodes' location and the finite elements, the design space is selected. The number of elements is limited by the available computational capability of the used computer. Ideally, more elements involved in the optimization process means the higher chance to improve the machine's performance further; however, the more element involved in the optimization process, the more computation capability is required. The second step of the process is calculating the sensitivity of the objective function with respect to each element in the design space and optimizing the design accordingly. At each iteration of the optimization process, the torque of the machine is calculated with JMAG, and the sensitivity of the objective function is calculated based on the updated information from the latest FEA, as shown in Figure 6.2. The optimization process is circulating in the second step loop till the termination condition is reached. the termination condition depends on the optimization algorithm as described in Sections 5.1 and 5.2. The last step is to evaluate the final design and export the torque information from

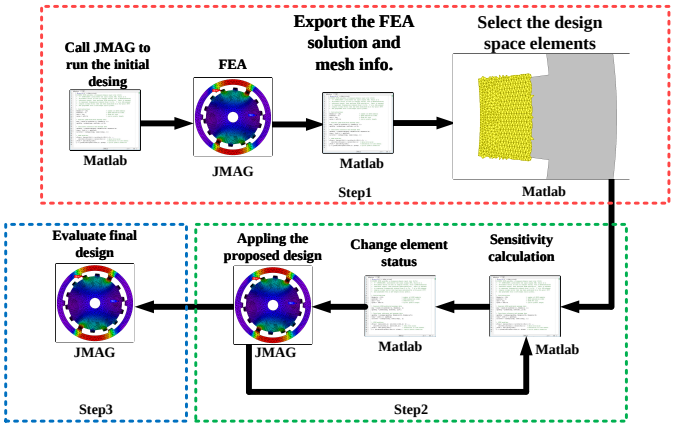

Figure 6.2: Flowchart of the optimization process numerical implementation using JMAG and MATLAB.

JMAG for that design.

The objective of the optimization problem is to increase the mean torque and reduce the torque ripples of the machine. The target mean torque for the application is 6 N.m, so the objective function is formulated as follows:

$$f = \frac{\sum_{i=1}^{N} (t_i - 6)^2}{N} \tag{6.1.1}$$

where N is the number of rotor positions simulated for one electrical cycle, and t_i is the rotor torque at position number i. In this study, the number of rotor positions used for one electrical cycle is 100 . The lowest possible value of the objective function shown in Equation (6.1.1) is zero, at which the mean torque of the machine is 6 N.m, and the torque ripple is zero. The optimization objective is to reduce the function in Equation (6.1.1) to get closer to the target torque and reduce the torque ripples as much as possible.

6.2 Generative and Topology Optimization of the Stator Design Domain with the Conventional Annealing-based ON/OFF Optimization Method

6.2.1 Generative Optimization of the Stator Design Domain

Figure 5.5.a shows the 6/14 SRM before optimization, while Figure 5.5.b shows the design domain elements on one of the stator teeth. 5940 elements are considered for topology and generative optimization in the stator teeth design domain, with 990 design elements in each stator tooth.

The conventional annealing-based ON/OFF optimization is used for GO of the design domain shown in Figure 5.5. The algorithm reaches mean torque of 5.45 N.m and an r.m.s torque ripple of 0.387 N.m or 7.1%. Figure 6.3 shows the objective function value at the different iterations of the optimization process. As shown in the figure, the optimization process reached the optimum point after 24 iterations which required 5 days, 10 hours, and 17 minutes to be finished using a computer with Intel(R) Core(TM) i7-8700 CPU @ 3.20GHz processor and 32.0 GB ram memory. That computer was used for all the studies presented in this chapter. The torque ripple and the mean torque at the different iteration steps of the algorithm is shown in Figure 6.4.

The final stator design after the GO with the annealing-based method is shown inFigure 6.5. A closer look to one of the stator teeth after the optimization is shown in Figure 6.6. The flux density contour plots and the flux lines of the original design and the optimized design at three different positions, the turn-on instant of phase

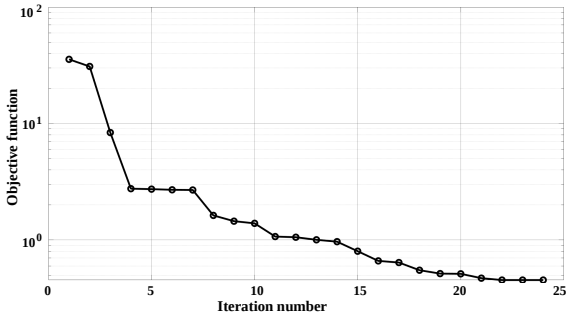

Figure 6.3: The objective function value at the different iterations of the generative optimization based on the conventional annealing-based ON/OFF method.

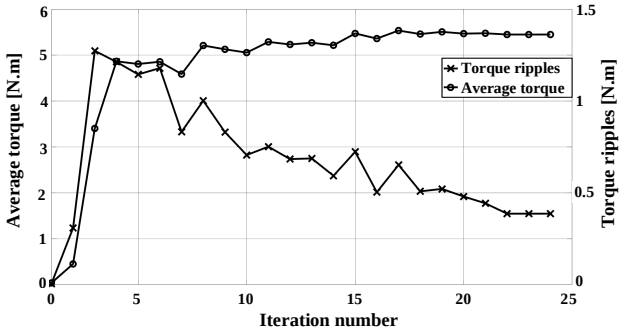

Figure 6.4: The motor torque ripples and mean torque at the different iterations of the optimization process.

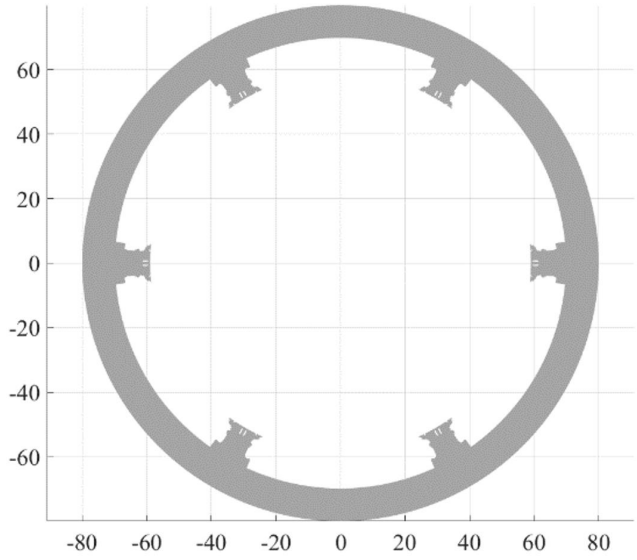

Figure 6.5: The final stator shape after the GO of the stator teeth with the conventional annealing-based ON/OFF optimization method.

1, the middle of phase1 excitation, and the turn-off instant of phase1, are shown in Figure 6.7 and Figure 6.8. It can be noticed from Figure 6.7 and Figure 6.8 that the optimization algorithm tries to introduce flux barriers to the flux path in order to direct the flux.

To confirm the torque waveform and the torque calculation, a 3D model is built for the design shown in Figure 6.6 on the same commercial software, JMAG. Figure 6.9 shows the 3D model built for the design. Please note that the end-turn effect is neglected, as shown in the 3D model. A comparison of the dynamic torque of the 2D model and the 3D model is shown in Figure 6.10. a Comparison of the average torque and the torque ripple of the 3D model and the 2D model is shown in Table 6.2. It can be concluded that the 2D model can be used in the analysis for the average torque and the torque ripple calculation.

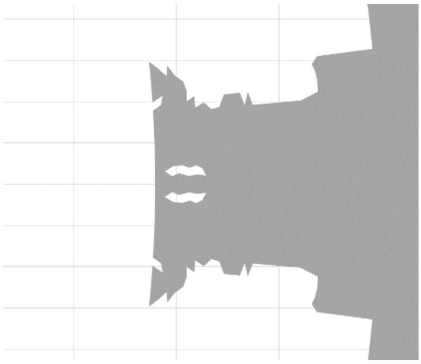

Figure 6.6: The shape of one stator tooth after the GO of the stator teeth with the conventional annealing-based ON/OFF optimization method The Final design is simulated with 2D simulation on a commercial FEA software.

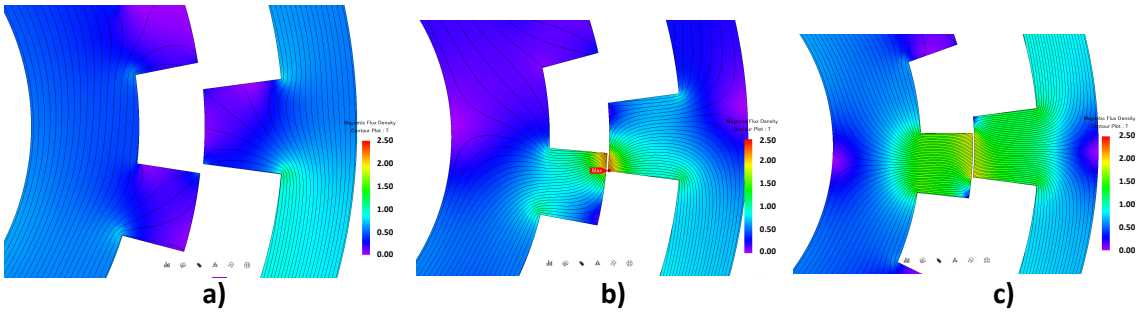

Figure 6.7: The Flux density contour plot and the flux density lines of the design at three positions of one of the phases excitation: for the initial design a) at the turn-on instant of phase1, b) at the at the middle of the duration of phase A excitation, c) at the turn-off instant of phase A.

Table 6.2: Comparison of the average torque and the torque ripple using the 2D model and the 3D model for the design shown in Figure 6.6.

	2D model	3D model	Error (N.m)
Torque (N.m)	5.45	5.393	−0.057
Torque ripple (N.m)	0.387	0.501	−0.114

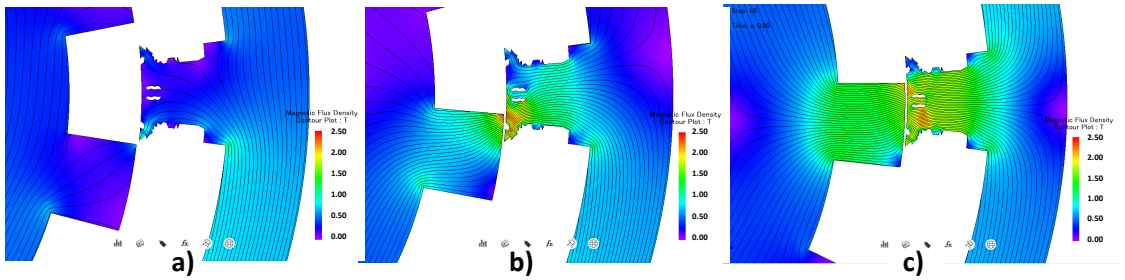

Figure 6.8: The Flux density contour plot and the flux density lines of the design at Figure 6.6 at three positions of one of the phases excitation for the optimized design: a) at the turn-on instant of phase1, b) at the at the middle of the duration of phase A excitation, c) at the turn-off instant of phase A.

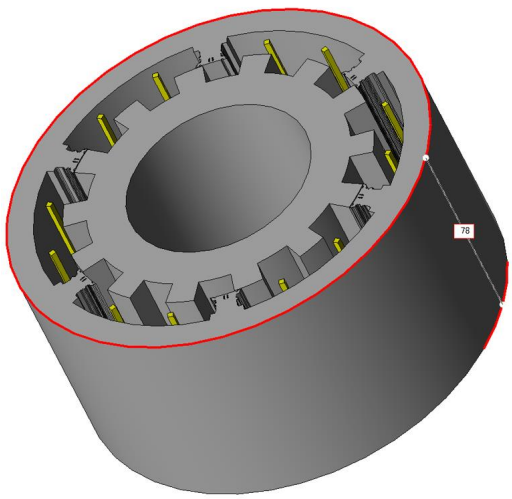

Figure 6.9: 3D model of the design shown in Figure 6.6 on JMAG software.

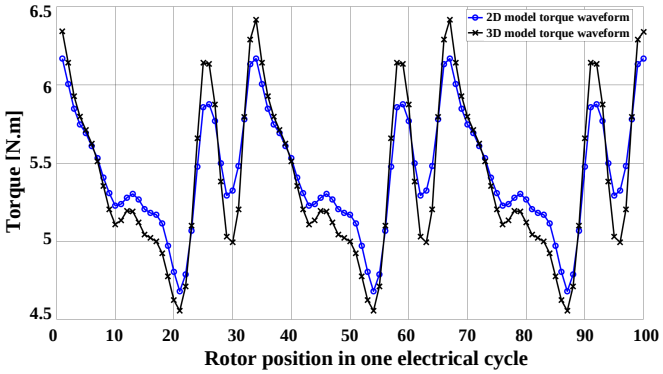

Figure 6.10: A comparison of the dynamic torque of the final design shown in Figure 6.6 using 2D model and 3D model on JMAG software.

6.2.2 Topology Optimization of the Stator Design Domain

In this case study, the conventional annealing-based ON/OFF optimization is used for TO of the design domain presented in Figure 5.5.b for the same objective shown in (22). The GO starts with an empty design domain; however, the TO starts with all the design domain elements assigned to iron material. The algorithm reached a mean torque of 5.725 N.m and an r.m.s torque ripple of 0.204 N.m or 3.6%. Figure 6.11 shows the objective function value at the different iterations of the optimization process. As shown in the figure, the optimization process reached the optimum point after 24 iterations which required 6 days, 23 hours, and 30 minutes. The torque ripple and the mean torque at the different iteration step of the algorithm is shown in Figure 6.12. The final design after the topology optimization with the annealing-based ON/OFF optimization is shown in Figure 6.13.

The flux density contour plot and the flux lines plot of the design in one of the stator teeth of phase1 at three different positions, at the instant turn-on of phase1, at the middle of phase1 excitation, and the instant of turn-off of phase1 is shown in

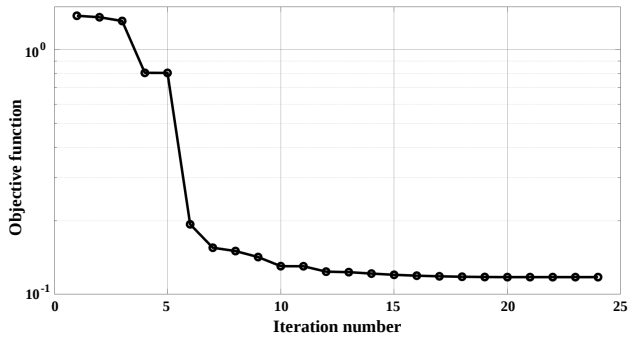

Figure 6.11: The objective function value at the different iterations of the TO based on the conventional annealing-based ON/OFF technique.

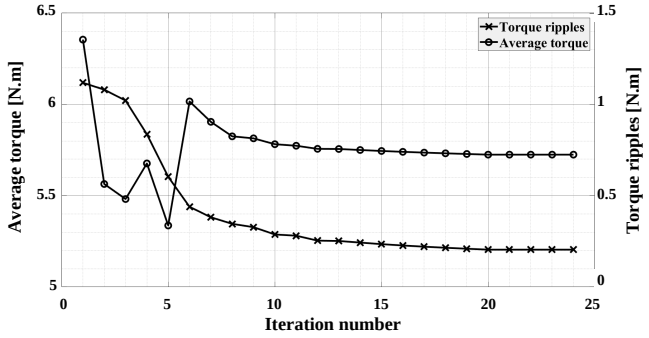

Figure 6.12: The objective function value at the different iterations of the TO based on the conventional annealing-based ON/OFF technique.

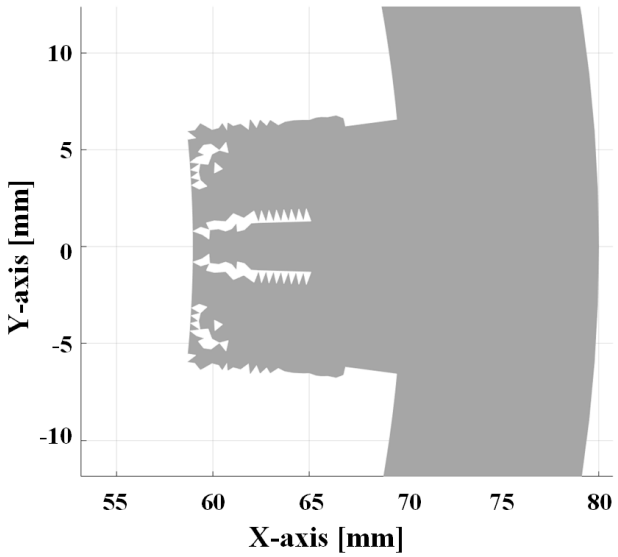

Figure 6.13: The stator final design after the TO with the annealing-based ON/OFF optimization technique.

Figure 6.14. It can be concluded from the figure that the optimization algorithm is introducing voids in the stator teeth to divert the flux lines from the middle of the stator teeth, which results in improving the torque of the machine.

The main manufacturing strategy to realize this part is to use additive manufacturing. The Somaloy 700 HR 3P material is chosen for that reason. There are 3 types of the Somaloy 700 HR material, 1P, 3P, and 5P. The Somaloy 700 HR 3P material is selected in this research as it has higher mechanical strength compared to the Somaloy 700 HR 1P and the Somaloy 700 HR 5P as described in [235, 236].

However, suppose the laser cutting method or the lamination stamping method will be used for manufacturing this design. In that case, the design should be smoothed further, as shown in Figure 6.15. However, the core material should be

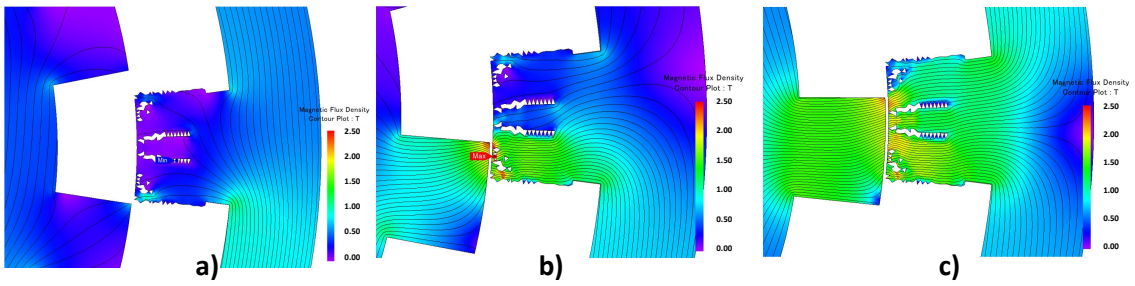

Figure 6.14: The Flux density contour plot and the flux density lines of the design shown in Figure 6.13 at three positions of one of the phases excitation: a) at the turn-on instant of phase1, b) at the at the middle of the duration of phase A excitation, c) at the turn-off instant of phase A

Table 6.3: Comparison of the design shown in Figure 6.13 before soothing and after soothing using the Somaloy 700 HR 3P.

	Design before smoothing Figure 6.13	Design after smoothing Figure 6.15
Torque (N.m)	5.725	5.665
Torque ripple (N.m)	0.204	0.455

also changed to non-oriented silicon steel or cobalt steel laminations. A torque performance comparison of the machine before and after the design smoothing is presented in Table 6.3 and Figure 6.16. It can be noticed from that comparison that the smoothing of the design shifts the performance of the machine from the optimal point which results in a reduction in the average torque and an increase in the torque ripples.

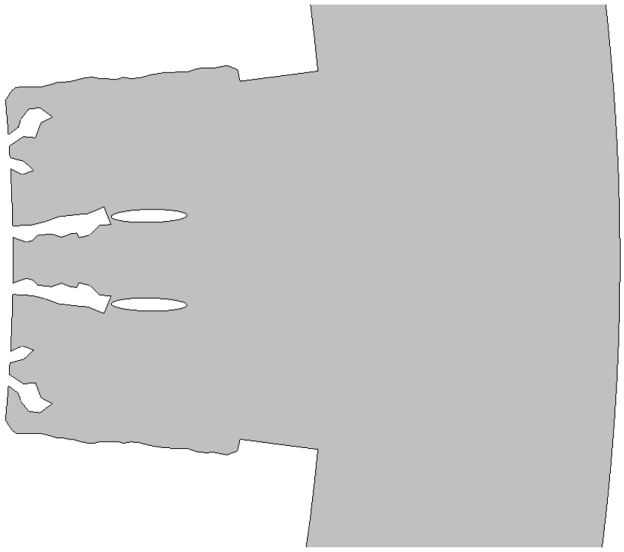

Figure 6.15: The stator final design shown in Figure 6.13 after smoothing.

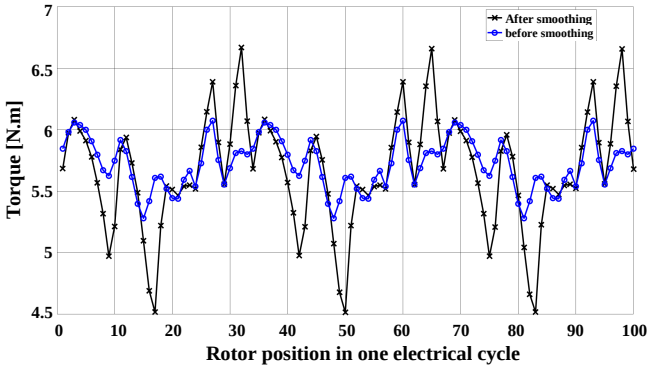

Figure 6.16: A comparison of the dynamic torque of the final design shown in Figure 6.13 before and after smoothing.

6.3 Generative and Topology Optimization of the Stator Design Domain with The linesearch-based optimization

The proposed linesearch-based optimization approach illustrated in Section III is used for generative and topology optimization of the stator design domain shown in Figure 5.5.b with the same objective function shown in (22). The same PC was used for the optimization to compare the time required for each method.

6.3.1 Generative optimization of the stator design domain

In this case, the initial topology of the design domain is assigned to air, and the optimization algorithm fills the space with the magnetic material to minimize the objective function (22). The mean torque at the final iteration of the generative optimization based on the proposed linesearch-based method is 5.8 N.m, and the r.m.s torque ripple is 0.3523 N.m or 6.074%. Figure 6.18 shows the torque ripple and the mean torque at all optimization iterations.

The flux density contour plot and the flux lines of the final optimized design in one of the stator teeth of phase1 at three different positions, at the instant of the phase1 turn-on, at the middle of the phase1 excitation, and at the turn-off instant of phase1, are presented in Figure 6.19. It can be concluded from the flux density contour plot that the optimization algorithm tries to divert the flux lines from the middle of the stator teeth, which results in a lower torque ripple compared to the initial design.

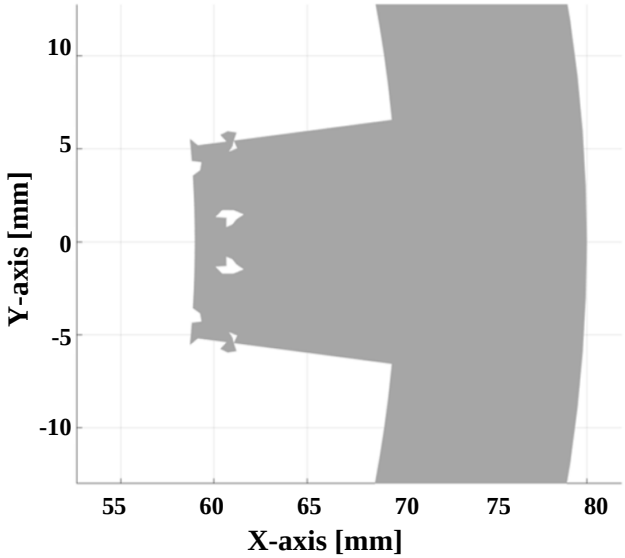

Figure 6.17: The shape of one stator teeth after the GO of the stator teeth with the linesearch-based ON/OFF optimization method.

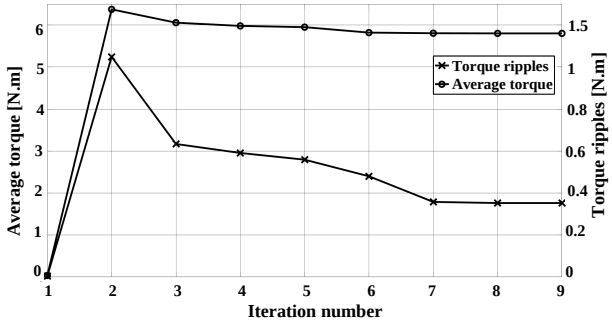

Figure 6.18: The motor torque ripples and mean torque at the different iterations of the linesearch-based GO

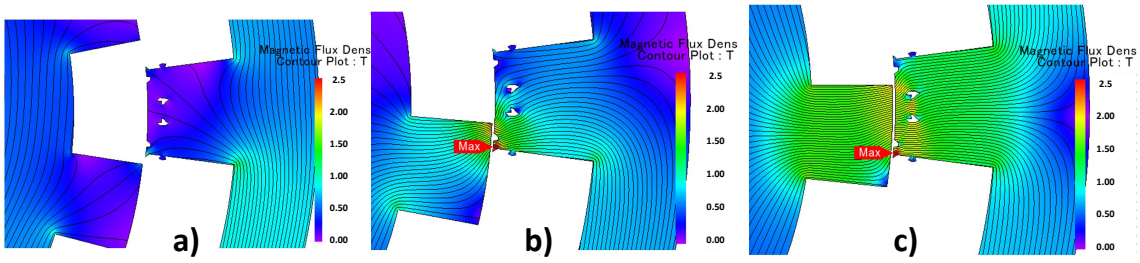

Figure 6.19: The Flux density contour plot and the flux density lines of the design shown in Figure 6.17 at three positions of one of the phases excitation: a) at the turn-on instant of phase1, b) at the at the middle of the duration of phase A excitation, c) at the turn-off instant of phase A

Table 6.4: Comparison between the GO of the Stator Teeth of the 6/14 SRM with the Linesearch-Based and annealing-based ON/OFF Optimization Methods.

	Linesearchbased ON/OFF method	Annealing-based ON/OFF method
Mean torque (N.m)	5.8	5.45
Torque ripples %	6.074	7.1
Iron loss (stator +rotor)	111.23(W)	106.4(W)
Number of iterations	9	24
Optimization time (mins)	3205	7817

A comparison between the results of GO using the linesearch-based and conventional ON/OFF optimization methods is shown in Table 6.4. The linesearch-based GO also reaches a better solution than the one reached by annealing-based ON/OFF GO. The mean torque is increased by 0.35 N.m and the torque ripple is decreased by $\sim 1\%$, as indicated in Table 6.4. The dynamic torque for one electrical cycle of the final designs based on the two methods is shown in Figure 6.21.

The linesearch-based ON/OFFGO only required 9 iterations to converge to the local optimal solution as compared to 24 iterations with the annealing-based ON/OFFGO, as illustrated in Figure 6.21. As shown in Table 6.4, the linesearchbased GO reduces the optimization time by $\sim 60\%$ as compared to the time required for the annealing-based ON/OFF GO.

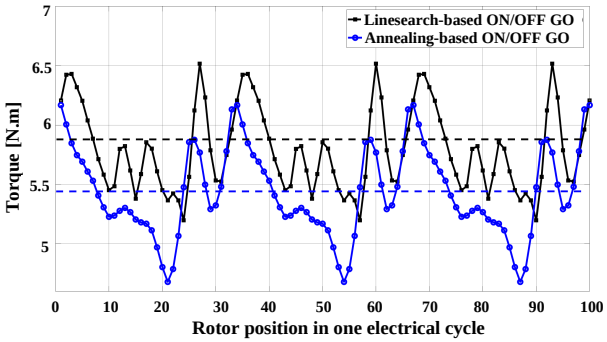

Figure 6.20: A comparison of the dynamic torque of the final design for one electrical cycle using the proposed line search and the annealing-based method for GO.

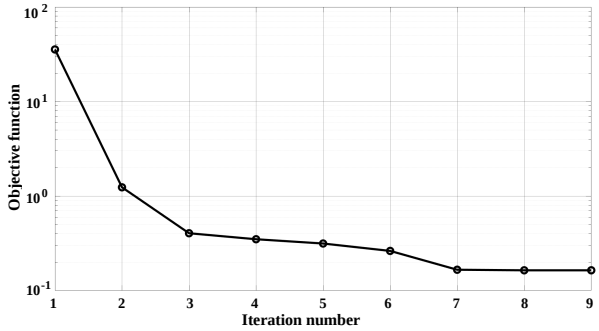

Figure 6.21: The objective function of value at the different iterations of the linesearch-based ON/OFF GO.

6.3.2 Topology optimization of the stator design domain

Topology optimization is accomplished using the proposed linesearch-based technique on the design domain presented in Figure 5.5.b. The TO results based on the proposed method is compared to the TO results using the annealing-based technique.

Figure 6.22 presents the torque ripple and the mean torque of the motor at the different iterations of the TO based on the proposed linesearch-based ON/OFF approach. Figure 6.23 Shows the final design of one of the stator teeth after TO. The figure shows that TO requires more iterations to converge to the final solution than the GO with the same method. The TO with the proposed method is able to achieve mean torque of 5.74 and r.m.s Torque ripple of 0.298 N.m or 5.19%. The flux density lines and the contour plot of the design at three different rotor positions corresponding to three different instants of the excitation of phase1 is shown in Figure 6.24. It can be concluded from Figure 6.24 that the optimization algorithm tries to introduce flux barriers in the middle of the stator teeth to guide the flux in a way to reduce the torque ripples.

The linesearch-based TO requires only 14 iterations to converge to the local optimal solution as compared to 24 iterations with the annealing-based TO optimization (See Figure 6.11). Both optimization methods converge to almost the same mean torque as indicated in Table 6.5. However, the annealing-based TO achieves a lower torque ripple as shown inTable 6.5 and Figure 6.25. The advantage of the linesearch-based method is the shorter simulation time compared to the annealing-based technique. The newly proposed technique reduces the optimization time by 49.3% as illustrated in Table 6.5.

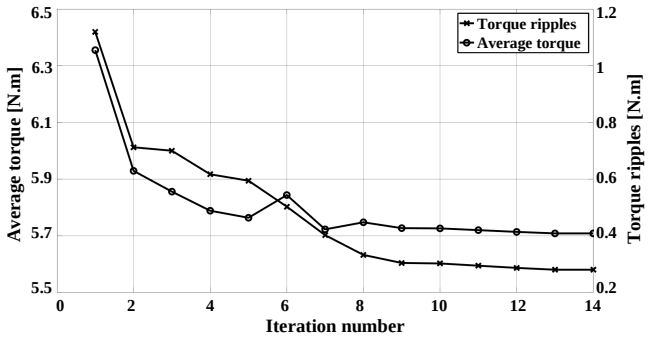

Figure 6.22: The motor torque ripples and mean torque at the different optimization iterations with the linesearch-based TO.

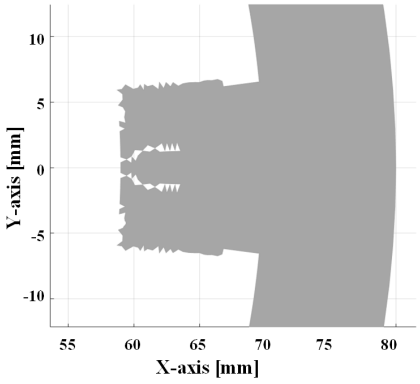

Figure 6.23: The final design of the stator teeth with the linesearch-based TO.

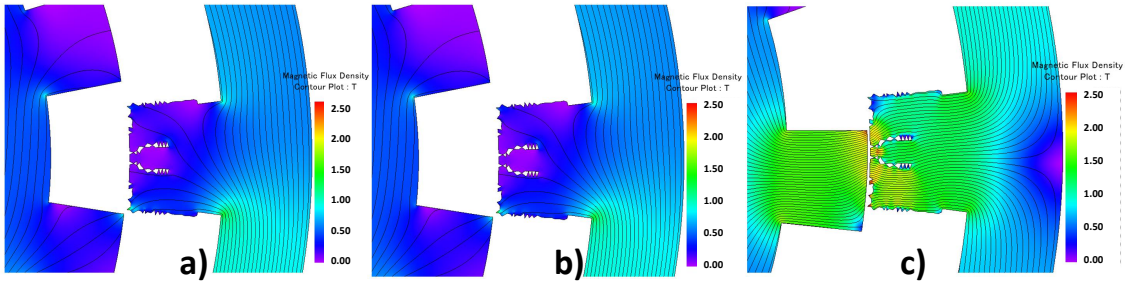

Figure 6.24: The Flux density contour plot and the flux density lines of the design shown in Figure 6.23 at three positions of one of the phases excitation: a) at the turn-on instant of phase1, b) at the at the middle of the duration of phase A excitation, c) at the turn-off instant of phase A.

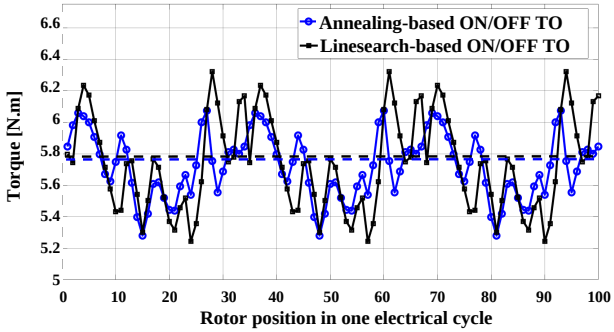

Figure 6.25: A comparison of the dynamic torque of the final design for one electrical cycle between the annealing-based and linesearch-based ON/OFF topology optimizations.

Table 6.5: Comparison between the TO of the stator teeth of the 6/14 SRM with the linesearch-based and annealing-based ON/OFF optimization methods

	Linesearch based ON/OFF method	Annealing-based ON/OFF method
Mean torque (N.m)	5.74	5.725
Torque ripples %	5.19	3.6
Number of iterations	14	24
Optimization time (mins)	5120	10110
Iron loss (stator+rotor)	102.5 W	98.7 W

The design shown in Figure 6.23 can be realized experimentally by using 3D printing of the Somaloy 700HR3P material, as indicated in [230, 231, 235, 236]. If silicon steel material is used for this design and a conventional manufacturing approach is used, such as laser cutting or stamping of the silicon steel sheets, the shape shown in Figure 6.23 should be smoothed further. Figure 6.26 shows the smoothed design of the stator teeth shown in Figure 6.23. In the smoothed design shown in Figure 6.26, the sharp edges shown in the original design were replaced by oval and circular ships, which will be feasible if the laser cutting or stamping process is considered for manufacturing that design.

However, the smoothing process shifts the design from the optimal point and affect the machine performance, as shown in the torque waveforms comparison in Figure 6.27. The average torque of the design after the smoothing process shown in Figure 6.23 is 5.54 N.m, reduced by 3.4%, and the torque ripple is 9.09%, increased by 3.9%.

Based on the linesearch-based topology and generative optimization results, the initial topology affects the final optimized structure of the design domain, as indicated in Figure 6.23 and Figure 6.17. However, the difference between the mean torque and the torque ripple between the topology and generative optimization is relatively small, as indicated in Table 6.6. Also, the objective function converges to almost the same value but with different steps, as shown in Figure 6.28.

The only significant difference between the topology and generative optimization based on the proposed method is that the GO saves 34.4% of the optimization time required for the TO.

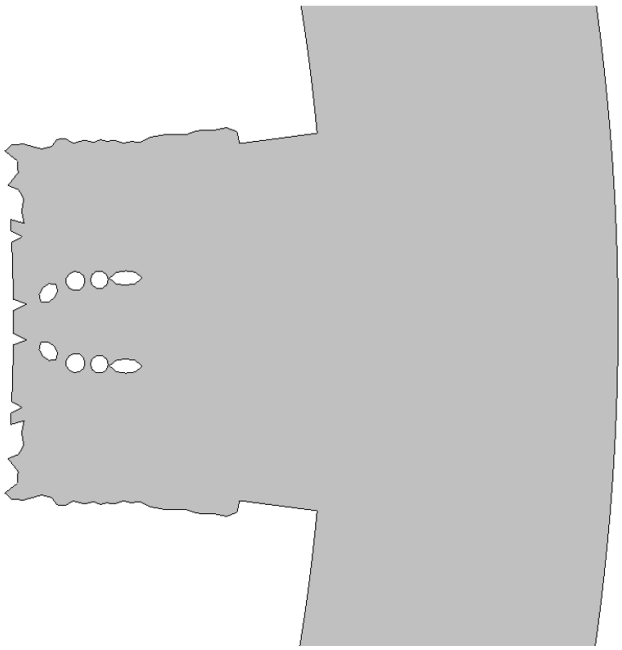

Figure 6.26: Smoothed design of the stator teeth shown in Figure 6.23.

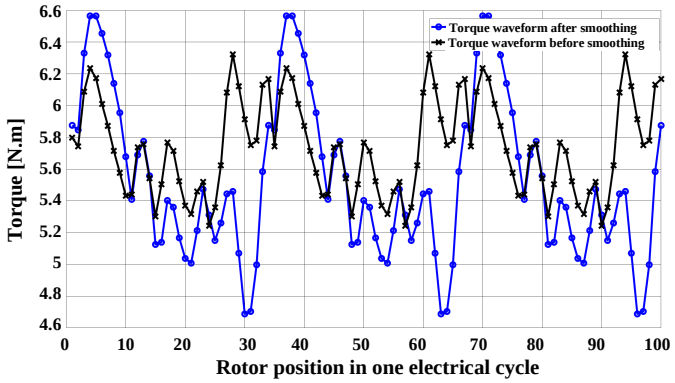

Figure 6.27: A comparison of the dynamic torque of the final design for one electrical cycle between the original optimized design shown in Figure 6.23 before smoothing and the design after smoothing shown in Figure 6.26.

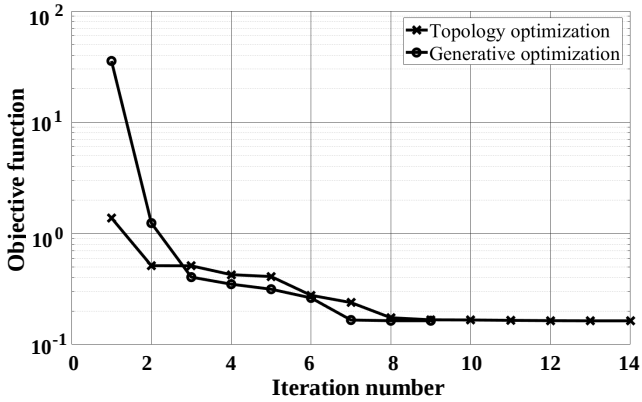

Figure 6.28: The objective function of value at the different iterations of the line-search-based ON/OFF generative and topology optimizations.

Table 6.6: Comparison between the GO and TO with the linesearch based ON/OFF methods.

Method	Generative optimization	Topology optimization
Mean torque (N.m)	5.8	5.74
Torque ripples %	6.074	5.19
Number of iterations	9	14
Optimization time (mins)	3205	4890
Iron loss (stator+rotor)	111.23 W	102.5 W

6.4 Generative optimization of the Rotor Design Domain

It is evident from the simulation results that the proposed linesearch-based optimization technique outperforms the conventional ON/OFF optimization based on the annealing technique. The ON/OFF optimization based on the linesearch method reduces the optimization time by almost 60% for the GO and 50% for the TO as compared to the time required for the conventional annealing-based method. Also, the final optimlized design shows a better performance than the one optimized by the conventional method, as shown in Sections 6.2 and 6.3.

In this case study, the rotor teeth of the rotor region are selected as the design domain for the GO based on the newly proposed linesearch-based ON/OFF method and the annealing-based ON/OFF method. The design domain of the rotor region is illustrated in Figure 6.29, which consists of 446 elements for each rotor tooth. The total number of elements for all 14 teeth is 6244 elements.

The objective function of the optimization is the same one used for the stator design domain optimization given by (22). The GO using the proposed linesearch-based optimization method reaches a mean torque of 5.72 N.m and torque ripples of $0.529\ \mathrm{N}\cdot\mathrm{m}(9.25\%)$ after seven optimization iterations, as indicated in Figure 6.30. The final design of the rotor teeth based on that method is presented in Figure 6.31.

The Flux density contour plot and the flux density in on of the rotor teeth corresponding to phase 1 at three different instants of phase1 excitation, at the turn-on instant of phase1, at the middle of phase1 excitation, and at the turn-off instants of phase1, are presented in Figure 6.32.

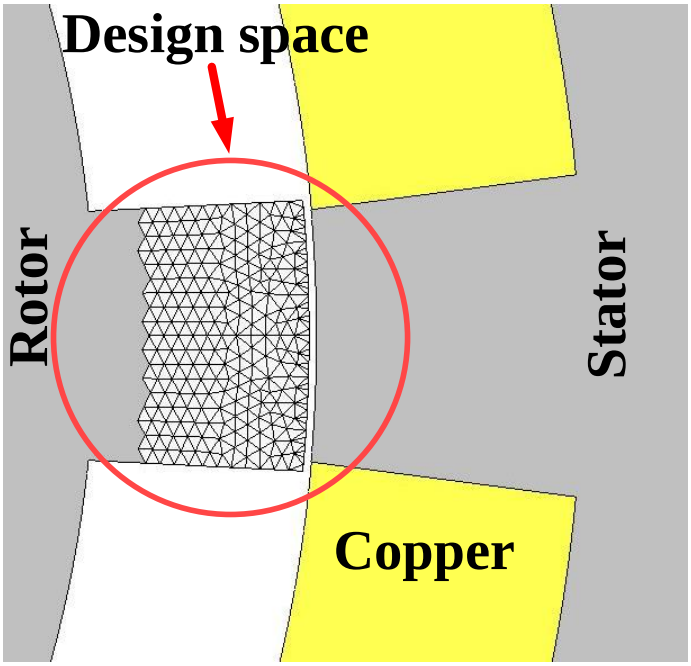

Figure 6.29: One tooth of 14 teeth rotor design domain for GO.

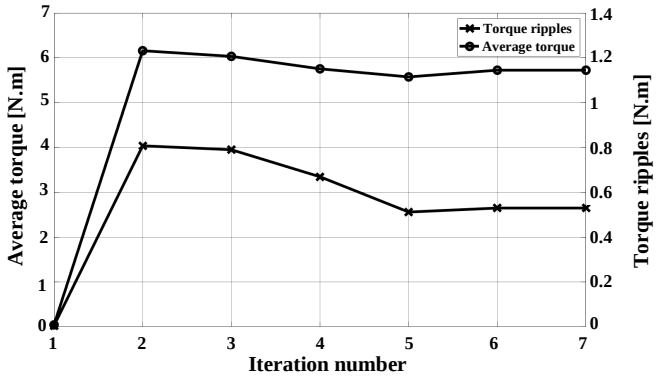

Figure 6.30: The motor torque ripples and mean torque at the different optimization iterations of the GO using the linesearch-based ON/OFF method of the rotor teeth region.

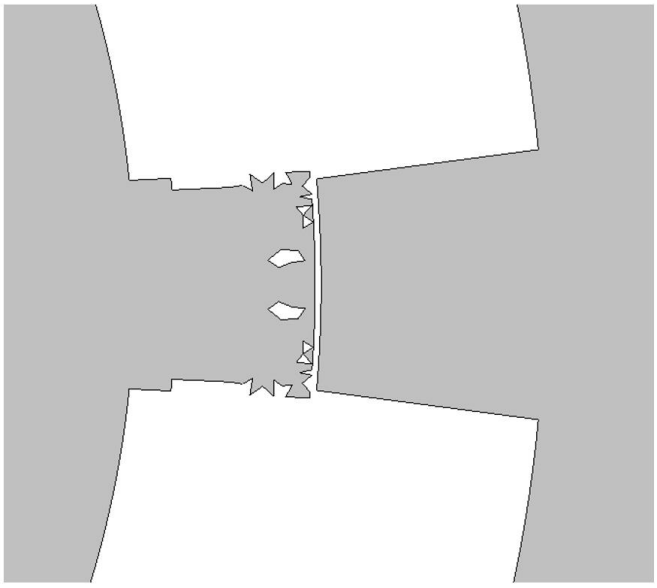

Figure 6.31: The shape of one rotor tooth after the GO of the rotor teeth with the linesearch-based ON/OFF optimization method.

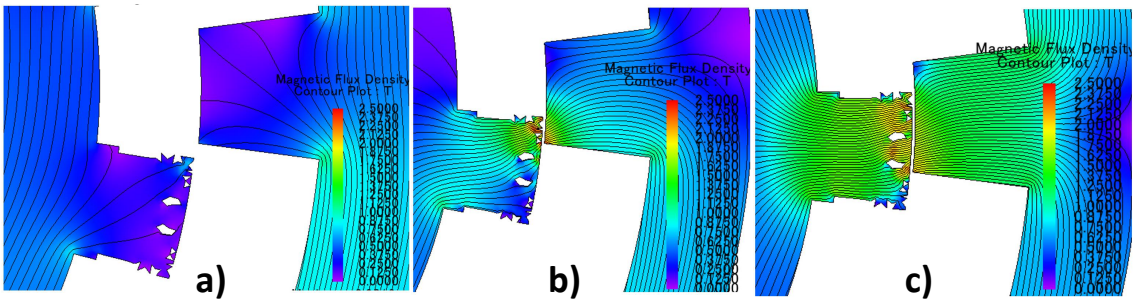

Figure 6.32: The Flux density contour plot and the flux density lines of the design shown in Figure 6.31 at three positions of one of the phases excitation: a) at the turn-on instant of phase1, b) at the at the middle of the duration of phase A excitation, c) at the turn-off instant of phase A.

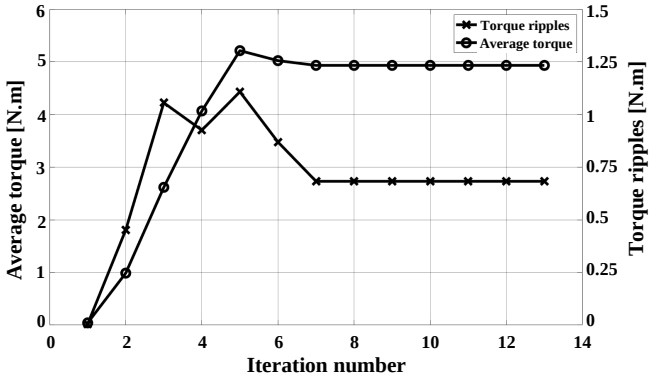

Figure 6.33: The motor torque ripples and mean torque at the different optimization iterations of the GO using the annealing-based ON/OFF method of the rotor teeth region.

On the other hand, the GO using the annealing-based ON/OFF method on the same rotor design domain reaches a mean torque of 4.93 N.m and torque ripples of 0.683 N.m (13.84%). The optimization process stops after 13 optimization iterations as presented in Figure 6.33. The final design of the generative optimization using the annealingbased ON/OFF technique is presented in Figure 6.34. The Flux density contour plot and the flux density in one of the rotor teeth corresponding to phase 1 at three different instants of phase 1 excitation, at the turn-on instant of phase 1 , at the middle of phasel excitation, and at the turn-off instants of phase1, are presented in Figure 6.35. The voids that the optimization process introduced in the design create flux barriers to direct the flux lines if compared to the original design shown in Figure 6.7.

Figure 6.36 illustrates the dynamic torque of the final design for each method for one electrical cycle. As clear from Figure 6.37, the proposed linesearch-based method is able to enhance the motor mean torque and torque ripple better than the annealing-based method. Also, it is clear from the objective function results

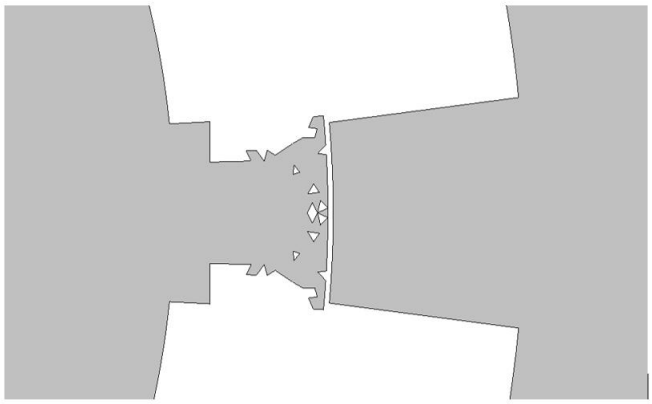

Figure 6.34: The shape of one rotor teeth after the GO of the rotor teeth with the annealing-based ON/OFF optimization method.

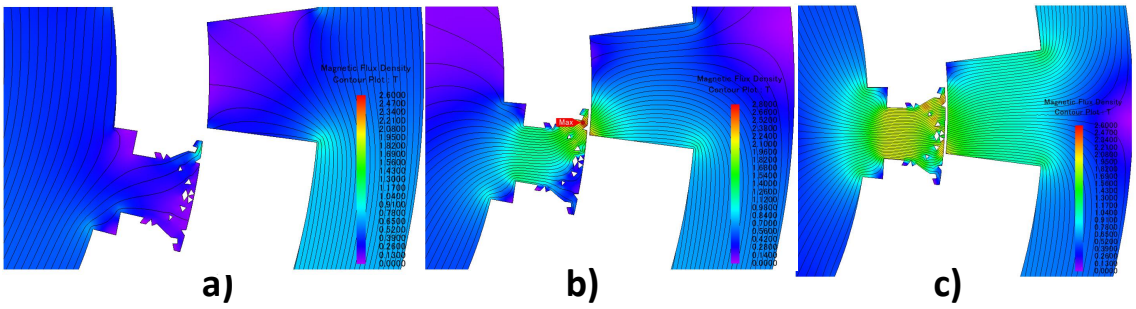

Figure 6.35: The Flux density contour plot and the flux density lines of the design shown in Figure 6.34 at three positions of one of the phases excitation: a) at the turn-on instant of phase1, b) at the at the middle of the duration of phase A excitation, c) at the turn-off instant of phase A.

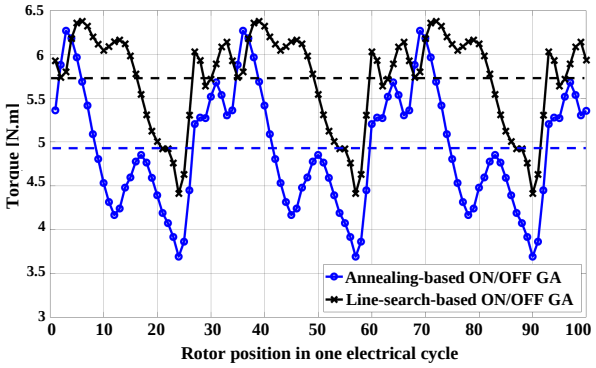

Figure 6.36: A comparison of dynamic torque of the final designs of both methods for one electrical cycle.

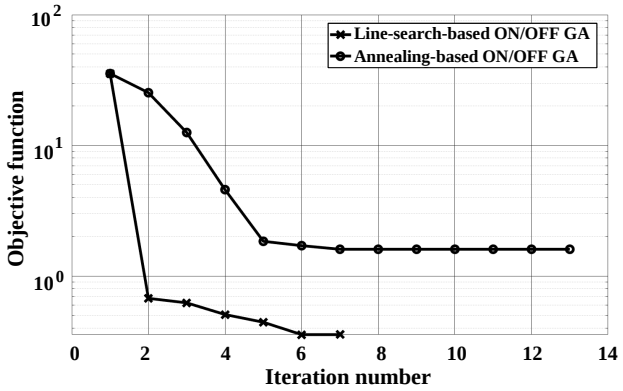

Figure 6.37: The objective function of value at the different iterations of the generative optimizations based on the linesearch-based ON/OFF method and the conventional ON/OFF method.

shown in Figure 6.37 that fast convergence characterizes the GO using the proposed linesearch-based ON/OFF optimization method as compared to the GO based on the annealing-based ON/OFF optimization method.

As discussed before, the main manufacturing technique for realizing these designs is additive manufacturing by 3D printing the Somaloy 700HR 3P material, as presented in [230, 231]. However, if traditional manufacturing approaches, such as laser cutting or lamination stamping, are used, the material should change to non-oriented

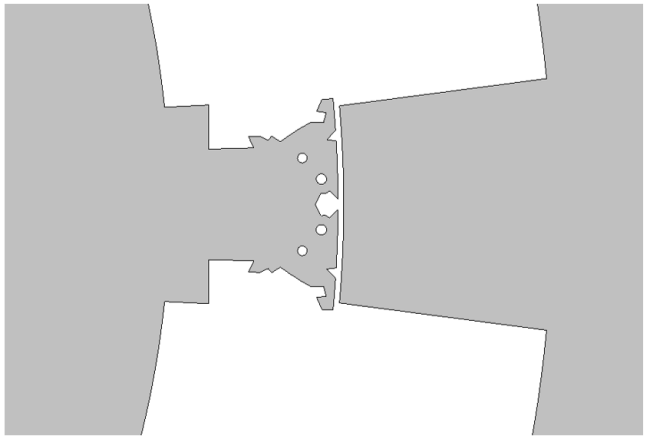

Figure 6.38: The shape of one rotor teeth after smoothing the design space shown in Figure 6.34

silicon steel lamination or cobalt steel lamination. The material change and the smoothing of the design required for the classic manufacturing approach will change the optimal solution achieved through the ON/OFF optimization. To show the effect of smoothing the design, the final design shown in Figure 6.34 is smoothed as presented in Figure 6.38 . It is clear from Figure 6.39 that the aggressive smoothing of the design shifts the design performance to a point with lower average torque and higher torque ripples.

6.5 Summary

This chapter presents a new linesearch-based ON/OFF optimization algorithm for topology and generative optimization of switched reluctance machines. The method reduced the optimization time compared to the conventional annealing-based ON/OFF algorithm for both topology and generative optimization. The proposed linesearch-based ON/OFF algorithm and the conventional annealing-based ON/OFF algorithm

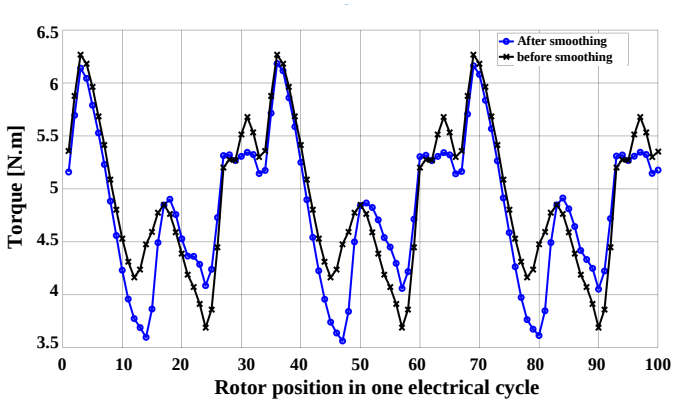

Figure 6.39: A comparison of the dynamic torque of the final design for one electrical cycle between the original optimized design shown in Figure 6.34 before smoothing and the design after smoothing shown in Figure 6.38

were used for topology and generative optimization of two different design domains of a 6/14 SRM configuration. The proposed method was shown to reduce the optimization time by around 60% for the generative optimization and around 50% for the topology optimization as compared to the conventional annealing-based ON/OFF method for the stator design domain. Also, the optimization time using the proposed method was reduced by around 40% for the generative optimization as compared to the conventional annealing-based ON/OFF method for the rotor design domain. As shown in the paper, the proposed method also outperforms the conventional annealing-based ON/OFF method in the final optimized design performance. The new approach was demonstrated for both topology and generative optimization of both the stator and rotor of SRMs. The topology and the generative optimizations with the proposed linesearch-based method converged to almost the same objective function value but with different final solution designs. As the proposed method is a gradient-based method, the adjoint sensitivities were utilized to calculate the gradient of the objective function with respect to the reluctivity of all elements of the design

domain in this research.

Chapter 7

A New Technique for Radial Force Calculation Time Reduction for the Optimization Process of SRMs

This chapter introduces a new technique for reducing the time of calculating radial force density waves of switched reluctance machines (SRMs). The method is based on the finite element (FE) simulation of a fraction of an electrical cycle. The new approach shows that a significant time reduction is achieved as compared to the time required for stator radial force density and the rotor tangential force calculation based on the one mechanical cycle simulation method. As the switched reluctance motors introduce new challenges in aspects such as acoustic noise, vibrations, and torque ripples, the method introduced in this paper will help reduce the time of the optimization process of switched reluctance machines in the design stage to improve the machine performance. The proposed method is applied to radial flux switched reluctance machines. Three different topologies were used to show the effectiveness of this technique in different force components with minimal error as compared to the benchmark method based on the FE simulation of one mechanical cycle.

The optimization process to reduce the acoustic noise and vibration of SRMs requires the evaluations of the radial force and tangential force density components at each iteration of the process. The evaluation process is usually done based on Finite element analysis (FEA) simulation of one mechanical cycle to obtain stator and rotor force density waves components [24]. In [85], the study shows that the stator force density wave components can be estimated based on the FEA simulation of one electrical cycle. However, this method cannot be applied to the rotor force density components as the FEA simulation of one mechanical cycle is required to get the accurate rotor force density components. This point is illustrated throughout this paper.

7.1 Conventional Approaches of Stator Radial Force Density Components Calculation

This section reviews the methods of stator force decomposition illustrated in the literature. The radial force density is usually calculated on the stator structure of the SRMs to evaluate and reduce the machine acoustic noise and vibration. The radial force density spectrum is given by [20]:

$$\begin{cases} u = N_r \times N_{ph} \times j - N_r \times k \\ v = \frac{N_s}{N_{ph}} k \end{cases} \tag{7.1.1}$$

where u is the mechanical temporal order, v is the circumferential order, N_s is the number of stator teeth, N_r is the number of rotor teeth, N_{ph} is the number of the machine phases, and j and k are integer numbers [20]. As indicated in [20], the stator radial force density and tangential force density components have the same pattern which is given by (1). The discussion in this chapter will be limited to the stator radial force density decomposition. However, the same analysis can be used for the stator tangential force density decomposition as well.

Based on Equation (7.1.1), the greatest common division (GCD) of all the mechanical temporal orders of the radial force density acting on the stator structure is N_r as j and k are any integer numbers. This means that there are N_r radial force wave repetitions in each mechanical cycle. As the mechanical cycle consists of N_r electrical cycles, only one electric cycle is enough to find all the stator force density components in electric temporal order. The temporal order of the radial force density components based on one electrical cycle are then multiplied by N_r (the number of repetitions in

Table 7.1: Temporal Order of Part of The Radial Force Density Wave Components of a Three-Phase 6/14 SRM.

	J = −4	**J = −3**	**J = −2**	**J = −1**	**J = 0**	**J = 1**	**J = 2**	**J = 3**	**GCD**
K = −2	−140	−98	−56	−14	28	70	112	154	**14**
K = −1	−154	−112	−70	−28	14	56	98	140	
K = 0	−168	−126	−84	−42	0	42	84	126	
K = 1	−182	−140	−98	−56	−14	28	70	112	
K = 2	−196	−154	−112	−70	−28	14	56	98	

Table 7.2: Temporal Order of Part of The Radial Force Density Wave Components of a Three-Phase 6/4 SRM.

	J = −4	**J = −3**	**J = −2**	**J = −1**	**J = 0**	**J = 1**	**J = 2**	**J = 3**	**GCD**
K = −2	−40	−28	−16	−4	8	20	32	44	**4**
K = −1	−44	−32	−20	−8	4	16	28	40	
K = 0	−48	−36	−24	−12	0	12	24	36	
K = 1	−52	−40	−28	−16	−4	8	20	32	
K = 2	−56	−44	−32	−20	−8	4	16	28	

one mechanical cycle) to get the radial force density components represented in the mechanical temporal order.

Tables 7.1 and 7.2 show part of the stator radial force density wave components of a three-phase 6/14 SRM and a three-phase 6/4 SRM, respectively. As shown in these tables, the GCD of all the mechanical temporal orders is N_r which means that only one electrical cycle is required to find all the radial force density component of SRM if the structure of the machine is symmetric.

7.2 Fraction of an Electrical Cycle Method for Stator Radial Force Density Components Calculation

As discussed in the Section 7.1, the stator force density wave based on one electrical cycle of the SRMs FEA simulation can be used to get the accurate stator force density components. That leads to a significant amount of simulation time reduction equals to $(N_r - 1)$ times the computational time of the force density wave calculation based on the FEA simulation of one mechanical cycle.

However, by taking a closer look into the stator radial force density wave, it can be noticed that a further reduction in the required cycles can be achieved. Figure 7.1 shows a typical electromagnetic radial force density waveform acting on the stator structure of a three-phase 6/4 SRM for one electrical cycle. The electrical cycle in that Figure is divided into 100 rotor positions and the stator circumference, where the radial force density is calculated, is divided into 7770 points for this example. It can be noticed that the waveform is divided into three symmetrical temporal parts that are shifted in the circumferential direction (see Figure 7.1). These three parts are due to the three-phase machine structure. The number of the symmetrical temporal but shifted parts is equal to the number of machine phases. This means that if only one part is computed, the other two parts can be reproduced by shifting the calculated part in the circumferential direction with a proper shift angle. This assumption is valid if the machine structure is symmetrical. The symmetry of the machine is usually the assumption in the machine design stage, so this technique can be used to reduce the time of the design and optimization of the machine as a huge time can be saved.

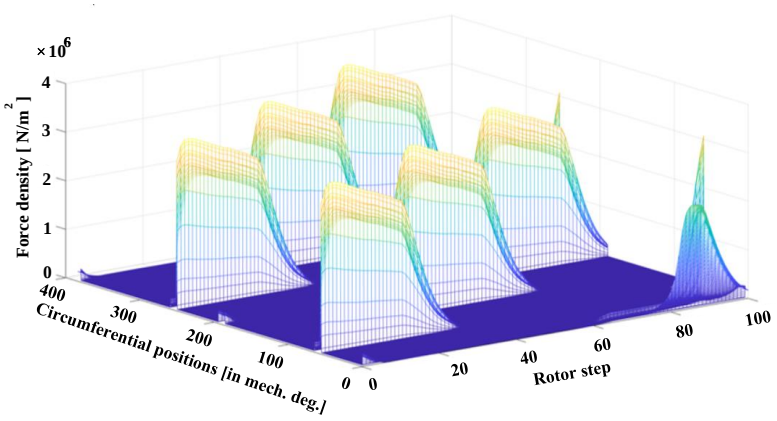

Figure 7.1: A typical radial force density waveform of a three-phase 6/4 SRM over one electric cycle (100 rotor steps) and the whole stator inner circumference.

Figure 7.2 shows a contour plot of the radial force density wave shown in Figure 7.1. It is clear from the contour plot that the radial force density wave is divided into three parts, and each part is shifted by a certain mechanical circumferential angle on the stator circumference. To illustrate that, a graphical representation of the radial force density for one electrical cycle of the three-phase 6/4 SRM configuration is presented in Figure 7.3. The hatched cells in the Figure represent that there is a higher value of the force density at that circumferential position compared to the white cells. The number of the hatched cells shown in the Figure indicated the number of the phase excited at the corresponding rotor position. It can be concluded from the contour plot in Figure 7.2 and the graphical representation in Figure 7.3 that by moving the excitation from one phase to another phase, the radial force density waveform is shifted circumferentially by 60 mechanical degrees on the stator circumference in the direction of phase excitation or 120 mechanical degrees on the stator circumference in the direction of rotor rotation.

For a three-phase 6/4SRM, 1/3 of an electrical cycle is required to reproduce the

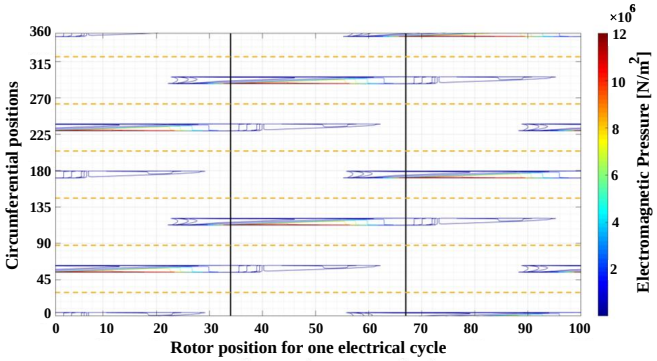

Figure 7.2: A contour plot of the radial force density waveform shown in Figure 7.1.

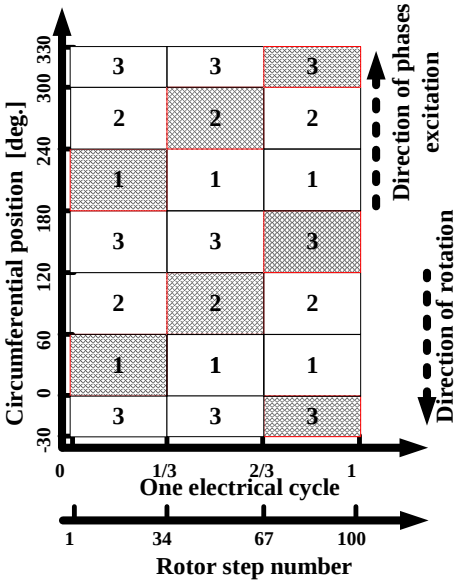

Figure 7.3: A graphical representation of the radial force density waveform regions.

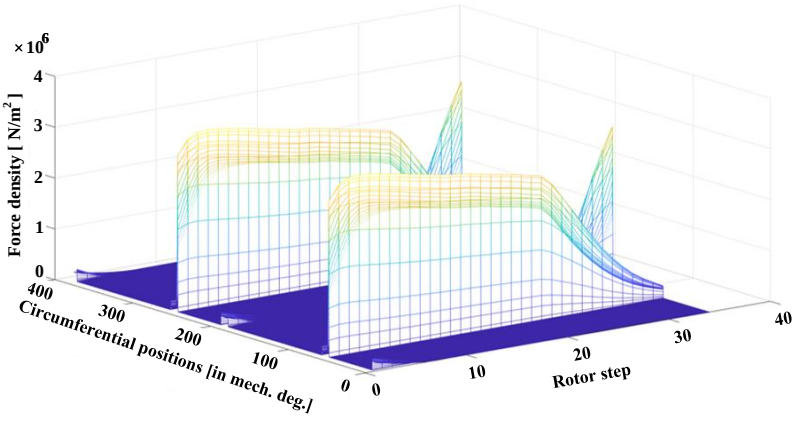

Figure 7.4: The stator radial force density wave of the three-phase 6/4 SRM over 1/3 electric cycle (37 rotor steps).

radial force density wave, shown in Figure 7.4 . The other two parts of the radial force density wave can be reproduced by shifting the calculated part by 60 mechanical degrees on the stator circumference in the direction of phases excitation or 120 mechanical degrees on the stator circumference in the direction of rotor rotation, as illustrated in Figure 7.5. As shown in Figure 7.5, any three-phase six teeth configuration will require the same shift. The required shift should be changed if the number of stator teeth changes as shown in Figure 7.6 for a three-phase with 12 teeth SRM.

The required shift based on the machine slot/pole configuration can be estimated from the following equation:

$$\begin{cases} \theta_{\text{shift}} = \frac{360}{N_s} \text{ in the direction of pahse excitation, or} \\ \theta_{\text{shift}} = \frac{360}{N_s}\,(N_{ph}-1) \text{ in the direction of rotation} \end{cases} \tag{7.2.1}$$

In the simulation of the three-phase 6/4SRM shown in Figure 7.2 and Figure 7.1, the stator inner circumference is divided to 7770 equal-angle points. That means that in order to shift the wave 60 degrees on the stator circumference (in the direction of

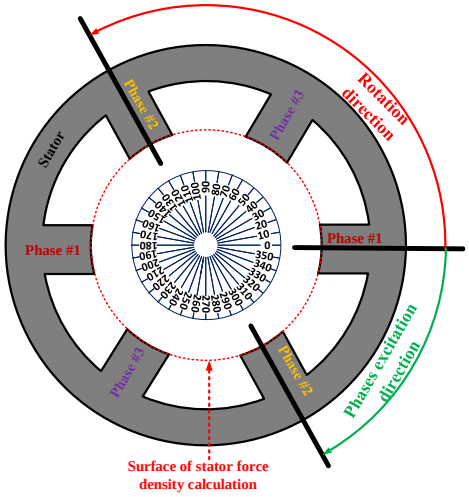

Figure 7.5: The amount of shift applied to regenerate the stator force density for a three-phase with six teeth SRMs configurations(such as 6/14 , 6/4 SRMs) Note: phase excitation sequence is (Phase1, Phase2, then Phase3)

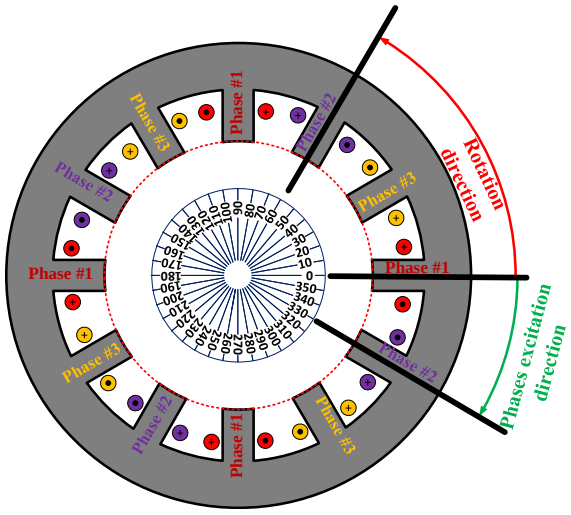

Figure 7.6: The amount of shift applied to regenerate the stator force for a three-phase with 12 teeth SRMs configurations (such as 12/8 or 12/16 SRMs) Note: phase excitation sequence is (Phase1, Phase3, then Phase2).

phase excitation), the 1/3 electrical cycle wave should be shifted 1295 points. To shift the wave by 120 degrees on the stator circumference, it should be shifted by 2590 point. To ensure an integer number results from the shifting process, the stator inner circumference, where the stator force is calculated, should be divided into a number of points equal to $N_r \times N_{ph} \times I$, where I is an integer number.

Based on this proposed method, the number of FEA simulation points required for obtaining the stator radial force density waves of SRMs is reduced significantly. In general, the stator radial force density wave of a certain SRM configuration can be reproduced by only simulating $1/N_{ph}$ of an electrical cycle of the machine, and the other $(N_{ph} - 1)$ parts of the stator radial force density wave can be produced by shifting the calculated part circumferentially with a shift angle θ_{shift} which can be calculated based on Equation (7.1.1). Numerical examples to compare the one mechanical cycle method, the one electrical cycle method and the proposed fraction of an electrical cycle method of stator radial force density wave generation and decomposition are presented in Section 7.3.

7.3 Numerical Examples of Stator radial Force Density Waves Generation and Decomposition Methods

In this section, the complete radial force density wave is simulated for one mechanical cycle, for one electrical cycle, and regenerated using a fraction of an electrical cycle method by the FE simulation of $1/N_{ph}$ of an electrical cycle. The radial force density waves of three different SRM configurations are obtained based on the three methods

and then decomposed with a two-dimensional fast fourier transform (2D FFT) to calculate the stator radial force density harmonic spectrum. The harmonic spectrum based on one electrical cycle and the reduced data method introduced in this paper are compared to the harmonic spectrum based on the simulation of one mechanical cycle as a benchmark method.

7.3.1 Numerical Examples of Stator radial Force Density Waves Generation and Decomposition Methods

The radial force density wave for three different configurations of SRMs, three-phase 6/4 SRM, three-phase 6/14 SRM, and four-phase 8/6 SRM, are calculated based on the simulation of one complete mechanical cycle and one complete electrical cycle to evaluate the effectiveness of using one electrical cycle to get all the radial force density components.

The radial force density wave of a 6/4 SRM is obtained based on one mechanical cycle and one electrical cycle. The two radial force density waves based on the two methods are then decomposed to the wave components with 2D FFT decomposition. After obtaining the radial force density spectrum based on the one electrical cycle method, the temporal order of the spectrum is multiplied by 6 (the number of rotor teeth) to represent the spectrum in the mechanical temporal order, as illustrated in Section 7.1. The stator radial force density waves harmonics spectrum for the one mechanical cycle method and the one electrical cycle method are presented in Figure 7.7 and Figure 7.8, respectively.

The relative error of the stator radial force density harmonics spectrum calculated based on the one electrical cycle method with respect to the spectrum calculated based

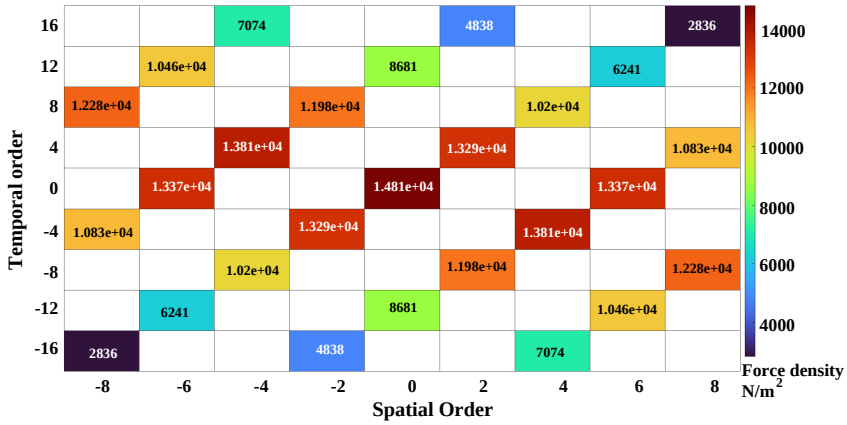

Figure 7.7: The radial force density of a 6/4 SRM based on a complete mechanical cycle.

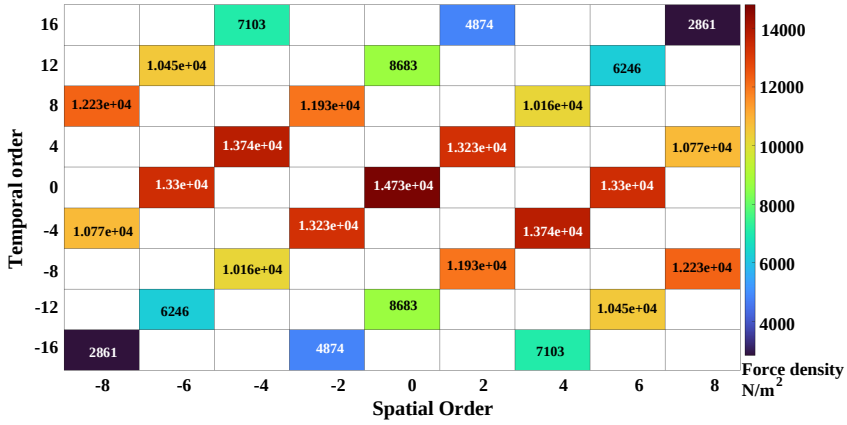

Figure 7.8: The radial force density on the stator of a 6/4 SRM based on a complete electrical cycle.

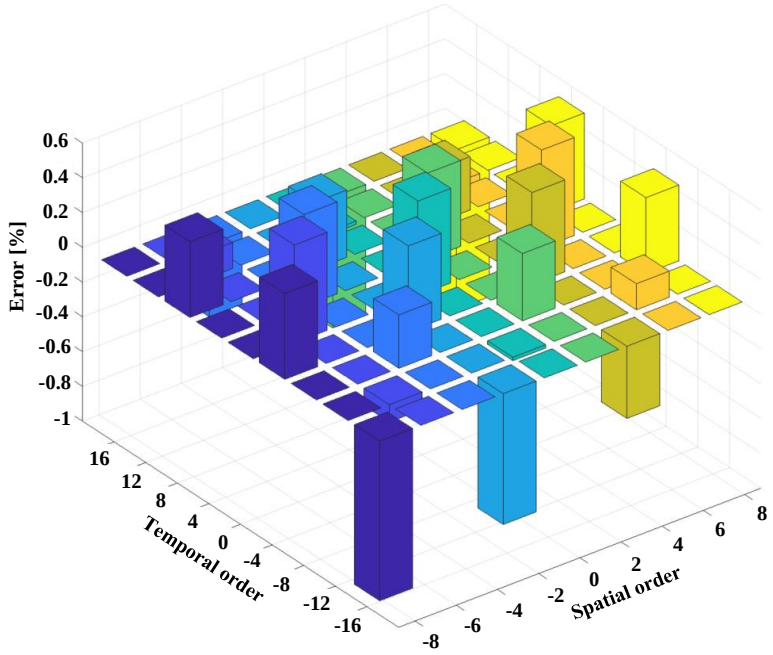

Figure 7.9: The error of stator radial force density spectrum calculated based on the one electrical cycle method with respect to the spectrum calculated based on the one mechanical cycle method for the case study three-phase 6/4 SRM.

on the one mechanical cycle method is shown in Figure 7.9. It can be noticed that one electrical cycle can be effectively used for the decomposition of the radial force density components of the 6/4 SRM to get its harmonics spectrum with a reduced simulation time and simulation effort. Figure 7.9 shows that the maximum error between the two methods for the displayed spectrum is less than 1%.

Figure 7.10 shows the stator radial force density harmonics spectrum of a three-phase 6/14 SRM calculated based on the FEA simulation of one mechanical cycle. That machine's radial force density spectrum is then obtained based on the one electrical cycle method. The error of the stator radial force density harmonics spectrum calculated based on the one electrical cycle method with respect to the spectrum calculated based on the one mechanical cycle method is then calculated (see Figure 7.11).

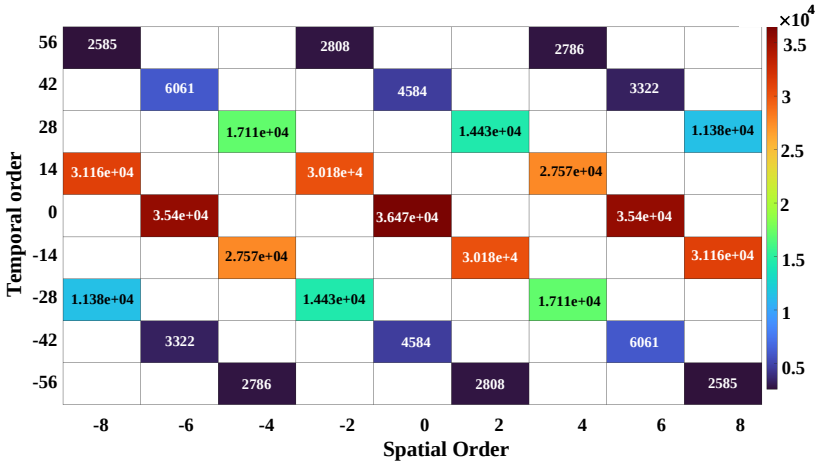

Figure 7.10: The stator radial force density components of a 6/14 SRM based on a complete mechanical cycle.

As shown in Figure 7.11, the maximum error of the radial force density based on the one electric cycle method with respect to one mechanical cycle method for the case study three-phase 6/14 SRM on the displayed spectrum is about 1.8%.

The stator radial force density waveform is obtained for a third case study, four-phase 8/6 SRM, based on the simulation of one mechanical cycle and then the waveform is decomposed to the harmonic spectrum as shown in Figure 7.12. The stator radial force density harmonics spectrum is then calculated based on the radial force density waveform obtained using the one electrical cycle method. The error of the stator radial force density harmonics spectrum calculated based on the one electrical cycle method with respect to the spectrum calculated based on the one mechanical cycle method is then calculated as presented in Figure 7.13. As shown in Figure 7.13, the maximum error of the radial force density spectrum calculated based on the case study four-phase 8/6 SRM is less than 0.6%.

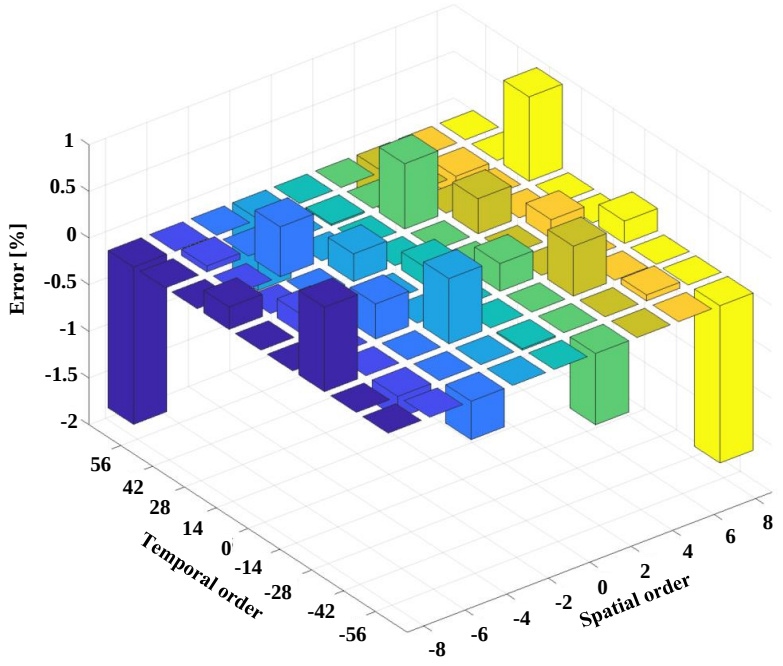

Figure 7.11: The error of stator radial force density spectrum calculated based on the one electrical cycle method with respect to the spectrum calculated based on the one mechanical cycle method for the case study three-phase 6/14 SRM.

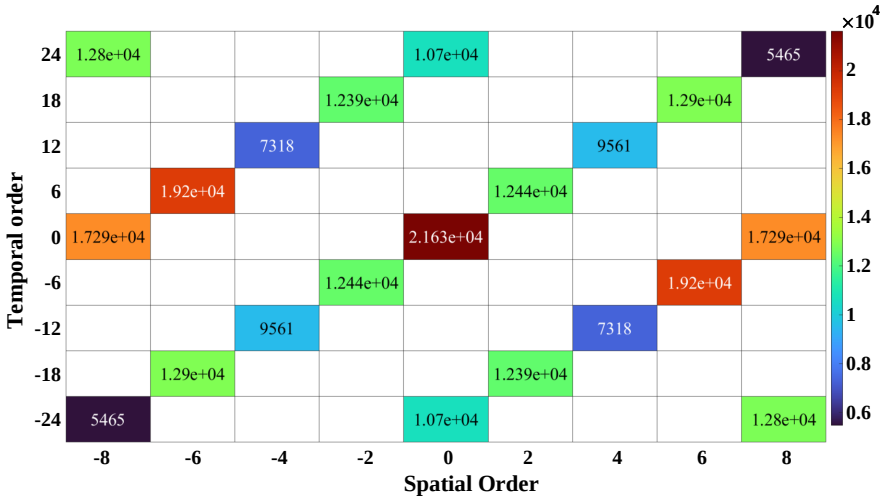

Figure 7.12: The stator radial force density components of a four-phase 8/6 SRM based on a complete mechanical cycle.

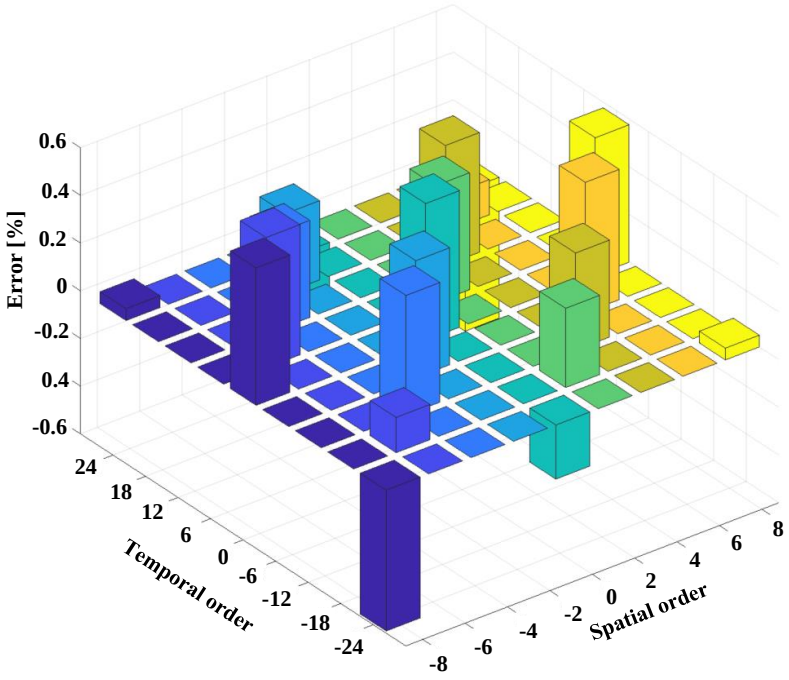

Figure 7.13: The error of stator radial force density spectrum calculated based on the one electrical cycle method with respect to the spectrum calculated based on the one mechanical cycle method for the case study four-phase 8/6 SRM.

7.3.2 Using fraction of an electrical cycle method for Stator radial Force Density Waves Generation and Decomposition

The stator radial force density waves for the three case studies SRM configurations mentioned before are regenerated based on the fraction of an electrical cycle method introduced in section 7.2. The regenerated stator radial force density waves for the three configurations are then decomposed into the radial force density harmonics spectrum, and the error is calculated with respect to the stator radial force density spectrum calculated based on the one mechanical cycle benchmark method.

A faction of an electrical cycle method is used to regenerated the stator radial force density wave for a three-phase 6/4 SRM. As indicated in section II, for the three-phase 6/4 SRM, only 1/3 of an electrical cycle is sufficient to generate one repetition of the stator radial force density wave. The three-phase 6/4 SRM is simulated for 1/3 of an electrical cycle (37 rotor steps are used in the simulation), as shown in Figure 7.4. Then, one electrical cycle of the stator radial force density of the machine is generated based on the simulated part of the stator radial force density wave by shifting that part of the wave (see Figure 7.4) two times by 60 degrees mechanically on the stator circumference in the opposite direction to the rotor rotation. The regenerated wave represents one electrical cycle of the stator radial force density wave. The wave is then decomposed using 2D FFT, and the error is calculated for the stator radial force density spectrum estimated based on the proposed method with respect to the spectrum obtained by the benchmark one mechanical cycle method shown in Figure 7.7. As indicated in Figure 7.14, the maximum error of the displayed force spectrum for the fraction of an electrical cycle method for the three-phase 6/4 SRM

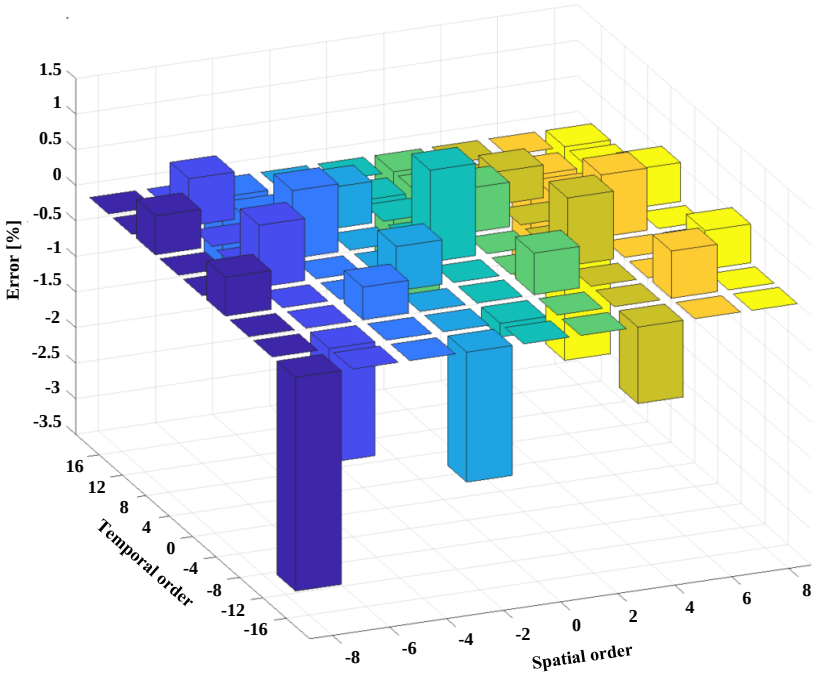

Figure 7.14: The error of stator radial force density spectrum calculated based on the proposed method with respect to the spectrum calculated based on the one mechanical cycle method for the case study three-phase 6/4 SRM

is less than 3.5%.

For the three-phase 6/4 SRM, the fraction of an electrical cycle method requires simulating the machine for 1/3 of an electrical cycle; however, the electrical cycle method requires the simulation of one electrical cycle, and the one mechanical cycle method requires the simulation of 4 electrical cycles. For the fractional cycle method, the machine is simulated for 34 rotor steps; however, the machine is simulated for 100 rotor positions for the one electrical cycle method and 397 rotor positions for the one mechanical cycle method. So, it is also clear that the calculation time required for the proposed method is 1/12 the time required for the one mechanical cycle method and 1/3 the time required for one electrical cycle method. Table 7.3 summarizes

Table 7.3: A comparison of the simulation time required and the maximum error for obtaining the stator radial force density wave spectrum of the case study three-phase 6/4 SRM for the three methods discussed in the paper.

	Based on one mechanical cycle (4 electrical cycles)	Based on one radial force repetition (one electrical cycle)	Fraction of an electrical cycle method (1/3 of an electrical cycle)
Time used for FEA	12 p.u.	3 p.u.	1 p.u.
Maximum error	0%	<1%	<3.5%

the comparison of the three methods for obtaining the stator radial force density wave components for the case study three-phase 6/4 SRM. The table shows the FEA simulation time and the maximum error in the displayed spectrum with respect to the one mechanical cycle benchmark method.

The proposed method is used to generate the stator radial force density wave for the case study three-phase 6/14 SRM. For the case study three-phase 6/14SRM, the maximum error of the method of fraction of an electrical cycle is less than 2.5% compared to the one mechanical cycle benchmark method, as illustrated Figure 7.15 .

The proposed approach for calculating the stator radial force density wave and its components reduces the calculation FEA simulation computational burden and time to (1/42) of the time required for the complete mechanical cycle method with a maximum error of less than 2.5%. Also, the method reduces the FEA simulation time and computational burden requirements to (1/3) of that of the one electrical cycle method. The summary of the FEA simulation time and the maximum error for each method with respect to the benchmark one mechanical cycle method in the displayed spectrum is summarized in Table 7.4.

The method is also used to generate the stator radial force density wave for the

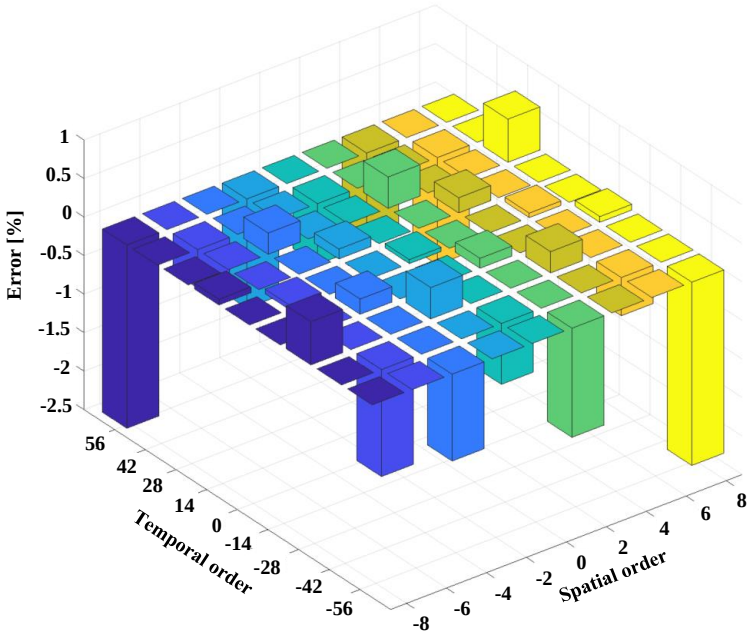

Figure 7.15: The error of stator radial force density spectrum calculated based on the proposed method with respect to the spectrum calculated based on the one mechanical cycle method for the case study three-phase 6/14 SRM

Table 7.4: A comparison of the simulation time required and the maximum error for obtaining the stator radial force density wave spectrum of the case study three-phase 6/14 SRM for the three methods discussed in the paper.

	Based on one mechanical cycle (14 electrical cycles)	Based on one radial force repetition (one electrical cycle)	Fraction of an electrical cycle method (1/3 of an electrical cycle)
Time used for FEA	42 p.u.	3 p.u.	1 p.u.
Maximum error	0%	<1.8%	<2.5%

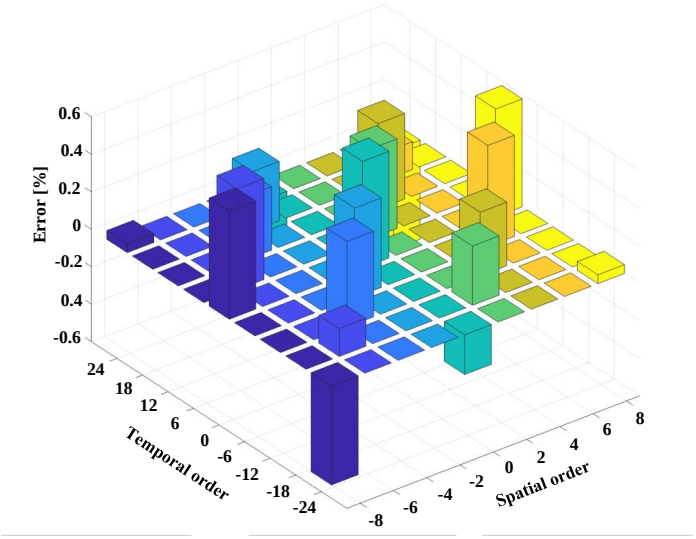

Figure 7.16: The error of stator radial force density spectrum calculated based on the proposed method with respect to the spectrum calculated based on the one mechanical cycle method for the case study four-phase 8/6 SRM

case study four-phase 8/6 SRM. For the case study machine, the maximum error of the method of fraction of an electrical cycle is less than 0.6% compared to the one mechanical cycle benchmark method, as illustrated in Figure 7.16.

The proposed method only required the machine to be simulated for 1/4 of an electrical cycle for the four-phase 8/6 SRM, as indicated in Section 7.2. The FEA simulation time and the maximum error for each method with respect to the benchmark one mechanical cycle method in the displayed spectrum is summarized in Table 7.5.

7.4 Summary

This chapter presents a new method of generating the stator radial force density wave based on the FE simulation of $1/N_{ph}$ of an electrical cycle. The method is

Table 7.5: Comparison of the simulation time required and the maximum error for obtaining the stator radial force density wave spectrum of the case study four-phase 8/6 SRM for the three methods discussed in the paper.

	Based on one mechanical cycle (6 electrical cycles)	Based on one radial force repetition (one electrical cycle)	Fraction of an electrical cycle method (1/4 of an electrical cycle)
Time used for FEA	24 p.u.	4 p.u.	1 p.u.
Maximum error	0%	<0.6%	<0.6%

able to generate the full stator radial force density wave by means of shifting the fractional cycle of the radial force density wave data based on FE simulation of $1/N_{ph}$ of an electrical cycle. By simulating $1/N_{ph}$ of an electrical cycle, the stator radial force density wave can be estimated by using the proper shift angle and the proper circumferential number shifts of the regenerated parts, as illustrated in this chapter. This results in a huge time and computational effort reduction compared to the existing method of using one electrical cycle and one mechanical cycle simulation.

As presented in the chapter, the amount of time reduction depends on the SRM configuration and the number of the machine's phases. The proposed method should be useful for geometry and topology optimizations of SRMs that target the mitigation of the stator radial force density for acoustic noise mitigation. Optimizing the SRMs design to mitigate acoustic noise requires many stator radial force density evaluations during the optimization process. So, any reduction in the time and the computational effort required to evaluate these components will result in a reduction on the overall optimization time.

Chapter 8

Topology and Generative Optimization of the 6/14 SRM for Stator Radial Force Reduction

8.1 Introduction

Nowadays, the performance improvement of Switch Reluctance Motors (SRMs) is attractive. Due to the continuously increasing price of rare-earth PM, extensive research focuses on removing or reducing the PMs from the design of electrical machines. Also, the absence of the windings and magnets from the rotor enables the SRM to run at high speed and elevated temperatures [12]. The winding of the stator of SRMs is usually a concentrated winding which reduces the assembly and maintenance cost of the machine. This type of winding also reduces the magnetic coupling between the machine's different phases, which improves the fault-tolerance capability of the machine [6]. SRMs have other important benefits, such as low cost and a simple and robust structure [12]. All the mentioned advantages of the SRMs make these types of machines a reliable choice for different applications [7–9].

However, the double salient structure of the SRMs creates challenges such as high acoustic noise, vibrations, and high-level machine torque ripples [12]. The radial forces acting on the stator structure are the primary cause of the acoustic noise of the machine [10, 28, 29]. However, the torque ripples are mainly due to the rotor tangential force harmonics.

In the inner rotor SRM configurations, the radial force acting on the stator is the main source of the machine's acoustic noise and vibrations [237]. In that case, the machine structure can be optimized to reduce the most significant radial force density components that excite the natural frequencies of main radial stator modes [85]. The radial force acting on the rotor structure in the external rotor SRMs configurations also contributes to that configuration's acoustic noise and vibrations [238]. In order to reduce the acoustic noise and vibrations of external rotor SRM configurations,

the rotor radial force density components and the stator tangential force density components should be minimized [238].

One of the ways to reduce the SRMs' acoustic noise and vibrations is through structural optimization by shifting the frequency of the critical circumferential vibration modes to avoid exciting these vibration modes with the force density components [87]. Another way is to reduce the amplitude of the critical force density components that can excite the vibration modes of the machine structure through electromagnetic optimization of the key design parameters of the machine [150, 239]. Optimizing the control parameters was used in the literature also to reduce the amplitude of the critical force density components of the machine for the same purpose [240, 241]. The reader can refer to [12, 85, 242] for more information about the interaction between the force components and the SRMs circumferential vibration modes.

In this chapter, Topology and generative optimization is used to design the stator and the rotor teeth of a 6/14 SRM to reduce the radial force components acting of the stator stricture.

The radial magnetic pressure in the airgap is shown in Equation (4.5.2), so the radial force density acting in the stator is given by:

$$F_r = \frac{1}{2\mu_0}\left(B_\rho^2 - B_\phi^2\right) \tag{8.1.1}$$

It can be concluded form Equations (4.5.5) and (8.1.1) that optimizing the design SRM to reduce the stator radial force without constraining the torque value will reduce the machine average torque significantly.

8.2 Optimization of the Rotor Design Domain for Radial Force Mitigation

In this section, the rotor design domain shown in Figure 6.29 is optimized to reduce one of the radial force density components of the three-phase 6/14 SRM case study machine. The radial force density component selected for the minimization process should be selected based on the model analysis and the vibration analysis of the stator structure. This part is not discussed in this work; however, after selecting the most dominant stator radial force density component that excites the stator structure, that component should be the optimization objective.

The objective function of the optimization process is adopted as follows in order to maintain the proper balance between reducing the redial force and keeping the torque at the desired value:

$$f_{\text{obj}} = \omega_f \frac{(f_r - w_p F_{\text{norm}})^2}{F_{\text{norm}}^2} + \omega_t \frac{\sum_{i=1}^{S_t} (t_i - T_{\text{ref}})^2}{T_{ref}}, \tag{8.2.1}$$

where f_{obj} is the objective function need to be minimized, f_r is the iteration's radial force density component, F_{norm} is the intial value of the radial force density component at iteration number 1, t_i is the torque at the ith rotor step, S_t is the number of rotor steps in one electrical cycle, T_{ref} is the target average torque, w_p is the target percentage of the radial force component, ω_f is the radial force optimization weight, and ω_t is the torque optimization weight. The summation of ω_f and ω_t should be always one. If the value of ω_f or ω_t is greater than 0.5, it means much more focus is given to radial force minimization or the average torque maximization, respectively.

Table 8.1: The objective function parameter of the rotor TO targeting the radial force and the average torque of the case study machine.

Parameter	**Value**
ω_f	0.5
ω_t	0.5
$F_{\mathbf{norm}}$	3.28e4
T_{ref}	6
w_p	0.8
S_t	100

8.2.1 Topology Optimization with The Linesearch-Based ON/OFF Method

In this subsection, the TO is applied to the rotor design space to minimize the objective function shown in equation (8.2.1). The optimization parameters of the objective is set as shown in Table 8.1.

The Figure 8.1 shows the machine after the TO of the rotor teeth using the linesearch-based ON/OFF optimization method. A closer look at the design of one of the rotor teeth after the TO is shown in Figure 8.2. Figure 8.3 shows the stator radial force of the optimized design. It can be concluded from the figure that the radial force density wave acting on the stator structure has been significantly reduced if compared to the radial force of the original design before optimization, see Figure 8.4.

Figures 8.5 and 8.6 show the amplitude radial force density component, the average torque, and the torque ripple through the TO iterations. Due to the torque constraint imposed in the objective function, Equation (8.2.1), the average torque and the torque ripple remain within acceptable ranges. As illustrated before, the average torque of the machine can not be maximized while minimizing the radial force. However, the torque could be constrained while the radial force density is reduced. The role of the optimization is to find a point that satisfies all the optimization objectives based on

Table 8.2: The change of the performance parameters of the machine through the optimization process.

	Original design	**Final design**	**Change %**
$F_r(4,2)$	3.28e3 N/m^2	2.415e3 N/m^2	-26.37%
T_{av}	6.46 N.m	5.81 N.m	-10.06%
T.R	1.09 N.m	0.4977 N.m	-54.34%

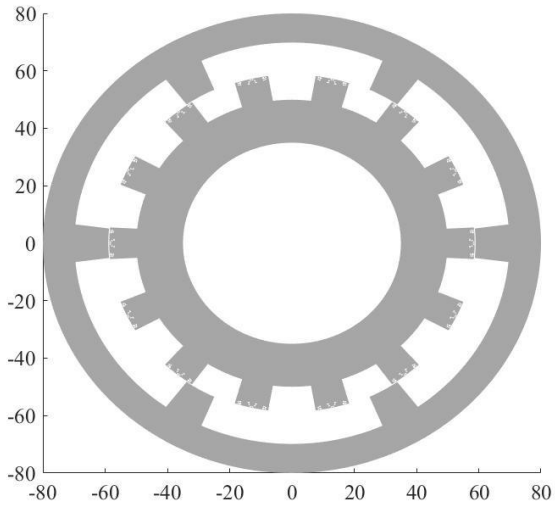

Figure 8.1: The 6/14 SRM machine after Generative optimization and before smoothing.

the assigned weights ω_f and ω_t in Equation (8.2.1).

Table 8.2 shows the change in the average torque, the torque ripple, and the amplitude redial force density component before and after the optimization process. As shown the Selected radial force density component and the torque ripples of the machine was reduced by 26.37% and 54.34% respectively, while the average torque reduced by 10%. It can be concluded from the table that the optimization process was trying to make the balance between reducing the selected radial force density component and keeping the torque around 6 N.m as defined by the objective function.

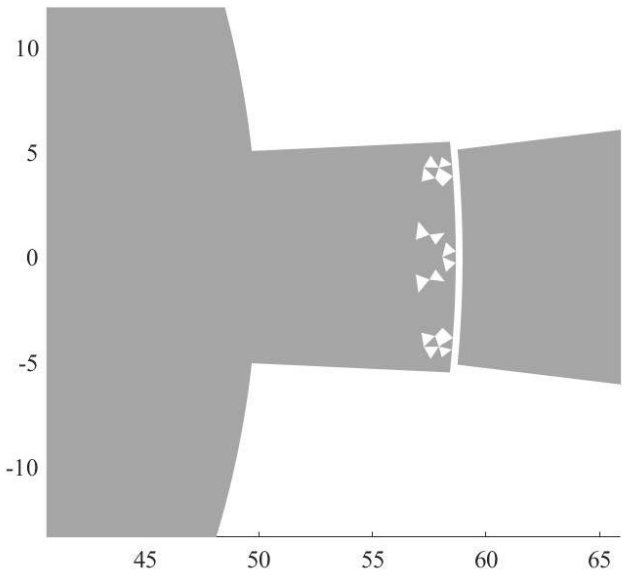

Figure 8.2: A rotor tooth of the 6/14 SRM after TO of the rotor teeth.

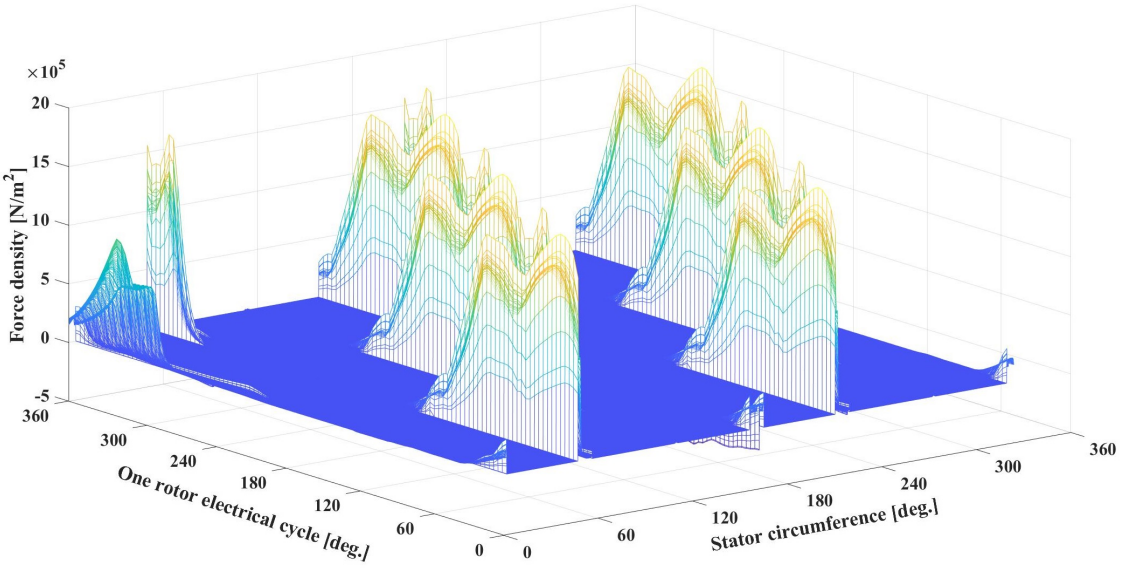

Figure 8.3: The stator radial force for one electrical cycle for the optimized design shown in figure 8.2.

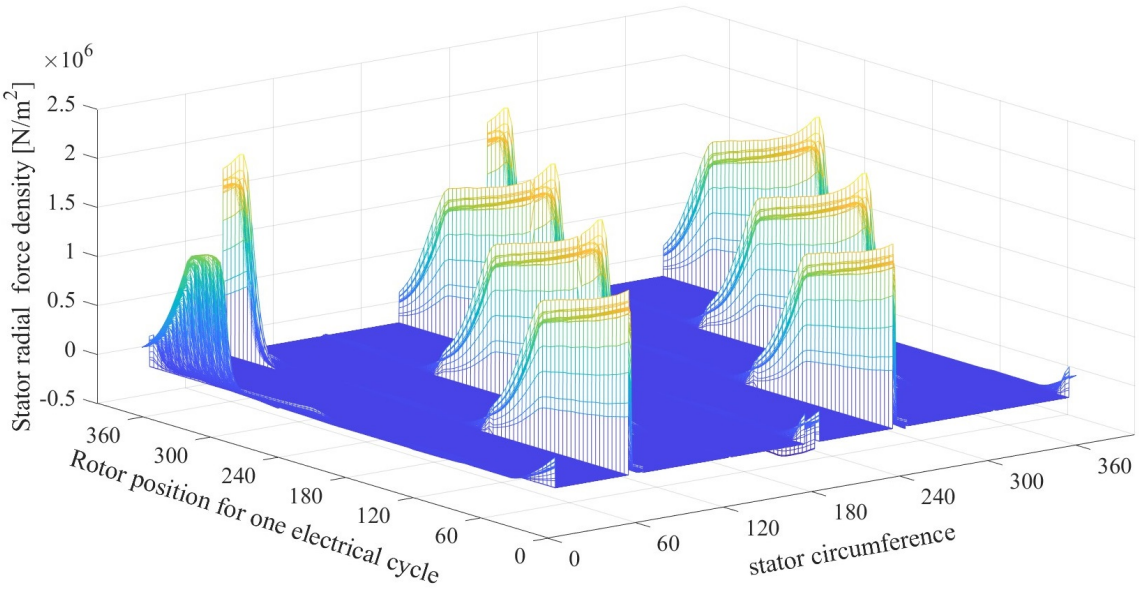

Figure 8.4: The stator radial force for one electrical cycle for the original design before optimization shown in figure 5.5.a.

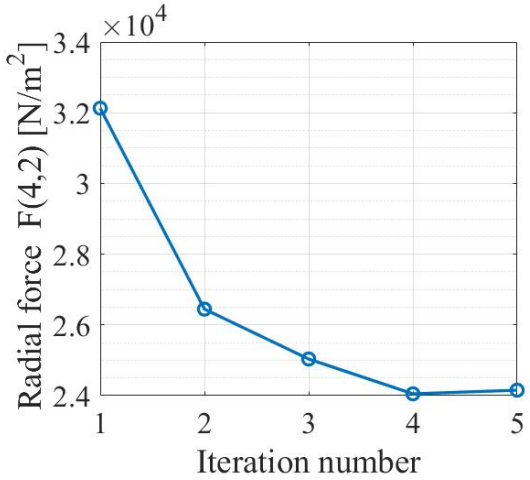

Figure 8.5: The amplitude of the selected radial force density component through the optimization's iteration.

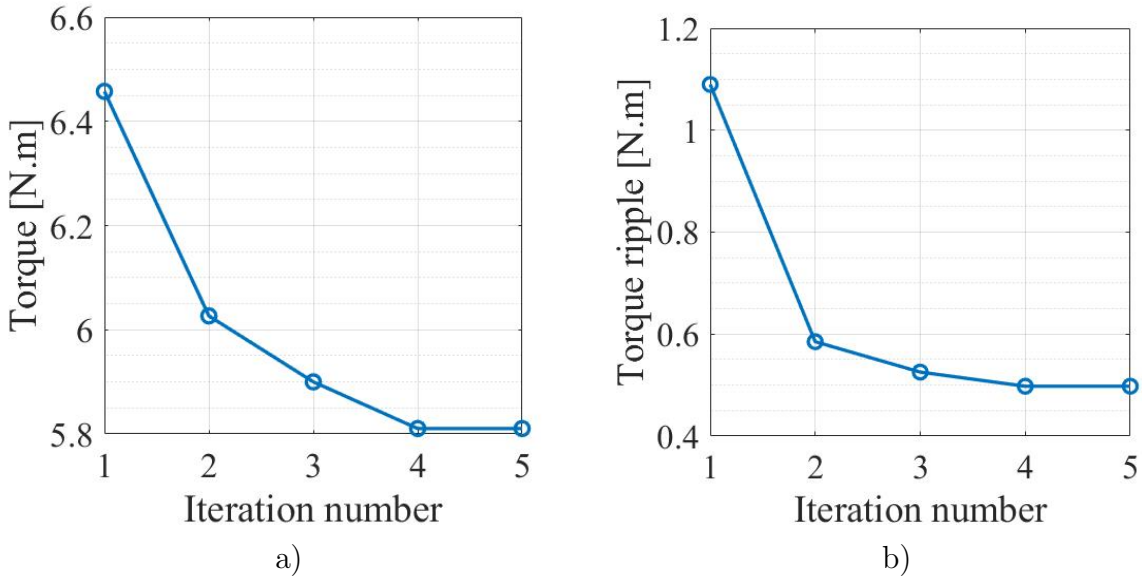

Figure 8.6: The machine torque and torque ripples through the optimization's iterations: a) average torque b) torque ripple.

Figure 8.7 shows the radial force density components of the waveform shown in Figure 8.3. To illustrated the effect on all the other components the percentage of change on all the components with respect to the initial design is shown in Figure 8.8. As shown in Figure 8.8, There is a hug reduction in the other components as well which

Figure 8.9 shows the flux density contour plot and the flux density lines at three different potions of the rotor. It can be concluded that the optimization algorithm tries to introduce voids in the rotor stricture in order to tilt the flux lines in the circumferential direction if compared to the original design flux density lines at the same rotor positions shown in Figure 6.7.

The main manufacturing strategy to realize these shapes is by using 3D printing of the Somaloy 700HR3P material as discussed in Chapter 6. However, If laminated

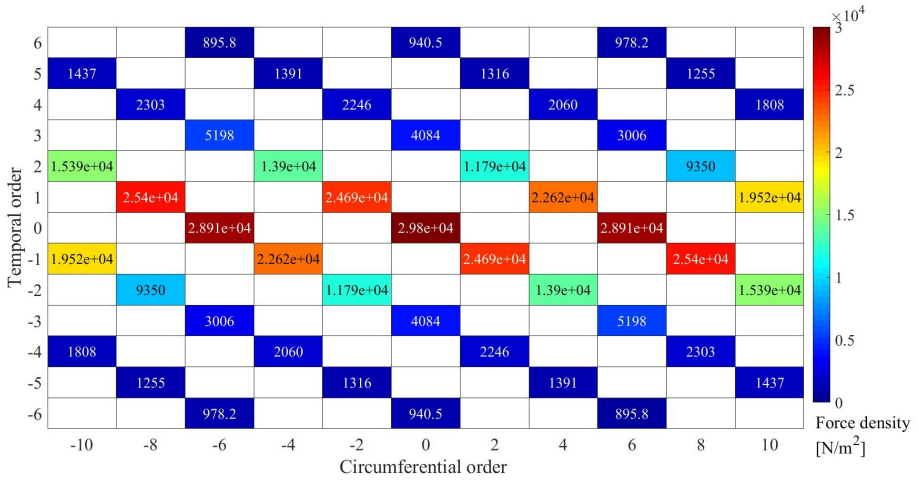

Figure 8.7: The radial force density components of the final design.

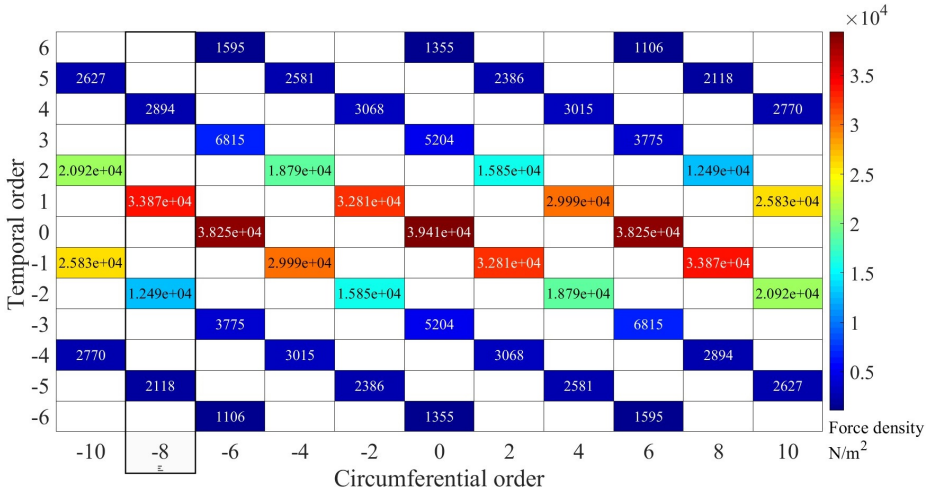

Figure 8.8: The radial force density components of the initial design.

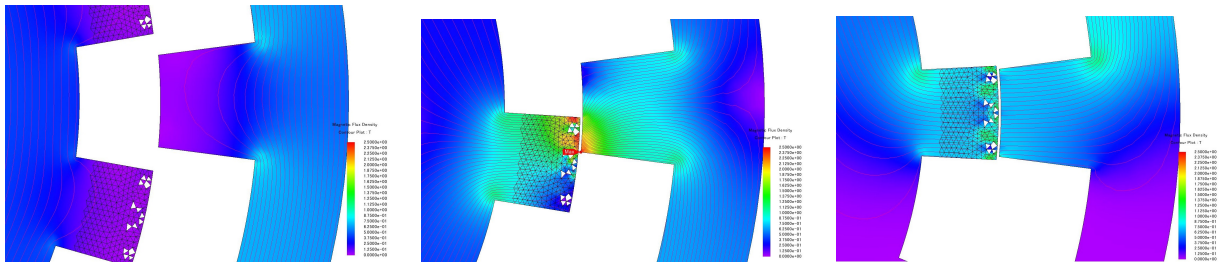

a) b) c)

Figure 8.9: The flux density lines and the flux density contour plot of the optimized design at three different positions of a rotor teeth: a) Unaligned position b)Mid-aligned position, and c) aligned position

steel materials are used for this design with a conventional manufacturing approach, such as laser cutting or stamping of steel sheets, the shape shown in Figure 8.2 should be smoothed further. Figure 8.9 shows the smoothed design of the stator teeth shown in Figure 8.2. In the smoothed design shown in Figure 8.9, the sharp edges shown in the original design were replaced by oval and circular ships, which will be feasible if the laser cutting or stamping process is considered for manufacturing that design.

The smoothing is performed in the design without changing the material. The dynamic torque comparison of the machine before and after smoothing is shown in Figure 8.11. The average torque of the design after the smoothing process was reduced to 5.5 $N.m$, and the torque ripple increased to 12.7%. That is because the smoothing process shifts the design from the optimal point achieved by the optimization algorithm. However, the target radial force density component reduced to 2.218e3 N/m^2.

The radial force density spectrum of the machine after the optimization process is shown in Figure 8.12. The percentage of change after smoothing with respect to the optimized design before smoothing is presented in Figure 8.2 to show the effect of the smoothing on all the force density components. The smoothing of this design

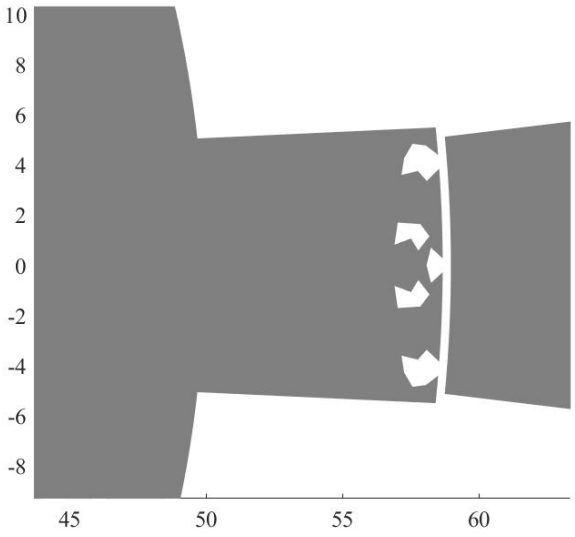

Figure 8.10: The final design after smoothing process.

is based on removing material to remove the sharp edges and the parts that could not be realized by the conventional manufacturing methods such as laser cutting or bunching of the rotor lamination. As presented in Figure 8.2, the smoothing process comes with the advantage of reducing the radial force density components; however, it results in lower torque and high torque ripple. This reason is that the smoothing process shifts the design from the optimal point.

Figure 8.9 shows the flux density contour plot and the flux density lines at three different potions of the rotor after the smoothing process.

8.2.2 Topology optimization by Giving More Weight to the Radial Force Density Minimization

In this subsection, the TO is applied to the rotor design space to minimize the objective function shown in equation (8.2.1). The optimization parameters of the objective

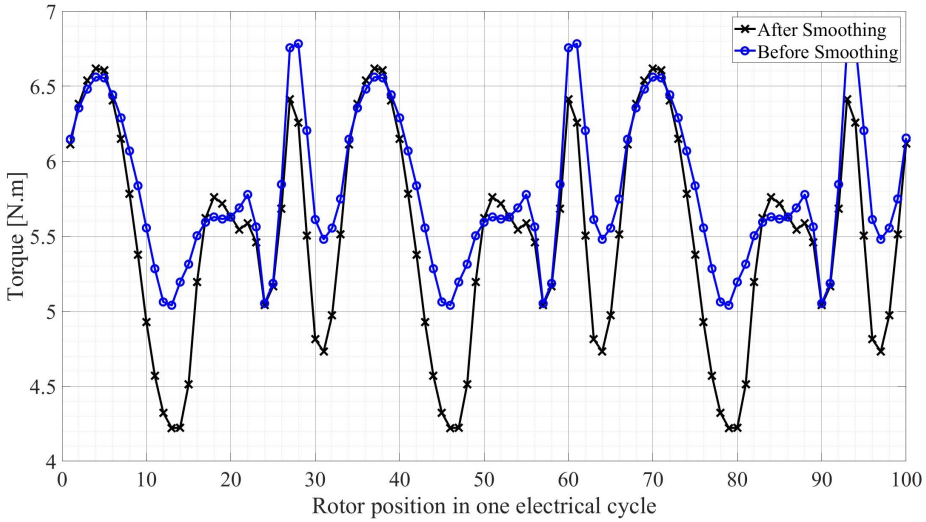

Figure 8.11: The dynamic torque of the machine before and after the smoothing process

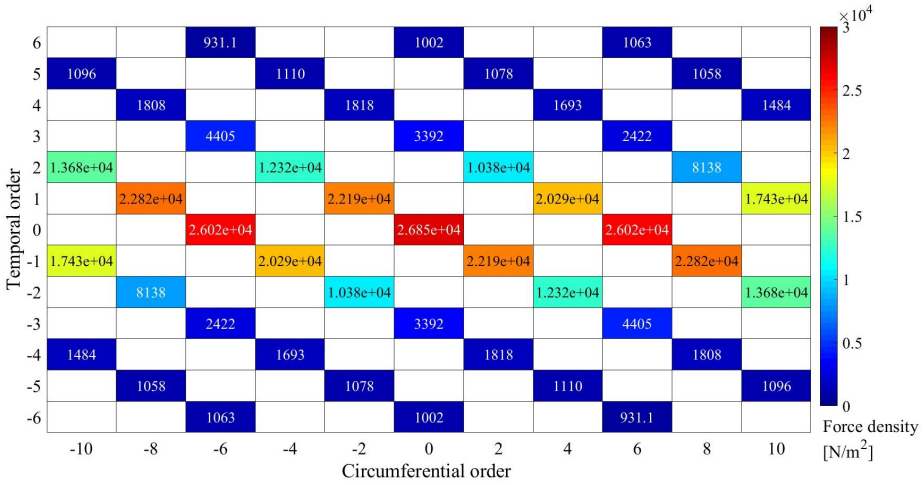

Figure 8.12: The force density spectrum of the case study machine after the design smoothing

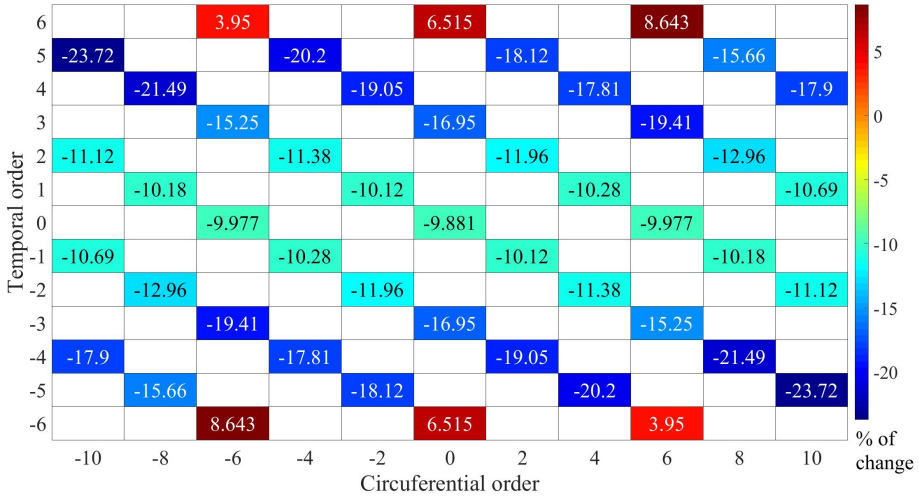

Figure 8.13: The percentage of change to the radial force density spectrum due to the smoothing

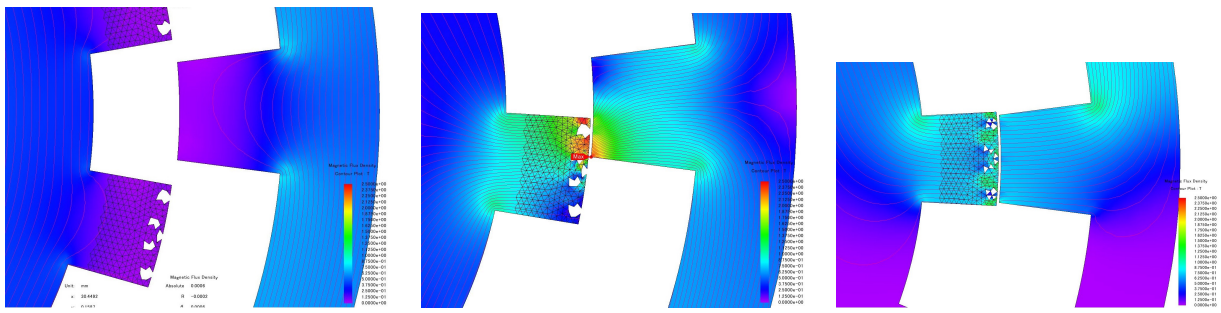

a) b) c)

Figure 8.14: The flux density lines and the flux density contour plot of the optimized design at three different positions of a rotor teeth after the smoothing process: a) Unaligned position b)Mid-aligned position, and c) aligned position

Table 8.3: Objective function parameter of the rotor TO targeting the radial force and the average torque of the case study machine.

Parameter	**Value**
ω_f	0.5
ω_t	0.5
$F_{\mathbf{norm}}$	3.28e4
T_{ref}	6
w_p	0.5
S_t	100

is set as shown in Table 8.3. As shown in the table, the objective function parameter is making the optimization more aggressive in minimizing the selected redial force density component by setting $w_p = 0.5$.

Figure 8.15 shows the design after the TO of the rotor teeth using the linesearch-based ON/OFF optimization method. Figure 8.16 shows the stator radial force density wave of the optimized design.

Figures 8.17 and 8.18 show the amplitude radial force density component, the average torque, and the torque ripple through the TO iterations. As compared to the case in section 8.2.1, the average torque is lower due to the lower redial force density required by the objective function. Figure 8.19 shows the redial force density spectrum of the final optimized design. Figure 8.20 shows the flux density contour plot and the flux density lines at three different potions of the rotor.

Table 8.4 shows the change in the average torque, the torque ripple, and the amplitude redial force density component before and after the optimization process. As shown the Selected radial force density component and the torque ripples of the machine was reduced by 38.32% and 41.03% respectively, while the average torque reduced by 21.78%.

AS shown in Figure 8.15, the smoothing is required for the design to be realized.

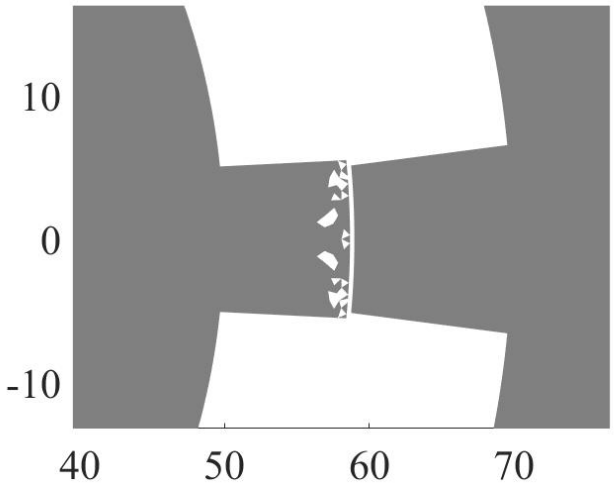

Figure 8.15: A rotor tooth of the 6/14 SRM after TO of the rotor teeth.

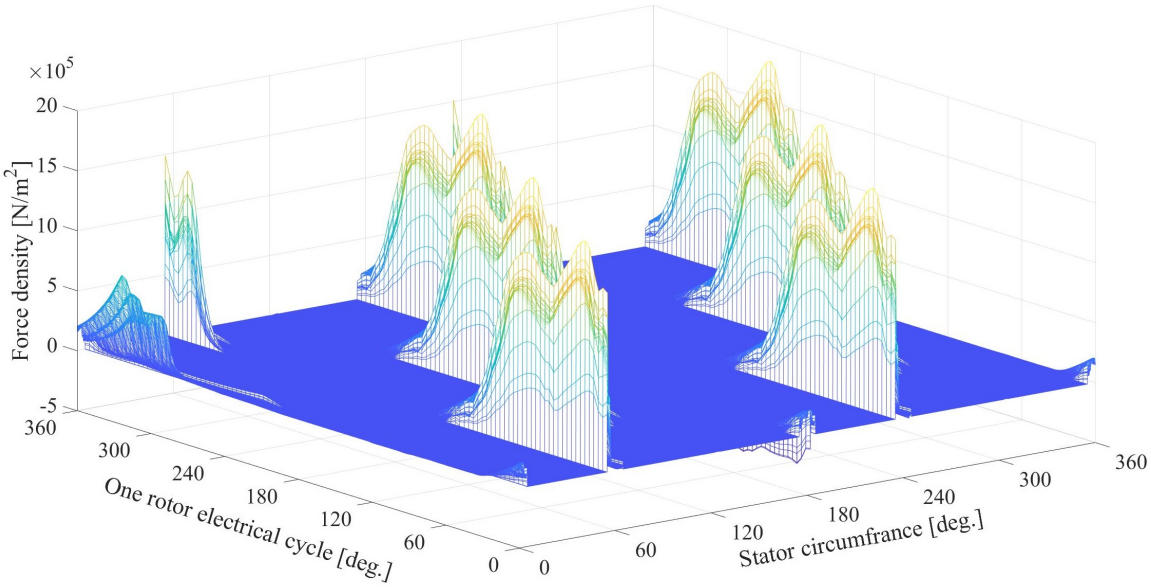

Figure 8.16: The stator radial force for one electrical cycle for the optimized design shown in figure 8.15.

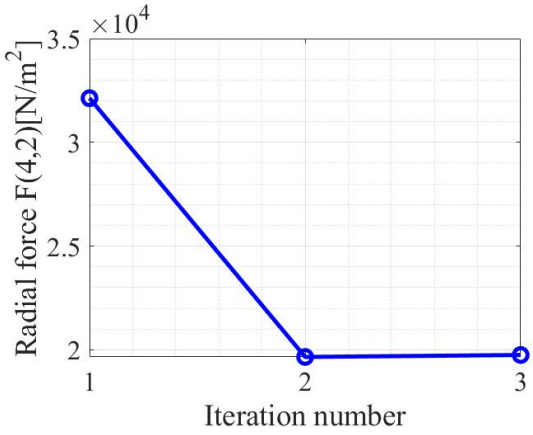

Figure 8.17: The amplitude of the selected radial force density component through the optimization's iteration.

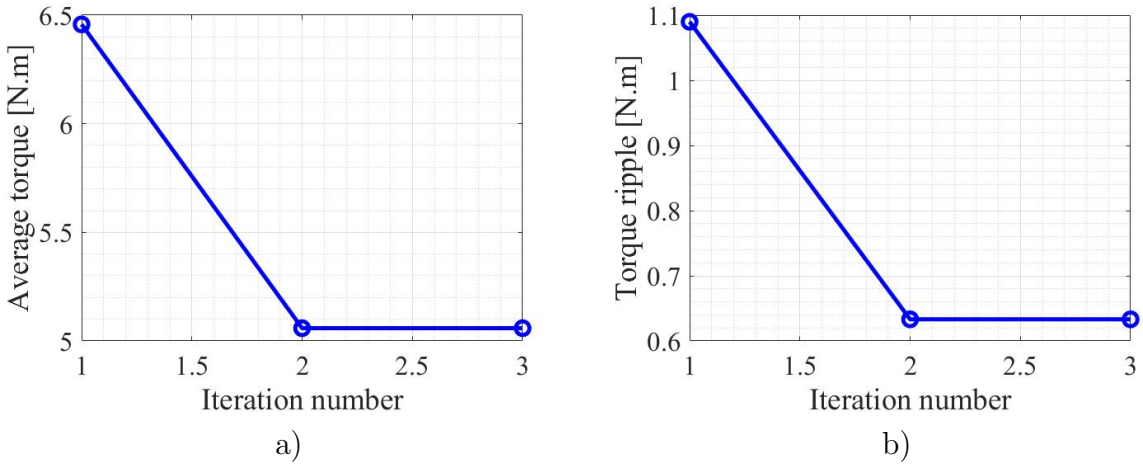

Figure 8.18: The machine torque and torque ripples through the optimization's iterations: a) average torque b) torque ripple.

Table 8.4: The change of the performance parameters of the machine through the optimization process.

	Original design	**Final design**	**Change %**
$F_r(1,2)$	3.28e3 N/m^2	2.023e3 N/m^2	-38.32%
T_{av}	6.46 N.m	5.05 N.m	-21.78%
T.R	1.09 N.m	0.64 N.m	-41.03%

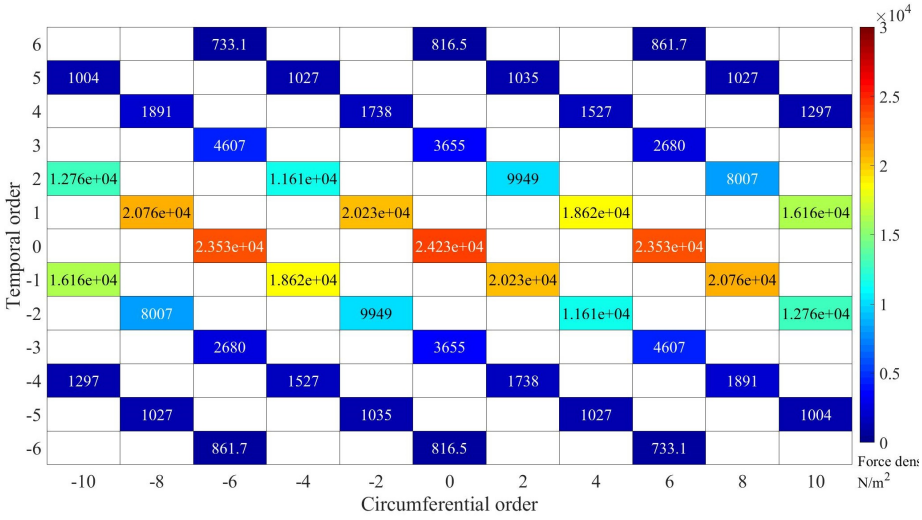

Figure 8.19: The force density spectrum of the case study machine after TO optimization

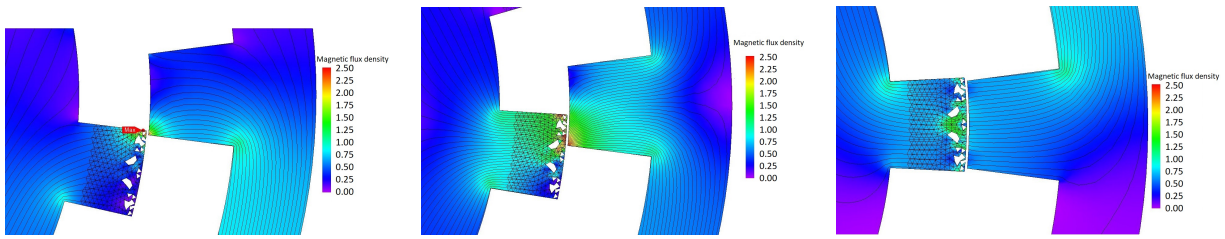

a) b) c)

Figure 8.20: The flux density lines and the flux density contour plot of the optimized design at three different positions of a rotor teeth: a) Unaligned position b)Mid-aligned position, and c) aligned position

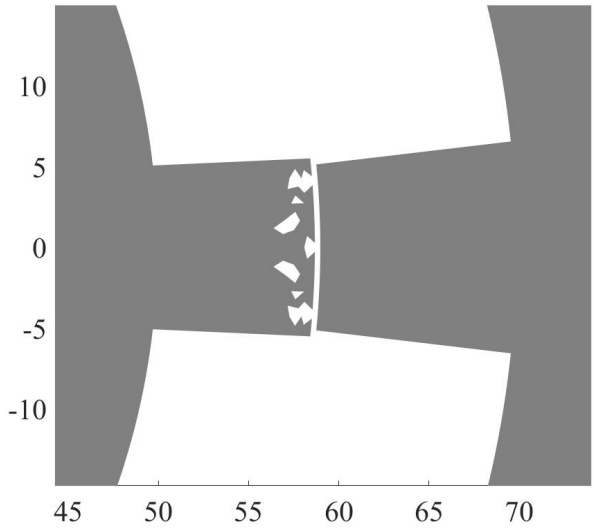

Figure 8.21: The final design after smoothing process.

A smoothing process is applied to the design and the smoothed design is shown in Figure 8.21.

Figure 8.22 shows the stator force density spectrum of the optimized design. The percentage of change of the force density components with respect to the design before smoothing is calculated to quantify the effect of smoothing process. As shown Figure 8.23, some redial force density components reduced and other increased due to the smoothing effect. The target redial force density increased by 6.87% due to the smoothing effect.

The dynamic torque of the machine is also effected by the smoothing process, as shown in Figure 8.24. The average torque increased to 5.314 N.m and the torque ripple increased to 0.68 N.m.

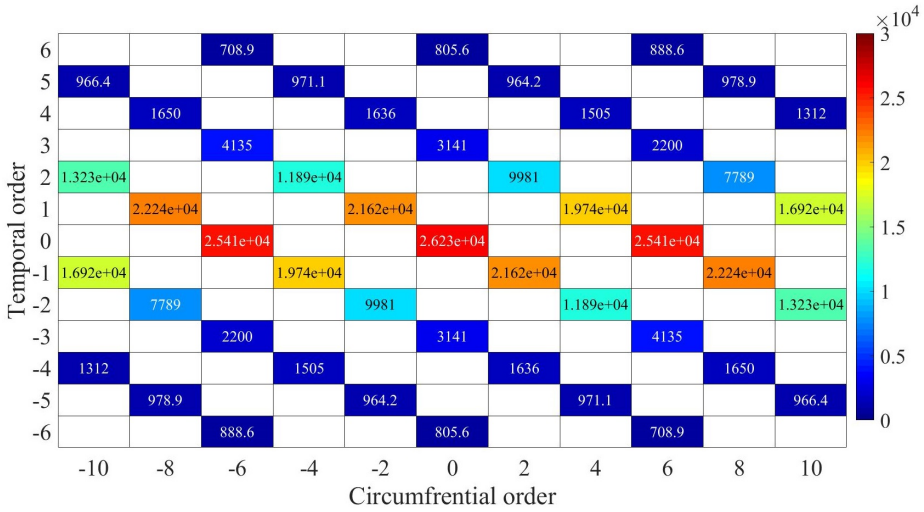

Figure 8.22: The force density spectrum of the case study machine after the design smoothing

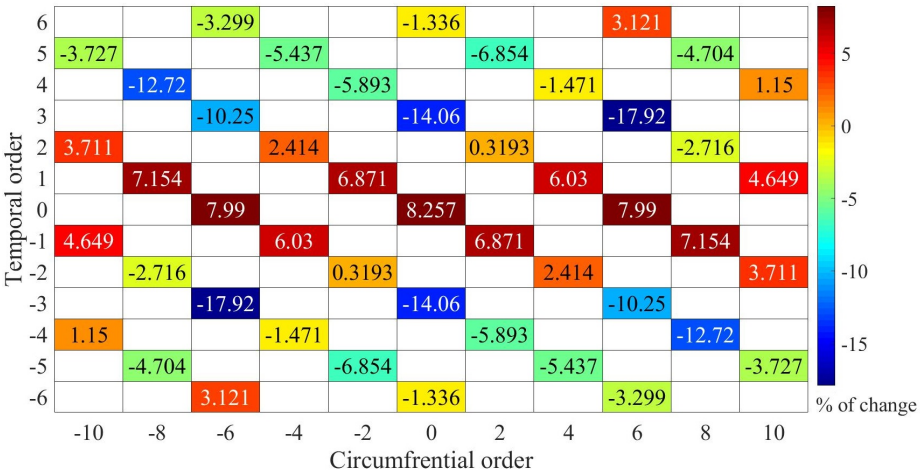

Figure 8.23: The percentage of change to the radial force density spectrum due to the smoothing

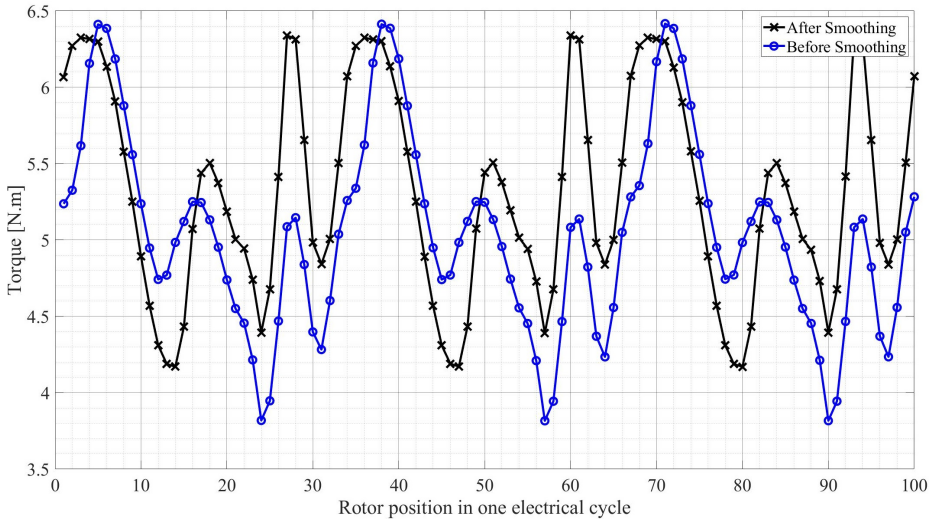

Figure 8.24: The dynamic torque of the machine before and after the smoothing process

Chapter 9

Conclusions, Future Work, and Publications

This Thesis includes the topology and the geometry optimization of SRMs. The machine is modeled in JMAG and the information required for the torque, radial force, torque sensitivity, radial force sensitivity are exported after the FEA conversions. This link enable the fast optimization of the design as the FEA is not needed to be solved in MATLAB.

This work also presents a new linesearch-based ON/OFF optimization algorithm for topology and generative optimization of switched reluctance machines. The method reduced the optimization time compared to the conventional annealing-based ON/OFF algorithm for both topology and generative optimization. The proposed linesearch-based ON/OFF algorithm and the conventional annealing-based ON/OFF algorithm were used for topology and generative optimization of two different design domains of a 6/14 SRM configuration. The proposed method was shown to reduce the optimization time by around 60% for the generative optimization and around 50% for the topology optimization as compared to the conventional annealing-based ON/OFF method for the stator design domain. Also, the optimization time using the proposed method was reduced by around 40% for the generative optimization as compared to the conventional annealing-based ON/OFF method for the rotor design domain. As presented, the proposed method also outperforms the conventional annealing-based ON/OFF method in the final optimized design performance. The new approach was demonstrated for both topology and generative optimization of both the stator and rotor of SRMs. The topology and the generative optimizations with the proposed linesearch-based method converged to almost the same objective function value but with different final solution designs. As the proposed method is a gradient-based

method, the adjoint sensitivities were utilized to calculate the gradient of the objective function with respect to the reluctivity of all elements of the design domain in this research. The new proposed method also used to reduce the radial force acting on the stator of the case study machine. As presented, the linesearch-based ON/OFF topology optimization was able to keep the balance between reducing the stator radial force and keeping the machine torque at acceptable level.

The thesis also presents a new method of generating the stator radial force density wave based on the FE simulation of $1/N_{ph}$ of an electrical cycle. The method is able to generate the full stator radial force density wave by means of shifting the fractional electrical cycle radial force density wave data based on FE simulation of $1/N_{ph}$ of an electrical cycle. By simulating $1/N_{ph}$ of an electrical cycle, the stator radial force density wave can be estimated by using the proper shift angle and the proper circumferential number shifts of the regenerated parts. This results in a huge time and computational effort reduction compared to the existing method of using one electrical cycle and one mechanical cycle simulation. The amount of time reduction depends on the SRM configuration and the number of the machine's phases. The proposed method is useful for geometry and topology optimizations of SRMs that target the mitigation of the stator radial force density. Optimizing the SRMs design to mitigate these components requires many times stator radial force density evaluations during the optimization process. So, any reduction in the time and the computational effort required to evaluate these components results in a reduction on the overall optimization time.

9.1 Future Work

The Model used in the optimization process of the case study machine is a 2-D. the 2-D FEA model ignores the effect of the end-tun and dose not consider the skewing of the rotor and the stater as part of the design parameters. As a future work, the linearsearch-based ON/OFF optimization algorithm will be modified for 3-D models of SRMs. The optimization time is expected to be longer than using 2-D model, however, the 3-D model will add additional dimension to the optimization. The smoothing algorithm is needed to be modified to remove any unfeasible cavity in the design that cannot be realized by 3D printing.

The Force density optimization performed in this study is not based on acoustic noise analysis. The case study was focus on showing the ability of the proposed algorithm for targeting a specific radial force density components and reduce them. As a future work, the acoustic noise and vibrations of the machine will be simulated at the base speed and the full torque. Based on that simulation the critical radial force density component responsible for the acoustic noise and vibration will be targeted by the optimization algorithm for minimization.

It was observed during the study that reducing the size of the design space elements improve the optimization performance and results in more feasible designs. The only limitation for that is the high computational cost of the fine elements design domain. As a future work, the elements' size of the design space will be reduced and wider design space will be considered for optimization.

One of the research directions that will be investigated in the future is using the stator and the rotor design space simultaneously for the TO and the GO optimization. The only limiting factor of that is the high computational cost and long optimization

time. As a future plan, the simulation will be done on a high performance computer to be able to optimize the rotor and the stator space simultaneously.

9.2 Publications

9.2.1 Journal Papers

[1] **M. Abdalmagid**, E. sayed, M. Bakr, and A. Emadi, "Geometry and Topology Optimization of Switched Reluctance Machines: A Review", in *IEEE Access*, vol. 10, pp. 5141-5170, Jan. 2022.

[2] E. sayed, **M. Abdalmagid**, G Pietrini, N. M. Sa'adeh, A. Callegaro, and A. Emadi, "Review of electric machines in more-/hybrid-/turbo-electric aircraft", in *IEEE Transactions on Transportation Electrification*, vol. 7, no. 4, pp. 2976-3005, June 2021.

[3] **M. Abdalmagid**, M. Bakr, and A. Emadi, "A Linesearch-Based Algorithm for Topology and Generative Optimization of Switched Reluctance Machines", in *IEEE Transactions on Transportation Electrification*, Feb. 2023.

[3] **M. Abdalmagid**, M. Bakr, and A. Emadi, "A New Technique for Radial and Tangential Force Calculation Time Reduction for the Optimization process of SRMs", IEEE access (under review).

[4] M. Omar, E. Sayed,**M. Abdalmagid**, M. H. Bakr, B. Bilgin and A. Emadi, "Review of Machine Learning Applications to the Modeling and Design Optimization of Switched Reluctance Motors", in *IEEE Access*, , vol. 10, pp. 130444 - 130468, Dec. 2022.

[5] **M. Abdalmagid**, M. H. Bakr and A. Emadi, " Linesearch-Based Topology and Generative Optimization of Switched Reluctance Machines for Radial Force minimization," (To be published).

9.2.2 Conference Papers

[1] **M. Abdalmagid**, E. sayed, M. Bakr, and A. Emadi, "Adjoint sensitivity analysis of radial force components of switched reluctance machines", *2021 IEEE Transportation Electrification Conference and Expo (ITEC)*, Chicago, IL, USA, 2021, pp. 395 – 400.

[2] C. Goldstein , E. sayed, **M. Abdalmagid**, A. Callegaro, M. Goykhman, and A. Emadi, "Design of a Compact Stator Winding in an Axial-Flux Permanent Magnet Machine for Aerospace Applications", *2021 IEEE Transportation Electrification Conference and Expo (ITEC)*, Chicago, IL, USA, 2021, pp. 181 – 186.

[3] **M. Abdalmagid**, G. Pietrini, A. Callegaro, M. Goykhman, and A. Emadi, "Bearing Current Modelling and Investigation in Axial Flux Permanent Magnet Synchronous Motors for Aerospace Applications", *2022 IEEE Transportation Electrification Conference and Expo (ITEC)*, Anaheim, CA, USA, 2022, pp. 1087 – 1092.

[4] A. Manikandan, **M. Abdalmagid**, G. Pietrini, M. Goykhman and A. Emadi, "Rotor Durability Optimization by Means of Finite Element Multiphysics Analysis for High-Speed Surface Permanent Magnet Electric Machines", 2023 SAE World Conference Experience (WCX), Detroit, MI, USA, 2023.

[5] **M. Abdalmagid**, M. H. Bakr and A. Emadi, "Linesearch-Based Geometry optimization of SRM," (To be published).

[6] A. Manikandan, **M. Abdalmagid**, G. Pietrini, M. Goykhman and A. Emadi, "Structural Design Evaluation of Integrated Rotor Hub and Shaft for a High-Speed Surface Mounted Radial Flux Permanent Magnet Synchronous Motor." 2023 IEEE Transportation Electrification Conference & Expo, (accepted).

[7] D. Choudhary, S. Jones-Jackson, **M. Abdalmagid**, G. Pietrini, M. Goykhman and A. Emadi, "Cooling System Design of a High-Speed Radial-Flux Permanent Magnet Machine for Aerospace Propulsion Applications." 2023 IEEE Transportation Electrification Conference & Expo, (accepted).

[8] S. Pillai, A. Forsyth, **M. Abdalmagid**, G. Pietrini, M. Goykhman and A. Emadi, "INVESTIGATION OF THE THREE-LEVELS PWM CURRENT EFFECTS ON A HIGH-SPEED PMSM FOR AN AEROSPACE APPLICATIONS." 2023 IEEE Transportation Electrification Conference & Expo, (accepted).

[9]I. Zaher, A. Manikandan, **M. Abdalmagid**, G. Pietrini, M. Goykhman and A. Emadi, "Thermo-structural Design of the Rotor in High-Speed Permanent Magnet Machines for Aerospace Propulsion Applications." 2023 IEEE Transportation Electrification Conference & Expo, (accepted).

[10] S. Pillai, A. Forsyth, J. Doan,**M. Abdalmagid**, G. Pietrini, M. Goykhman and A. Emadi, "Analysis of a High-Speed PMSM for an Aerospace Application." International Electric Machines and Drives Conference (IEMDC 2023), (accepted).

9.2.3 Patents

[1] Axial flux motor with cooling jacket, by M. Goykhman, G. Chui, P. Suntharalingham, R Lau, E. Sayed, A. Callegaro, F. Duperly, and M. Abdalmagid . (2022, Dec. 8). US2022/0393543A1. [Online]. Available: https://patentimages.storage.googleapis.com

/aa/b9/76/81da4ca5b1de78/US20220393543A1.pdf

References

[1] N. Zabihi and R. Gouws, "A review on switched reluctance machines for electric vehicles," in *2016 IEEE 25th International Symposium on Industrial Electronics (ISIE)*, pp. 799–804, IEEE, 2016.

[2] B. Bilgin, A. Emadi, and M. Krishnamurthy, "Comprehensive evaluation of the dynamic performance of a 6/10 srm for traction application in phevs," *IEEE Transactions on Industrial Electronics*, vol. 60, no. 7, pp. 2564–2575, 2012.

[3] C.-T. Liu, Y.-M. Chen, and D.-C. Pang, "Optimal design of a micro axial flux switched-reluctance motor," in *IEEE International Conference on Electric Machines and Drives, 2005.*, pp. 1130–1134, IEEE, 2005.

[4] C.-T. Liu and T.-S. Chiang, "Design and performance evaluation of a microlinear switched-reluctance motor," *IEEE transactions on magnetics*, vol. 40, no. 2, pp. 806–809, 2004.

[5] H.-U. Shin and K.-B. Lee, "Optimal design of a 1 kw switched reluctance generator for wind power systems using a genetic algorithm," *IET Electric Power Applications*, vol. 10, no. 8, pp. 807–817, 2016.

[6] Y. Hu, C. Gan, W. Cao, J. Zhang, W. Li, and S. J. Finney, "Flexible fault-tolerant topology for switched reluctance motor drives," *IEEE Transactions on Power Electronics*, vol. 31, no. 6, pp. 4654–4668, 2015.

[7] J. W. Jiang, B. Bilgin, and A. Emadi, "Three-phase 24/16 switched reluctance machine for a hybrid electric powertrain," *IEEE Transactions on Transportation Electrification*, vol. 3, no. 1, pp. 76–85, 2017.

[8] E. Bostanci, M. Moallem, A. Parsapour, and B. Fahimi, "Opportunities and challenges of switched reluctance motor drives for electric propulsion: A comparative study," *IEEE transactions on transportation electrification*, vol. 3, no. 1, pp. 58–75, 2017.

[9] J. Lin, N. Schofield, and A. Emadi, "External-rotor $6-10$ switched reluctance motor for an electric bicycle," *IEEE Transactions on Transportation electrification*, vol. 1, no. 4, pp. 348–356, 2015.

[10] H. Zhang, W. Xu, S. Wang, Y. Huangfu, G. Wang, and J. Zhu, "Optimum design of rotor for high-speed switched reluctance motor using level set method," *IEEE transactions on magnetics*, vol. 50, no. 2, pp. 765–768, 2014.

[11] J. Liang, A. D. Callegaro, B. Bilgin, and A. Emadi, "A novel three-dimensional analytical approach for acoustic noise modeling in switched reluctance machines," *IEEE Transactions on Energy Conversion*, vol. 36, no. 3, pp. 2099–2109, 2021.

[12] M. Abdalmagid, E. Sayed, M. Bakr, and A. Emadi, "Geometry and topology optimization of switched reluctance machines: A review," *IEEE Access*, 2022.

[13] B. Mirzaeian, M. Moallem, V. Tahani, and C. Lucas, "Multiobjective optimization method based on a genetic algorithm for switched reluctance motor design," *IEEE Transactions on Magnetics*, vol. 38, no. 3, pp. 1524–1527, 2002.

[14] H. Sasaki and H. Igarashi, "Topology optimization accelerated by deep learning," *IEEE Transactions on Magnetics*, vol. 55, no. 6, pp. 1–5, 2019.

[15] J. Yoo, "Reduction of vibration caused by magnetic force in a switched reluctance motor by topology optimization," *J. Appl. Mech.*, vol. 69, no. 3, pp. 380–387, 2002.

[16] N. Takahashi, "Application of on/off method to new conceptual design of magnetic devices," *COMPEL: The International Journal for Computation and Mathematics in Electrical and Electronic Engineering*, 2013.

[17] A. N. A. Hermann, N. Mijatovic, and M. L. Henriksen, "Topology optimisation of pmsm rotor for pump application," in *2016 XXII International Conference on Electrical Machines (ICEM)*, pp. 2119–2125, IEEE, 2016.

[18] G. U. Jang, S. Cho, J. Moon, K. Jeon, and C.-w. Kim, "Topology optimization to reduce electromagnetic force induced vibration for the specific frequency of pmsm motor using electromagnetic-structural coupled analysis," *Energies*, vol. 14, no. 2, p. 431, 2021.

[19] J. Lee, J. H. Seo, and N. Kikuchi, "Topology optimization of switched reluctance motors for the desired torque profile," *Structural and multidisciplinary optimization*, vol. 42, no. 5, pp. 783–796, 2010.

[20] B. Bilgin, A. Emadi, and M. Krishnamurthy, "Comprehensive evaluation of the dynamic performance of a 6/10 srm for traction application in phevs," *IEEE Transactions on Industrial Electronics*, vol. 60, no. 7, pp. 2564–2575, 2013.

[21] H.-U. Shin and K.-B. Lee, "Optimal design of a switched reluctance generator for small wind power system using a genetic algorithm," in *2015 9th International Conference on Power Electronics and ECCE Asia (ICPE-ECCE Asia)*, pp. 2209–2214, 2015.

[22] C.-T. Liu, Y.-M. Chen, and D.-C. Pang, "Optimal design of a micro axial flux switched-reluctance motor," in *IEEE International Conference on Electric Machines and Drives, 2005.*, pp. 1130–1134, 2005.

[23] C.-T. Liu and T.-S. Chiang, "Design and performance evaluation of a micro-linear switched-reluctance motor," *IEEE Transactions on Magnetics*, vol. 40, no. 2, pp. 806–809, 2004.

[24] B. Bilgin, J. W. Jiang, and A. Emadi, "Switched reluctance motor drives: fundamentals to applications," *Boca Raton, FL*, 2018.

[25] V. R and B. G. Fernandes, "Design methodology for high-performance segmented rotor switched reluctance motors," *IEEE Transactions on Energy Conversion*, vol. 30, no. 1, pp. 11–21, 2015.

[26] H. Torkaman, N. Faraji, and M. S. Toulabi, "Influence of rotor structure on fault diagnosis indices in two-phase switched reluctance motors," *IEEE Transactions on Magnetics*, vol. 50, no. 3, pp. 136–143, 2013.

[27] M. Asgar, E. Afjei, and H. Torkaman, "A new strategy for design and analysis of a double-stator switched reluctance motor: Electromagnetics, fem, and experiment," *IEEE Transactions on Magnetics*, vol. 51, no. 12, pp. 1–8, 2015.

[28] E. Afjei, A. Siadatan, and H. Torkaman, "Magnetic modeling, prototyping, and comparative study of a quintuple-set switched reluctance motor," *IEEE Transactions on Magnetics*, vol. 51, no. 8, pp. 1–7, 2015.

[29] M. M. Nezamabadi, E. Afjei, and H. Torkaman, "Design, dynamic electromagnetic analysis, fem, and fabrication of a new switched-reluctance motor with hybrid motion," *IEEE Transactions on Magnetics*, vol. 52, no. 4, pp. 1–8, 2015.

[30] H. Torkaman and E. Afjei, "Sensorless method for eccentricity fault monitoring and diagnosis in switched reluctance machines based on stator voltage signature," *IEEE Transactions on Magnetics*, vol. 49, no. 2, pp. 912–920, 2012.

[31] H. Torkaman, A. Ghaheri, and A. Keyhani, "Axial flux switched reluctance machines: a comprehensive review of design and topologies," *IET Electric Power Applications*, vol. 13, no. 3, pp. 310–321, 2019.

[32] B. G. Joseph and P. Thomas, "Variable reluctance axial flux alternator incorporating air gap variation," in *2016 Biennial International Conference on Power and Energy Systems: Towards Sustainable Energy (PESTSE)*, pp. 1–8, IEEE, 2016.

[33] N. K. Sheth and K. Rajagopal, "Effects of nonuniform airgap on the torque characteristics of a switched reluctance motor," 2004.

[34] B. Bilgin, B. Howey, A. D. Callegaro, J. Liang, M. Kordic, J. Taylor, and A. Emadi, "Making the case for switched reluctance motors for propulsion applications," *IEEE Transactions on Vehicular Technology*, vol. 69, no. 7, pp. 7172–7186, 2020.

[35] R. Vandana, S. Nikam, and B. Fernandes, "Criteria for design of high performance switched reluctance motor," in *2012 XXth International Conference on Electrical Machines*, pp. 129–135, IEEE, 2012.

[36] B. Bilgin, A. Emadi, and M. Krishnamurthy, "Design considerations for switched reluctance machines with a higher number of rotor poles," *IEEE Transactions on Industrial Electronics*, vol. 59, no. 10, pp. 3745–3756, 2011.

[37] P. C. Desai, M. Krishnamurthy, N. Schofield, and A. Emadi, "Novel switched reluctance machine configuration with higher number of rotor poles than stator poles: Concept to implementation," *IEEE Transactions on Industrial Electronics*, vol. 57, no. 2, pp. 649–659, 2009.

[38] J. D. Widmer and B. C. Mecrow, "Optimized segmental rotor switched reluctance machines with a greater number of rotor segments than stator slots," *IEEE Transactions on Industry Applications*, vol. 49, no. 4, pp. 1491–1498, 2013.

[39] V. Rallabandi and B. G. Fernandes, "Design procedure of segmented rotor switched reluctance motor for direct drive applications," *IET Electric Power Applications*, vol. 8, no. 3, pp. 77–88, 2014.

[40] T. J. Miller, "Converter volt-ampere requirements of the switched reluctance motor drive," *IEEE Transactions on Industry Applications*, no. 5, pp. 1136–1144, 1985.

[41] J. Zhu, K. Cheng, and X. Xue, "Torque analysis for in-wheel switched reluctance motors with varied number of rotor poles," in *2016 International Symposium on Electrical Engineering (ISEE)*, pp. 1–5, IEEE, 2016.

[42] B. Wang, D.-H. Lee, and J.-W. Ahn, "Characteristic analysis of a novel segmental rotor axial field switched reluctance motor with single teeth winding," in *2014 IEEE international conference on industrial technology (ICIT)*, pp. 175–180, IEEE, 2014.

[43] D.-C. Pang and C.-T. Wang, "A wireless-driven, micro, axial-flux, single-phase switched reluctance motor," *Energies*, vol. 11, no. 10, p. 2772, 2018.

[44] F. Sass, J. A. Santisteban, and E. Sanches, "Design and implementation of a digital control system for an axial flux switched reluctance motor," in *2009 Brazilian Power Electronics Conference*, pp. 138–144, IEEE, 2009.

[45] H. Arihara and K. Akatsu, "A basic property of axial type switched reluctance motor," in *2010 International Conference on Electrical Machines and Systems*, pp. 1687–1690, IEEE, 2010.

[46] T. Kellerer, O. Radler, T. Sattel, S. Purfuerst, and S. Uske, "Axial type switched reluctance motor of soft magnetic composite," in *Innovative Small Drives and Micro-Motor Systems; 9. GMM/ETG Symposium*, pp. 1–6, VDE, 2013.

[47] J. Ma, R. Qu, and J. Li, "Optimal design of axial flux switched reluctance motor for electric vehicle application," in *2014 17th International Conference on Electrical Machines and Systems (ICEMS)*, pp. 1860–1865, IEEE, 2014.

[48] J. Ma, R. Qu, and J. Li, "A novel axial flux switched reluctance motor with grain oriented electrical steel," in *2015 IEEE International Magnetics Conference (INTERMAG)*, pp. 1–1, IEEE, 2015.

[49] D. W. Pulle and I. Petersen, "A unified approach to switched reluctance drive modeling: application to an axial flux (sraf) motor," in *PESC 98 Record. 29th Annual IEEE Power Electronics Specialists Conference (Cat. No. 98CH36196)*, vol. 2, pp. 1681–1686, IEEE, 1998.

[50] B.-S. Lee, H.-K. Bae, P. Vijayraghavan, and R. Krishnan, "Design of a linear switched reluctance machine," in *Conference Record of the 1999 IEEE Industry Applications Conference. Thirty-Forth IAS Annual Meeting (Cat. No. 99CH36370)*, vol. 4, pp. 2267–2274, IEEE, 1999.

[51] H. Chen, R. Nie, and W. Yan, "A novel structure single-phase tubular switched reluctance linear motor," *IEEE Transactions on Magnetics*, vol. 53, no. 11, pp. 1–4, 2017.

[52] Q. Wang, H. Chen, and R. Nie, "Unbalanced normal force reduction in the eccentric double-sided linear switched reluctance machine," *IET Electric Power Applications*, vol. 10, no. 5, pp. 384–393, 2016.

[53] J. Pan, N. C. Cheung, and Y. Zou, "Design and analysis of a novel transverse-flux tubular linear machine with gear-shaped teeth structure," *IEEE transactions on magnetics*, vol. 48, no. 11, pp. 3339–3343, 2012.

[54] L. Yan, W. Li, Z. Jiao, and I.-M. Chen, "Novel tubular switched reluctance motor with double excitation windings: Design, modeling, and experiments," *Review of Scientific Instruments*, vol. 86, no. 12, p. 125004, 2015.

[55] X. Xue, K. W. E. Cheng, and Z. Zhang, "Model, analysis, and application of tubular linear switched reluctance actuator for linear compressors," *IEEE Transactions on Industrial Electronics*, vol. 65, no. 12, pp. 9863–9872, 2018.

[56] M.-T. Khor, R. Sotudeh, and D. Lee, "Switched reluctance motor based on short flux path control method," in *39th International Universities Power Engineering Conference, 2004. UPEC 2004.*, vol. 2, pp. 559–562, IEEE, 2004.

[57] X. Zhang, L. Xiong, and M. Zhang, "The research on an inter-phase coupling switched reluctance motor with short flux path," in *2019 IEEE 4th Advanced Information Technology, Electronic and Automation Control Conference (IAEAC)*, vol. 1, pp. 490–493, IEEE, 2019.

[58] H. Hwang, J. Hur, and C. Lee, "Novel permanent-magnet-assisted switched reluctance motor (i): Concept, design, and analysis," in *2013 International Conference on Electrical Machines and Systems (ICEMS)*, pp. 602–608, IEEE, 2013.

[59] J. Jeong, J. Her, and C. Lee, "Novel permanent-magnet-assisted switched reluctance motor (ii): Concept, design, and analysis," in *2013 International Conference on Electrical Machines and Systems (ICEMS)*, pp. 609–614, 2013.

[60] M. Vosswinkel, A. Lohner, V. Platte, and T. Hirche, "Design, production, and verification of a switched-reluctance wheel hub drive train for battery electric vehicles," *World Electric Vehicle Journal*, vol. 10, no. 4, p. 82, 2019.

[61] V. Hanaeinejad and M. Abbasian, "A non-segmental outer rotor switched reluctance machine for in-wheel electric vehicle application," *Iranian Journal of Science and Technology, Transactions of Electrical Engineering*, vol. 43, no. 4, pp. 909–918, 2019.

[62] M. A. Cinar and F. E. Kuyumcu, "Design and torque profile analysis of an outer-rotor sr motor with different winding configurations," *Prz. Elektrotech*, vol. 2, pp. 328–331, 2012.

[63] N. Arbab, H. Karim, H. Torkaman, and E. Afjei, "New external rotor switched reluctance motor in comparison with conventional srm," *International Review of Electrical Engineering*, vol. 6, no. 2, pp. 679–684, 2011.

[64] M. A. Kabir and I. Husain, "Concentrated winding segmented rotor switched reluctance machine (srm) using three-phase standard inverters," in *2015 IEEE Energy Conversion Congress and Exposition (ECCE)*, pp. 5567–5572, IEEE, 2015.

[65] W. Bo, D.-H. Lee, and J.-W. Ahn, "A novel axial field srm with segmental rotor: Concept, design and analysis," in *2013 Workshop on Power Electronics and Power Quality Applications (PEPQA)*, pp. 1–6, IEEE, 2013.

[66] T. Shibamoto, K. Nakamura, H. Goto, and O. Ichinokura, "A design of axial-gap switched reluctance motor for in-wheel direct-drive ev," in *2012 XXth International Conference on Electrical Machines*, pp. 1160–1165, IEEE, 2012.

[67] R. Madhavan and B. Fernandes, "A novel axial flux segmented srm for electric vehicle application," in *The XIX International Conference on Electrical Machines-ICEM 2010*, pp. 1–6, IEEE, 2010.

[68] R. Madhavan and B. Fernandes, "Comparative analysis of axial flux srm topologies for electric vehicle application," in *2012 IEEE International Conference on Power Electronics, Drives and Energy Systems (PEDES)*, pp. 1–6, IEEE, 2012.

[69] H. Goto, S. Murakami, and O. Ichinokura, "Design to maximize torque-volume density of axial-flux srm for in-wheel ev," in *IECON 2015-41st Annual Conference of the IEEE Industrial Electronics Society*, pp. 005191–005196, IEEE, 2015.

[70] M. Sengupta, S. Ahmad, and D. Mukherjee, "Experimental investigations on a novel laboratory prototype of axial flux switched reluctance motor," in *2012 IEEE International Conference on Power Electronics, Drives and Energy Systems (PEDES)*, pp. 1–5, IEEE, 2012.

[71] F. Daldaban and N. Ustkoyuncu, "New disc type switched reluctance motor for high torque density," *Energy conversion and management*, vol. 48, no. 8, pp. 2424–2431, 2007.

[72] D. Wang, C. Shao, and X. Wang, "Design and performance evaluation of a tubular linear switched reluctance generator with low cost and high thrust density," *IEEE Transactions on Applied Superconductivity*, vol. 26, no. 7, pp. 1–5, 2016.

[73] W. Li, C.-Y. Chen, L. Yan, Z. Jiao, and I.-M. Chen, "Design and modeling of tubular double excitation windings linear switched reluctance motor," in *2015 IEEE 10th Conference on Industrial Electronics and Applications (ICIEA)*, pp. 1686–1691, IEEE, 2015.

[74] E. Sayed, M. H. Bakr, B. Bilgin, and A. Emadi, "Gradient-based design optimization of a switched reluctance motor for an hvac application," in *2020 IEEE Transportation Electrification Conference & Expo (ITEC)*, pp. 1031–1037, IEEE, 2020.

[75] D. Jonathan, D. Bruno, and B. A. Hamid, "Simulated annealing and genetic algorithms in topology optimization tools: A comparison through the design of a switched reluctance machine," in *SPEEDAM 2010*, pp. 1247–1252, IEEE, 2010.

[76] H. Li, B. Bilgin, and A. Emadi, "An improved torque sharing function for torque ripple reduction in switched reluctance machines," *IEEE Transactions on Power Electronics*, vol. 34, no. 2, pp. 1635–1644, 2018.

[77] S. Li, S. Zhang, T. G. Habetler, and R. G. Harley, "Modeling, design optimization, and applications of switched reluctance machines—a review," *IEEE Transactions on Industry Applications*, vol. 55, no. 3, pp. 2660–2681, 2019.

[78] Y. Yasa, Y. SÖZER, and M. Garip, "High-power density switched reluctance machine development for high-speed spindle applications," *Turkish Journal of Electrical Engineering and Computer Sciences*, vol. 26, no. 3, pp. 1572–1586, 2018.

[79] H. Hayashi, K. Nakamura, A. Chiba, T. Fukao, K. Tungpimolrut, and D. G. Dorrell, "Efficiency improvements of switched reluctance motors with high-quality iron steel and enhanced conductor slot fill," *IEEE Transactions on Energy Conversion*, vol. 24, no. 4, pp. 819–825, 2009.

[80] A. Chiba, Y. Takano, M. Takeno, T. Imakawa, N. Hoshi, M. Takemoto, and S. Ogasawara, "Torque density and efficiency improvements of a switched reluctance motor without rare-earth material for hybrid vehicles," *IEEE Transactions on Industry Applications*, vol. 47, no. 3, pp. 1240–1246, 2011.

[81] M. Morimoto, "Efficiency improvement of induction motor by 3-d core made of smc," in *2012 15th International Power Electronics and Motion Control Conference (EPE/PEMC)*, pp. LS1b–3, IEEE, 2012.

[82] C. Lin and B. Fahimi, "Prediction of acoustic noise in switched reluctance motor drives," *IEEE Transactions on Energy Conversion*, vol. 29, no. 1, pp. 250–258, 2013.

[83] M. Elamin, "Acoustic noise mitigation of switched reluctance machines through skewing methods," *The Graduate Faculty of the University of Akron, Master of Science*, vol. 76, 2017.

[84] D. Tekgun, *Acoustic noise and vibration reduction on switched reluctance machines through hole placement in stator/rotor laminations*. PhD thesis, University of Akron, 2017.

[85] A. D. Callegaro, J. Liang, J. W. Jiang, B. Bilgin, and A. Emadi, "Radial force density analysis of switched reluctance machines: The source of acoustic noise," *IEEE Transactions on Transportation Electrification*, vol. 5, no. 1, pp. 93–106, 2018.

[86] M. Abdalmagid, M. Bakr, E. Sayed, and A. Emadi, "Adjoint sensitivity analysis of radial force components of switched reluctance machines," in *2021 IEEE Transportation Electrification Conference & Expo (ITEC)*, pp. 395–400, IEEE, 2021.

[87] S. Hosseini and Y. Alinejad-Beromi, "Noise reduction in switched reluctance motor by modifying the structures," *IET Electric Power Applications*, vol. 14, no. 14, pp. 2863–2872, 2020.

[88] A. D. Callegaro, B. Bilgin, and A. Emadi, "Radial force shaping for acoustic noise reduction in switched reluctance machines," *IEEE Transactions on Power Electronics*, vol. 34, no. 10, pp. 9866–9878, 2019.

[89] J. Furqani, M. Kawa, K. Kiyota, and A. Chiba, "Comparison of current waveforms for noise reduction in switched reluctance motors," in *2017 IEEE Energy Conversion Congress and Exposition (ECCE)*, pp. 752–759, IEEE, 2017.

[90] J. Chai, Y. Lin, and C. Liaw, "Comparative study of switching controls in vibration and acoustic noise reductions for switched reluctance motor," *IEE Proceedings-Electric Power Applications*, vol. 153, no. 3, pp. 348–360, 2006.

[91] C. Ma, L. Qu, R. Mitra, P. Pramod, and R. Islam, "Vibration and torque ripple reduction of switched reluctance motors through current profile optimization," in *2016 IEEE Applied Power Electronics Conference and Exposition (APEC)*, pp. 3279–3285, IEEE, 2016.

[92] M. Cavazzuti, *Optimization methods: from theory to design scientific and technological aspects in mechanics*. Springer Science & Business Media, 2012.

[93] M. Bakr, *Nonlinear optimization in electrical engineering with applications in matlab*. The Institution of Engineering and Technology, 2013.

[94] M. D. Kulkarni, *Continuum sensitivity analysis using boundary velocity formulation for shape derivatives*. PhD thesis, Virginia Tech, 2016.

[95] E. Sayed, *Adjoint-based optimization of switched reluctance motors*. PhD thesis, 2019.

[96] L. S. Kalantari, O. Ahmed, M. H. Bakr, and N. K. Nikolova, "Adjoint sensitivity analysis of 3d problems with anisotropic materials," in *2014 IEEE MTT-S International Microwave Symposium (IMS2014)*, pp. 1–3, IEEE, 2014.

[97] Y. Zhang, O. S. Ahmed, and M. H. Bakr, "Adjoint sensitivity analysis of plasmonic structures using the fdtd method," *Optics letters*, vol. 39, no. 10, pp. 3002–3005, 2014.

[98] G. Dziatkiewicz, "Complex variable step method for sensitivity analysis of effective properties in multi-field micromechanics," *Acta Mechanica*, vol. 227, no. 1, pp. 11–28, 2016.

[99] K.-L. Lai and J. Crassidis, "Extensions of the first and second complex-step derivative approximations," *Journal of Computational and Applied Mathematics*, vol. 219, no. 1, pp. 276–293, 2008.

[100] E. Sayed, M. H. Bakr, B. Bilgin, and A. Emadi, "A matlab toolbox for adjoint-based sensitivity analysis of switched reluctance motors," in *2018 IEEE Electrical Power and Energy Conference (EPEC)*, pp. 1–4, IEEE, 2018.

[101] S.-B. Park, H.-B. Lee, S.-Y. Hahn, and I.-H. Park, "Stator slot shape design of induction motors for iron loss reduction," *IEEE transactions on magnetics*, vol. 31, no. 3, pp. 2004–2007, 1995.

[102] S.-H. Lee, D.-H. Kim, J.-H. Lee, B.-S. Kim, and I.-H. Park, "Shape design sensitivity for force density distribution of magnetic systems," *IEEE transactions on applied superconductivity*, vol. 12, no. 1, pp. 1471–1474, 2002.

[103] K. H. Lee, S. G. Hong, M. K. Baek, H. S. Choi, Y. S. Kim, and I. H. Park, "Adaptive level set method for accurate boundary shape in optimization of electromagnetic systems," *COMPEL: The International Journal for Computation and Mathematics in Electrical and Electronic Engineering*, 2014.

[104] K. H. Lee, C. Y. Choi, and I. H. Park, "Continuum sensitivity analysis and shape optimization of dirichlet conductor boundary in electrostatic system," *IEEE Transactions on Magnetics*, vol. 54, no. 3, pp. 1–4, 2017.

[105] I.-H. Park, J.-L. Coulomb, and S.-Y. Hahn, "Implementation of continuum sensitivity analysis with existing finite element code," *IEEE transactions on magnetics*, vol. 29, no. 2, pp. 1787–1790, 1993.

[106] E. Kuci, F. Henrotte, P. Duysinx, P. Dular, and C. Geuzaine, "Design sensitivity analysis for shape optimization of nonlinear magnetostatic systems," *IEEE Transactions on Magnetics*, vol. 52, no. 3, pp. 1–4, 2015.

[107] M. H. Bakr, O. S. Ahmed, M. H. El Sherif, and T. Nomura, "Time domain adjoint sensitivity analysis of electromagnetic problems with nonlinear media," *Optics express*, vol. 22, no. 9, pp. 10831–10843, 2014.

[108] S. Akbarzadeh, J. Hückelheim, and J.-D. Müller, "Consistent treatment of incompletely converged iterative linear solvers in reverse-mode algorithmic differentiation," *Computational Optimization and Applications*, vol. 77, no. 2, pp. 597–616, 2020.

[109] W. R. W. Mohd and L. Abdullah, "Aggregation methods in group decision making: A decade survey," *Informatica*, vol. 41, no. 1, 2017.

[110] C. Sauvey, J.-F. Antoine, C. Visa, and G. Abba, "Optimization of the design for a switched reluctance drive controlled by trapezoidal shaped currents," in *Proceedings of the 44th IEEE Conference on Decision and Control*, pp. 3892–3897, IEEE, 2005.

[111] G. Lei, J. Zhu, Y. Guo, C. Liu, and B. Ma, "A review of design optimization methods for electrical machines," *Energies*, vol. 10, no. 12, p. 1962, 2017.

[112] Y. Göynük, "Development of an electrical machines analysis and optimum design software package," Master's thesis, Middle East Technical University, 2008.

[113] X.-S. Yang, *Engineering mathematics with examples and applications*. Academic Press, 2016.

[114] V. Dehdari and D. S. Oliver, "Sequential quadratic programming for solving constrained production optimization–case study from brugge field," *SPE journal*, vol. 17, no. 03, pp. 874–884, 2012.

[115] G. Astfalk, I. Lustig, R. Marsten, and D. Shanno, "The interior-point method for linear programming," *IEEE software*, vol. 9, no. 4, pp. 61–68, 1992.

[116] R. H. Hoppe, C. Linsenmann, and S. I. Petrova, "Primal-dual newton methods in structural optimization," *Computing and Visualization in Science*, vol. 9, no. 2, pp. 71–87, 2006.

[117] D. Den Hertog, *Interior point approach to linear, quadratic and convex programming: algorithms and complexity*, vol. 277. Springer Science & Business Media, 2012.

[118] R. Poli, J. Kennedy, and T. Blackwell, "Particle swarm optimization," *Swarm intelligence*, vol. 1, no. 1, pp. 33–57, 2007.

[119] W. Hu and G. G. Yen, "Adaptive multiobjective particle swarm optimization based on parallel cell coordinate system," *IEEE Transactions on Evolutionary Computation*, vol. 19, no. 1, pp. 1–18, 2013.

[120] C. Ma and L. Qu, "Multiobjective optimization of switched reluctance motors based on design of experiments and particle swarm optimization," *IEEE Transactions on Energy Conversion*, vol. 30, no. 3, pp. 1144–1153, 2015.

[121] M. Reyes-Sierra, C. C. Coello, *et al.*, "Multi-objective particle swarm optimizers: A survey of the state-of-the-art," *International journal of computational intelligence research*, vol. 2, no. 3, pp. 287–308, 2006.

[122] S. Kirkpatrick, C. D. Gelatt Jr, and M. P. Vecchi, "Optimization by simulated annealing," *science*, vol. 220, no. 4598, pp. 671–680, 1983.

[123] R. Naayagi and V. Kamaraj, "A comparative study of shape optimization of srm using genetic algorithm and simulated annealing," in *2005 annual IEEE India conference-INDICON*, pp. 596–599, IEEE, 2005.

[124] P. Guo, X. Wang, and Y. Han, "The enhanced genetic algorithms for the optimization design," in *2010 3rd international conference on biomedical engineering and informatics*, vol. 7, pp. 2990–2994, IEEE, 2010.

[125] C. W. Ahn, *Advances in evolutionary algorithms*. Springer, 2006.

[126] M. Gendreau, J.-Y. Potvin, *et al.*, *Handbook of metaheuristics*, vol. 2. Springer, 2010.

[127] B. Wang, "A novel artificial bee colony algorithm based on modified search strategy and generalized opposition-based learning," *Journal of Intelligent & Fuzzy Systems*, vol. 28, no. 3, pp. 1023–1037, 2015.

[128] F. S. Abu-Mouti and M. El-Hawary, "Optimal distributed generation allocation and sizing in distribution systems via artificial bee colony algorithm," *IEEE transactions on power delivery*, vol. 26, no. 4, pp. 2090–2101, 2011.

[129] L. Cheng, M. Yu, J. Yang, and Y. Wang, "An improved artificial bee colony algorithm based on beetle antennae search," in *2019 Chinese Control Conference (CCC)*, pp. 2312–2316, IEEE, 2019.

[130] X.-S. Yang, Z. Cui, R. Xiao, A. H. Gandomi, and M. Karamanoglu, *Swarm intelligence and bio-inspired computation: theory and applications*. Newnes, 2013.

[131] D. Fodorean, L. Idoumghar, A. N'diaye, D. Bouquain, and A. Miraoui, "Simulated annealing algorithm for the optimisation of an electrical machine," *IET electric power applications*, vol. 6, no. 9, pp. 735–742, 2012.

[132] A.-H. Zhou, L.-P. Zhu, B. Hu, S. Deng, Y. Song, H. Qiu, and S. Pan, "Traveling-salesman-problem algorithm based on simulated annealing and gene-expression programming," *Information*, vol. 10, no. 1, p. 7, 2018.

[133] X. Dong, D. Ouyang, D. Cai, Y. Zhang, and Y. Ye, "A hybrid discrete pso-sa algorithm to find optimal elimination orderings for bayesian networks," in *2010 2nd International Conference on Industrial and Information Systems*, vol. 1, pp. 510–513, IEEE, 2010.

[134] R. L. Haupt, "An introduction to genetic algorithms for electromagnetics," *IEEE Antennas and Propagation Magazine*, vol. 37, no. 2, pp. 7–15, 1995.

[135] A. Plerou, E. Vlamou, and V. Papadopoulos, "Fuzzy genetic algorithms: Fuzzy logic controllers and genetics algorithms," *Global Journal For Research Analysis*, vol. 5, no. 11, pp. 497–500, 2016.

[136] M. Vannucci, V. Colla, S. Dettori, and V. Iannino, "Fuzzy adaptive genetic algorithm for improving the solution of industrial optimization problems," *Journal of Intelligent Systems*, vol. 29, no. 1, pp. 409–422, 2020.

[137] A. Conn, N. Gould, and P. Toint, "A globally convergent lagrangian barrier algorithm for optimization with general inequality constraints and simple bounds," *Mathematics of Computation*, vol. 66, no. 217, pp. 261–288, 1997.

[138] J.-Y. Lee, J.-H. Chang, D.-H. Kang, S.-I. Kim, and J.-P. Hong, "Tooth shape optimization for cogging torque reduction of transverse flux rotary motor using design of experiment and response surface methodology," *IEEE Transactions on Magnetics*, vol. 43, no. 4, pp. 1817–1820, 2007.

[139] G. G. Wang, "Adaptive response surface method using inherited latin hypercube design points," *J. Mech. Des.*, vol. 125, no. 2, pp. 210–220, 2003.

[140] C. Huang and G. Yang, "Optimization design of switched reluctance motor based on response surface method," in *2018 IEEE Student Conference on Electric Machines and Systems*, pp. 1–6, IEEE, 2018.

[141] R. Tugrul Ogulata and S. Mavruz Mezarcioz, "Optimization of air permeability of knitted fabrics with the taguchi approach," *The Journal of the Textile Institute*, vol. 102, no. 5, pp. 395–404, 2011.

[142] Y. Gong, S. Zhao, and S. Luo, "Design and optimization of switched reluctance motor by taguchi method," in *2018 13th IEEE Conference on Industrial Electronics and Applications (ICIEA)*, pp. 1876–1880, IEEE, 2018.

[143] K. Diao, X. Sun, G. Lei, G. Bramerdorfer, Y. Guo, and J. Zhu, "Robust design optimization of switched reluctance motor drive systems based on system-level sequential taguchi method," *IEEE Transactions on Energy Conversion*, vol. 36, no. 4, pp. 3199–3207, 2021.

[144] W. Yan, H. Chen, X. Liu, X. Ma, Z. Lv, X. Wang, R. Palka, L. Chen, and K. Wang, "Design and multi-objective optimisation of switched reluctance machine with iron loss," *IET Electric Power Applications*, vol. 13, no. 4, pp. 435–444, 2019.

[145] M. Afifi, H. Rezk, M. Ibrahim, and M. El-Nemr, "Multi-objective optimization of switched reluctance machine design using jaya algorithm (mo-jaya)," *Mathematics*, vol. 9, no. 10, p. 1107, 2021.

[146] X. Gao, R. Na, C. Jia, X. Wang, and Y. Zhou, "Multi-objective optimization of switched reluctance motor drive in electric vehicles," *Computers & Electrical Engineering*, vol. 70, pp. 914–930, 2018.

[147] O. B. Augusto, F. Bennis, and S. Caro, "A new method for decision making in multi-objective optimization problems," *Pesquisa Operacional*, vol. 32, pp. 331–369, 2012.

[148] R. REBBAH, B. H. R. EL-HANA, B. AMAR, and R. FARES, "Multi-objective optimization design of 8/6 switched reluctance motor using ga and pso algorithms," *Journal of Electrical Engineering*, vol. 15, no. 4, pp. 8–8, 2015.

[149] R. Naayagi and V. Kamaraj, "Shape optimization of switched reluctance machine for aerospace applications," in *31st Annual Conference of IEEE Industrial Electronics Society, 2005. IECON 2005.*, pp. 4–pp, IEEE, 2005.

[150] M. Belhadi, G. Krebs, C. Marchand, H. Hannoun, and X. Mininger, "Geometrical optimization of srm on operating mode for automotive application," *Electrical Engineering*, vol. 100, no. 1, pp. 303–310, 2018.

[151] J. Zhang, H. Wang, L. Chen, C. Tan, and Y. Wang, "Multi-objective optimal design of bearingless switched reluctance motor based on multi-objective genetic particle swarm optimizer," *IEEE Transactions on Magnetics*, vol. 54, no. 1, pp. 1–13, 2017.

[152] J. Gao, H. Sun, L. He, Y. Dong, and Y. Zheng, "Optimization design of switched reluctance motor based on particle swarm optimization," in *2011 International Conference on Electrical Machines and Systems*, pp. 1–5, IEEE, 2011.

[153] X. Xue, K. W. E. Cheng, T. W. Ng, and N. C. Cheung, "Multi-objective optimization design of in-wheel switched reluctance motors in electric vehicles," *IEEE Transactions on industrial electronics*, vol. 57, no. 9, pp. 2980–2987, 2010.

[154] M. Balaji and V. Kamaraj, "Design optimization of switched reluctance machine using particle swarm optimization," in *2011 1st International Conference on Electrical Energy Systems*, pp. 164–169, IEEE, 2011.

[155] A. Oshaba, E. S. Ali, and S. M. Abd Elazim, "Speed control of srm supplied by photovoltaic system via ant colony optimization algorithm," *Neural Computing and Applications*, vol. 28, no. 2, pp. 365–374, 2017.

[156] H. Torkaman, E. Afjei, H. Babaee, and P. Yadegari, "Novel method of aco and its application to rotor position estimation in a srm under normal and faulty conditions," *Journal of Power Electronics*, vol. 11, no. 6, pp. 856–863, 2011.

[157] M. Yaich and M. Ghariani, "Metaheuristic design and optimization of fuzzy-based srm speed controller using ant colony algorithm," *J. Eng. Appl. Sci.*, vol. 12, no. 23, pp. 7382–7388, 2017.

[158] S. S. Kumar, J. Jayakumar, *et al.*, "Torque modeling of switched reluctance motor using lssvm-de," *Neurocomputing*, vol. 211, pp. 117–128, 2016.

[159] J. Liu, L. Wang, L. Yi, G. Zhu, and X. Yin, "Optimization of srm direct instantaneous torque control strategy based on improved firefly algorithm," in *2019 IEEE 3rd Conference on Energy Internet and Energy System Integration (EI2)*, pp. 364–368, IEEE, 2019.

[160] A. YILDIZ, M. POLAT, and M. T. Özdemir, "Design optimization of inverted switched reluctance motor using ant colony optimization algorithm," in *2018 International Conference on Artificial Intelligence and Data Processing (IDAP)*, pp. 1–6, IEEE, 2018.

[161] S. Dufour, G. Vinsard, and B. Laporte, "Generating rotor geometries by using a genetic method," *IEEE Transactions on Magnetics*, vol. 36, no. 4, pp. 1039–1042, 2000.

[162] L. Moreau, M. Zaïm, and M. Machmoum, "Electromagnetic design optimization of a low speed slotted switched reluctance machine using genetic algorithm," in *2012 XXth International Conference on Electrical Machines*, pp. 233–237, IEEE, 2012.

[163] S. Owatchaiphong, C. Carstensen, and R. W. De Doncker, "Optimization of predesign of switched reluctance machines cross section using genetic algorithms," in *2007 7th International Conference on Power Electronics and Drive Systems*, pp. 707–711, IEEE, 2007.

[164] A. El-Wakeel and A. Smith, "Optimal design of switched reluctance motors using genetic algorithms," in *Proceedings of ICEM*, 2002.

[165] S. Smaka, S. Konjicija, S. Masic, and M. Cosovic, "Multi-objective design optimization of 8/14 switched reluctance motor," in *2013 International Electric Machines & Drives Conference*, pp. 468–475, IEEE, 2013.

[166] S. I. Nabeta, I. E. Chabu, L. Lebensztajn, D. Correa, W. Da Silva, and K. Hameyer, "Mitigation of the torque ripple of a switched reluctance motor through a multiobjective optimization," *IEEE Transactions on Magnetics*, vol. 44, no. 6, pp. 1018–1021, 2008.

[167] X. Cui, J. Sun, C. Gan, C. Gu, and Z. Zhang, "Optimal design of saturated switched reluctance machine for low speed electric vehicles by subset quasi-orthogonal algorithm," *IEEE Access*, vol. 7, pp. 101086–101095, 2019.

[168] E. Öksüztepe, "In-wheel switched reluctance motor design for electric vehicles by using a pareto-based multiobjective differential evolution algorithm," *IEEE Transactions on Vehicular Technology*, vol. 66, no. 6, pp. 4706–4715, 2016.

[169] A. M. Omekanda, "Robust torque-and torque-per-inertia optimization of a switched reluctance motor using the taguchi methods," in *IEEE International Conference on Electric Machines and Drives, 2005.*, pp. 521–526, IEEE, 2005.

[170] S. A. Pardo, "Taguchi methods® and robust design," in *Empirical Modeling and Data Analysis for Engineers and Applied Scientists*, pp. 223–239, Springer, 2016.

[171] J. G. Amorós, P. Andrada, B. Blanque, and M. Marin-Genesca, "Influence of design parameters in the optimization of linear switched reluctance motor under thermal constraints," *IEEE Transactions on Industrial Electronics*, vol. 65, no. 2, pp. 1875–1883, 2017.

[172] C. K. Yeo, M. M. Ghazaly, S. H. Chong, and I. W. Jamaludin, "A review: Design variables optimization and control strategies of a linear switched reluctance actuator for high precision applications," *International Journal of Power Electronics and Drive Systems*, vol. 8, no. 2, p. 963, 2017.

[173] M. R. Soltanpour, H. Abdollahi, and S. Masoudi, "Optimisation of double-sided linear switched reluctance motor for mass and force ripple minimisation," *IET Science, Measurement & Technology*, vol. 13, no. 4, pp. 509–517, 2019.

[174] D. Wang, X. Du, D. Zhang, and X. Wang, "Design, optimization, and prototyping of segmental-type linear switched-reluctance motor with a toroidally

wound mover for vertical propulsion application," *IEEE transactions on industrial electronics*, vol. 65, no. 2, pp. 1865–1874, 2017.

[175] J. Faiz and J. W. Finch, "Aspects of design optimisation for switched reluctance motors," *IEEE Transactions on Energy conversion*, vol. 8, no. 4, pp. 704–713, 1993.

[176] X. Song, Y. Park, J. Li, and J. Lee, "Optimization of switched reluctance motor for efficiency improvement using response surface model and kriging model," in *2011 Fourth International Joint Conference on Computational Sciences and Optimization*, pp. 259–260, IEEE, 2011.

[177] M. Balaji and V. Kamaraj, "Particle swarm optimization approach for optimal design of switched reluctance machine," *American Journal of Applied Sciences*, vol. 8, no. 4, p. 374, 2011.

[178] J. Ma, J. Li, H. Fang, Z. Li, Z. Liang, Z. Fu, L. Xiao, and R. Qu, "Optimal design of an axial-flux switched reluctance motor with grain-oriented electrical steel," *IEEE Transactions on Industry Applications*, vol. 53, no. 6, pp. 5327–5337, 2017.

[179] M. R. Soltanpour, H. Abdollahi, and S. Masoudi, "Optimisation of double-sided linear switched reluctance motor for mass and force ripple,"

[180] F. Sahin, H. B. Ertan, and K. Leblebicioglu, "Optimum geometry for torque ripple minimization of switched reluctance motors," *IEEE Transactions on Energy Conversion*, vol. 15, no. 1, pp. 30–39, 2000.

[181] Z.-L. Gaing, Y.-Y. Hsiah, M.-C. Tsai, M.-F. Hsieh, and M.-H. Tsai, "Hybrid design model for optimal designing of a switched reluctance motor," in *2013 International Conference on Electrical Machines and Systems (ICEMS)*, pp. 505–510, IEEE, 2013.

[182] Z. Zhang, K. W. E. Cheng, N. C. Cheung, X. Xue, and J. Lin, "Design optimization of a multi-modular linear switched reluctance actuator," in *2013 5th International Conference on Power Electronics Systems and Applications (PESA)*, pp. 1–6, IEEE, 2013.

[183] A. S. El-Wakeel, *Design optimisation for fault tolerant switched reluctance motors*. PhD thesis, Ph. D. dissertation, Dept. Elec. Eng. and Electronics, Univ. MIST, Manchester, 2003.

[184] F. Cupertino, G. Pellegrino, and C. Gerada, "Design of synchronous reluctance motors with multiobjective optimization algorithms," *IEEE Transactions on Industry Applications*, vol. 50, no. 6, pp. 3617–3627, 2014.

[185] J. Barta and C. Ondrusek, "Rotor design and optimization of synchronous reluctance machine," *Science journal*, pp. 555–559, 2015.

[186] G. Pellegrino, F. Cupertino, and C. Gerada, "Barriers shapes and minimum set of rotor parameters in the automated design of synchronous reluctance machines," in *2013 International Electric Machines & Drives Conference*, pp. 1204–1210, IEEE, 2013.

[187] S. Sato, T. Sato, and H. Igarashi, "Topology optimization of synchronous reluctance motor using normalized gaussian network," *IEEE transactions on magnetics*, vol. 51, no. 3, pp. 1–4, 2015.

[188] M. P. Bendsøe, "Optimal shape design as a material distribution problem," *Structural optimization*, vol. 1, no. 4, pp. 193–202, 1989.

[189] J.-k. Byun and S.-y. Hahn, "Topology optimization of switched reluctance motor using mutual energy method," *International Journal Of Applied Electromagnetics And Mechanics*, vol. 13, no. 1-4, pp. 421–426, 2002.

[190] E. M. Dede, T. Nomura, and J. Lee, "Multiphysics simulation," *Springer-Verlag London*, 2014.

[191] A. Manninen, J. Keränen, J. Pippuri-Mäkeläinen, S. Metsä-Kortelainen, T. Riipinen, and T. Lindroos, "Topology optimization for additive manufacturing of switced reluctance machines," in *Presented at CEFC 2018*, 2018.

[192] A. Manninen, J. Keränen, J. Pippuri-Mäkeläinen, T. Riipinen, S. Metsä-Kortelainen, and T. Lindroos, "Impact of topology optimization problem setup on switched reluctance machine design," in *2019 22nd International Conference on the Computation of Electromagnetic Fields (COMPUMAG)*, pp. 1–4, IEEE, 2019.

[193] Y. S. Kim and I. H. Park, "Topology optimization of rotor in synchronous reluctance motor using level set method and shape design sensitivity," *IEEE Transactions on Applied Superconductivity*, vol. 20, no. 3, pp. 1093–1096, 2010.

[194] K. Watanabe, T. Suga, and S. Kitabatake, "Topology optimization based on the on/off method for synchronous motor," *IEEE Transactions on Magnetics*, vol. 54, no. 3, pp. 1–4, 2017.

[195] J. Lee, *Structural design optimization of electric motors to improve torque performance*. PhD thesis, University of Michigan, 2010.

[196] Y. Okamoto, R. Hoshino, S. Wakao, and T. Tsuburaya, "Improvement of torque characteristics for a synchronous reluctance motor using mma-based topology optimization method," *IEEE transactions on magnetics*, vol. 54, no. 3, pp. 1–4, 2017.

[197] S. Liu, Q. Li, J. Liu, W. Chen, and Y. Zhang, "A realization method for transforming a topology optimization design into additive manufacturing structures," *Engineering*, vol. 4, no. 2, pp. 277–285, 2018.

[198] F. Zhao and R. Yan, "Topology optimization of magnetic actuator using the improved on/off method," in *2012 Sixth International Conference on Electromagnetic Field Problems and Applications*, pp. 1–4, IEEE, 2012.

[199] Y. Okamoto, K. Akiyama, and N. Takahashi, "3-d topology optimization of single-pole-type head by using design sensitivity analysis," *IEEE Transactions on Magnetics*, vol. 42, no. 4, pp. 1087–1090, 2006.

[200] T. Ishikawa, K. Nakayama, N. Kurita, and F. P. Dawson, "Optimization of rotor topology in pm synchronous motors by genetic algorithm considering cluster of materials and cleaning procedure," *IEEE transactions on magnetics*, vol. 50, no. 2, pp. 637–640, 2014.

[201] Y. Okamoto, Y. Tominaga, S. Wakao, and S. Sato, "Topology optimization of rotor core combined with identification of current phase angle in ipm motor using multistep genetic algorithm," *IEEE transactions on magnetics*, vol. 50, no. 2, pp. 725–728, 2014.

[202] T. Sato, K. Watanabe, and H. Igarashi, "A modified immune algorithm with spatial filtering for multiobjective topology optimisation of electromagnetic devices," *COMPEL: The International Journal for Computation and Mathematics in Electrical and Electronic Engineering*, vol. 33, no. 3, pp. 821–833, 2014.

[203] T. Sato, K. Watanabe, and H. Igarashi, "Multimaterial topology optimization of electric machines based on normalized gaussian network," *IEEE transactions on magnetics*, vol. 51, no. 3, pp. 1–4, 2015.

[204] F. Shiyang and K. Watanabe, "Topology optimization of rotor design in switched reluctance motor using immune algorithm," *International Journal of Applied Electromagnetics and Mechanics*, vol. 64, no. 1-4, pp. 413–420, 2020.

[205] S. Lammers, G. Adam, H. J. Schmid, R. Mrozek, R. Oberacker, M. J. Hoffmann, F. Quattrone, and B. Ponick, "Additive manufacturing of a lightweight rotor for a permanent magnet synchronous machine," in *2016 6th International Electric Drives Production Conference (EDPC)*, pp. 41–45, IEEE, 2016.

[206] T. Riipinen, S. Metsä-Kortelainen, T. Lindroos, J. S. Keränen, A. Manninen, and J. Pippuri-Mäkeläinen, "Properties of soft magnetic fe-co-v alloy produced by laser powder bed fusion," *Rapid Prototyping Journal*, vol. 25, no. 4, pp. 699–707, 2019.

[207] T. Labbe and B. Dehez, "Topology optimization method based on the maxwell stress tensor for the design of ferromagnetic parts in electromagnetic actuators," *IEEE transactions on magnetics*, vol. 47, no. 9, pp. 2188–2193, 2011.

[208] S. Metsä-Kortelainen, T. Lindroos, M. Savolainen, A. Jokinen, A. Revuelta, A. Pasanen, K. Ruusuvuori, and J. Pippuri, "Manufacturing of topology optimized soft magnetic core through 3d printing," in *NAFEMS Exploring the Design Freedom of Additive Manufacturing through Simulation*, 2016.

[209] H. Zhang and S. Wang, "Topology optimization of rotor pole in switched reluctance motor for minimum torque ripple," *Electric Power Components and Systems*, vol. 45, no. 8, pp. 905–911, 2017.

[210] M. Tahkola, J. Keränen, D. Sedov, M. F. Far, and J. Kortelainen, "Surrogate modeling of electrical machine torque using artificial neural networks," *IEEE Access*, vol. 8, pp. 220027–220045, 2020.

[211] R. H. Myers, D. C. Montgomery, and C. M. Anderson-Cook, *Response surface methodology: process and product optimization using designed experiments*. John Wiley & Sons, 2016.

[212] Y. Duan and D. M. Ionel, "A review of recent developments in electrical machine design optimization methods with a permanent-magnet synchronous motor benchmark study," *IEEE Transactions on Industry Applications*, vol. 49, no. 3, pp. 1268–1275, 2013.

[213] S. Xiao, M. Rotaru, and J. K. Sykulski, "Adaptive weighted expected improvement with rewards approach in kriging assisted electromagnetic design," *IEEE Transactions on magnetics*, vol. 49, no. 5, pp. 2057–2060, 2013.

[214] G. Crevecoeur, L. Dupré, and R. Van de Walle, "Space mapping optimization of the magnetic circuit of electrical machines including local material degradation," *IEEE transactions on magnetics*, vol. 43, no. 6, pp. 2609–2611, 2007.

[215] S. Shimokawa, H. Oshima, K. Shimizu, Y. Uehara, J. Fujisaki, A. Furuya, and H. Igarashi, "Fast 3-d optimization of magnetic cores for loss and volume reduction," *IEEE Transactions on Magnetics*, vol. 54, no. 11, pp. 1–4, 2018.

[216] J. Asanuma, S. Doi, and H. Igarashi, "Transfer learning through deep learning: application to topology optimization of electric motor," *IEEE transactions on magnetics*, vol. 56, no. 3, pp. 1–4, 2020.

[217] D. Zhong, Y. Yang, and X. Du, "Palmprint recognition using siamese network," in *Chinese conference on biometric recognition*, pp. 48–55, Springer, 2018.

[218] S. Doi, H. Sasaki, and H. Igarashi, "Multi-objective topology optimization of rotating machines using deep learning," *IEEE transactions on magnetics*, vol. 55, no. 6, pp. 1–5, 2019.

[219] N. Bianchi, *Electrical machine analysis using finite elements*. CRC press, 2017.

[220] S. J. Salon, *Finite element analysis of electrical machines*, vol. 101. Kluwer academic publishers Boston, 1995.

[221] N. Sadowski, Y. Lefèvre, M. Lajoie-Mazenc, and J. Cros, "Finite element torque calculation in electrical machines while considering the movement," *IEEE transactions on magnetics*, vol. 28, no. 2, pp. 1410–1413, 1992.

[222] M. Popescu, D. Ionel, T. Miller, S. Dellinger, and M. McGilp, "Improved finite element computations of torque in brushless permanent magnet motors," *IEE Proceedings-Electric Power Applications*, vol. 152, no. 2, pp. 271–276, 2005.

[223] I. Lolova, J. Barta, G. Bramerdorfer, and S. Silber, "Topology optimization of line-start synchronous reluctance machine," in *2020 19th International Conference on Mechatronics-Mechatronika (ME)*, pp. 1–7, IEEE, 2020.

[224] H. S. Forberg, T. F. Nygaard, and M. E. Høvin, "Generative truss optimization for support-free fused filament fabrication," in *2020 International Conference on Computational Science and Computational Intelligence (CSCI)*, pp. 1491–1497, IEEE, 2020.

[225] T. H. T. Tran, D. S. Nguyen, N. T. Vo, and H. N. Le, "Design of delta robot arm based on topology optimization and generative design method," in *2020 5th International Conference on Green Technology and Sustainable Development (GTSD)*, pp. 157–161, IEEE, 2020.

[226] N. Takahashi, S. Nakazaki, and D. Miyagi, "Examination of optimal design method of electromagnetic shield using on/off method," *IEEE transactions on magnetics*, vol. 45, no. 3, pp. 1546–1549, 2009.

[227] M. Kasprzak, *6/14 Switched Reluctance Machine Design for Household HVAC System Applications*. PhD thesis, 2017.

[228] "Somaloy 3p material data - höganäs ab." Available: https://www.hoganas.com/globalassets/download-media/sharepoint/brochures-and-datasheets---all-documents/somaloy_somaloy-3p-material-data_2273hog.pdf. 08-Oct-2022.

[229] "Somaloy höganäs." https://www.hoganas.com/en/powder-technologies/soft-magnetic-composites. 08-Oct-2022.

[230] T. N. Lamichhane, L. Sethuraman, A. Dalagan, H. Wang, J. Keller, and M. P. Paranthaman, "Additive manufacturing of soft magnets for electrical machines—a review," *Materials Today Physics*, vol. 15, p. 100255, 2020.

[231] M. U. Naseer, A. Kallaste, B. Asad, T. Vaimann, and A. Rassõlkin, "A review on additive manufacturing possibilities for electrical machines," *Energies*, vol. 14, no. 7, p. 1940, 2021.

[232] Z. Lin, D. S. Reay, B. W. Williams, and X. He, "Torque ripple reduction in switched reluctance motor drives using b-spline neural networks," *IEEE Transactions on Industry Applications*, vol. 42, no. 6, pp. 1445–1453, 2006.

[233] X. Sun, J. Wu, G. Lei, Y. Guo, and J. Zhu, "Torque ripple reduction of srm drive using improved direct torque control with sliding mode controller and observer," *IEEE Transactions on Industrial Electronics*, vol. 68, no. 10, pp. 9334–9345, 2020.

[234] M. L. Kimpara, R. R. Reis, L. E. Da Silva, J. O. Pinto, and B. Fahimi, "A two-step control approach for torque ripple and vibration reduction in switched reluctance motor drives," *IEEE Access*, vol. 10, pp. 82106–82118, 2022.

[235] "Somaloy höganäs." Available:https://www.hoganas.com/en/powder-technologies/soft-magnetic-composites. Accessed: 2022-11-10.

[236] "Somaloy 3p material data - höganäs ab." Available: https://www.hoganas.com/globalassets/download-media/sharepoint/brochures-and-datasheets---all-documents/somaloy_somaloy-3p-material-data_2273hog.pdf.. Accessed: 2022-11-10.

[237] J. Li, X. Song, and Y. Cho, "Comparison of 12/8 and 6/4 switched reluctance motor: Noise and vibration aspects," *IEEE transactions on magnetics*, vol. 44, no. 11, pp. 4131–4134, 2008.

[238] J. Liang, B. Howey, B. Bilgin, and A. Emadi, "Source of acoustic noise in a 12/16 external-rotor switched reluctance motor: Stator tangential vibration and rotor radial vibration," *IEEE Open Journal of Industry Applications*, vol. 1, pp. 63–73, 2020.

[239] G. F. Lukman and J.-W. Ahn, "Radial force reduction method of switched reluctance motor with partial holes in the rotor," *Journal of Electrical Engineering & Technology*, vol. 17, no. 3, pp. 1775–1784, 2022.

[240] M. E. Abdollahi, N. Vaks, and B. Bilgin, "A multi-objective optimization framework for the design of a high power-density switched reluctance motor," in *2022 IEEE Transportation Electrification Conference & Expo (ITEC)*, pp. 67–73, IEEE, 2022.

[241] M. Zhang, I. Bahri, X. Mininger, C. Vlad, and E. Berthelot, "Vibration reduction control of switched reluctance machine," *IEEE Transactions on Energy Conversion*, vol. 34, no. 3, pp. 1380–1390, 2019.

[242] P. Azer, B. Bilgin, and A. Emadi, "Mutually coupled switched reluctance motor: fundamentals, control, modeling, state of the art review and future trends," *IEEE Access*, vol. 7, pp. 100099–100112, 2019.